CARDIFF UNIVERSITY
PRIFYSGOL CAERDYDD

A Study of the Hydrogen Evolution Reaction on Platinum and Platinum Group Metal Surfaces.

Simon Smale

Ph.D Thesis 2008

ProQuest LLC
789 East Eisenhower Parkway
P.O. Box 1346
Ann Arbor, MI 48106-1346

Summary

The hydrogen evolution reaction (HER) has been examined on a variety of Pt and Pt-group metal surfaces to investigate the rate of the reaction. Pt stepped single crystal surfaces were investigated in relation to the HER using cyclic voltammetry, linear sweep voltammetry and multi-frequency AC voltammetry. It was found that the hydrogen evolution reaction activity did not show a dependence on the structure of single crystal platinum electrode surfaces. Thick films of Au, Rh and Pd were deposited onto Pt{111} and successfully annealed to give pseudomorphic surfaces of the bulk metal. The aim of such measurements was to investigate whether strains within the crystal lattice of these films would result in enhanced HER activity. None of the surfaces investigated showed significant HER enhancement. Rather, results similar to those observed using the bulk metals were obtained.

Rough Ir and Pt deposits on Pt{111} were also investigated. Enhanced HER activity was observed on these surfaces. This enhancement was interpreted in terms of the structural arrangement of the Ir and Pt deposits.

For Pd films on Pt{111} ($0 < \theta_{Pd} < 2$ monolayers); it was observed that Pt dominated the HER kinetics for Pd coverages up to one monolayer and was still influential on the HER at two monolayers of Pd. Similarly Pd-Pt surface alloys also showed that Pd had little or no influence on the HER kinetics even with 75 % Pd in the surface layer. Possible mechanisms for this behaviour have been proposed, in particular, the role of subsurface hydrogen in HER on Pt is discussed.

List of Symbols

English

Symbol	Description	Units
A	Electrode area	cm^2
A_{int}	Magnitude of attractive/repulsive interactions	(none)
a_i	Activity of species i	(none)
C	Capacitance	F
C_{DL}	Double Layer Capacitance	F
C_i^*	Bulk concentration of species i	mol cm^{-3}
C_i^σ	Surface concentration of species i	mol cm^{-3}
D_o	Diffusion coefficient	$cm^2\ s^{-1}$
d	distance between capacitor plates	cm
D_H	Diffusivity of hydrogen in solution	$cm^2\ s^{-1}$
d_{Pt}	Atomic diameter of Pt = 2.78 x 10^{-10}	m
E	Generalised potential	V
$\dot{E}$	Sinusoidal potential vector	V
E^0	Standard cell potential	V
$E^{0'}$	Formal potential of a reaction	V
e_0	Elementary charge = 1.602 x 10^{-19}	C
E_{AC}	AC potential	V
E_{DC}	DC potential	V
E_p^{Ox}	Potential of oxidation current peak	V
E_p^{Red}	Potential of reduction current peak	V
F	Faraday Constant = 9.649 x 10^4	C
ΔG	Gibbs free energy	J
$\Delta G°$	Standard Gibbs free energy	J
h	Planck constant = 3.626 x 10^{-34}	J s^{-1}
$\Delta H^{0\#}$	Activation energy of hydrogen oxidation	J mol^{-1}

Symbol	Description	Units
ΔH_D^o	Standard enthalpy of adsorption	J mol^{-1}
ΔH_{vap}^o	Standard heat of adsorption	J mol^{-1}
I	Generalised current	A
$\dot{I}$	Sinusoidal current vector	A
I_{DC}	DC current	A
I_{AC}	AC Current	A
i_0	Exchange current	A
i_d	Diffusion limited current	A
i_p	Peak current	A
j	Current density	A cm^{-2}
j_0	Exchange current density	A cm^{-2}
j_d	Diffusion limited current density	A cm^{-2}
j_{im}	Imaginary number = $\sqrt{-1}$	(none)
j_k	Current density in absence of mass transport effects	A cm^{-2}
k^0	Standard rate constant	cm s^{-1}
K_1	k_1/k_{-1} ratio	mol^{-1} cm^3
k_1	Forward Volmer rate constant	cm s^{-1}
k_1^o	Standard forward Volmer rate constant	cm s^{-1}
k_{-1}	Backward Volmer rate constant	mol cm^{-2} s^{-1}
k_{-1}^o	Standard backward Volmer rate constant	mol cm^{-2} s^{-1}
K_2	k_2/k_{-2} ratio	(none)
k_2	Forward Tafel rate constant	cm s^{-1}
k_{-2}	Backward Tafel rate constant	cm s^{-1}
K_3	k_3/k_{-3} ratio	mol^{-1} cm^3
k_3	Forward Heyrovsky rate constant	cm s^{-1}
k_{-3}	Backward Heyrovsky rate constant	mol cm^{-2} s^{-1}
k_a	Associative adsorption rate constant	cm s^{-1}
k_a'	Dissociative adsorption rate constant	cm s^{-1}
k_B	Boltzmann constant = 1.38 x 10^{-23}	J K^{-1}

Symbol	Description	Units
k_d	Associative desorption rate constant	cm s^{-1}
k_d'	Dissociative desorption rate constant	cm s^{-1}
k_f	Homogeneous rate constant	cm s^{-1}
N	Number of available adsorption sites on a surface	(none)
N_A	Number of adsorbate molecules on a surface	(none)
N_{SD}	Crystallographic step density	m^{-1}
n	Number of electrons involved in a reaction	(none)
n_i	Stoichiometric coefficient of species i	(none)
P	Pressure	Pa
P_S	Saturated vapour pressure	Pa
Q	Charge	C
R_0	Pre-exponential factor of R_{CT}	Ω
R_{CT}	Charge transfer resistance	Ω
R_{DC}	DC resistance	Ω
R_g	Universal gas constant = 8.314	J mol^{-1} K^{-1}
R_S	Series resistance	Ω
R_Ω	Uncompensated solution resistance	Ω
s_0	Solubility of hydrogen	M
T	Temperature	K
t	Time	s
v	Potential scan rate	V s^{-1}
v_1	Volmer reaction rate	mol cm^{-2} s^{-1}
v_2	Tafel reaction rate	cm s^{-1}
v_3	Heyrovsky reaction rate	mol cm^{-2} s^{-1}
Y	Admittance density	Ω^{-1} cm^{-2}
Y_{lim}	Limiting admittance density	Ω^{-1} cm^{-2}
Z	Impedance	Ω
Z_f	Faradaic impedance	Ω
Z_{Im}	Imaginary component of impedance	Ω
Z_{Re}	Real component of impedance	Ω
Z_W	Warburg impedance	Ω

Greek Symbol	Description	Units
α	Transfer coefficient	(none)
γ'	kinematic viscosity	$cm^2\ s^{-1}$
$\gamma'_{F\ S}$	Surface free energy of a film	J
γ'_I	Interfacial energy between a film and a substrate	J
γ'_S	Surface free energy of a substrate	J
δ	Diffusion layer thickness	cm
ε	Dielectric constant of a material	(none)
ε_0	Permittivity of free space = 8.854×10^{-8}	$C^2\ N^{-1}\ cm^{-2}$
η	Overpotential	V
θ_i	Atomic surface coverage of species *i*	(none)
σ	Charge density	$C\ cm^{-2}$
ϕ	Phase angle	°
Φ_{Bi}	Fractional Bi surface coverage	(none)
ω	Rotational frequency	$rad\ s^{-1}$

Contents

Chapter 1 Introduction

1.1 Hydrogen as a fuel 1

1.2 The hydrogen evolution reaction 5

1.3 Hydrogen evolution on platinum group metals 9

1.4 Single crystal surfaces 12

1.4.1 Pt single crystals 12

1.4.2 Non-Pt single crystals 15

1.5 Deposition of metal films onto single crystal electrode surfaces 15

1.6 Hydrogen evolution on alloys 16

1.7 Project aims 18

Chapter 2 Theoretical Background

2.1 Analysis Methods 23

2.1.1 Direct Current Techniques 23

2.1.1.1 Linear Sweep Voltammetry/ Tafel Data 23

2.1.1.2 Cyclic Voltammetry 27

2.1.1.3 Rotating Disk Electrode 32

2.1.1.4 Chronoamperometry/Chronocoulometry 35

2.1.2 AC Techniques 36

2.1.2.1 AC Circuits 36

2.1.2.2 AC Impedance Spectroscopy 40

2.1.2.3 AC Voltammetry 41

2.1.2.4 Multi-Frequency AC Voltammetry 42

2.2 Preparation of electrodes 44

2.2.1 Electrodeposition 44

2.2.2 Thermal Decomposition 45

2.2.3 Flame and Plasma Spraying 46

2.2.4 Pressing and Sintering 47

2.2.5 Electroless Deposition 47

2.2.6 Single Crystals 48

2.3 Single crystal nomenclature 48

2.4 Reference electrodes 57

2.5 The electrical double layer 58
2.5.1 The Helmholtz model 58
2.5.2 The Gouy-Chapman model 59
2.5.3 The Stern model 61
2.5.4 The Grahame model 62
2.6 Growth modes of deposited metal layers 64
2.7 Adsorption isotherms 65
2.8 Types of adsorption 69

Chapter 3 Experimental

3.1 Rotating disc electrode experiments 73
3.1.1 Hydrogen oxidation on Pt 73
3.1.2 Hydrogen evolution 75
3.1.2.1 Electroplating Ru 75
3.2 Multi-Frequency AC Voltammetry (MFACV) 76
3.3 Single crystal cyclic voltammetry 77
3.4 Preparation of single crystal electrodes 80
3.5 Deposition of metal films onto Pt single crystals 82
3.6 CO and the hanging-meniscus and submerged-bead electrode configurations 83

Chapter 4 Results

4.1 Hydrogen evolution and hydrogen oxidation on polycrystalline Pt 86
4.1.1 Hydrogen electro-oxidation on polycrystalline Pt 86
4.1.1.1 HOR on Pt in 0.1 M $HClO_4$ 86
4.1.1.2 Pt in 0.05 M H_2SO_4 90
4.1.2 Hydrogen evolution on Pt-group metal electrodes 90
4.1.2.1 Hydrogen evolution on Pt in 0.1 M H_2SO_4 90
4.1.2.2 Hydrogen evolution on Ir in 0.1 M H_2SO_4 92
4.1.2.3 Hydrogen evolution on Ru plated on Pt 92
4.2 Multi-Frequency AC Voltammetry 94
4.2.1 Varying acid strength 94
4.2.2 Varying the H_2 overpressure 95
4.2.3 Rotating Disk MFACV 96

4.2.4 Temperature dependence of MFACV 97
4.2.5 DC temperature dependence measurements 98
4.3 Single crystal electrode studies 101
4.3.1 Cyclic voltammetry and MFACV studies 101
4.3.1.1 Model circuit analysis of MFACV data 109
4.3.2 CO blocking experiments 114
4.3.2.1 Fitting rate constants to single crystal Tafel data 120
4.3.3 Pt{111} crystals of different sizes 127
4.3.4 Pt{110} and different cooling methods 127
4.4 Surface modified Pt{*hkl*} electrodes 130
4.4.1 Epitaxial single crystal metal films 130
4.4.1.1 Model circuit analysis of epitaxial films MFACV data 136
4.4.1.2 Fitting rate constants to epitaxial metal film Tafel data 136
4.4.2 Ir deposited onto Pt{111} 137
4.4.2.2 Fitting rate constants to Ir modified Pt Tafel data 139
4.4.3 Pt deposited onto Pt{111} 141
4.4.3.1 Fitting rate constants to Tafel data from Pt on Pt 143
4.4.4 Pd films on Pt 144
4.4.4.1 Fitting rate constants to Tafel data from Pd films on Pt 146
4.4.5 Pd-Pt alloys 147
4.4.5.1 Fitting rate constants to Pd-Pt alloy Tafel data 149
4.4.6 Bi overlayers on Pt single crystals 150

Chapter 5 Discussion

5.1 Hydrogen evolution and hydrogen oxidation on polycrystalline Pt 152
5.1.1 Hydrogen electro-oxidation on polycrystalline Pt 152
5.1.1.1 HOR on Pt in 0.1 M $HClO_4$ 152
5.1.1.2 Pt in 0.05 M H_2SO_4 156
5.1.2 Hydrogen evolution on Pt-group metal electrodes 168
5.1.2.1 Hydrogen evolution on Pt in 0.1 M H_2SO_4 168
5.1.2.2 Hydrogen evolution on Ir in 0.1 M H_2SO_4 169
5.1.2.3 Hydrogen evolution on Ru plated on Pt 160
5.2 Multi-Frequency AC Voltammetry 162
5.2.1 Varying acid strength 162

5.2.2 Varying the H_2 overpressure 163
5.2.3 Rotating Disk MFACV 163
5.2.4 Temperature dependence of MFACV 164
5.2.5 DC temperature dependence measurements 165
5.3 Single crystal electrode studies 168
5.3.1 Cyclic voltammetry and MFACV studies 169
5.3.1.1 Model circuit analysis of MFACV data 172
5.3.2 CO blocking experiments 174
5.3.2.1 Fitting rate constants to single crystal Tafel data 178
5.3.3 Pt{111} crystals of different sizes 179
5.3.4 Pt{110} and different cooling methods 180
5.4 Surface modified Pt{*hkl*} electrodes 182
5.4.1 Epitaxial single crystal metal films 182
5.4.1.1 Model circuit analysis of epitaxial films MFACV data 187
5.4.1.2 Fitting rate constants to epitaxial metal film Tafel data 187
5.4.2 Ir deposited onto Pt{111} 188
5.4.2.2 Fitting rate constants to Ir modified Pt Tafel data 189
5.4.3 Pt deposited onto Pt{111} 190
5.4.3.1 Fitting rate constants to Tafel data from Pt on Pt 196
5.4.4 Pd films on Pt 196
5.4.4.1 Fitting rate constants to Tafel data from Pd films on Pt 197
5.4.5 Pd-Pt alloys 199
5.4.5.1 Fitting rate constants to Pd-Pt alloy Tafel data 202
5.4.6 Bi overlayers on Pt single crystals 203

Chapter 6 Summary and Conclusions 208

Chapter 1
Introduction

The recent award of the 2007 Nobel Prize for Chemistry to Gerhart Ertl reflects the importance of interfacial phenomena, particularly the physics and chemistry of solid surfaces in the physical sciences. A central theme of Ertl's work has been the investigation of mechanisms in heterogeneous catalysis[1-4]. Catalysts play such an important role in industrial chemical processes that even small improvements in performance or selectivity can generate great profits for the companies that develop such materials. When heterogeneous catalysis is coupled with electrochemical charge transfer behaviour (using an electrochemical cell), one denotes such phenomena as belonging to the set of reactions broadly termed *electrocatalytic*.

Electrocatalysis relates to the study of rates of reactions at different electrode materials involving electron transfer and more specifically, attempting to increase these rates or reducing the overpotential required to drive the reaction. It is a rapidly expanding area of research due to its applied and fundamental relevance.

1.1 Hydrogen as a fuel

Greenhouse gas formation is currently a major global concern[5]. Toxic NO_2 and SO_2 (which can cause acid rain) are formed in the combustion of fossil fuels, as well as man-made CO_2 which has been largely attributed to be the cause of global warming, an environmental and political issue. A further disadvantage of using fossil fuels is their non-renewability which will lead to the eventual depletion of available sources, possibly as early as 2050 in the case of petroleum[6]. Hence, the importance of researching electrocatalytic reactions, which may, in future, become sufficiently economically viable to replace the use of less efficient systems which employ the burning of fossil fuels[7].

An alternative to the internal combustion engine (i.e. the common petrol or diesel engine) used in the vast majority of automotive vehicles, could be an electrocatalytic fuel cell[8]. Proton exchange membrane fuel cells (PEMFCs) are of significant interest as they function using hydrogen and oxygen as reactants[9].

A wide range of fuel cells which use hydrogen gas as a fuel are currently under investigation, including SOFCs[10] (solid oxide fuel cells), MCFCs[11] (molten-carbonate fuel cells), PAFCs[12] (phosphoric acid fuel cells) and AFCs[12] (alkaline fuel cells). Nevertheless the type which are considered the most promising for future implementation are proton exchange membrane fuel cells (PEMFCs), often referred to as polymer electrolyte membrane fuel cells (keeping the same acronym). The advantages of these fuel cells include a more environmentally friendly source of power than combustion engines, and lower operating temperatures than the other types of fuel cell (~ 80 °C compared to 200 °C for PAFCs, 800 °C for MCFCs and 500 - 1000 °C for SOFCs, AFCs have a similar operating temperature ~ 70 °C).
The overall reaction in the hydrogen fuel cell is given by:

$$2\ H_{2\,(g)} + O_{2\,(g)} \rightarrow 2\ H_2O_{\,(l)} \qquad \textbf{(1.1.1)}$$

Hence, the by-product of the reaction is pure water, making this reaction a much more environmentally friendly source of power than the burning of fossil fuels[13].

In PEMFCs, hydrogen gas is passed into the cell where it is oxidised at the anode, the protons then pass across a polymer electrolyte membrane to the cathode, whilst the electrons flow through an external circuit, producing power (see fig. 1.1.1). At the cathode, the protons and electrons react with oxygen to give pure water as a by-product.
The anode reaction is therefore:

$$H_2 \rightarrow 2\ H^+ + 2\ e^- \qquad \textbf{(1.1.2)}$$

Whilst at the cathode:

$$4\ H^+ + 4\ e^- + O_2 \rightarrow 2\ H_2O \qquad \textbf{(1.1.3)}$$

One of the most commonly used membranes is Nafion®, though polybenzimidazole and phosphoric acid may also be used and others are being investigated.
Air is generally used as a source of oxygen, rather than flowing pure oxygen into the cell. It is also economically advantageous to use hydrogen from reformed hydrocarbons as hydrogen storage is not yet advanced enough to be economically viable[6]. However this poses problems as the reformation of hydrocarbons requires

an external fuel processor. An external fuel processor will raise the cost of the system and more importantly, produce CO which blocks the electrode surface, reducing the activity of the cell dramatically. Therefore, in order to avoid hydrocarbon reformation, a more economical means of hydrogen production must be developed. One of the main alternatives is the use of water electrolysis which is able to produce pure hydrogen gas. In order to improve the efficiency of this process, more effective hydrogen evolution catalysts are required.

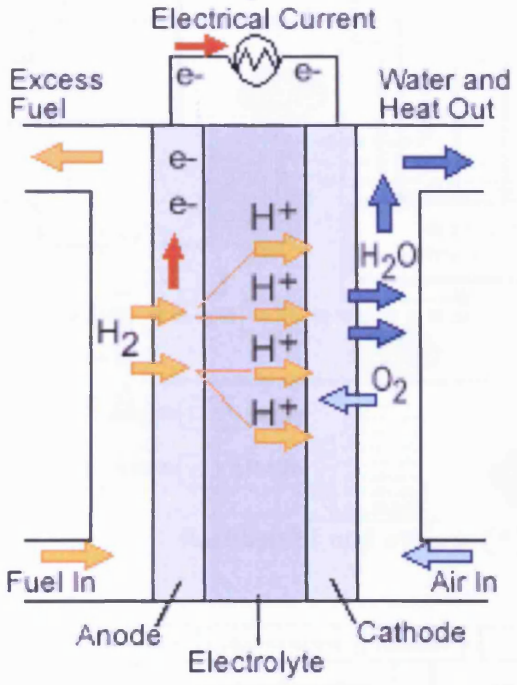

Fig 1.1.1 Schematic diagram of a PEMFC.

The development of fuel cells has also led to an increased interest in the planning for a *hydrogen economy*[6], which is the effort to utilise the cleanliness of hydrogen as an energy carrier with the efficiency of fuel cell systems to transform this energy into electricity and heat[6, 14, 15]. Some communications even predict that hydrogen will be the main carrier of energy by 2050[6]. Fig. 1.1.2 (a) shows the present energy situation, with the primary fuel sources, the types of energy they are converted into and the areas to which the energy is distributed. It can be seen that there is currently a heavy dependence upon non-renewable fuels such as oil, particularly for transport but also for heating and industry. Increasing amounts of biomass (which currently contributes the greatest amount of energy from a renewable source) and natural gas

are also noteworthy in the heating and industry area. Coal is a major source of electricity. Fig. 1.1.2 (b) shows a predicted energy model for 2050 based on a *hydrogen economy*[6], though it does not quote direct figures of how the energy is sourced. The model removes oil as a fuel and incorporates a hydrogen network, catering for industry, residential and transport sectors.

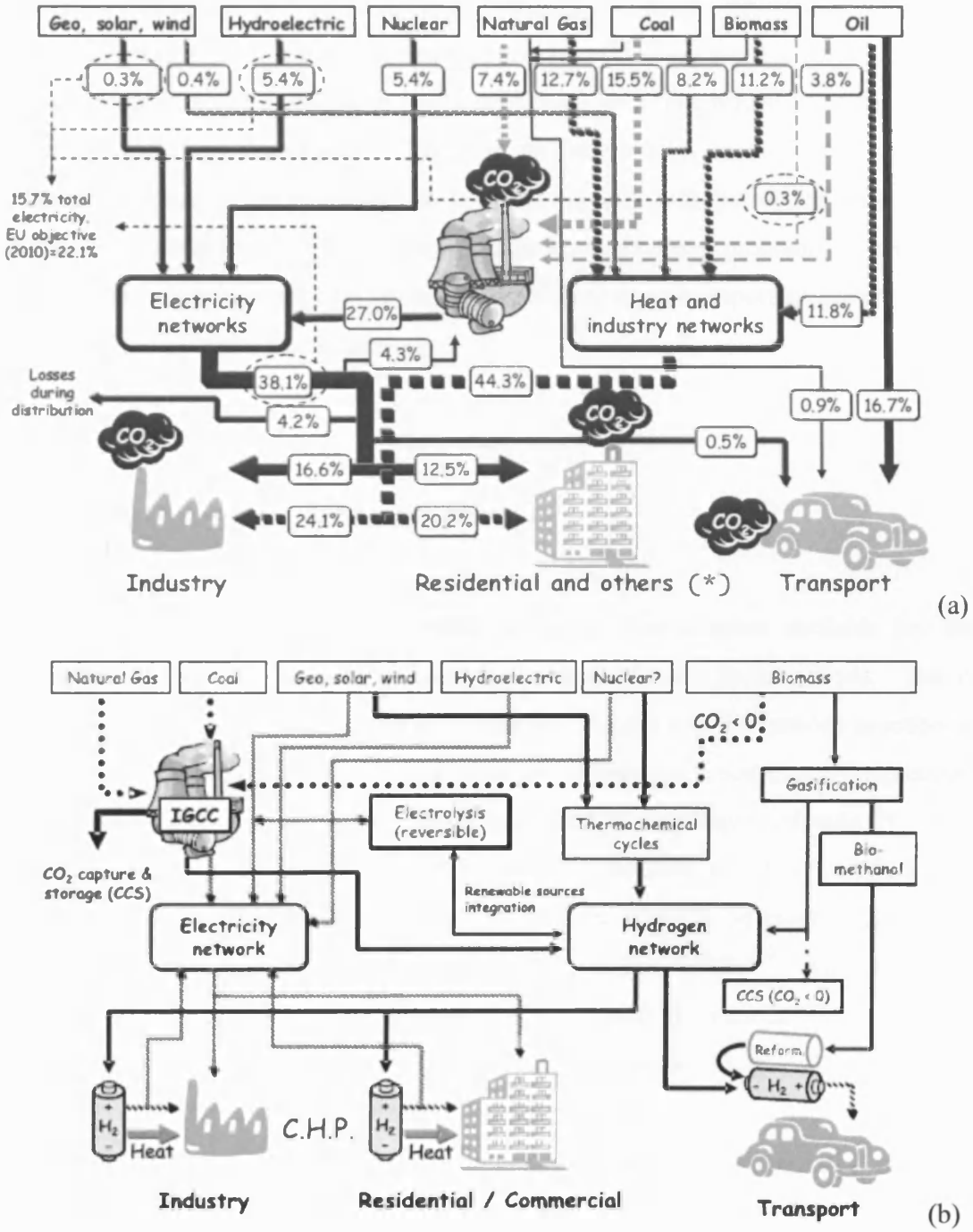

Fig. 1.1.2 Diagram showing energy sources (a) at present and (b) predicted for future (possibly as early as 2050). * includes agriculture commerce and services[6].

Hydrogen as a fuel is currently used on a relatively small scale (though it is growing) with 227 fuel stations in operation globally as of May 2006[6] (with the highest density in Japan). Most of these fuel stations generally provide fuel to government projects involving public transport, such as fleets of buses, which use hydrogen internal combustion engines (ICE-H_2) as opposed to PEMFCs. The ICE-H_2 systems offer energy efficiencies of 20 – 38 % whereas PEMFCs give rise to efficiencies of 50 – 60 %[6]. Moreover PEMFCs are pollutant free and silent[6]. However the presence of the ICE-H_2 engines may be enough to implement more hydrogen refuelling stations until PEMFC technology draws level. There is still much work to do before hydrogen technology becomes cheap enough to compete directly with petrol for general use. Increasing the efficiency of hydrogen production, overcoming problems of hydrogen storage and achieving more CO-tolerant PEMFCs[6] are all important factors in the cost reduction of hydrogen technology.

1.2 The hydrogen evolution reaction

The hydrogen evolution reaction (HER) is one of the simplest methods for the production of hydrogen[16] and has been the subject of many investigations. This is due, in part, to its common occurrence in industry, where it is the cathode reaction in some chlor-alkali cells[17, 18]. It is also a competing reaction in some metal deposition reactions[19-21] e.g. the electrolytic reduction of Ir(IV) to Ir deposited onto Pt. This reaction occurs via the intermediate Ir(I) where the reaction of Ir(IV) → Ir(I) has to compete with the HER (which occurs at a more positive potential than the Ir reduction), as the hydrogen produced oxidises the Ir(I) to Ir(III)[21]. Also, the HER can be involved in corrosion[22-24]. When iron is oxidised as an anode ($Fe \rightarrow Fe^{2+} + 2\ e^-$) hydrogen may be evolved as the parallel cathode reaction ($2\ H^+ + 2\ e^- \rightarrow H_2$)[24]. Moreover, the HER is the desired reaction for hydrogen production via the electrolysis of water and hence is becoming more relevant as society tries to move towards hydrogen as a fuel and away from fossil fuels. However, the electrolysers which produce the hydrogen are currently far from ideal as the cathodes are made of expensive materials (generally Pt or Pt-group metals). Also water electrolysis

requires electrical energy which must itself be sourced from fuels which are likely to be non-renewable and polluting. Hence, efforts to find a more effective or inexpensive catalyst and to lower the amount of energy required to drive the reaction are of great importance for obvious economical and environmental reasons. Alternative fuel sources for the water electrolysis stage could also be implemented, such as photovoltaic cells (which will, themselves require improvement before becoming a major power source). Nuclear energy (though public opinion is generally still sceptical of the associated safety aspects and decontamination processes are detrimental to the environment) is another possibility in this regard. Hydrogen may also be produced by the reforming of fossil fuels or hydrocarbons, i.e. the removal of hydrogen atoms from these organic compounds. Reforming is currently used as a source of hydrogen in preference to using electrolysis of water, yet requires an external fuel processor. As mentioned earlier, residual compounds such as CO may adsorb onto the working electrodes, blocking the surface and decreasing fuel cell activity. Also, reformation will produce greenhouse gases and, in the case of fossil fuels as reformates, remains a non-renewable source of hydrogen.

The hydrogen evolution reaction has two main forms depending on the type of electrolyte (acid/basic)[23].

The overall reaction in acid solution is:

$$2\ H_3O^+ + 2\ e^- \rightarrow H_2 + 2\ H_2O \qquad \textbf{(1.2.1)}$$

and under basic conditions:

$$2\ H_2O + 2\ e^- \rightarrow H_2 + 2\ OH^- \qquad \textbf{(1.2.2)}$$

The reaction rates have been found to be faster in acid electrolytes than in alkali[25, 26], due to the facility for the abstraction of hydrogen atoms decreasing on going from H_3O^+ (i.e. acid solution) to H_2O (i.e. basic conditions), which has led to the reaction being studied much more commonly under acidic conditions.

The HER in acid involves an initial discharge step known as the Volmer reaction[27]:

$$M + H_3O^+ + e^- \leftrightarrow MH_{ads} + H_2O \qquad \text{(I)} \qquad \textbf{(1.2.3)}$$

where M is the metal (or cathode material) at which the reaction takes place.

This can then be followed by one of, or a combination of a recombination step (Tafel reaction)[27]:

$$MH_{ads} + MH_{ads} \rightarrow 2\,M + H_2 \qquad \text{(II)} \qquad \textbf{(1.2.4)}$$

and an electrochemical desorption step (Heyrovsky reaction)[27]:

$$MH_{ads} + H_3O^+ + e^- \leftrightarrow M + H_2O + H_2 \qquad \text{(III)} \qquad \textbf{(1.2.5)}$$

Each of the three reactions gives rise to its own rate equation[28],

$$\text{Volmer: } v_1 = k_1 C^*_{H^+}(1-\theta_H)e^{-\alpha f\eta} - k_{-1}\theta_H e^{(1-\alpha)f\eta} \qquad \text{(I)} \qquad \textbf{(1.2.6)}$$

$$\text{Tafel: } v_2 = k_2\theta_H^{\,2} - k_{-2}(C^{\sigma}_{H_2}/C^*_{H_2})(1-\theta_H)^2 \qquad \text{(II)} \qquad \textbf{(1.2.7)}$$

$$\text{Heyrovsky: } v_3 = C^*_{H^+}\theta_H e^{-\alpha f\eta} - k_{-3}(C^{\sigma}_{H_2}/C^*_{H_2})(1-\theta_H)e^{(1-\alpha)f\eta} \qquad \text{(III)} \qquad \textbf{(1.2.8)}$$

where k_1, k_2 and k_3 are the rate constants for the forward reactions of I, II and III respectively, k_{-1} and k_{-2} are the rate constants for the back reaction of I and II respectively, α is the transfer coefficient, θ_H is the surface coverage of H, η is overpotential, $f = nF/R_gT$, where F is the Faraday constant (9.649 x 10^4 C mol^{-1}), R_g is the universal gas constant (8.314 J mol^{-1} K^{-1}), T is the temperature in K and n is the number of electrons involved in the reaction (one in each case), $C^*_{H^+}$ is the concentration of H^+ in the electrolyte, $C^{\sigma}_{H_2}$ is the concentration of H_2 at the electrode surface and $C^*_{H_2}$ is the concentration in the bulk in mol cm^{-3}.

If it is assumed that the Tafel and Heyrovsky steps are independent, we obtain four possible reaction mechanisms[23].

A.	$M + H_3O^+ + e^- \leftrightarrow MH_{ads} + H_2O$	Volmer step slow
	$MH_{ads} + MH_{ads} \rightarrow 2\ M + H_2$	Tafel step fast
B.	$M + H_3O^+ + e^- \leftrightarrow MH_{ads} + H_2O$	Volmer step fast, pre-equilibrium
	$MH_{ads} + MH_{ads} \rightarrow 2\ M + H_2$	Tafel step slow
C.	$M + H_3O^+ + e^- \leftrightarrow MH_{ads} + H_2O$	Volmer step slow
	$MH_{ads} + H_3O^+ + e^- \leftrightarrow M + H_2O + H_2$	Heyrovsky step fast
D.	$M + H_3O^+ + e^- \leftrightarrow MH_{ads} + H_2O$	Volmer step fast, pre-equilibrium
	$MH_{ads} + H_3O^+ + e^- \leftrightarrow M + H_2O + H_2$	Heyrovsky step slow

Different parameters are often used to measure the relative rates of HER on a material (see section 2.1). The rate constant, k, can be determined and is probably the most direct indicator of the reaction rate. However, k is often disregarded in favour of the exchange current density, j_0, which is also indicative of the overall reaction rate and is easier to calculate from raw data. j_0 is the cathodic (or the equal and opposite anodic) current density when an electrochemical system is at its equilibrium potential (the net current is zero)[29]. The Tafel slope (i.e. the gradient of a plot of log current versus overpotential (the "excess" potential, from the equilibrium potential, required to force a particular reaction rate to occur)) is also commonly quoted. The Tafel slope is not a direct indicator of rate, but provides an insight into the nature of the reaction mechanism. The basic reaction mechanisms for HER have distinct associated Tafel slopes, assuming α is 0.5 (which indirectly relate to reaction rate as certain mechanisms are associated with faster rates than others). When the Volmer step (equation (1.2.3)) is rate-limiting, the Tafel slope should be -118 mV/dec[30] (this is observed with metals such as Pb, Tl, Cd and Hg[23]). If the Tafel step is the rate-limiting step (which is the case for HER on Pt and Pt-group metals (Ir, Os, Rh, Ru)[23]) it should be –29 mV/dec[30] and for the Heyrovsky step being the slowest, the Tafel slope should be –42 mV/dec[30] (observed for Ag, Au, Ni and Ti amongst others[23]). These values have been calculated for steady state conditions and at low hydrogen coverage (negative potential close to 0 V *vs.* RHE).

1.3 Hydrogen evolution on platinum group metals

Research into the HER in the 1950s by Bockris and co-workers[31-33] discovered that Pt had a low free energy of activation for the reaction. Hence, Pt worked well as a catalyst for the HER. Further work by the same authors investigated the effects of electrode preparation on the rate, finding that the system was sensitive to contamination and required high purity electrolytes and clean equipment for reliable electrochemical measurements[34]. Roger Parsons'[35] work on the HER then investigated the relationship between the free energy of adsorption of hydrogen on metal surfaces (ΔG^{o}, i.e. the amount of energy required to transfer a proton from the bulk of solution to the electrode interface[36]) and the exchange current, i_0, (or exchange current density, j_0) for hydrogen evolution. Using the equation:

$$j_o = a_{H^+}^{(1-\alpha)}\left(P_{H_2}^{\frac{1}{2}}\exp\frac{-\Delta G^{o}}{2k_BT}\right)^{\alpha}\left(1+P_{H_2}^{\frac{1}{2}}\exp\frac{-\Delta G^{o}}{2k_BT}\right)^{-1}G_1 \qquad \textbf{(1.3.1)}$$

where a_{H+} is the activity of H^+ ions in solution, α is the transfer coefficient (see section 2.1.1.1) P_{H2} is the hydrogen pressure, k_B is the Boltzmann constant, T is temperature and

$$G_1 = \frac{e_0 k_B T}{h}\exp-[(1-\alpha)\vec{\Delta}G_1^{o} + \alpha\overleftarrow{\Delta}G_1^{o}]/k_BT \qquad \textbf{(1.3.2)}$$

where e_0 is the charge on an electron (1.602 x 10^{-19} C) and $\vec{\Delta}G_1^{o}$ and $\overleftarrow{\Delta}G_1^{o}$ are the free energies associated with the forward and backward processes of the Volmer reaction respectively. From equation (1.3.1) Parsons determined that when $\Delta G^{o}/2k_BT$ >> 1 there was little tendency for hydrogen to adsorb at the metal surface and j_0 would increase with ΔG^{o}, whereas, for 1 >> $\Delta G^{o}/2k_BT$, the adsorption of hydrogen was strong and j_0 decreased as ΔG^{o} increased. Hence, there would be an optimum point for exchange current density where ΔG^{o} is zero. A plot of log j_0 versus ΔG^{o} confirmed this, giving a "volcano" shaped graph (fig. 1.3.1 (a)).

It was also predicted that the best electrode materials for the reaction are the Pt group metals (Pt, Ir, Os, Pd, Rh, Ru) as they have relatively low ΔG^{o} values, and that those

with higher ΔG° values, such as Hg and Pb, would be much less effective for catalysing HER. This was confirmed experimentally by various groups using a range of metal cathodes[37-43] (different types of electrode were studied under a range of conditions in different acid electrolytes in various concentrations, but averages were taken for comparison). The resultant data was compiled into a plot by Trasatti[44] in 1972 (though ΔG° was replaced on the x-axis by an equivalent energy, the metal-hydride bond energy, fig. 1.3.1 (b)) giving a shape very close to that predicted by Parsons[35] (shown schematically in fig. 1.3.1 (a)).

Hence, it is unsurprising that Pt and the other Pt-group metals have been, and still remain, a source of great interest in this field[45-49].

When the cathode in the HER is a Pt-group metal electrode, the intermediate species in the mechanism (MH_{ads}) refers to "overpotentially deposited" hydrogen (OPD-H)[30], that is, hydrogen which is adsorbed at potentials negative to 0 V versus the reversible hydrogen electrode (RHE). This is because the PGMs possess a large $-\Delta G^{\circ}$ value which results in a full surface coverage ($\theta_{Hads} = 1$) of underpotentially deposited hydrogen (UPD-H), i.e. hydrogen which adsorbs to the metal surface at potentials positive to 0 V *vs.* RHE (fig. 1.3.2). Whether or not UPD-H is actually involved in the HER is a subject which has been much discussed[30, 50-52].

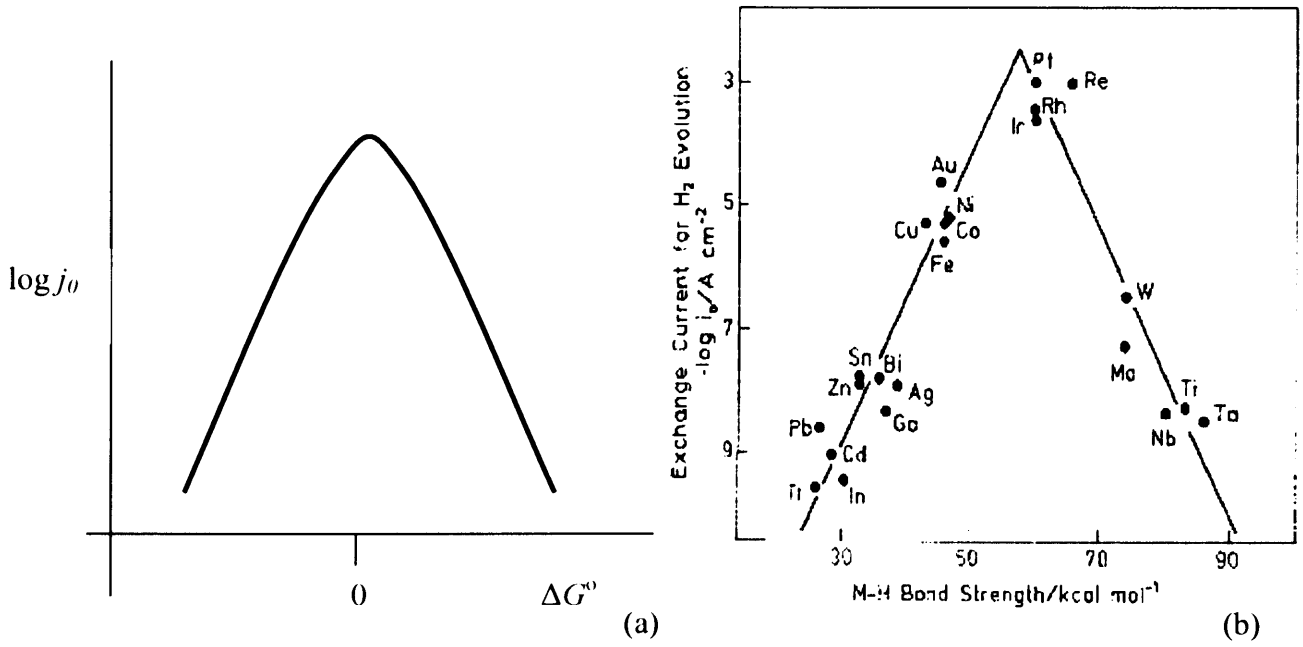

Fig. 1.3.1 "Volcano" curves of the logarithm of exchange current *versus* (a) free energy of hydrogen adsorption, predicted by Parsons[35] (schematic) and (b) metal-hydride bond strength, compiled by Trasatti[44].

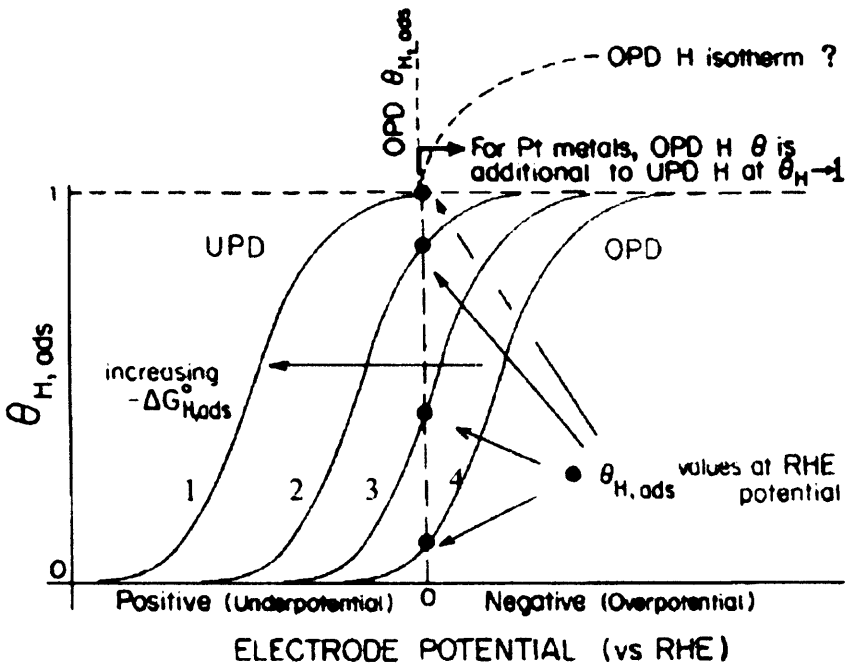

Fig. 1.3.2 Langmuir-type isotherms (see section 2.7) for various, arbitrary, values of $-\Delta G°$ (1,2,3 and 4, where isotherm 1 represents a platinum group metal) showing H-coverage, $\theta_{H,ads}$ as a function of potential *vs.* RHE[53].

Fig. 1.3.2 shows a schematic depiction of hydrogen coverage as a function of potential, the positions of the isotherms being arbitrary. However, the most negative isotherm (number 1) is a semi-quantitative representation of a PGM, showing full UPD-H coverage ($\theta_{H,ads}$ = 1) at 0 V *vs.* RHE. OPD-H is still seen, despite the full UPD-H coverage, which leads to the debate as to its nature. Proposed theories include those of Conway, who suggested that UPD-H resides beneath the surface with OPD-H bonded in atop metal sites[30]. This model is similar to that suggested by Horvat-Radošević where hydrogen absorbs within the metal surface layer[54] (fig. 1.3.3 (a)). Conway's second proposal was a communal array arrangement[55], similar to that suggested by Horiuti and Toya[56]. The model consists of both UPD-H and OPD-H occupying surface sites on the metal, but with each of the two species having distinct, discrete energies or different weakly and strongly bound states (fig. 1.3.3 (b)).

(a) 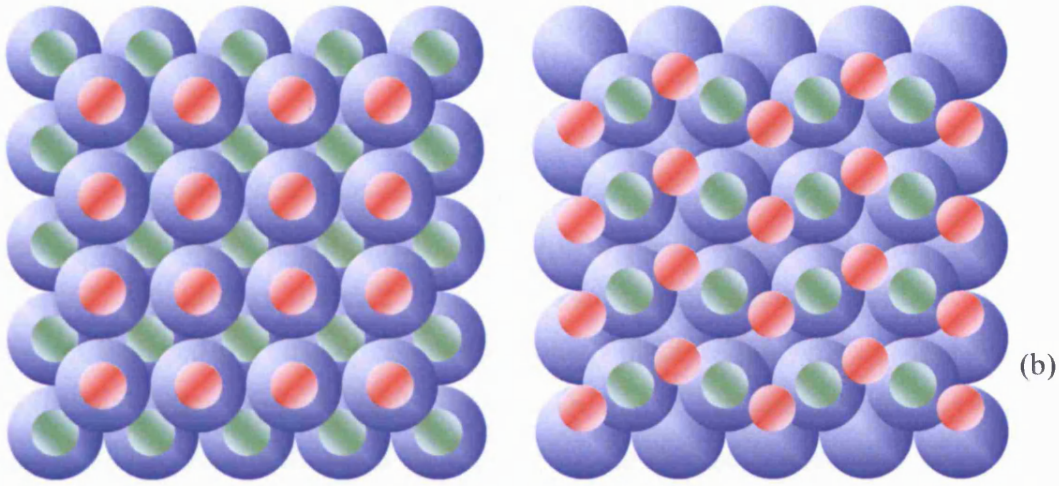 (b)

Fig. 1.3.3 Schematic diagrams of proposed structures for arrangements of OPD-H (red) and UPD-H (green) on a Pt group metal (blue) with (a) UPD-H absorbed below the surface layer of the metal and OPD-H atop surface sites and (b) UPD-H and OPD-H occupying surface sites in a communal arrangement.

1.4 Single crystal surfaces

1.4.1 Pt single crystals

Single crystal electrodes are electrodes formed in such a way as to expose a specific crystal plane of the bulk lattice (for further details, see section 2.3). They are of great importance in electrochemistry as rates of certain reactions are enhanced by particular crystal electrode orientations. Examples of such reactions include that found by Koper *et al* showing the reduction of NO_2 to be structure sensitive with more activity observed on Pt{111} than on Pt{100}[57]. The activity of ethylene glycol oxidation was also found to be faster on Pt{100} than on Pt{111} by Clavilier *et al*[58]. Other examples of structure specific behaviour include the reduction of CO_2 in experiments investigating the reaction on the three basal plane Pt single crystals (where Pt{110} was found to be the most active surface and Pt{111} was the least active)[59]. Electro-oxidation of D-mannitol shows a dependence on single crystal structure, where Pt{110} is found to be the least active of the three basal plane surfaces (whilst Pt{111} and {100} show similar activity to each other)[60].

Single crystals are useful for isolating specific sites for investigation. The surfaces can simplify analysis of what may be a more complicated system by separating out

contributions from individual surface components that would be present at polycrystalline surfaces.

Single crystal electrodes have been in use since the 1950s, gaining more popularity in the 1960s[61-65], when Will's investigations using cyclic voltammetry on Pt led to the assignment of weakly and strongly adsorbed hydrogen states at {110} and {100} sites respectively on polycrystalline Pt[66] (see section 2.1.1.2). Methods of single crystal formation included the Bridgman method, which involves drawing an ingot from a molten metal, allowing it to cool slowly such that it adopted a single crystalline structure. The ingot could then be aligned to the desired orientation using X-ray diffraction and cut/polished. Another method involved solidifying molten metal droplets *in vacuo* in glass capillaries so that they formed oriented wires, which were cleaved at a specific angle to obtain the desired single crystal surface plane[64]. However, both of the Bridgman method and the oriented wires procedure were very difficult and few groups were able to construct single crystal electrodes in this way, although it was possible to purchase single crystals from specific manufacturing companies.

Electrochemical research on single crystals was revolutionised with the advent of Clavilier's "bead" method[67] for single crystal electrode construction, which made the manufacture and manipulation of single crystal electrodes more simple and accessible to a greater number of groups. The process involves melting a length of wire into a molten bead form and, after cooling, cutting and polishing this single crystal bead to generate the desired Miller index plane surface (for further experimental details see section 3.4). These bead electrodes exhibit a significantly greater surface area as compared to the oriented wires used prior to this technique. Other advantages of the Clavilier bead electrodes over oriented wires are that they are easier to manipulate in terms of contact with electrolyte. Pre-electrolysis treatments such as flame annealing, to clean or order the surface may also be facilitated Consequently, these electrodes have been a major area of interest for the HER ever since, in order to elucidate structural effects[25, 30, 50, 68-72]. The manufacturing technique for single crystal electrodes has become much more refined, making it easier to construct electrodes of any desired Miller index structure, and is now employed by a number of groups throughout the world[46, 68, 73-84].

The HER on Pt single crystals has caused an ongoing debate surrounding the question as to whether or not there is a structural dependence for the reaction, i.e. whether

hydrogen evolution occurs faster on different Miller index crystal electrode orientations. Certain groups believe that there is no dependence of HER on crystal structure[68-70]. For example, Feliu and co-workers observe similar values for exchange current density on the Pt{111} and {100} surfaces (see table 1.4.1) with a higher value on the Pt{110} surface which is claimed to be within experimental error[70]. Prior to Feliu's investigations, Lipkowski *et al* had stated that the HER was not sensitive to surface crystallography after observing j_0 values between 1.7 mA cm^{-2} (on Pt{511}) and 3.0 mA cm^{-2} (on Pt{111}) despite also quoting an error of 10 %[69]. However other groups disagree[50, 71]. Markovic *et al* state that there is a dependence on surface structure, with HER rate increasing on the basal Miller plane surfaces in the order Pt{111} < Pt{100} << Pt{110} in acid solution[71] (with a different order in alkaline solution, Pt{100} < Pt{111} < Pt{110}[85]). Barber and Conway agree that there is a structural dependence[50], but these authors are not in agreement with Markovic in terms of the order of particular surface planes in relation to increasing HER rate as they quote Pt{100} < Pt{111} < Pt{110}[50]. Conway's observation is obtained from rate constants (for Volmer reaction) rather than exchange current densities which are used in the Markovic work.

j_0/ mA cm^{-2}	Pt{111}	Pt{100}	Pt{110}	Electrolyte
Feliu *et al*[70]	0.84	0.84	0.97	0.5 M H_2SO_4
Lipkowski *et al*[69]	3.0	1.8		0.1 M $HClO_4$
Markovic *et al*[71]	0.45	0.60	0.98	0.05 M H_2SO_4

Table 1.4.1 Comparing exchange current density values for the basal plane single crystal surfaces of platinum from three different research groups.

Looking at table 1.4.1, it is difficult to draw a conclusion concerning the structure sensitive nature of the reaction. It can be seen that there is a variation in all three data sets, with Markovic's showing the greatest variation in percentage terms. It is interesting to note the high values found by Lipkowski compared to the other groups, when the only obvious experimental difference is the electrolyte used. It is also interesting to see that Lipkowski finds the highest value of j_0 on Pt{111}, whereas Markovic finds this surface to have the lowest value.

1.4.2 Non-Pt single crystals

It is also possible to prepare single crystal electrodes from metals other than Pt e.g. Rh[86], Ru[87, 88], Ir[89] and Pd[89, 90], using the same Clavilier bead preparation method.

HER data has been reported for Ru{0001} and Ru{10$\bar{1}$0} electrodes, with j_0 values of 0.13 and 0.16 mA cm^{-2} respectively[88], significantly lower than that for single crystal Pt which gave values of 0.45 and 0.98 mA cm^{-2} for Pt{111} and Pt{100} respectively from the same author[88]. No figures have been quoted for the HER on the other single crystal electrodes of Ir, Pd and Rh, though data for the polycrystalline surfaces of these metals have not shown an enhanced HER activity compared to (single crystalline) Pt electrodes[44, 88, 91].

1.5 Deposition of metal films onto single crystal electrode surfaces

Deposition of metals onto Pt single crystal substrates to give epitaxial films of the deposited metal with structures analogous to that of the Pt crystal has been achieved by evaporating the metal *in vacuo*, with the single crystal electrode substrate present, the evaporated metal coating the electrode and adopting its single crystal structure[92] (this technique has also been used for non-Pt substrates e.g. Pd deposited onto Au single crystal surfaces[93]). The nature of the deposited film depends on the growth mode of the deposited metal onto the substrate (see section 2.6). New electroless deposition methods of performing this task are an issue of interest at present[73], including novel methods for the formation of single crystal Ru surfaces[73], which involves "forced" deposition[94, 95]. In forced deposition a droplet of a metal ion in solution (in this case Ru from an aqueous Ru complex) is held in contact with a Pt single crystal electrode and reduced in a stream of hydrogen gas to leave a deposited layer of that metal, which can then be annealed subsequently by resistive heating under nitrogen atmosphere to give a surface analogous to the single crystal substrate[73]. One reason why these surfaces are of great interest is that they provide a less expensive means of forming a single crystal surface (particularly for metals

which may not form single crystals readily using the Clavilier bead method). In addition the deposition may cause strains within the crystal lattice to develop due to different relative sizes of the substrate and adsorbate atoms, which may lead to altered catalytic properties.

1.6 Hydrogen evolution on alloys

Trasatti found Pt to be the most electroactive pure metal catalyst for HER[44] from experiment and based on his "volcano" plot (fig. 1.3.1 (b)). However, many mixed metal systems have also been investigated, including a range of Pt alloys. These alloys include Pt_3Sn and PtRu which have shown good catalytic properties in relation to the electrochemical oxidation of CO[96-98]. In particular the $Pt_3Sn\{111\}$ single crystal alloy, where the potential for the onset of CO oxidation is 0.7 V lower than that on $Pt\{111\}$[97]. PtRu has also been found to be an extremely good catalyst for methanol electro-oxidation, with a limiting current > 1 A cm^{-2} compared to 0.3 A cm^{-2} on pure Pt[98]. Yet none of these alloys have been found to catalyse the HER more effectively than pure Pt.

Bockris published work on hydrogen evolution on noble metal alloys[99], none of which showed faster rates than Pt, though Pd and its associated alloys were found to give j_0 values which matched those on the Pt surface. The profiles of exchange current density versus percentage of metal composition within the alloy for Bockris' results[99] are shown in fig. 1.6.1.

Most alloys have proved significantly slower for hydrogen evolution than pure Pt[100, 101]. However, as research has progressed, alloys have been discovered which give rise to higher exchange current densities than Pt. Some of the most promising alloy areas of investigation are Ni-S[102] and Ni-S-Co[103] alloys which have been shown to give j_0 values of 4.6 and 6.2 mA cm^{-2} respectively.

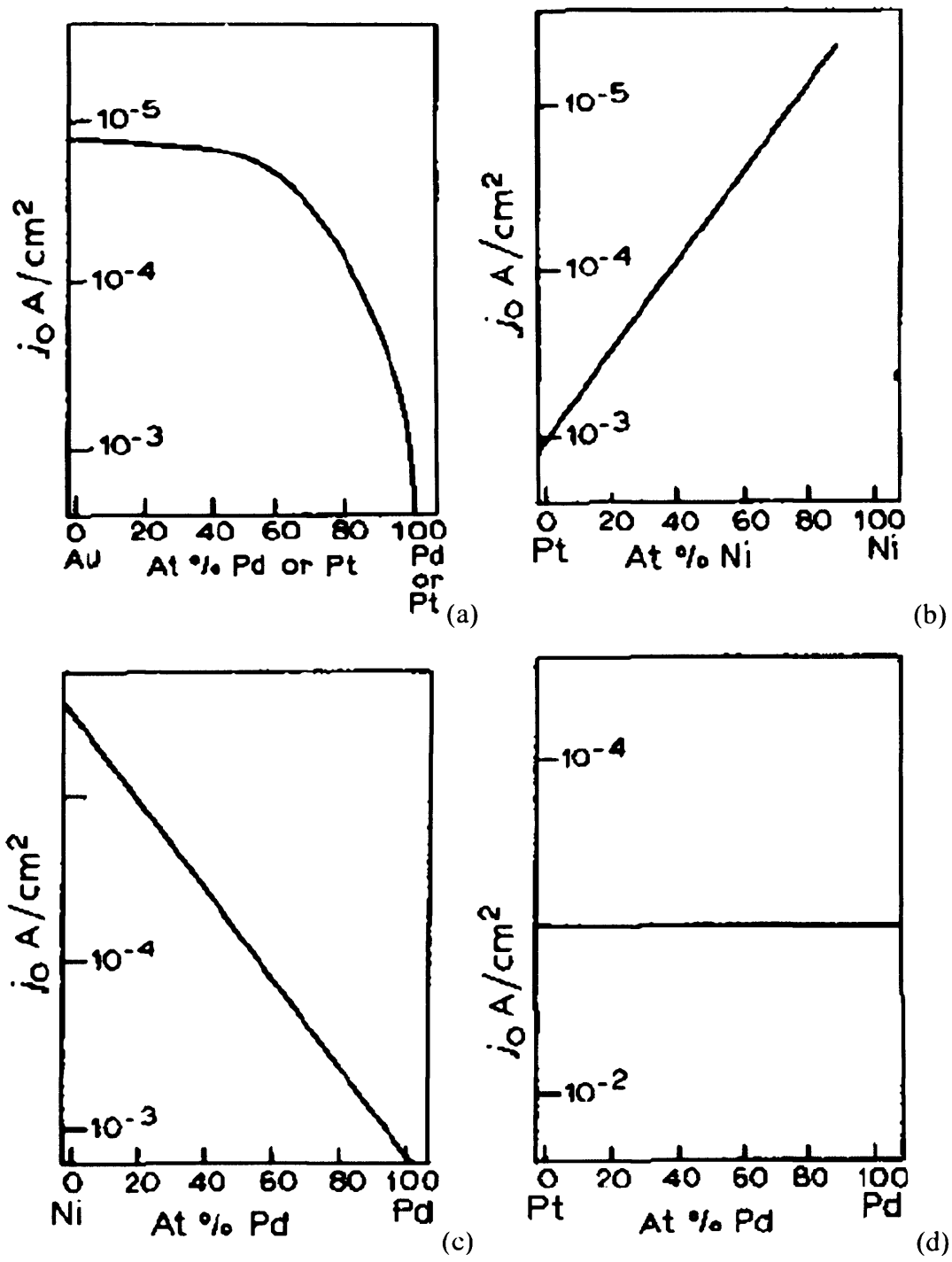

Fig. 1.6.1 Graphs of exchange current density versus alloy composition for (a) Au-Pd or Au-Pt (b)Pt-Ni (c) Ni-Pd and (d) Pt-Pd alloys as found by Bockris *et al.*[99].

Greeley *et al* have performed hydrogen evolution experiments on pseudomorphic Pd films on various substrates (Au, Pt, PtRu alloy, Rh, Ir, Ru and Re) and found greatly enhanced exchange current densities when the substrate was Pt or PtRu (1:1 segregated alloy), both giving j_0 values of 6.32 mA cm^{-2}[104]. The same group have more recently performed theoretical computational high-throughput screening density

functional theory (DFT) calculations on over 700 surface alloys with the aim of finding a more effective HER catalyst by using theory based techniques before exploring the surfaces experimentally[105]. These calculations predicted BiPt alloys to be of similar or better activity than bare Pt. Experiments were performed on Pt, Bi on Pt and annealed BiPt surface alloy all deposited on a fluorine-doped tin oxide substrate. It was found that the BiPt alloy gave a greater exchange current density than the Pt film (~0.95 mA cm^{-2} compared to 0.56 mA cm^{-2}) though it is similar to the values generally found for bare Pt electrodes and the Pt value was lower than is often reported.

1.7 Project Aims

- This project aims to investigate the HER reaction on a range of surfaces, in order to further the knowledge of the area and to explore areas of uncertainty within the literature.
- Polycrystalline and single crystal Pt electrodes will be studied in order to determine whether there is a structural dependence for the hydrogen evolution reaction.
- Epitaxial films of Pt-group metals will be deposited onto Pt single crystal electrodes to examine effects of lattice strain and whether these surfaces show an enhanced catalytic activity for the HER compared to their equivalent bare Pt{*hkl*} analogues.
- Alloys and other deposited metal surfaces will be investigated in order to study any changes in HER mechanism or rate.
- Overall it is hoped that a better understanding of the HER mechanism can be achieved, with a view to finding more effective catalysts for the reaction than are currently available.

References

[1] G. Ertl, *Journal of Molecular Catalysis A: Chemical* **2002**, *182-183*, 5.
[2] G. Ertl, *Applied Surface Science* **1997**, *121-122*, 20.
[3] G. Ertl, *Surface Science* **1994**, *299-300*, 742.
[4] G. Ertl, *Journal of Molecular Catalysis* **1989**, *54*, 343.
[5] E. Delarue, H. Lamberts, W. D'haeseleer, *Energy* **2007**, *32*, 1299.
[6] G. Marbán, T. Valdés-Solís, *International Journal of Hydrogen Energy* **2007**, *32*, 1625.
[7] T. Abe, M. Kaneko, *Progress in Polymer Science* **2003**, *28*, 1441.
[8] G. G. Harding, *Journal of Power Sources* **1999**, *78*, 193.
[9] G. J. K. Acres, *Journal of Power Sources* **2001**, *100*, 60.
[10] M. Yano, A. Tomita, M. Sano, T. Hibino, *Solid State Ionics* **2007**, *177*, 3351.
[11] D. Cao, Y. Sun, G. Wang, *Journal of Power Sources* **2007**, *167*, 250.
[12] F. Alcaide, P.-L. Cabot, E. Brillas, *journal of Power Sources* **2006**, *153*, 47.
[13] V. A. Goltsov, T. N. Veziroglu, L. F. Goltsova, *International Journal of Hydrogen Energy* **2006**, *31*, 153.
[14] G. Mulder, J. Hetland, G. Lenaers, *International Journal of Hydrogen Energy* **2007**, *32*, 1324.
[15] W. McDowall, M. Eames, *International Journal of Hydrogen Energy* **2007**, *In Press, Corrected Proof.*
[16] M. H. Miles, *Journal of Electroanalytical Chemistry* **1975**, *60*, 89.
[17] M. C. Tavares, S. A. S. Machado, L. H. Mazo, *Electrochimica Acta* **2001**, *46*, 4359.
[18] L. Hammer, G. Wranglen, *Electrochimica Acta* **1964**, *9*, 1.
[19] A. Chatterjee, J. Foord, *Diamond and Related Materials* **2006**, *15*, 664.
[20] R. L. Penven, W. Levason, D. Pletcher, *Journal of Applied Electrochemistry* **1990**, *20*, 399.
[21] P. J. Mayne, *Polyhedron* **1984**, *3*, 1013.
[22] A. J. Gellman, J. D. Horvath, M. T. Buelow, *Journal of Molecular Catalysis A: Chemical* **2001**, *167*, 3.
[23] D. B. Hibbert, *Introduction To Electrochemistry*, Macmillan Press Ltd., London, **1993**.
[24] B. N. Grgur, P. Zivkovic, M. M. Gvozdenovic, *Progress in Organic Coatings* **2006**, *56*, 240.
[25] J. H. Barber, B. E. Conway, *Journal of Electroanalytical Chemistry* **1999**, *461*, 80.
[26] B. E. Conway, L. Bai, *Electrochimica Acta* **1986**, *8*, 1013.
[27] R. Parsons, *Transactions of the Faraday Society* **1951**, *47*, 1332.
[28] A. Saraby-Rientjes, *Electrochimica Acta* **1986**, *31*, 251.
[29] A. J. Bard, L. R. Faulkner, *Electrochemical methods: fundamentals and applications*, 2nd ed., Jon Wiley and sons inc., New York, **2001**.
[30] B. E. Conway, B. V. Tilak, *Electrochimica Acta* **2002**, *47*, 3571.
[31] J. O. M. Bockris, B. E. Conway, *Transactions of the Faraday Society* **1952**, *48*.
[32] J. O. M. Bockris, A.M.Azzam, *Transactions of the Faraday Society* **1951**, *48*, 145.
[33] J. O. M. Bockris, R. Parsons, H. Rosenburg, *Transactions of the Faraday Society* **1951**, *47*, 766.

[34] J. O. M. Bockris, I.A.Ammar, A. K. M. S. Huq, *Journal of Physical Chemistry* **1957**, *61*, 879.
[35] R. Parsons, *Transactions of the Faraday Society* **1958**, *54*, 1053.
[36] R. Parsons, J. O. M. Bockris, *Transactions of the Faraday Society* **1951**, *47*, 914.
[37] J. A. Pryde, C. G. Titcomb, *Journal of Physics C: Solid State Physics* **1972**, *5*, 1293.
[38] A. T. Kuhn, P. M. Wright, *Journal of Electroanalytical Chemistry and Interfacial Electrochemistry* **1970**, *27*, 319.
[39] A. T. Kuhn, M. Byrne, *Electrochimica Acta* **1971**, *16*, 391.
[40] C. D. Kim, B. E. Wilde, *Journal of The Electrochemical Society* **1971**, *118*, 202.
[41] G. M. Rao, F. R. Smith, *Journal of The Chemical Society Chemistry Communications* **1972**, 266.
[42] A. K. Vijh, *Journal of Physical Chemistry* **1968**, *72*, 1148.
[43] J. O. M. Bockris, S. Srinivasan, *Electrochimica Acta* **1964**, *9*, 31.
[44] S. Trasatti, *Journal of Electroanalytical Chemistry* **1972**, *39*, 163.
[45] J. Greeley, J. K. Norskov, *Surface Science* **2007**, *601*, 1590.
[46] E. Skulason, B. S. Karlberg, J. Rossmeisl, T. Bligaard, J. Greeley, H. Jonsson, J. K. Norskov, *Physical Chemistry Chemical Physics* **2007**, *9*, 3241.
[47] A. C. D. Angelo, *International Journal of Hydrogen Energy* **2007**, *32*, 542.
[48] N. Amokrane, C. Gabrielli, R. P. Nogueira, *Electrochimica Acta* **2007**, *52*, 4202.
[49] C. Ma, J. Sheng, N. Brandon, C. Zhang, G. Li, *International Journal of Hydrogen Energy* **2007**, *32*, 2824.
[50] J. H. Barber, S. Morin, B. E. Conway, *Journal of Electroanalytical Chemistry* **1998**, *446*, 125.
[51] N. Nanbu, F. Kitamura, T. Ohsaka, K. Tokuda, *Journal of Electroanalytical Chemistry* **2000**, *485*, 128.
[52] B. Ren, X. Xu, X. Q. Li, W. B. Cai, Z. Q. Tian, *Surface Science* **1999**, *427-428*, 157.
[53] B. E. Conway, G. Jerkiewicz, *Solid State Ionics* **2002**, *150*, 93.
[54] V. Horvat-Radosevic, K. Kvastek, *Electrochimica Acta* **2002**, *48*, 311.
[55] B. E. Conway, G. Jerkiewicz, *Electrochimica Acta* **2000**, *45*, 4075.
[56] J. Horiuti, T. Toya, *Solid state surface science*, New York, **1969**.
[57] G. E. Dima, G.L.Beltramo, M. T. M. Koper, *Electrochimica Acta* **2005**, *50*, 4318.
[58] J. M. Orts, A. Fernandez-Vega, J. M. Feliu, A. Aldaz, J. Clavilier, *Journal of Electroanalytical Chemistry* **1990**.
[59] S. Taguchi, A. Aramata, *Electrochimica Acta* **1994**, *39*, 2533.
[60] A. J. Silva, L.Proenca, M. I. S. Lopes, I. Fonseca, A. Rodes, A. Aldaz, *Electrochimica Acta* **2001**, *46*, 3147.
[61] E. Budewski, W. Bostanoff, *Electrochimica Acta* **1964**, *9*, 477.
[62] M. Bonnemay, A. Hamelin, M. S. D. Haro, *Electrochimica Acta* **1963**, *8*, 509.
[63] I. S. Toschev, B. Mutaftschiew, *Electrochimica Acta* **1964**, *9*, 1203.
[64] J. P. G. Farr, N. A. Hampson, *Journal of Electroanalytical Chemistry and Interfacial Electrochemistry* **1967**, *13*, 433.
[65] F. G. Will, *Journal of The Electrochemical Society* **1965**, *112*, 451.
[66] F. G. Will, C. F. Knorr, *Zeitschrift fur Elektrochemie* **1960**, *64*, 258.

[67] J. Clavilier, R. Faure, G. Guinet, R. Durand, *Journal of Electroanalytical Chemistry* **1980**, *107*, 205.
[68] H. Kita, S. Ye, Y. Gao, *Journal of Electroanalytical Chemistry* **1992**, *334*, 351.
[69] K. Seto, A. Ianelli, B. Love, J.Lipkowski, *Journal of Electroanalytical Chemistry* **1987**, *226*, 351.
[70] R. Gomez, A. Fernandez-Vega, J. M. Feliu, A.Aldaz, *Journal of Physical Chemistry* **1993**, *97*, 4769.
[71] N. M. Markovic, B. N. Grgur, P. N. Ross, *Journal of Physical Chemistry B* **1997**, *101*, 5405.
[72] R. J. Nichols, A. Bewick, *Journal of Electroanalytical Chemistry* **1988**, *243*, 445.
[73] S. E. Huxter, G. A. Attard, *Electrochemistry Communications* **2006**, *8*, 1806.
[74] N. Hoshi, T. Suzuki, Y. Hori, *Electrochimica Acta* **1995**, *41*, 1647.
[75] T. H. M. Housmans, M. T. M. Koper, *Journal of Electroanalytical Chemistry* **2005**, *575*, 39.
[76] Y. Ishikawa, J. M. Mateo, D. A. Tryk, C. R. Cabrera, *Journal of Electroanalytical Chemistry* **2007**, *607*, 37.
[77] Z. Kerner, T. Pajkossy, L. A. Kibler, D. M. Kolb, *Electrochemistry Communications* **2002**, *4*, 787.
[78] N. M. Markovic, C. A. Lucas, V. Climent, V. Stamenkovic, P. N. Ross, *Surface Science* **2000**, *465*, 103.
[79] S. Morin, H. Dumont, B. E. Conway, *Journal of Electroanalytical Chemistry* **1998**, *412*, 39.
[80] E. Sibert, R. Faure, R. Durand, *Journal of Electroanalytical Chemistry* **2002**, *528*, 39.
[81] E. Herrero, J. M. Feliu, A. Wieckowski, J. Clavilier, *Surface Science* **1995**, *325*, 131.
[82] R. Gomez, J. M. Feliu, A. Aldaz, *Electrochimica Acta* **1996**, *42*, 1675.
[83] M. B. Vukmirovic, R.L.Sabatini, R. R. Adzic, *Surface Science* **2004**, *572*, 269.
[84] P. J. Welford, B. A. Brookes, V. Climent, R. G. Compton, *Journal of Electroanalytical Chemistry* **2001**, *513*, 8.
[85] N. M. Markovic, S. T. Sarraf, H. A. Gasteiger, P. N. Ross, *Journal of The Chemical Society Faraday Transactions* **1996**, *92*, 3719.
[86] M. Hourani, A. Wieckowski, *Journal of Electroanalytical Chemistry* **1988**, *244*, 147.
[87] F. M. Hoffmann, N. J. Levinos, B. N. Perry, P. Rabinowitz, *Physics Review B.: Condensed Matter and Materials Physics* **1986**, *33*, 4309.
[88] H. Inoue, J. X. Wang, K. Sasaki, R. R. Adzic, *Journal of Electroanalytical Chemistry* **2003**, *554*, 77.
[89] P. J. Berlowitz, C. H. F. Peden, D. W. Goodman, *Journal of Physical Chemistry* **1988**, *92*, 5213.
[90] P. M. Rigano, C. Mayer, T. Chierchie, *Electrochimica Acta* **1990**, *35*, 1189.
[91] M. Baldauf, D. M. Kolb, *Electrochimica Acta* **1993**, *38*, 2145.
[92] R. F. Miller, J. Koshy, *Journal of Physics D: Applied Physics* **1974**, *7*, 1472.
[93] K. Haeupl, P. Wissmann, *Thin Solid Films* **1989**, *174*, 105.
[94] J. Clavilier, M. J. Llorca, J. M. Feliu, A. Aldaz, *Journal of Electroanalytical Chemistry* **1991**, *310*, 429.
[95] G. Rangelov, T. Fauster, U. Struber, J. Kuppers, *Surface Science* **1995**, *331-333*, 948.

[96] P. Liu, A. Logadottir, J. K. Norskov, *Electrochimica Acta* **2003**, *48*, 3731.
[97] N. M. Markovic, P. N. R. Jr., *Surface Science Reports* **2002**, *45*, 117.
[98] M. Watanabe, M. Uchida, S. Motoo, *Journal of Electroanalytical Chemistry* **1987**, *229*, 395.
[99] J. O. M. Bockris, A. Damjanovic, R. J. Mannan, *Journal of Electroanalytical Chemistry and Interfacial Electrochemistry* **1968**, *18*, 349.
[100] N. V. Krstajic, B. N. Grgur, M. Zdujic, M. V. Vojnovic, M. M. Jaksic, *Journal of Alloys and Compounds* **1997**, *257*, 245.
[101] A. Jukic, J. Piljac, M. Metikos-Hukovic, *J. Molecular Catalysis A: Chemical* **2001**, *166*, 293.
[102] Q. Han, K. Liu, J. Chen, X. Wei, *International Journal of Hydrogen Energy* **2003**, *28*, 1207.
[103] Q. Han, K. Liu, J. Chen, X. Wei, *International Journal of Hydrogen Energy* **2003**, *28*, 1345.
[104] J. Greeley, J. K. Norskov, L. A. Kibler, A. M. El-Aziz, D. M. Kolb, *Chem Phys Chem* **2006**, *7*, 1032.
[105] J. Greeley, T. F. Jaramillo, J. Bonde, I. Chorkendorff, J. K. Norskov, *Nature Materials* **2006**, *5*, 909.

Chapter 2

Theoretical Background

2.1 Electrochemical Analysis Methods

2.1.1 Direct Current Techniques

Direct current (DC) analysis techniques are important in electrochemistry, as they supply useful current versus potential information for electrochemical systems. This can either be at steady state (where a reaction is controlled by electron transfer rate) or controlled by mass transport of reactants (the rate of diffusion of a species from the bulk of the solution to the electrode surface) to the electrode. In comparison with alternating current (AC) analysis techniques, steady state DC experiments are easier to perform and interpret. As a result of this, they are more widely used in electrochemistry. Some of the most significant DC electrochemical techniques are described in the following section.

2.1.1.1 Linear Sweep Voltammetry/ Tafel Data

Linear sweep voltammetry (LSV) is the simplest voltammetric technique as it involves measuring the current produced by an electrode as a function of potential applied between a working electrode and a reference electrode (see section 2.4) in a stationary solution. This potential is swept at a constant rate between two potential limits and gives rise to a current which flows between the working electrode and a third electrode, the counter electrode.

A typical potential ramp and a current-potential response curve for an electroactive redox species are shown in fig. 2.1.1. The rise in current on the current-potential plot represents the release of electrons as a species, R, is oxidized to species O at a particular potential.

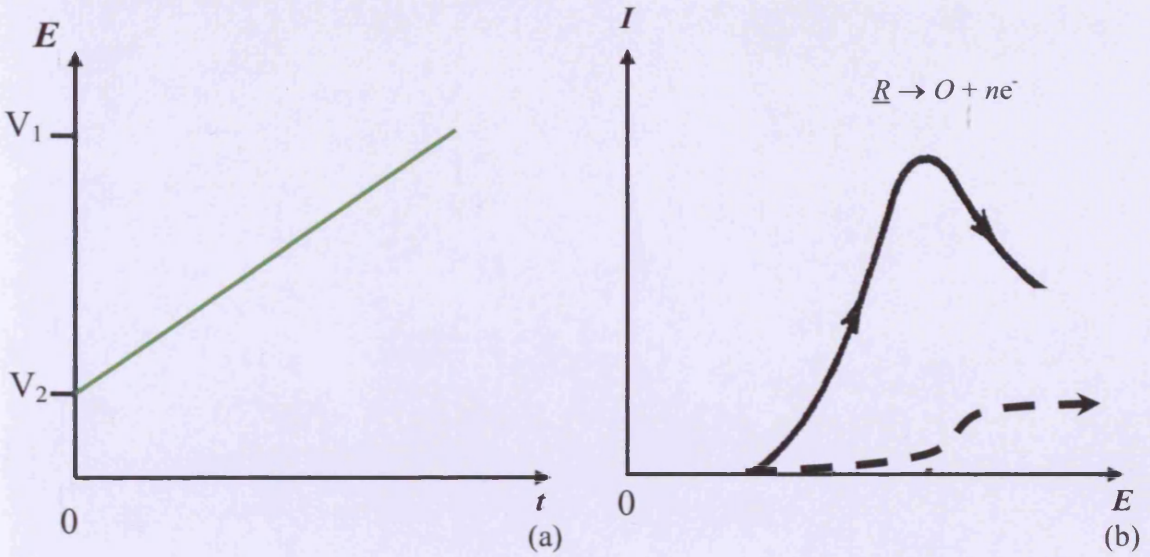

Fig. 2.1.1 (a) Potential ramp and (b) generalized current-potential response for redox species in LSV experiments at steady state (dashed line) and at a fast, non-steady state, sweep rate (solid line).

One of the important applications for linear sweep voltammetry, with particular reference to the hydrogen evolution reaction is to provide data for analysis using the Tafel equation. Measurement of Tafel parameters involves applying a slow (steady state) scan rate linear potential sweep and monitoring the current response (i.e. slow enough that the response did not change at slower scan rates). The Tafel equation is derived from Butler-Volmer kinetics. For a one-electron transfer at steady state (with no mass-transport effects) the Butler-Volmer equation relating a current response to an applied overpotential is applicable:

$$i = i_0 \left\{ \exp\left[\frac{-\alpha F}{R_g T} \eta \right] - \exp\left[\frac{(1-\alpha) F}{R_g T} \eta \right] \right\} \qquad \textbf{(2.1.1)}$$

where η is overpotential, R_g is the universal gas constant, T is temperature, α is the transfer coefficient, F is the Faraday constant, i is current and i_0 is the exchange current (current density, j and exchange current density, j_0 may be used instead of i and i_0 respectively by normalising the current to the electrode area, making it easier for comparison of results where different electrode areas are used and hence different currents produced).

At steady state (and at large overpotentials), the anodic current component is negligible, giving:

$$i = i_0 \exp\left[\frac{-\alpha F}{R_g T}\eta\right] \qquad \textbf{(2.1.2)}$$

This leads to the Tafel equation:

$$\eta = \frac{2.3R_g T}{\alpha F}\log i_0 - \frac{2.3R_g T}{\alpha F}\log i \qquad \textbf{(2.1.3)}$$

If

$$a = \frac{2.3R_g T}{\alpha F}\log i_0 \qquad \textbf{(2.1.4)}$$

and

$$b = \frac{-2.3R_g T}{\alpha F} \qquad \textbf{(2.1.5)}$$

the common form of the Tafel equation is obtained:

$$\eta = a + b\log i \qquad \textbf{(2.1.6)}$$

Tafel experiments are important in the study of the hydrogen evolution reaction, where the system potential is swept sufficiently negative that hydrogen is evolved from the working electrode. Rearrangement of equation (2.1.2) gives:

$$\log i = \log i_0 - \frac{\alpha F}{2.3R_g T}\eta \qquad \textbf{(2.1.7)}$$

Tafel plots of log current versus overpotential (i.e. the excess potential, from the equilibrium potential, required to force a particular reaction rate to occur) (fig. 2.1.2) are used to obtain kinetic parameters for the HER. The exchange current, i_0, is a good indicator of electrode activity and may be obtained from the intercept on the log i axis

at $\eta = 0$. The Tafel slope is independent of area and can take distinct values for each of the HER mechanisms, as explained in section 1.2. The slope also gives the transfer coefficient, α, which is a measure of the symmetry of the energy barrier (or reaction coordinate for a redox couple), it takes the value 0.5 for a perfectly symmetrical energy barrier[1] and is involved in many equations in electrochemistry, particularly Butler-Volmer kinetics.

The HER is not a simple, one electron transfer process as explained in section 1.2, though the Tafel equations may be applied to the individual steps of the reaction, where the Tafel kinetics (and the Tafel slope) for the reaction will be related to the rate determining step.

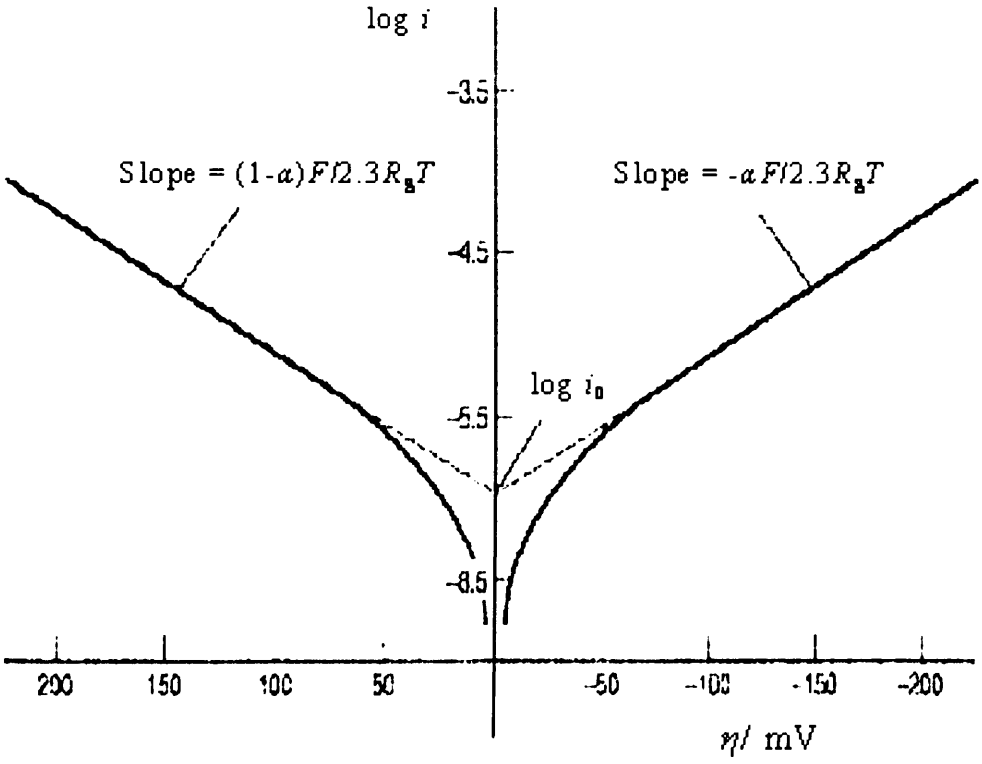

Fig. 2.1.2[1] Tafel plots for anodic and cathodic branches of a redox couple with transfer coefficient, α = 0.5.

2.1.1.2 Cyclic Voltammetry

Cyclic voltammetry is an important method for characterising electrode surfaces and testing the cleanliness and reproducibility of an electrochemical system. This method is similar to that of linear sweep voltammetry though the applied potential is increased and decreased in a sawtooth waveform (fig. 2.1.3),

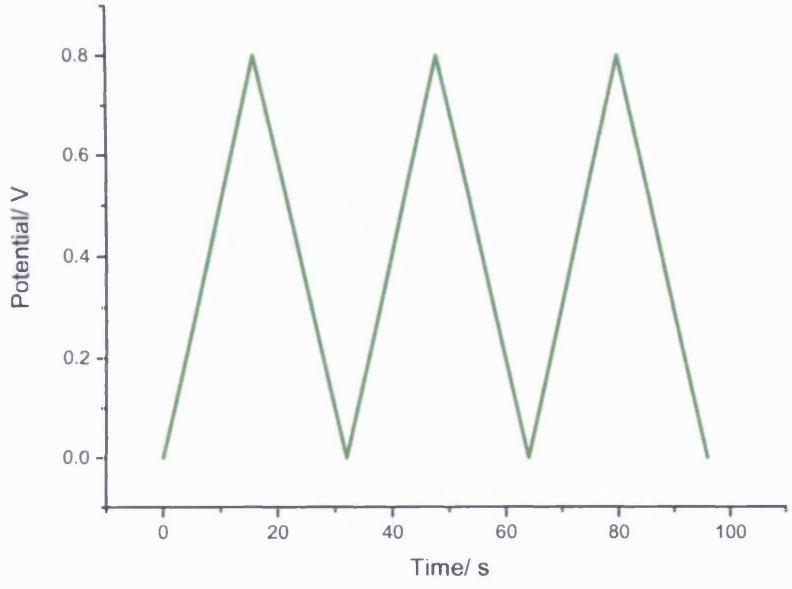

Fig. 2.1.3 Potential waveform applied to working electrode in cyclic voltammetry. This waveform shows three full potential sweeps between 0 and 0.8 V at a sweep rate of 0.05 V s^{-1}.

For a normal ohmic conductor, the voltammogram would show the current increasing and decreasing linearly with the voltage. However when we apply the potential to an electrode/electrolyte system a very different picture is seen.

For a simple redox couple of the form:

$$O + ne^- \leftrightarrow R \qquad \textbf{(2.1.8)}$$

where O is the oxidised species in the reaction, R is the reduced species, and n is the number of electrons involved in the reaction. If the process in equation (2.1.8) is fast and the reaction mechanism is the same (but opposite) for the forward and back reactions, it is said to be reversible and will give a cyclic voltammogram similar to that seen in fig. 2.1.4. The voltammogram in fig. 2.1.4 shows two equal but opposite

positive and negative current peaks corresponding to the oxidation of species R and the reduction of species O respectively. The peak current for such a process is given by:

$$i_p = 2.75x10^{-5} n^{3/2} v^{1/2} C_o^* D_o^{1/2} \qquad \textbf{(2.1.9)}$$

where v is the potential sweep rate in V s^{-1}, C_o^* is the bulk concentration of the electroactive species in bulk solution in mol cm^{-3} and D_o is the diffusion coefficient in cm^2 s^{-1}. The potential separation between the two peaks is given by the equation:

$$\left|E_p^{Ox} - E_p^{Red}\right| = 2.218 \frac{R_g T}{nF} \qquad \textbf{(2.1.10)}$$

where E_p^{Ox} and E_p^{Red} are the potentials of the oxidation and reduction peaks respectively.

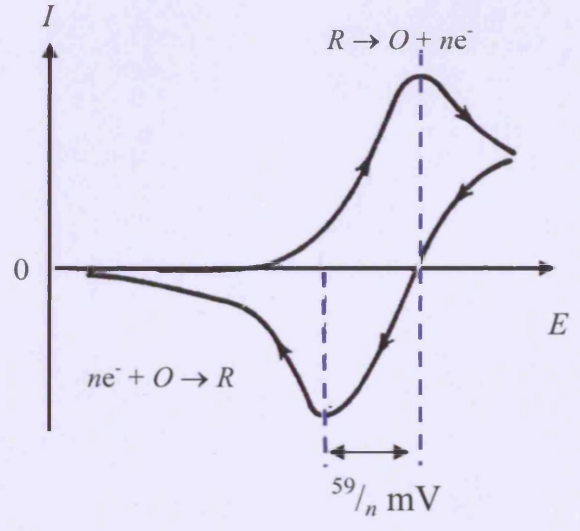

Fig. 2.1.4 Diagram of cyclic voltammogram for a simple reversible redox couple. Note that the separation of the redox peaks in this case is given by 59/n mV.

A more specific electrochemical system which is very relevant to this project is Pt in H_2SO_4, where a more intricate voltammogram is observed (fig. 2.1.5). This is due to the electrolyte and the surface reactions that occur at specific potentials i.e. the adsorption/desorption of H and OH on the Pt electrode surface. At sufficiently low sweep rate, the peak potentials and intensities are free of mass transport influence, hence surface adsorption peak intensities vary directly with sweep rate (i.e. $i_p \propto v$) instead of $i_p \propto v^{1/2}$ (for semi-infinite linear mass transport).

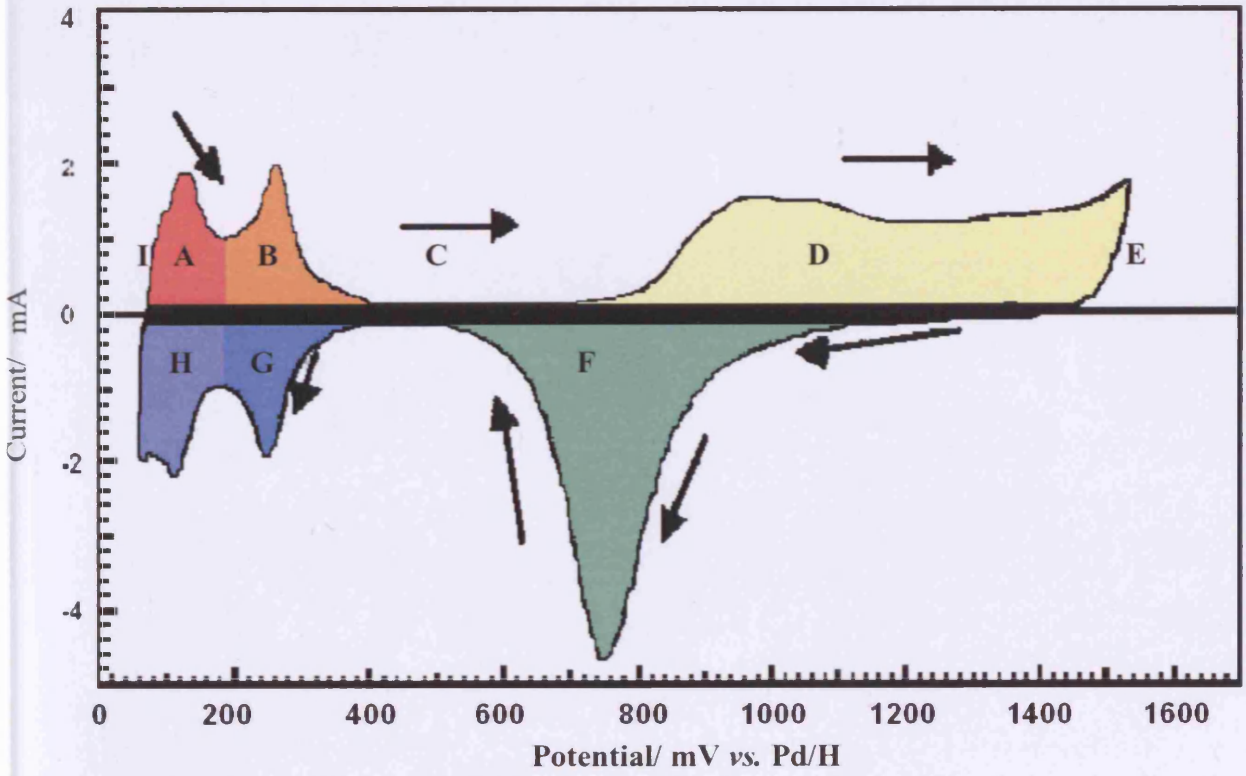

Fig. 2.1.5 Cyclic voltammogram of polycrystalline platinum in 0.1 M H_2SO_4. Sweep rate 0.05 V s^{-1}.

Fig. 2.1.5 shows a typical cyclic voltammogram (CV) observed when a polycrystalline Pt working electrode is used, with a Pt counter electrode and a palladium-hydride (Pd/H) reference electrode in 0.1 M H_2SO_4 at room temperature and a potential sweep rate of 0.05 V s^{-1}. Each of the coloured sections shows an electrochemical process occurring on the working electrode surface. Hence when different electrode materials are used (or indeed different electrolytes or even electrode orientations) the surface energetics of these processes are affected, resulting

in differently shaped peaks and shifts in potential. Therefore, a distinct, well-characterised, voltammogram for a given electrode/electrolyte combination may be described.

Regions A and B constitute the hydride stripping region, where H adsorbed on the electrode surface is electrochemically desorbed, producing electrons and therefore producing a current. The reaction in this region is:

$$H_{ads} \rightarrow H^{+}_{(aq)} + e^{-} \qquad \textbf{(2.1.11)}$$

The distinction between regions A and B stems from the types of adsorption sites for the hydrogen atoms. Region A is commonly referred to as "weakly" bound and region B as "strongly" bound at {110} and {100} step sites respectively[2].

Region C corresponds to the double layer region, where the only charge flowing is the capacitative current due to the charging of the electrochemical double layer. The thickness of the double layer region is significant as its size is proportional to the capacitance of the electrode, which not only depends on the material, but also the electrode surface area. Hence if an electrode is rough and unpolished the double layer region will be much wider than if it were not. There are numerous models proposed for the distribution of ions at the electrode/electrolyte interface leading to capacitative processes and these are discussed in more detail in section 2.5.

Region D is the oxide forming region, where water from solution adsorbs onto the electrode surface, forming OH and oxide species, which also produces electrons and a positive "anodic" current.

$$H_2O \rightarrow OH_{ads} + H^{+}_{(aq)} + e^{-} \qquad \textbf{(2.1.12)}$$

Point E is the switching potential point, i.e. the point at which the positive potential sweep is stopped and the reverse sweep is commenced (the peak potential on the sawtooth potential waveform). If the potential is swept above this point (1.55 V *vs.* Pd/H for this particular system) oxygen gas is evolved from the Pt electrode.

Region F is the oxide stripping region, where the reverse reaction to that of region D occurs. Hence a negative "cathodic" current is produced as electrons are transferred from the electrode to the electrolyte.

Regions G and H comprise the hydride forming region, where the reverse reaction of that in regions A and B occurs and again producing a cathodic current. Similarly to regions A and B, the hydrogen atoms adsorb strongly at {100} sites (region G) and weakly at {110} sites (region H).

Point I is the minimum potential applied to the electrode, it is the point where the negative potential sweep is switched to a positive going potential sweep. When the potential is swept negative of point I, 0.06 V *vs.* Pd/H (0 V *vs.* RHE), hydrogen gas is evolved.

The area of an electrode may be calculated from its cyclic voltammetry if the number of electrons involved in the surface reaction and the charge density of the electrode surface, σ, are known. In the case of polycrystalline Pt in H_2SO_4, the charge density of the surface, σ, is approximately 210 $\mu C\ cm^{-2}$ for the underpotentially deposited hydrogen in the potential range 0 - 0.4 V *vs.* Pd/H. This value is calculated by taking an average of the known atomic densities of the three basal plane surfaces and assuming that, in the formation of a hydrogen adsorption layer, one hydrogen atom adsorbs to one Pt atom (or, more specifically, one electron is transferred per Pt atom). The area can be calculated using the equation:

$$A = \frac{Q}{\sigma} \qquad \textbf{(2.1.13)}$$

where Q is the charge on the working electrode calculated from the area of the UPD-H peaks, i.e. regions G and H or regions A and B from fig. 2.1.5.

2.1.1.3 Rotating Disk Electrode

A significant problem faced when Tafel experiments for HER in acid are performed is the steady state problem; the reaction must be controlled by the rate of electron transfer rather than diffusion. For a stationary electrode, this involves performing the experiments very slowly (i.e. the rate at which the potential is swept must be slowed down until results are the same irrespective of sweep rate). However, it is found that hydrogen forming at the electrode will interfere with these results, since bubbles of gas often form and attach themselves to the electrode surface, blocking the electrolyte. A way around such problems is to rotate the electrode at high speed (assuming the electrode surface is flat) which results in the system reaching steady state at faster potential sweep rates. In addition the hydrogen gas is forced away from the surface due to the rotation of the electrode.

This "forced" mass transport of bulk electrolyte to the electrode surface (fig. 2.1.6) results in a layer of solution being formed at the surface which is rotating at the same rate as the electrode and is therefore effectively stationary. The thickness of this layer depends on the speed of rotation, from the relation:

$$\delta = [1.61\gamma^{1/2}D_o^{1/3}]\omega^{-1/2} \qquad \textbf{(2.1.14)}$$

where δ is the diffusion layer thickness, γ is the kinematic viscosity of the solution, D_o is the diffusion coefficient of the oxidized species and ω is the rotation rate in rad s^{-1}. Thus as rotation rate increases, the diffusion layer thickness decreases. The thinner the diffusion layer, the faster the diffusion rate, and hence the less influence diffusion has on the electrode kinetics, leading to steady state at higher scan rates.

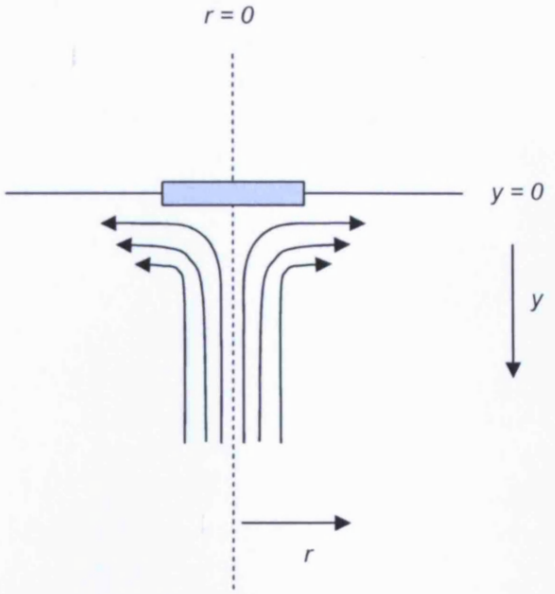

Fig. 2.1.6 Schematic diagram, showing the solution flow to a Rotating Disk Electrode, where r is the distance from the centre of the electrode along the electrode plane and y is the distance from the electrode surface perpendicular to the plane[3].

Taking Tafel data (section 2.1.1.1) using the rotating disk electrode at various rotation rates allows production of Koutecky-Levich plots[1] ($1/i$ versus $1/\omega^{1/2}$) from the relationship in equation (2.1.15), where i is the current at a particular potential and ω is rotational frequency in Hz. The current density, j, is often used in preference of i (as in fig. 2.1.7), as it enables the direct comparison of similar results on electrodes of different areas by normalising the figures to area.

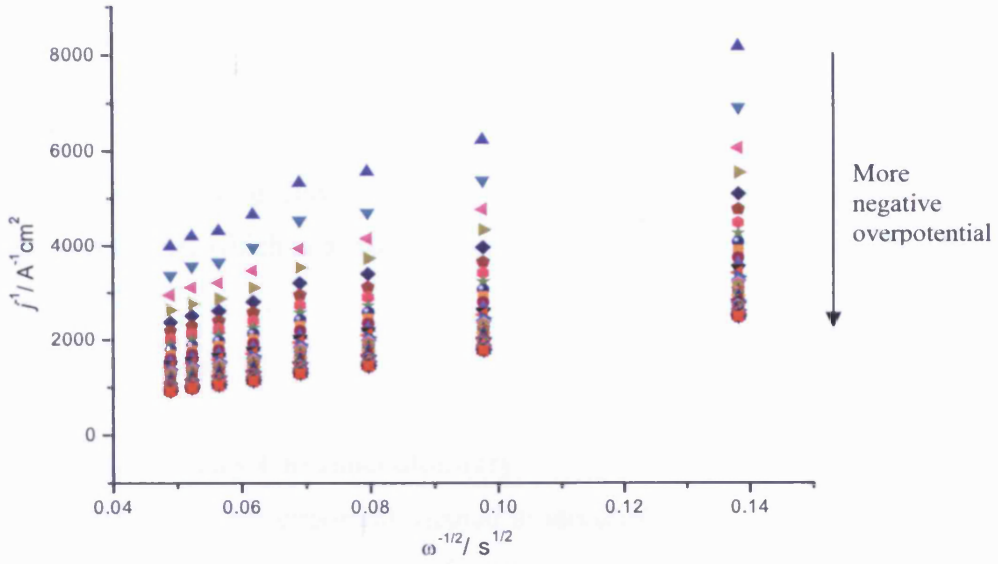

Fig. 2.1.7 Koutecky-Levich plots of $1/j$ versus $1/\omega^{1/2}$ at overpotential between 0 – 0.1 V at rotation rates between 500 and 4000 rpm for Pt electrode in 0.05M H_2SO_4.

From the Koutecky-Levich graph a value for j_k (the current in the absence of any mass transfer effects) can be found using the relation:

$$\frac{1}{j} = \frac{1}{j_k} + \frac{1}{0.620nFC_o^* D_o^{2/3} \gamma^{-1/6} \omega^{1/2}} \qquad \textbf{(2.1.15)}$$

where n is the number of electrons taking part in the reaction and C_o^* is the concentration of the oxidised species of the redox couple in the solution.

This then leads us to a value of k_f (the reaction rate constant) from the equation:

$$j_k = nFk_f C_o^* \qquad \textbf{(2.1.16)}$$

A plot of ln k_f versus overpotential, η, yields values of α and k^0 (the standard rate constant), since:

$$\ln k_f = \ln k^0 - \frac{\alpha nF\eta}{R_g T} \qquad \textbf{(2.1.17)}$$

where k^0 is the rate constant for a reaction at the formal potential of the couple. It thus reflects the intrinsic kinetic facility and hence the catalytic ability of the electrode material.

One drawback of the rotating disk method is that it may be rather mechanically stressful to the electrodes, which is a particular problem for metal plated electrodes if the coating is not robust.

2.1.1.4 Chronoamperometry/Chronocoulometry

Chronoamperometry is another important method in electrochemical analysis. In this technique, current is recorded as a function of time at constant potential. It may often be used for testing if the activity of an electrode is constant with time, an important feature in testing materials as catalysts which may be used over long time periods, e.g. for use in fuel cells.

Using the Cottrell equation[1]:

$$i(t) = \frac{nFAD_o^{1/2}C_o^*}{\pi^{1/2}t^{1/2}} \qquad \textbf{(2.1.18)}$$

i can be plotted against $1/t^{1/2}$ to obtain a straight line. From this, a value for the diffusion coefficient, D_o, the electrode area or concentration of the solution can be found (depending on which parameters are known) via the gradient.

Chronocoulometry is similar to chronoamperometry, but here, charge is recorded as a function of time and the Cottrell equation is modified slightly in terms of charge[1]:

$$Q = \frac{2nFAD_o^{1/2}C_o^*t^{1/2}}{\pi^{1/2}} \qquad \textbf{(2.1.19)}$$

Q is thus plotted against $t^{1/2}$ in this case, before the values of the various constants can be obtained from the gradient of the graph as in chronoamperometry.

2.1.2 AC Techniques

All of the DC techniques in section 2.1.1 have advantages. However, when studying the nature of OPD-H, DC techniques become less useful and AC techniques are required. This is due to the OPD-H coverage being governed by potential. Hence at any given potential the current would be constant and no further information could be obtained relating to the processes occurring. In AC studies, the DC bias determines the surface coverage whilst an applied AC signal may be used to obtain information relating to frequency dependences of processes occurring at the electrode[4]. For hydrogen evolution specifically, the DC techniques rely on steady state measurements which are not able to separate out the contributions from the different processes occurring (i.e. solution resistance, adsorption/desorption and diffusion), whereas AC methods may be used to break down the different contributions of these processes depending on their time constants.

2.1.2.1 AC Circuits

It is often useful to imagine the composite parts of an electrochemical system as an arrangement of electrical components. This allows for the measurement of current and potential responses being assigned to specific cell elements.

A sinusoidal voltage is most easily thought of as a rotating vector (or phasor) with a length of $\dot{E}$ and rotating with a frequency of ω (see fig 2.1.8). The observed voltage at a time t is a projection of this vector onto some axis (usually taken to be at 0 °). It may be expressed as:

$$E_{AC} = \dot{E}\sin\omega t \qquad \textbf{(2.1.20)}$$

Similarly, the sinusoidal current may be expressed as:

$$I_{AC} = \dot{I}\sin(\omega t + \phi) \qquad \textbf{(2.1.21)}$$

where ϕ is the phase angle between the current and voltage phasors.

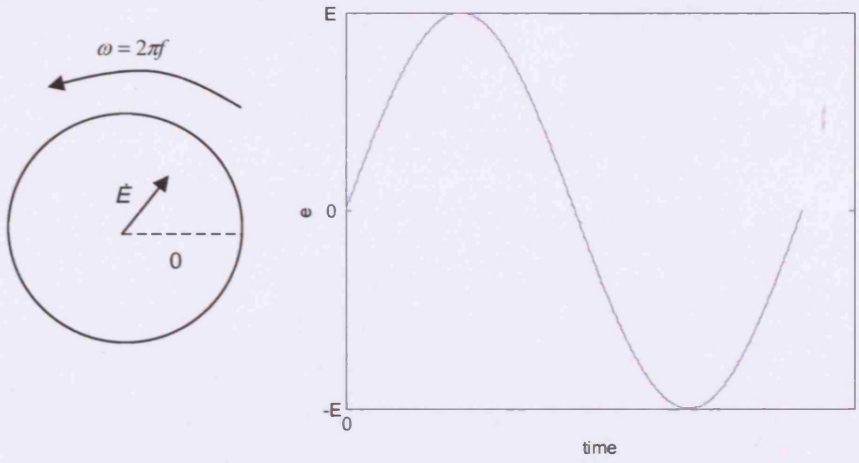

Fig. 2.1.8 Phasor diagram for an a.c. voltage signal, E, of frequency ω.

From Ohm's law, it is known (in direct current (DC) terms) that:

$$R_{DC} = \frac{E_{DC}}{I_{DC}} \tag{2.1.22}$$

where R_{DC} is resistance, E_{DC} is potential and I_{DC} is the DC current. A generalised form of this equation is:

$$Z = \frac{E}{I} \tag{2.1.23}$$

where Z is impedance (a generalised resistance term), E is total potential and I is total current. This holds true for AC circuits, where Z may be split into real and imaginary components:

$$Z(\omega) = Z_{Re} - j_{Im} Z_{Im} \tag{2.1.24}$$

Where Z_{Re} and Z_{Im} are the real and imaginary components of impedance respectively and j_{Im} is given by:

$$j_{Im} = \sqrt{-1} \tag{2.1.25}$$

Z_{Re} represents the in phase (resistive component of $Z(\omega)$ whilst Z_{Im} represents the out of phase (capacitative) component of $Z(\omega)$.

The real and imaginary terms are given by:

$$Z_{Re} = R_{DC} \tag{2.1.26}$$

and

$$Z_{Im} = X_C = \frac{1}{\omega C} \tag{2.1.27}$$

where C is capacitance and X_C is capacitative resistance.

Hence, the impedance may be given by:

$$Z = R_{DC} - \frac{j_{Im}}{\omega C} \tag{2.1.28}$$

The magnitude and phase angle of Z are given by equations (2.1.29) and (2.1.30) respectively.

$$|Z|^2 = R_{DC}^2 + \frac{1}{(\omega C)^2} = Z_{Re}^2 + Z_{Im}^2 \tag{2.1.29}$$

$$\tan\phi = \frac{Z_{Im}}{Z_{Re}} = \frac{1}{\omega R_{DC} C} \tag{2.1.30}$$

The impedance response of an electrochemical system can be modelled as a combination of capacitances and resistances such that the current passed has the equivalent amplitude and phase angle as the system as a function of frequency. The most commonly used circuit for this modelling procedure is the Randles equivalent circuit in fig. 2.1.9.

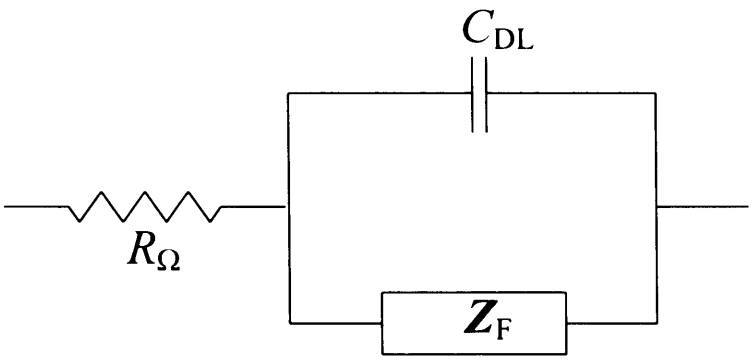

Fig. 2.1.9 Randles equivalent circuit, representing the capacitance and resistance in an electrochemical cell[5].

The components of the circuit represent the electrical contributions from the electrochemical cell. In fig. 2.1.9 the resistor, R_Ω, represents the solution resistance and the capacitor C_{DL}, represents the double layer capacitance (the effect seen when ions in the double layer between the electrode surface and solution are used to store charge, making it behave almost as a pure capacitor, see section 2.5). The faradaic term, Z_F, is more complicated and can not be represented as a simple circuit element in most situations as it is frequency dependent. The faradaic term is often represented in one of two ways, either using a series combination of a resistance, R_P, and a pseudo capacitance, C_P[6], or separating it into a pure (charge transfer) resistance, R_{CT}, and the Warburg impedance, Z_W[7] (a theoretical element used to represent mass transport effects). R_Ω and C_{DL} can be found experimentally or by mathematical calculation, therefore it is possible to monitor the effect of variation of R_{CT} and Z_W with changes in electrochemical system parameters.

2.1.2.2 AC Impedance Spectroscopy

AC Impedance spectroscopy keeps the concentration ratio of the redox couple constant by applying a constant DC potential while the frequency of the superimposed AC voltage is altered. By plotting a graph of real versus imaginary components (fig. 2.1.10) of the impedance it is possible to find the charge transfer resistance, R_{CT}, which is inversely proportional to k^0, and the uncompensated solution resistance R_Ω.

Fig. 2.1.10 shows an Argand diagram, which is a plot of the real component of impedance, Z_{re}, versus the imaginary component, Z_{im} at various frequencies. The system can be modelled using a Randles equivalent circuit with Z_f represented as a pure charge transfer resistance, R_{CT}, and a Warburg impedance, Z_W, as explained in section 2.1.2.1.

As the impedance varies with frequency, limiting factors involved in AC impedance processes[8, 9] may be observed from the plot. At high frequencies the curve represents the system under kinetic control (faradaic processes) where the charge transfer resistance dominates the total faradaic impedance, Z_f. In contrast, at lower frequencies, diffusion becomes more important and the plot is dominated by the Warburg impedance, producing a characteristic 45° slope in this impedance representation.

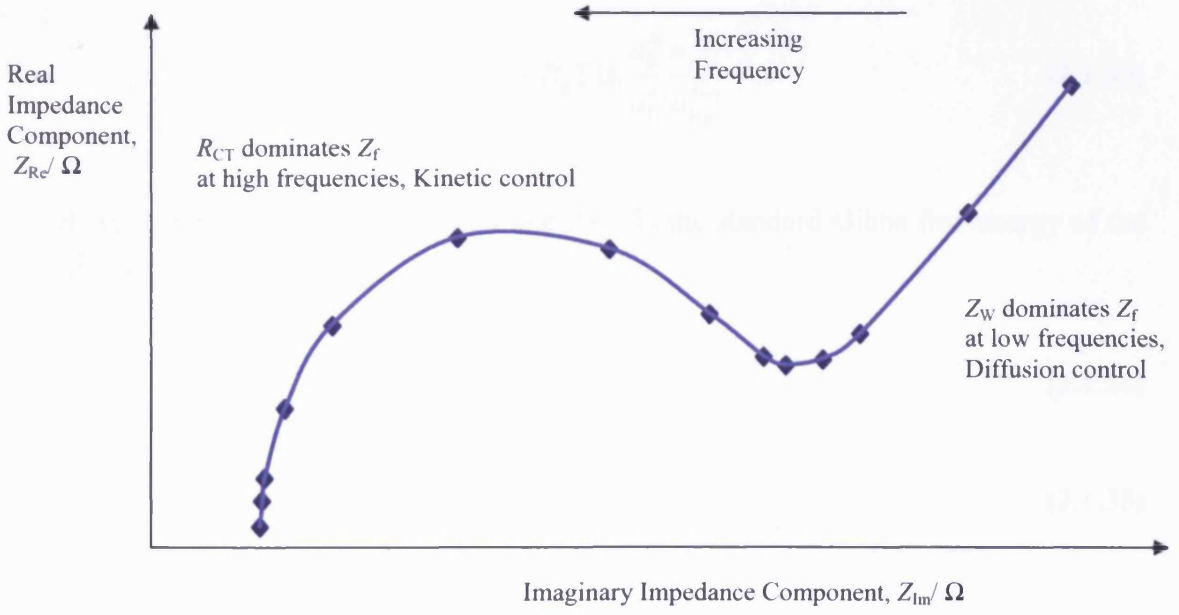

Fig. 2.1.10 Schematic Argand diagram/complex plane plot of real versus imaginary components of impedance for an electrochemical system[5].

2.1.2.3 AC Voltammetry[5]

Conventional AC Voltammetry is a slightly different technique to AC impedance spectroscopy as it applies a single AC frequency on top of a stepped DC potential, E_{DC}, potentiostatically. E_{DC} is varied over a long time scale compared to the AC voltage, E_{AC}, which allows the determination the surface concentrations for the oxidised and reduced species, using the Nernst equation, which is derived from a generalised half-cell reaction:

$$n_o O + ne^- \leftrightarrow n_r R \qquad \textbf{(2.1.31)}$$

where n_o and n_r are the stoichiometric coefficients of the oxidised and reduced species respectively. The cell reaction, when coupled with a hydrogen electrode, is then given by:

$$n_o O + n_{H_2} H_2 \leftrightarrow n_r R + n_{H^+} H^+ \qquad \textbf{(2.1.32)}$$

The free energy for this reaction is then given by:

$$\Delta G = \Delta G^\circ + R_g T \ln \frac{a_R^{n_r} a_{H^+}^{n_{H^+}}}{a_O^{n_o} a_{H_2}^{n_{H_2}}} \qquad \textbf{(2.1.33)}$$

where a_i is the activity of species i and ΔG° is the standard Gibbs free energy of the cell. It is known that

$$\Delta G = -nFE \qquad \textbf{(2.1.34)}$$

and

$$\Delta G^\circ = -nFE^\circ \qquad \textbf{(2.1.35)}$$

where E° is the standard cell potential.

As a_{H^+} and a_{H_2} are unity for the SHE, substitution of equations (2.1.34) and (2.1.35) into equation (2.1.33) and rearranging gives:

$$E = E^0 + \frac{R_g T}{nF} \ln \frac{a_O^{n_{ox}}}{a_R^{n_r}} \quad \textbf{(2.1.36)}$$

Equation (2.1.36) can be written as the Nernst equation:

$$E = E^{0'} + \frac{R_g T}{nF} \ln \frac{C_O^*}{C_R^*} \quad \textbf{(2.1.37)}$$

where $E^{0'}$ is the formal potential of the reaction, C_O^* and C_R^* are the bulk concentrations of species *O* and *R* respectively.

AC voltammetry is often performed at various frequencies to see the effect it has on the *I-E* characteristics of a system[10].

2.1.2.4 Multi-Frequency AC Voltammetry

To advance and improve the system of AC Voltammetry, Smith[11, 12] designed a system of Multi-Frequency AC Voltammetry (MFACV) which applies many AC signals at the same time. This is very useful for AC voltammetry results, since it has two very major advantages. Firstly, fewer experiments need to be performed to allow determination of kinetic parameters and secondly, the electrode surface is the same for each frequency, whereas, with standard AC voltammetry, the surface may change slightly after each run or between runs.

MFACV is very sophisticated, but very useful, so is regaining popularity as an analysis tool[13-15]. The technique works by applying a long time scale linear DC potential sweep (E_{DC}) as in standard AC Voltammetry but instead of a single frequency signal, a "noise" signal consisting of multiple AC sine waves is applied[16] (fig. 2.1.11). This signal is generated in the frequency domain and Fourier transformed[16-22] into the time domain, before application to the cell. The current response signal then has to be transformed back into the frequency domain for analysis.

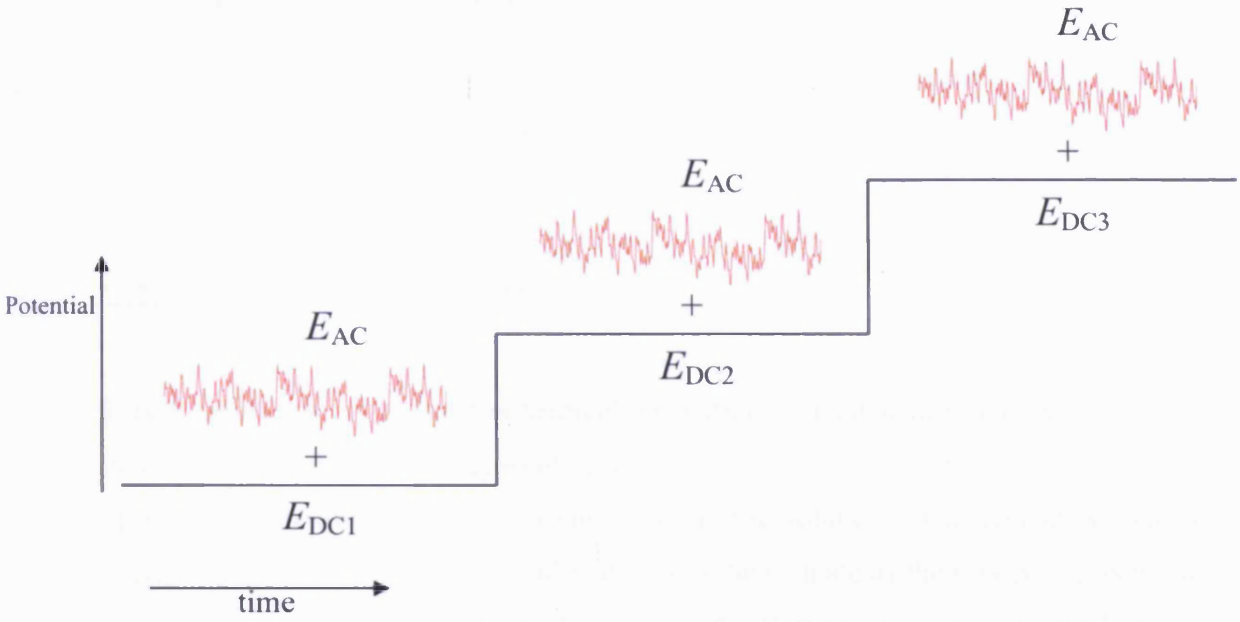

Fig. 2.1.11 schematic diagram showing the applied, long term potential, E_{DC}, and short term AC signal, E_{AC}, for MFACV.

Many parameters, including potential, frequency, admittance, complex impedance components (including phase angle) and time may be collected during the MFACV measurement. One of the most useful plots to observe the response is a three dimensional Bode plot with potential along the *x*-axis, frequency on the *y*-axis and admittance along the *z*-axis (fig. 2.1.12).

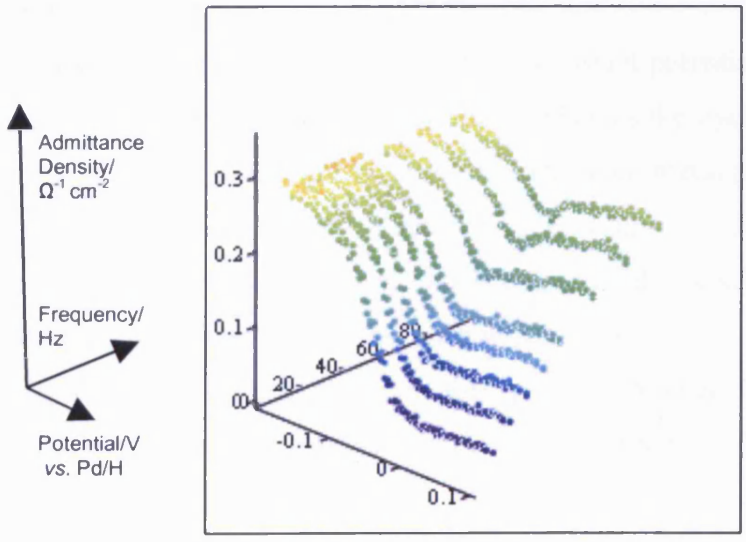

Fig. 2.1.12 MFACV of Pt{111} single crystal electrode in 0.1 M H_2SO_4, under N_2 atmosphere at room temperature, with DC potential sweep rate 0.00125 V s^{-1}.

2.2 Preparation of electrodes

Several electrode preparation treatments were used during the course of the present study. These techniques, along with some others are discussed in this section.

2.2.1 Electrodeposition[23-25]

Electrodeposition is the electrochemical deposition of a substance (also referred to as electroplating), from a plating solution (or plating bath), onto an existing electrode by applying a potential between two electrodes in the solution. The deposit is usually metallic (e.g. Pt[24, 25] or Ru[23]) and plates onto the cathode as the product of reducing a cation of a salt of the metal to be deposited. Various deposition methods exist, differing in their application of potential. Four of the main deposition methods[25] are

(i) constant potential (where the appropriate potential for plating is applied for a set length of time)

(ii) cyclic potential (where the potential is cycled between the deposition potential and a second, fixed potential which does not affect the reaction)

(iii) double potential step (consisting of numerous sharp potential pulses between the same limits as used for the cyclic potential method) and

(iv) constant current (where the appropriate current for plating is applied for a set length of time).

Each method has advantages, for example, the constant potential and constant current methods are quick and simple experimentally, whereas the cyclic potential is slower, but has a greater "throwing power"[5] i.e. the deposited metal plates more uniformly. The double potential step method is not thought to result in an even particle dispersion but can result in a large amount of deposited material. A schematic diagram of a generalised electroplating system is shown in fig. 2.2.1.

Electrodeposition has been used in this project to coat Ru onto Pt and the experimental details of the procedure are discussed in section 3.1.2.1.

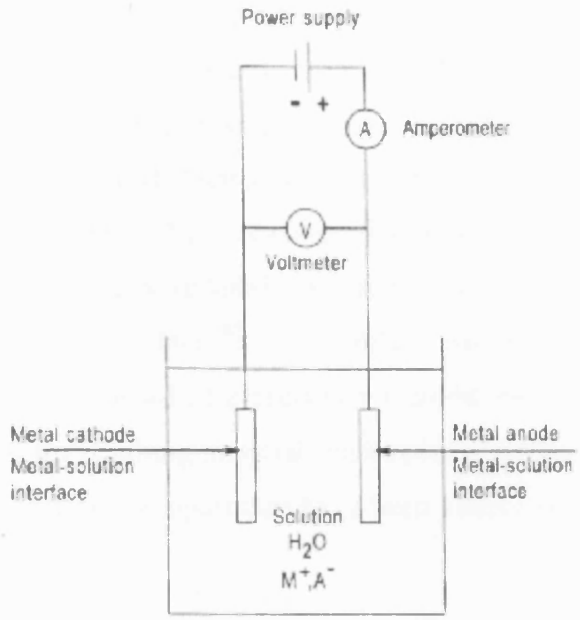

Fig. 2.2.1 Schematic diagram of general electroplating system, M will coat the cathode when current is applied.

2.2.2 Thermal Decomposition

When a precursor material is heated to a temperature high enough to make it "degrade" to the metal, it is referred to as thermal decomposition or thermal degradation[26]. This procedure can take various forms. Often it may be carried out over a relatively long period of time at high temperatures in a furnace (e.g. the decomposition of $CaCO_3$ to CaO on Pt electrodes at 850 °C for 30 minutes[27] or $RuCl_3$ decomposing to RuO_2 on Ti electrodes when heated for 30 minutes at 75 °C followed by calcinations at 400 °C for 1 hour[28]). Thermal decomposition is useful for forming porous electrodes[26]. A variation of thermal decomposition is the much faster process of flame annealing, which has been used in this project to reduce H_2IrCl_6 solution to Ir on a Pt electrode (section 3.5).

2.2.3 Flame and Plasma Spraying

A plasma is an electrically conducting gas containing charged particles. In this technique, a flame is used to heat gas atoms (helium, nitrogen, argon or hydrogen typically) to high energy levels, causing ionisation and thus producing a plasma[29, 30]. The plasma is then accelerated electrostatically onto a material where it cools rapidly and coats the surface (fig. 2.2.2). One drawback with this technique is that the particles are not very strictly ordered. Current research is looking into spraying complete layers onto the surface[30]. A similar method is flame spray pyrolysis (FSP)[31] which uses an aerosol of a precursor material fired through a flame which atomises it such that the resulting material can be plated onto a substrate material (e.g. SnO_2 and Pt/SnO_2 ceramic nanoparticles have been produced from a liquid precursor using this method[32]).

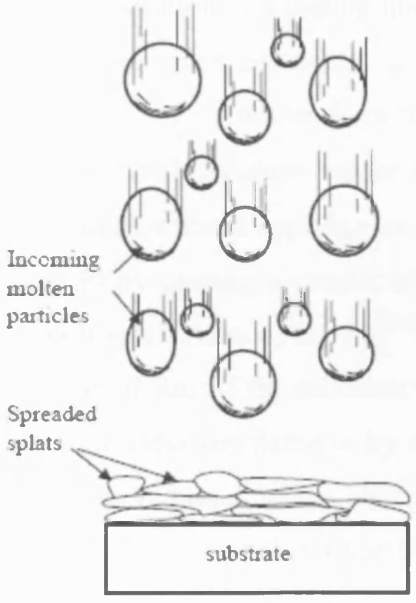

Fig. 2.2.2[29] Schematic diagram of plasma spraying. Molten particles hit the substrate, coating it with a fairly disordered layer.

2.2.4 Pressing and Sintering

In cases where a material is very fine (i.e. in powder form), pressing and sintering may be used to form a solid electrode[33]. The powder is heated to just below its melting point so that it starts to agglomerate (forming larger particles). It is then compacted under pressure to form a solid electrode material (e.g. electrodes of $Co_xB_yH_z$ have been constructed by pressing the material in powder form at pressures between 20 – 100 MPa and heating between 150 – 450 °C[33]).

2.2.5 Electroless Deposition

When an electrode is placed into a solution of a plating material it can become coated by that material due to differences in redox potentials. Since no current is involved, this is called electroless deposition[34, 35]. Another form of this process is possible if an electrode is immersed in a metal solution where the metal cation may be chemically reduced to its metal form without applying an electric current. Examples include Pd being reduced onto Pt by placing a droplet of a dilute K_2PdCl_4 solution onto a Pt electrode and holding it in a stream of H_2 gas[36]. A similar procedure may be implemented for the deposition of Ru. If the substrate used is a single crystal, the deposited film may be annealed in a Bunsen flame or by resistively heating to give a single crystal film of the deposited material. This procedure has been used in this project to form Au, Pd, Rh and Ru single crystal films on Pt (see section 3.5).

2.2.6 Single Crystals

Single crystal electrodes are oriented surfaces of a crystalline material, cut such that the exposed electrode face has a well-defined atomic structure with good long-range order[37-41].

The most popular method for manufacturing single crystal electrodes is the Clavilier method[39, 42-46]. A Pt wire is heated in a flame until the end forms a molten bead which, when cooled slowly and without vibration will adopt a single crystal structure. This spherical form is then oriented and ground/polished to give the desired surface. The experimental procedure is discussed in much greater detail in section 3.4.

Previous work has also been reported on mixing metals of similar atomic sizes (e.g. Platinum-Palladium[42]) within single crystals by melting portions of both metals into the same Clavilier bead.

Single crystals play an important role in the experimentation described in this thesis and are discussed in greater detail in section 2.3.

2.3 Single crystal nomenclature

Single crystal electrodes are of great electrochemical interest as it has been found that certain reactions occur at different rates on specific single crystal orientations (some examples are given in section 1.4). These surfaces are formed by exposing a metallic plane in which the atomic arrangement is well ordered and repeats throughout the surface.

Metals generally take one of three ordered crystal structures, face-centred cubic (fcc), hexagonal close-packed (hcp) and body-centred cubic (bcc). The unit cells for each of these structures are shown in fig. 2.3.1. Pt adopts the fcc structure and hence will be the predominant structure discussed for the remainder of this section, due to the importance of Pt in the present study.

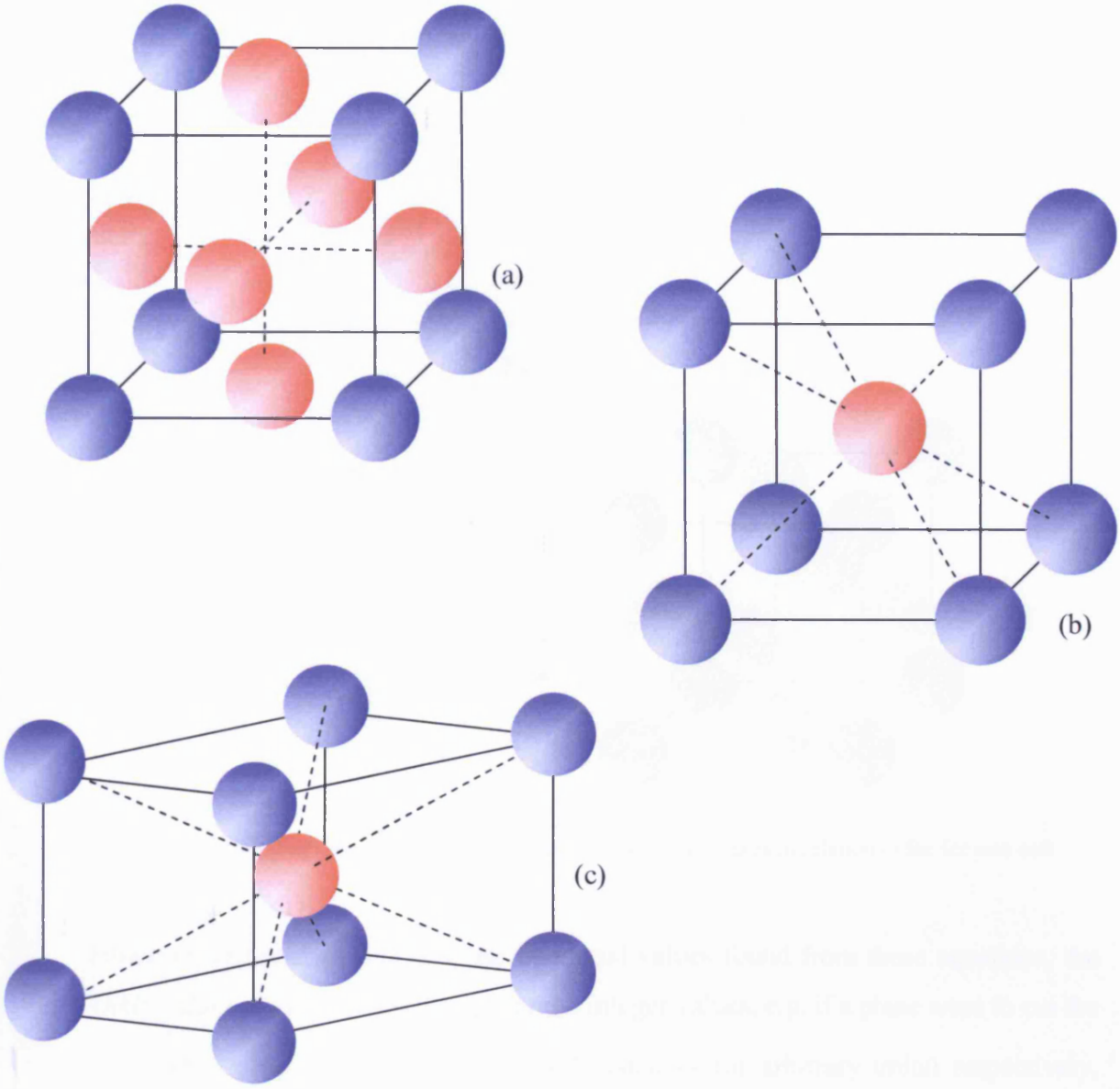

Fig. 2.3.1 Unit cells for (a) fcc, (b) bcc and (c) hcp crystalline structures. The red spheres are structurally identical to the blue spheres, they have simply been highlighted to make the diagram more clear.

If a plane is cut through an fcc crystal it may be labelled using Miller index notation (named after the British crystallographer who identified them, W.H. Miller). Miller indices for fcc crystal planes $\{hkl\}$ are defined using three vectors; $\vec{a}$, $\vec{b}$ and $\vec{c}$ (representing the three axes of the unit cell) with the points at which the plane cuts these axes, labelled a, b and c. Where:

$$h = \left|\vec{a}\right| / a \qquad \textbf{(2.3.1)}$$

$$k = \left|\vec{b}\right| / b \qquad \textbf{(2.3.2)}$$

and

$$l = \left|\vec{c}\right| / c \qquad \textbf{(2.3.3)}$$

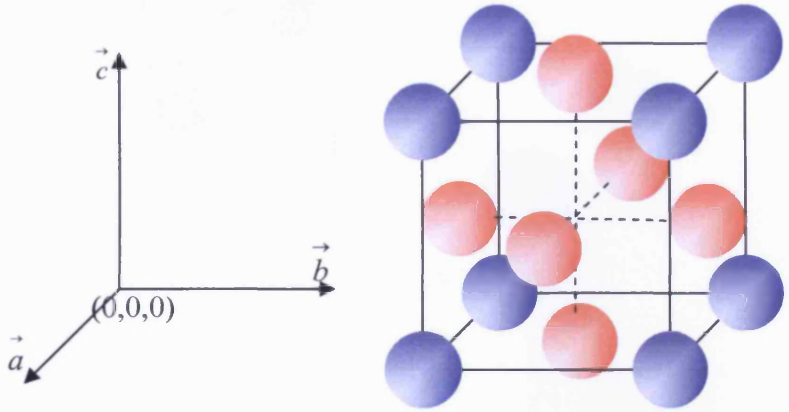

Fig. 2.3.2 Diagram showing the orientation of the *a*, *b* and *c* axes in relation to the fcc unit cell

However, rather than adopting the fractional values found from these equations, the {*hkl*} values are multiplied to appropriate integer values, e.g. if a plane were to cut the $\vec{a},\vec{b}$ and $\vec{c}$ axes at 1,2 and 3 unit cell distances (or arbitrary units) respectively, equations (2.3.1) – (2.3.3) would give {*hkl*} values of {1/1,1/2,1/3}, which would be multiplied by 3 to give integer {*hkl*} values of {321}.

The three most commonly investigated single crystal surfaces are the {111}, {110} and {100} surfaces. These are called the "basal" planes, and are depicted schematically in relation to the fcc unit cell in fig. 2.3.3, with the corresponding atomic arrangements in fig. 2.3.4. Fig. 2.3.5 shows the arrangement of Pt atoms in an fcc crystal structure and the corresponding cyclic voltammograms of the three basal planes.

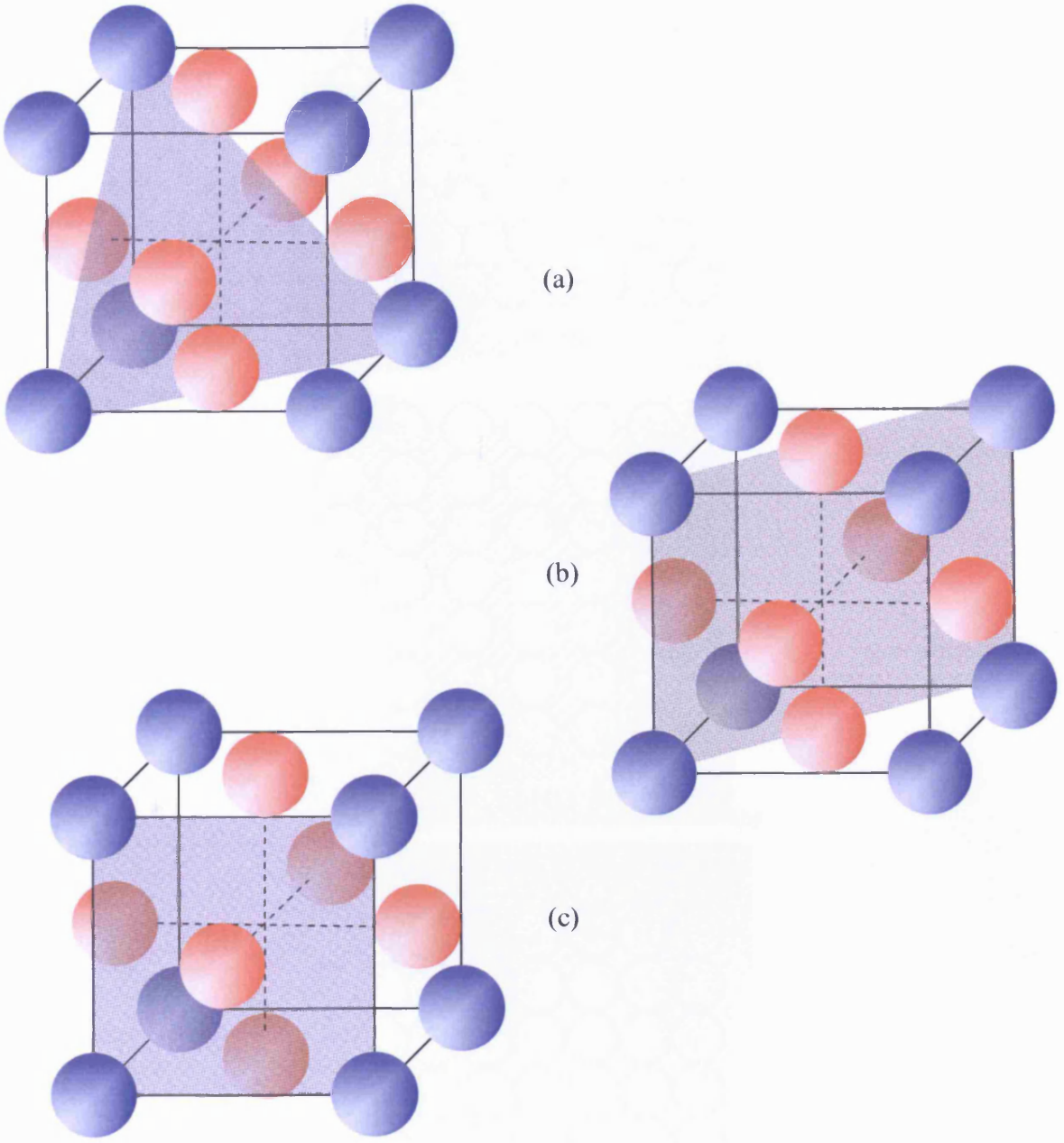

Fig. 2.3.3 Orientations of the (a) {111}, (b) {110} and (c) {100} crystallographic planes (basal planes) for fcc single crystal surfaces.

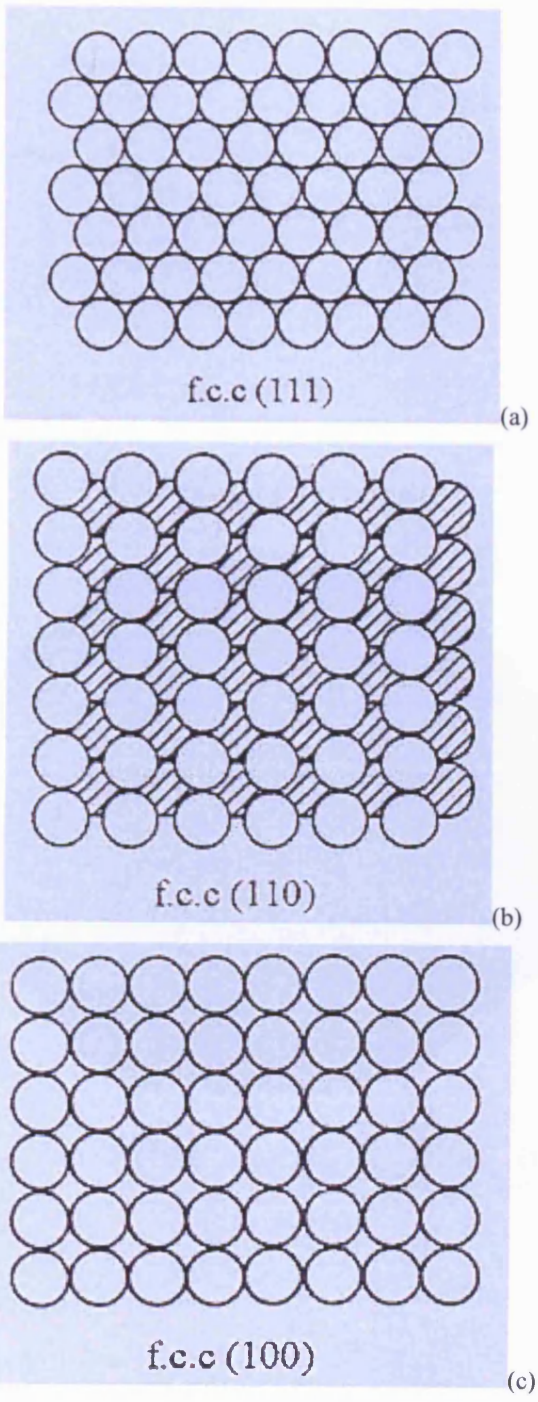

Fig. 2.3.4 Atomic arrangements for (a) {111}, (b) {110} and (c) {100} crystallographic planes (basal planes) for fcc single crystal surfaces[47].

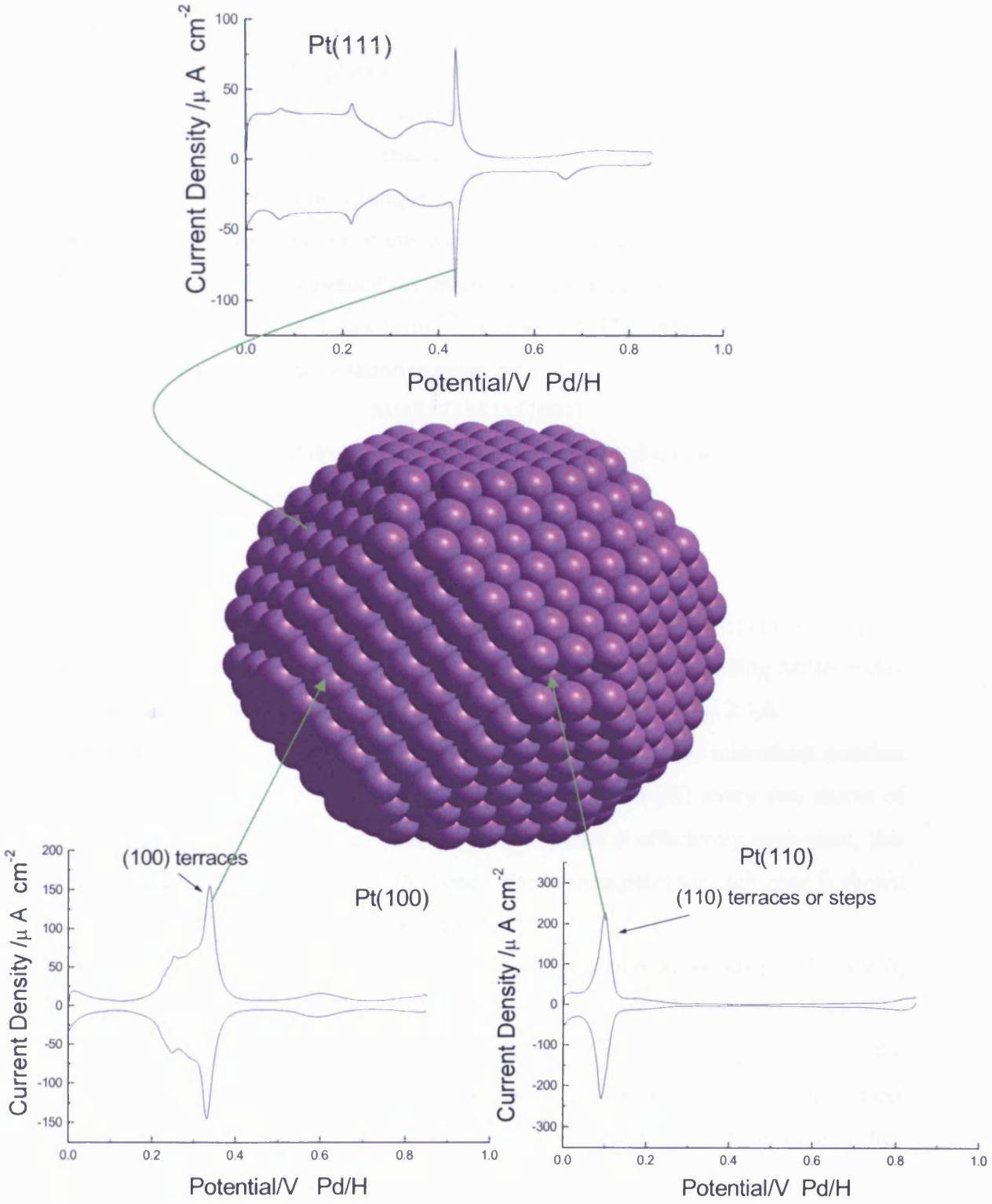

Fig. 2.3.5 Schematic diagram of the atomic arrangement within a cubo-octahedral fcc single crystal structure, showing the corresponding cyclic voltammograms of Pt for the thee basal planes (taken in 0.1 M H_2SO_4 at a potential sweep rate of 0.05 V s^{-1})[48].

If the plane of a fcc single crystal structure intersects any of the three crystal axes at fractional values of the lattice constant, the resulting surface is denoted as being stepped. These surfaces are shown schematically on the stereographic triangle (fig. 2.3.6) where the three basal planes are represented at the corners (poles). Each side of the stereographic triangle (zone) joining two poles represents the range of stepped surfaces associated with sites containing each pole. Taking the zone between fcc {111} and fcc {100} as an example, a surface which has a {111} terrace with a monatomic {100} step every 6 atoms will be labelled as a {755} plane (see fig 2.3.7). This value may be represented in microfacet notation, which is an alternative nomenclature to the Miller index form[47]. For a fcc {111} surface which has a {100} step every *n* atoms, the full notation is given by:

$$M(s)[n\{111\}x\{100\}]$$

(where M is the metal, (s) denotes the surface is stepped and n is an integer $\neq 1$)
and adopts the Miller index form:

$$\{h,k,l\} = (n+1,n-1,n-1) \qquad \textbf{(2.3.4)}$$

Thus, the {755} plane in microfacet notation is given by M(s)[6{111}x{100}] in microfacet notation. The microfacet notations and their corresponding Miller index forms for each region of the stereographic triangle are shown in fig. 2.3.6.
Each zone of the stereographic triangle has a point where *n* in the microfacet notation is 2, i.e. when there is a step (which is two atoms in length) every two atoms of terrace, hence the contributions from each basal plane is effectively equivalent, this point is called the *turning point* of the zone. The turning point for each zone is shown on fig. 2.3.6 as the corresponding Miller index.
If a crystallographic plane cuts all three basal planes at unequal points (i.e. $h \neq k \neq l$), a kinked surface is achieved. Kinked surfaces are more difficult than stepped surfaces to manufacture accurately due to the extra rotational alignment required before the crystal is cut. They are chiral in nature, which is an area currently under investigation[49, 50]. Kinked surfaces will not be discussed in great detail here as they have not been employed in the present study.

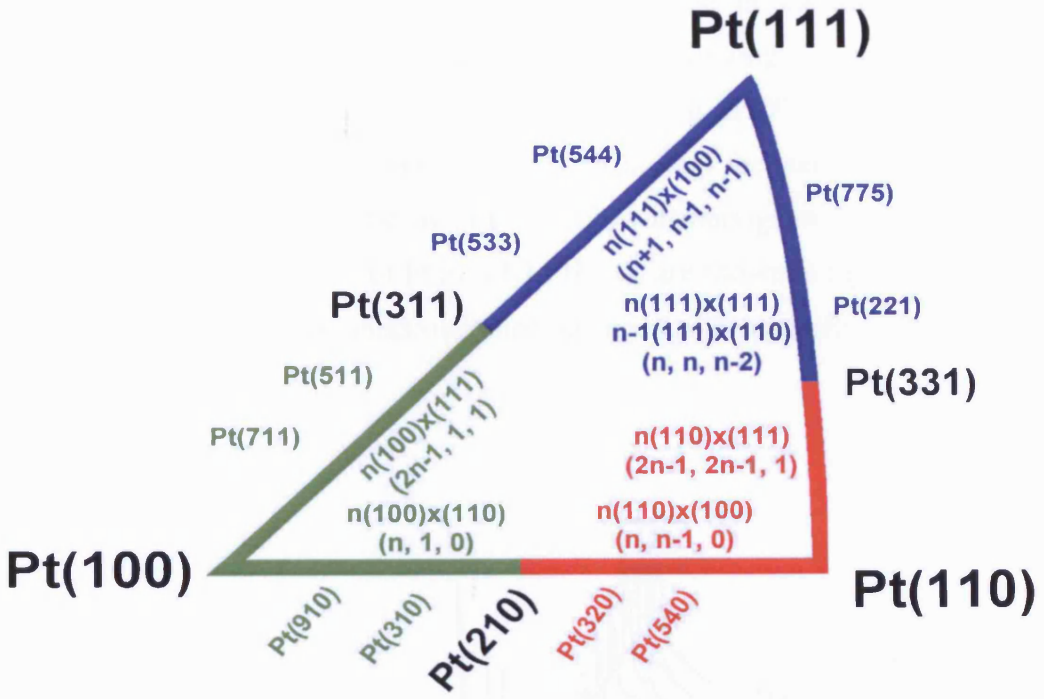

Fig. 2.3.6 The stereographic triangle showing the relative positions and microfacet notations for a range of fcc single crystal surfaces (Pt in this case). Pt{311}, Pt{331} and Pt{210} denote the turning points of the corresponding zones.

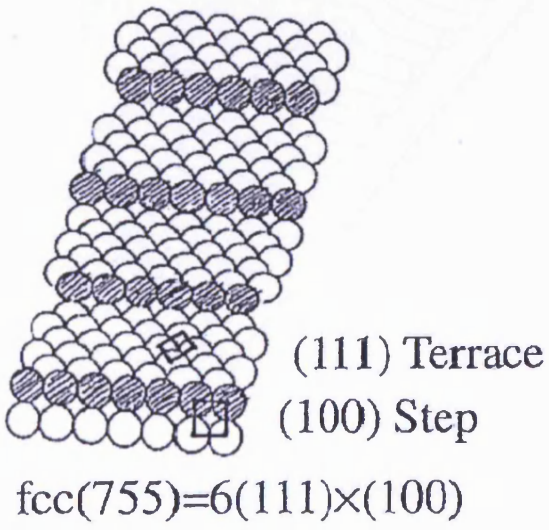

Fig. 2.3.7 Schematic diagram showing the atomic arrangement of a fcc{755} single crystal surface, consisting of a {111} terrace with a {100} step every 6 atoms[47].

Pt is the most commonly studied fcc metal surface in electrochemistry. A comprehensive set of clean cyclic voltammetric curves for single crystal Pt electrodes in sulphuric acid was published by Furuya and Koide in 1989[51] showing systematic changes in electrochemical response on moving around the stereographic triangle. The positive going potential sweeps of the cyclic voltammograms for these flat and stepped single crystal surfaces of Pt in 0.5 M H_2SO_4 are shown in fig. 2.3.8, showing how hydrogen and oxygen electrosorption changes systematically with Pt single crystal structure.

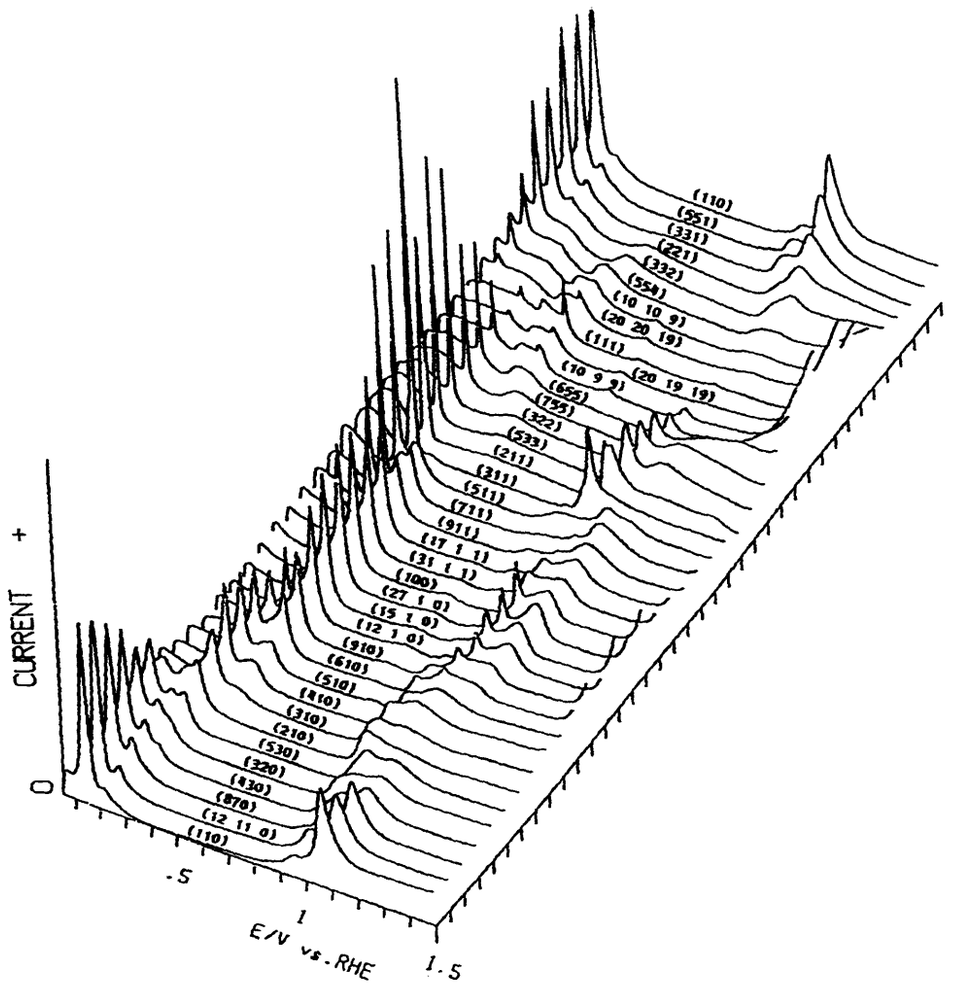

Fig. 2.3.8 Cyclic Voltammograms of a range of Pt stepped surfaces in 0.5 M H_2SO_4[51].

2.4 Reference electrodes

The reference electrode is an electrode of constant potential; it is beneficial in an electrochemical cell, both for physical and academic purposes. The variation of potential between the working and reference electrodes allows current to flow between the working and counter electrodes using a potentiostat.

All potentials are effectively meaningless unless quoted against a reference electrode as comparison of results across different experimental groups would not be possible. Physically, an electrochemical cell may function without the reference electrode, though potential control of the cell is sacrificed. The reference electrode experiences virtually zero current flow so is at a fixed potential. As mentioned in section 2.1.1.2, the potential between the reference electrode and the working electrode is varied and the current response monitored (using a counter electrode).

The internationally accepted zero-potential reference electrode is the standard or normal hydrogen electrode (SHE or NHE), consisting of a Pt electrode in contact with hydrogen gas in a strong acid solution, where all the redox active components are at unit activity (unit fugacity for $H_{2\,(g)}$). This electrode is seldom used experimentally, since the experimental setup is not very convenient. Therefore, electrode potentials are commonly quoted against a more practical reference electrode, e.g. the reversible hydrogen electrode (RHE). The RHE consists of platinised Pt in contact with H_2 at unit fugacity and can be used in contact with the given electrolyte, giving a potential just a few mV removed from the SHE in 0.1 M acidic solution.

Numerous reference electrodes have been produced, one of the most common being the saturated calomel electrode (SCE) which consists of Hg in contact with a paste of Hg_2Cl_2 (calomel) and saturated KCl solution (~0.241 V *vs.* SHE).

Another widely used reference electrode is the silver/silver chloride electrode which consists of a Ag wire in contact with AgCl in a KCl or NaCl solution. Depending on the concentration of the KCl and the temperature, the potential of the Ag/AgCl reference electrode can change, though by definition, it will stay constant throughout an experiment assuming KCl concentration and temperature remain constant.

This project initially used the Ag/AgCl electrode (~0.197 V *vs.* SHE) but changed to the Pd/H reference for reasons which will be discussed in Chapter 5. The Pd/H reference is a Pd wire which is heated in a Bunsen flame for cleaning purposes and

held in a stream of H_2 in order for hydrogen to absorb within the metal crystal lattice to give the β-phase of Pd which gives rise to a constant potential of ~ 0.06 V *vs.* SHE.

2.5 The electrical double layer

The electrical double layer arises from the capacitative nature of the electrode-electrolyte interface. It depends on electrode roughness, electrode material and the nature of the electrolyte. It is not fully understood on an atomic level, though there have been numerous models proposed regarding the distribution of molecules and ions at the electrode-electrolyte interface and the effects of electric field on the molecular arrangement. Some of the most prominent of these proposals are described here.

2.5.1 The Helmholtz model

The first model of the electrode-electrolyte interface was that proposed by Helmholtz[52]. The Helmholtz model assumes that an electrode in an aqueous electrolyte may be represented as two sheets of charge; that of the charged electrode, with the counter charge from the solution residing at the surface, hence the term "double layer". This model is equivalent to a parallel plate capacitor, following the relationship[1]:

$$\sigma = \frac{\varepsilon\varepsilon_0}{d} V \qquad \textbf{(2.5.1)}$$

Where σ is the stored charge density in C cm^{-2}, V is the potential drop between the plates in V, ε is the dielectric constant of the medium (dimensionless), ε_0 is the permittivity of free space, equal to 8.854 x 10^{-8} C^2 N^{-1} cm^{-2} and d is the distance between the "plates" in cm. The differential of charge density with potential gives the capacitance of the surface, from the equation[1]:

$$\frac{\partial\sigma}{\partial V} = C_H = \frac{\varepsilon\varepsilon_0}{d} \qquad \textbf{(2.5.2)}$$

Thus, this model predicts that capacitance is constant and independent of potential. A schematic diagram of the Helmholtz model is shown in fig. 2.5.1 along with the corresponding potential profile with respect to the distance from the electrode surface, showing that the potential change between the metal and electrolyte is linear.

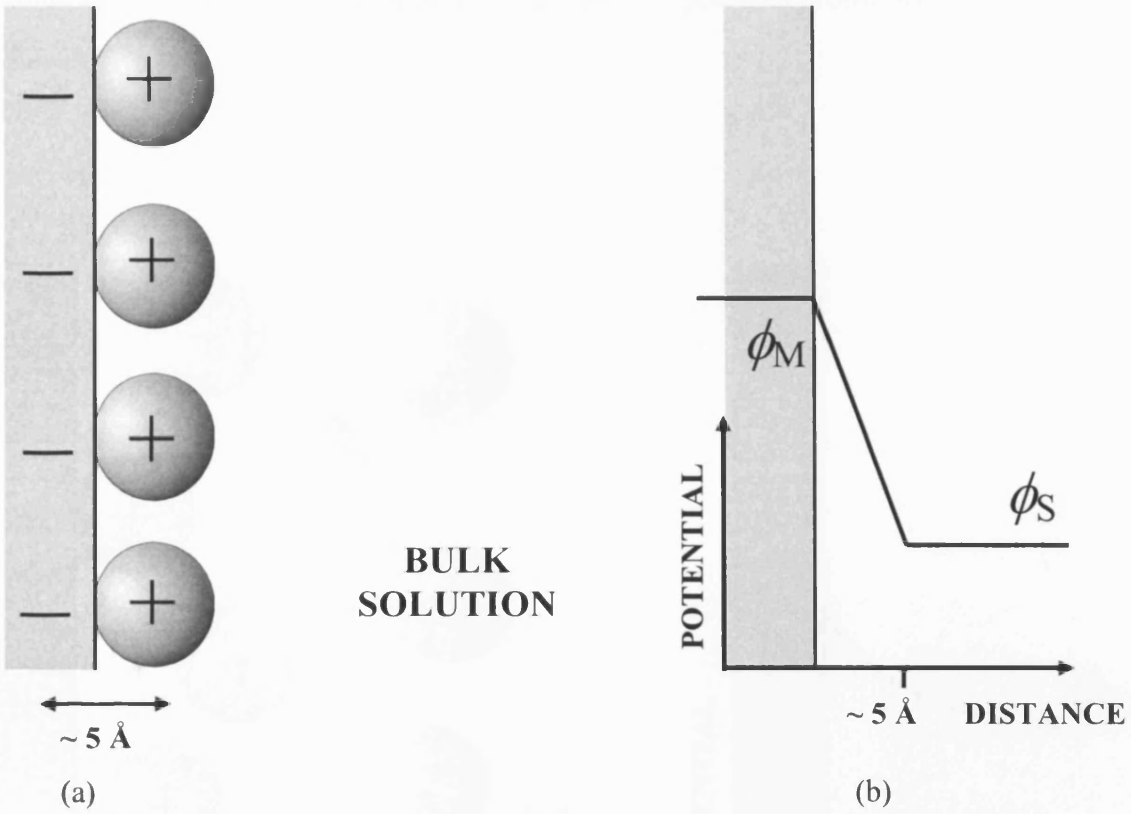

Fig. 2.5.1 (a) Diagram of Helmholtz model of electrode-electrolyte interface and (b) the potential profile of the region close to the interface, where ϕ_M is the potential of the metal and ϕ_S the potential of the solution.

2.5.2 The Gouy-Chapman model

Gouy and Chapman expanded upon the Helmholtz model as flaws had been observed[1]. It had been shown that double layer capacitance was not linear as a function of potential at low electrolyte concentrations. Hence the pure parallel plate capacitor model was not sufficiently robust to account for all capacitative behaviour. Gouy and Chapman independently proposed very similar models of the double

layer[53, 54]. Their statistical mechanical approach implied that the excess charge density would decrease exponentially from the electrode-electrolyte interface to the bulk solution, forming a diffuse layer as opposed to the rigid layer model adopted by Helmholtz[1]. The diffuse layer arises from a compromise between the applied electric field forcing the ions in solution (which are assumed to be point charges) to the electrode surface and the natural thermal randomisation of the ions within the solution. A schematic diagram of the model and the potential profile are shown in fig. 2.5.2.

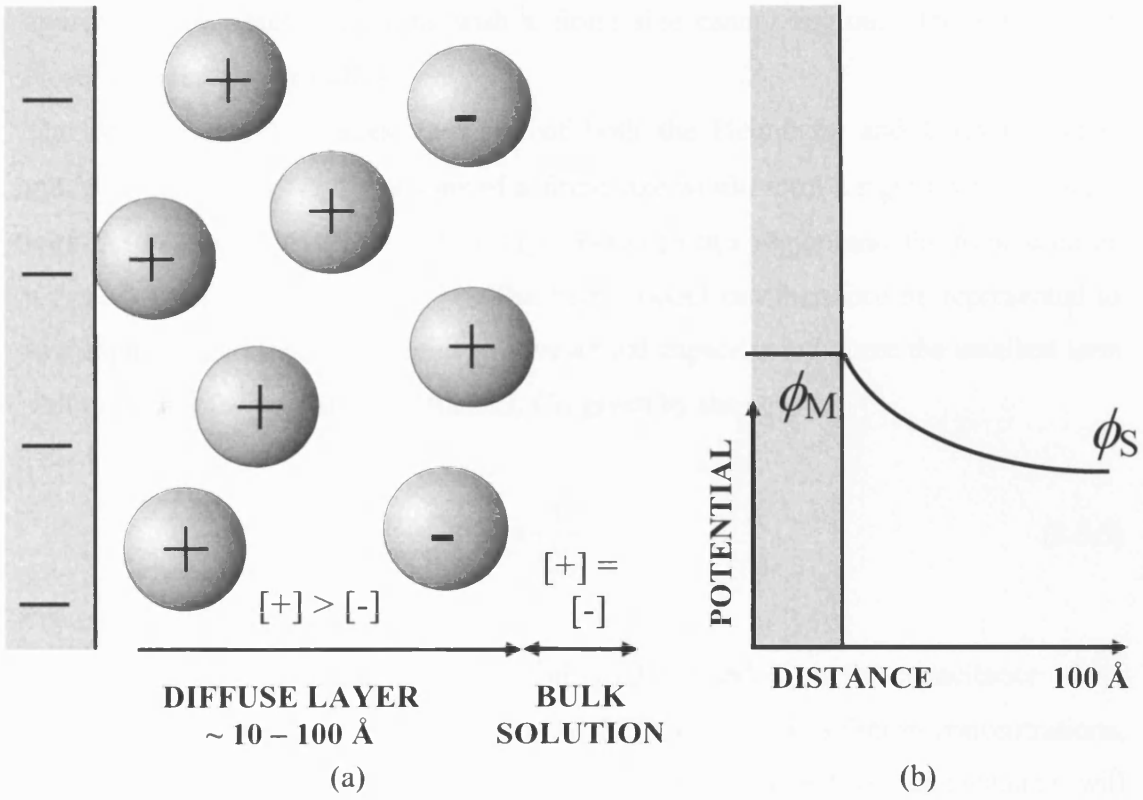

Fig. 2.5.2 (a) Diagram of the Gouy-Chapman model of electrode-electrolyte interface, where [+] and [-] represent the concentrations of positively and negatively charged ions in solution respectively and (b) the potential profile of the region close to the interface. This potential follows an exponential decay curve as a function of distance away from the electrode.

2.5.3 The Stern model

The Gouy-Chapman double layer model was imperfect as it only applied well to potentials near the potential of zero charge (PZC) (i.e. the potential at which there is no excess charge on the electrode surface) and for electrolytes of very low concentration (<0.001 M). The model breaks down due to the assumption that the ions in the solution may be considered as point charges[1]. Gouy and Chapman's assumption implies that at high surface charges on the electrode or at relatively high concentrations the separation between the solution and the electrode charges can approach zero. However, ions with a finite size cannot approach the surface any closer than their ionic radius.

The Stern model combines elements of both the Helmholtz and Gouy-Chapman models. Stern suggested that ions of a finite size would form a rigid layer in contact with the electrode, whilst a diffuse layer between this region and the bulk solution was also present (fig. 2.5.3)[1, 55]. The Stern model can therefore be represented as two capacitors connected in series to give a total capacitance (where the smallest term will dominate the overall capacitance), C_T, given by the equation[1]:

$$\frac{1}{C_T} = \frac{1}{C_H} + \frac{1}{C_D} \qquad \textbf{(2.5.3)}$$

where C_H is the capacitance of the Helmholtz layer and C_D is the capacitance of the diffuse layer. Thus, at potentials near the PZC and at low solution concentrations, where the Guoy-Chapman model is obeyed, the diffuse layer capacitance will dominate, but for other conditions, the total capacitance will be dominated by the Helmholtz layer capacitance.

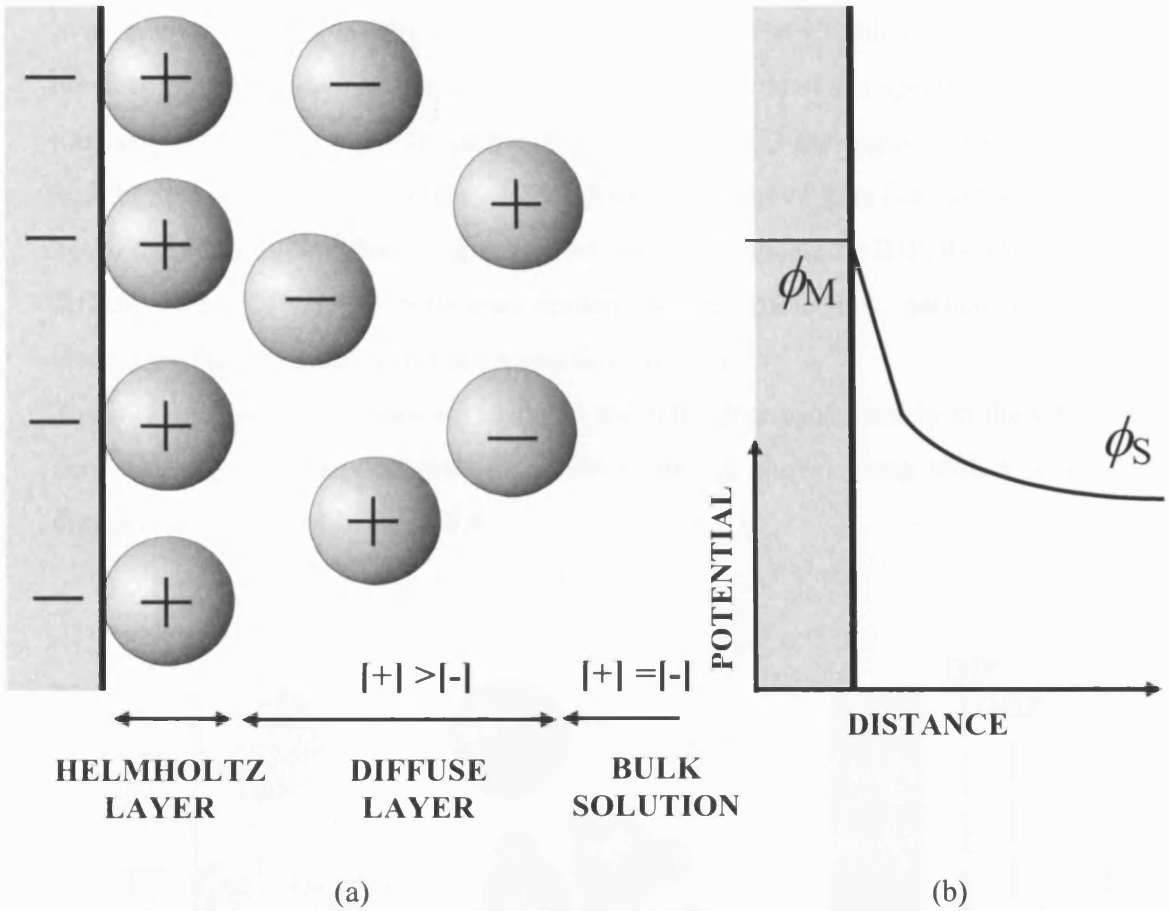

Fig. 2.5.3 (a) Diagram of the Stern model of electrode-electrolyte interface and (b) the potential profile of the region close to the interface.

2.5.4 The Grahame model

The Grahame model added further to the Stern model by the inclusion of a term for *specific adsorption*, i.e. adsorption of ions at an electrode surface over and above the number expected based on purely electrostatic considerations. Grahame suggests that such ions could come closer to the electrode surface than the Helmholtz layer by shedding their solvation shell and becoming specifically adsorbed[56]. Specific interactions are short-range in nature and the specifically adsorbed ions are tightly bound to the electrode surface[1]. Ions with the opposite charge to the electrode become specifically adsorbed, showing that the interaction must be greater than any

Coulombic force[57]. This suggestion led to the Helmholtz layer being modelled as two separate regions (i) the inner Helmholtz plane (IHP), which covers the region between the electrode surface and the loci of the centres of the specifically adsorbed ions and (ii) the outer Helmholtz plane (OHP), which is the region between the IHP and the loci of the centres of the non-specifically adsorbed ions (i.e. solvated ions)[1]. Thus, there are three distinct regions in the Grahame model, the IHP, the OHP and the diffuse layer. The IHP may also contain solvent molecules, particularly at low electrolyte concentrations and at low surface charges[1].

The potential profile increases linearly in the IHP, decreases linearly in the OHP and decreases exponentially in the diffuse layer; this is shown along with a schematic diagram of the model in fig. 2.5.4.

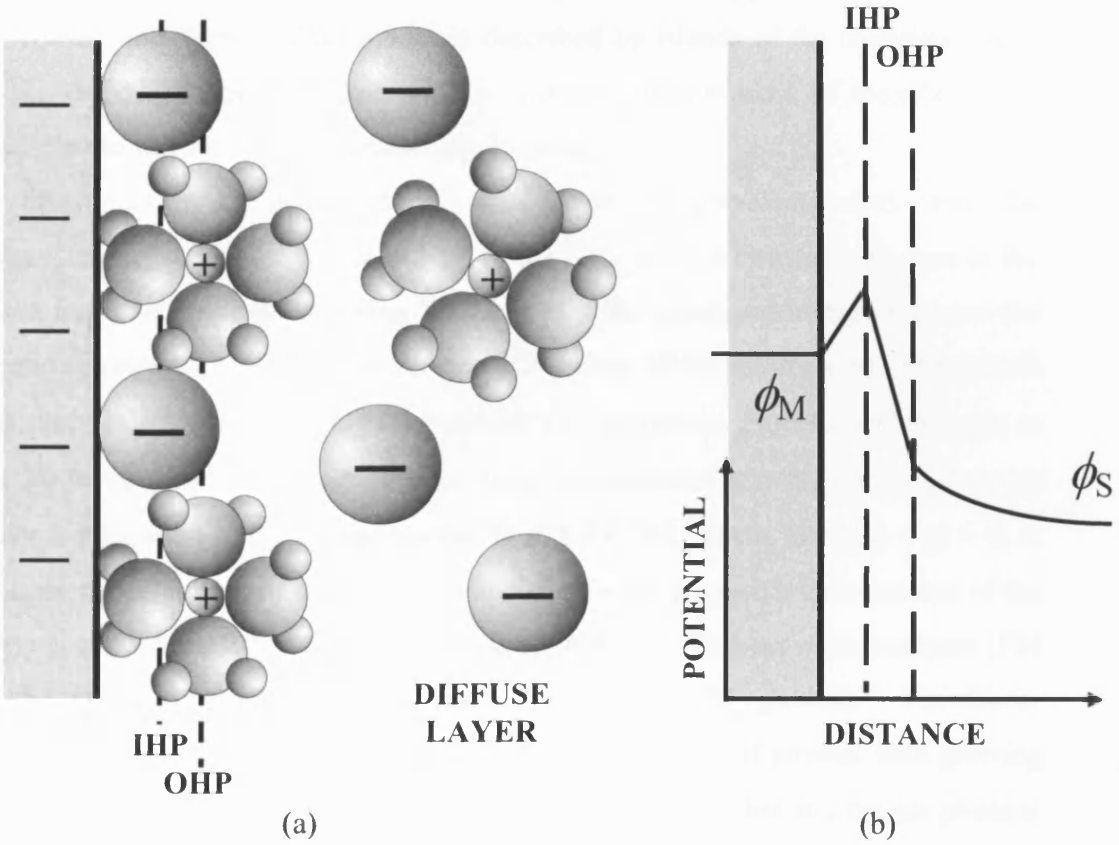

Fig. 2.5.4 (a) Diagram of the Grahame model of electrode-electrolyte interface and (b) the potential profile of the region close to the interface.

2.6 Growth modes of deposited metal layers

When metals are deposited onto solid surfaces, they may adopt different structures depending on the deposition conditions. There are three main types of growth mode, first classified by Ernst Bauer[58], (i) Frank and Van der Merwe, (ii) Stranski-Krastanov and (iii) Volmer and Weber.

The Frank and Van der Merwe (FM) growth model describes the deposited metal growing in distinct monolayers, such that when there is a complete monolayer coverage, the second layer may commence growing on top of the first layer. The third layer may then grow when the second layer is complete and so on[59, 60].

The Stranski-Krastanov (SK) model consists initially of the formation of a small number of monolayers of the deposited metal, followed by the growth of three-dimensional islands of the metal on top of the uppermost completed layer[61].

The Volmer and Weber (VW) model is described by islands of the deposited metal forming directly on the substrate surface, without the formation of monolayers[62]. These three models are shown schematically in fig. 2.6.1.

The determination of which growth mode will be prevalent arises from the comparison of the instability free energy of the film, $\gamma_{F/S} + \gamma_I$ (which is the sum of the surface free energy of the growing film, $\gamma_{F/S}$ and the interfacial energy between the film and the substrate, γ_I) with the surface free energy of the substrate, γ_S. FM growth takes place when $(\gamma_{F/S} + \gamma_I) < \gamma_S$ throughout the deposition process, which leads to layer by layer growth. VW growth (or three-dimensional growth) occurs when the surface energies are in the opposite sense to that for FM growth, i.e. $(\gamma_{F/S} + \gamma_I) > \gamma_S$ at all stages of metal deposition. SK growth occurs when a specific combination of the energy is obeyed, such that $(\gamma_{F/S} + \gamma_I) < \gamma_S$ must hold for a number of monolayers (FM growth) followed subsequently by $(\gamma_{F/S} + \gamma_I) > \gamma_S$ (VW growth). The Bauer classification relies solely on a thermodynamic interpretation of growth, with growing films and substrates being in constant equilibrium with each other and the gas phase at all times. However, kinetics of the growth can also play a significant role.

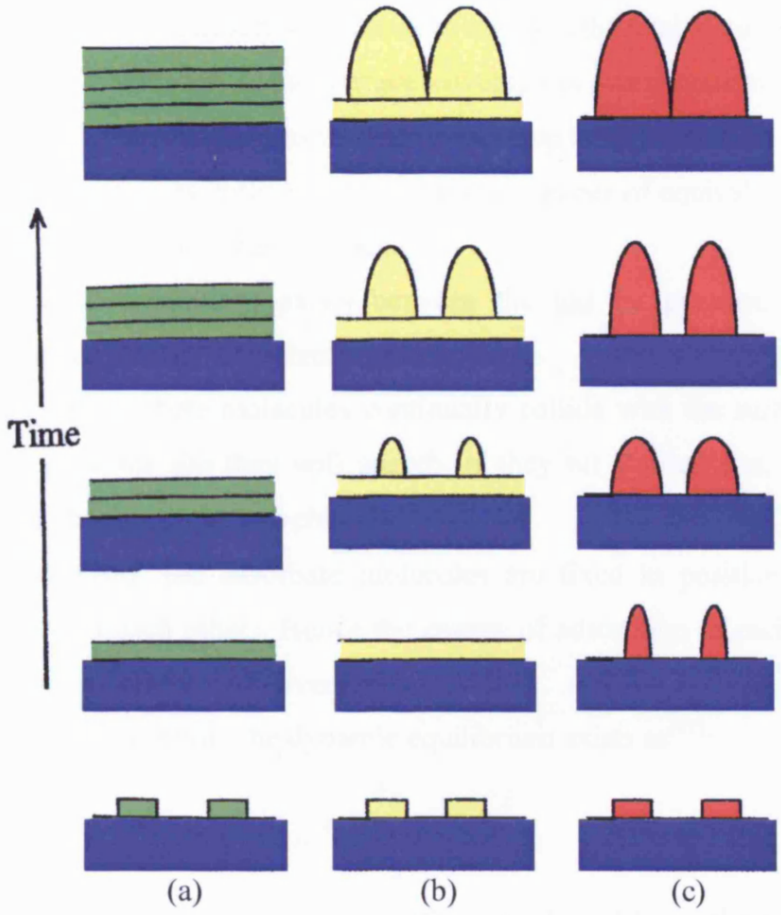

Fig. 2.6.1 Schematic diagram showing the three main growth modes associated with thin film metal deposition onto a metal substrate (a) FM growth (b) SK growth (c) VW growth. It should be noted that each of these growth modes ignore any kinetic processes that may also be occurring during metal deposition.

2.7 Adsorption isotherms

The process of adsorption may be described as

(i) associative, whereby a gas-phase molecule will adsorb onto a surface without fragmentation or

(ii) dissociative, where molecular fragmentation does occur.

Langmuir developed models for both processes in terms of the fractional adsorbate coverage, θ, where:

$$\theta = \frac{N_A}{N} \qquad \textbf{(2.7.1)}$$

where N_A is the number of adsorbate molecules and N is the total number of available adsorption sites. When θ = 1, the surface coverage is one monolayer. Langmuir made some simplifying assumptions in order to develop these models[47]

(i) The solid surface is uniform and contains a number of equivalent sites which each support one adsorbate molecule.

(ii) A dynamic equilibrium exists between the gas (at pressure, P) and the adsorbate layer at constant temperature.

(iii) Gas-phase adsorbate molecules continually collide with the surface. If they impact a vacant site they will adsorb, if they hit a filled site, they will be deflected back into the gas-phase.

(iv) Once adsorbed, the adsorbate molecules are fixed in position and do not interact with each other. Hence the energy of adsorption of each site will be the same, irrespective of coverage.

So, for associative adsorption, the dynamic equilibrium exists as[47]:

$$M_{(g)} + S \underset{k_d}{\overset{k_a}{\leftrightarrow}} M - S \qquad \textbf{(2.7.2)}$$

where M is an adsorbate molecule, S is a surface site, k_a and k_d are the adsorption and desorption rate constants respectively, giving, at pressure, P:

$$\text{rate of adsorption} = k_a P(1-\theta) \qquad \textbf{(2.7.3)}$$

and

$$\text{rate of desorption} = k_d\theta \qquad \textbf{(2.7.4)}$$

hence, at equilibrium:

$$k_a P(1-\theta) = k_d\theta \qquad \textbf{(2.7.5)}$$

rearrangement gives:

$$\theta = \frac{KP}{1+KP} = \frac{N_A}{N} \qquad \textbf{(2.7.6)}$$

where:

$$K = \frac{k_a}{k_d} \qquad \textbf{(2.7.7)}$$

Equation (2.7.6) is the Langmuir adsorption isotherm for associative adsorption processes and is often written in the form:

$$\frac{\theta}{(1-\theta)} = \frac{k_a}{k_d} P \qquad \textbf{(2.7.8)}$$

The gas-phase Langmuir isotherm may be adapted to electrochemical systems. Pressure, P, is replaced by the concentration of the aqueous oxidised species, $C^*_{M^{z+}}$, from the equilibrium:

$$M^{z+}_{(aq)} + Ze^- \leftrightarrow M_{(ads)} \qquad \textbf{(2.7.9)}$$

This leads to:

$$\frac{\theta}{(1-\theta)} = \frac{k_a}{k_d} C^*_{M^{z+}} \qquad \textbf{(2.7.10)}$$

Also, for an electrochemical system, the adsorption constant, *K*, is potential dependent since the adsorption reaction involves a transfer of charge across the metal-electrolyte interface. For a reaction taking place with a complete charge transfer, i.e. the formation of a neutral adatom at the electrode surface, the Gibbs energy of adsorption $\Delta G_{(ads)}$ is given by:

$$\Delta G_{(ads)} = \Delta G^{o}_{(ads)} + nFE \qquad \textbf{(2.7.11)}$$

where *E* is the electrode potential and $\Delta G^{o}_{(ads)}$ is the Gibbs energy of adsorption in the absence of an electric field. Hence, $\Delta G^{o}_{(ads)}$ represents the chemical potential of species *M* and *nFE* represents the electrochemical potential of M^{Z+}. The adsorption constant may then be expressed as:

$$K = \frac{k_a}{k_d} = \exp\left(\frac{-\Delta G_{(ads)}}{R_g T}\right) \qquad \textbf{(2.7.12)}$$

From equation (2.7.11):

$$K = \frac{k_a}{k_d} = \exp\left(\frac{-\Delta G^{o}_{(ads)} - nFE}{R_g T}\right) = \exp\left(\frac{-\Delta G^{o}_{(ads)}}{R_g T}\right)\exp\left(\frac{-nFE}{R_g T}\right) \qquad \textbf{(2.7.13)}$$

At constant temperature:

$$\exp\left(\frac{-\Delta G^{o}_{(ads)}}{R_g T}\right) = \text{constant} = K' \qquad \textbf{(2.7.14)}$$

Combination of equations (2.7.13) and (2.7.14) into equation (2.7.10) gives the Langmuir adsorption isotherm for an electrochemical system:

$$\frac{\theta}{(1-\theta)} = K' \exp\left(\frac{-nFE}{RT}\right) C^{*}_{M^{z+}} \qquad \textbf{(2.7.15)}$$

where K' is the adsorption equilibrium constant in the absence of an electric field.

An extended version of the Langmuir isotherm is the Frumkin isotherm, in which adsorbed molecules on the surface may interact with other species and can affect the further adsorption of other molecules by attractive or repulsive interactions[63].

$$\frac{\theta}{(1-\theta)} \exp\left(A_{\text{int}}\left(\theta - \frac{1}{2}\right)\right) = K' \exp\left(\frac{-nFE}{R_g T}\right) C^{*}_{M^{z+}} \qquad \textbf{(2.7.16)}$$

where $\exp\left(A_{\text{int}}\left(\theta - \frac{1}{2}\right)\right)$ is the van der Waals term for adlayer interactions, with A_{int} representing the magnitude of the attractive (- A_{int}) and repulsive interactions (+ A_{int}).

The BET isotherm (Brunauer, Emmett and Teller) is another variation on the Langmuir isotherm as it allows for the adsorption of more than one monolayer of adsorbate, assuming the second layer adsorbs on top of the first completed monolayer and the third on top of the second etc[47]. It takes the form:

$$\frac{P}{N_s(P_0 - P)} = \frac{1}{NB} + \frac{(B-1)}{NB}\frac{P}{P_0} \qquad \textbf{(2.7.17)}$$

where P_0 is the saturated vapour pressure of the adsorbate and

$$B \approx \exp\left(\frac{\Delta H^{o}_{D} - \Delta H^{o}_{vap}}{R_g T}\right) \qquad \textbf{(2.7.18)}$$

where ΔH^{o}_{D} is the standard enthalpy of desorption (equal to the negative enthalpy of adsorption) and ΔH^{o}_{vap} is the standard heat of vaporisation of the adsorbate.

2.8 Types of adsorption

Adsorptive/desorptive processes in electrochemistry are called non-Faradaic processes. They involve the charging of the electrode/electrolyte interface structure (though no charge is transferred) at potentials where no charge-transfer reactions occur (though external currents may flow due to changes in potential, electrode area or solution composition). An example of a non-Faradaic process is the charging of the electrical double layer (see section 2.5). Faradaic processes are electrochemical processes which obey Faraday's law, i.e. when the charge transfer involved is related to electrons (or charged particles) transferring across the metal-solution interface (causing oxidation or reduction to occur) into the bulk electrolyte. The extent of the resultant reaction is proportional to the applied electrical power. Both Faradaic and non-Faradaic processes occur when the electrode reaction takes place.

There are two distinct types of adsorptive bonding at a surface, chemisorption and physisorption.

Chemisorption involves the exchange of electrons between adsorbate and substrate forming chemical bonds which are relatively strong compared to physisorptive interactions. The adsorbate molecule bonds to the surface such that the coordination number is maximised with respect to the substrate. The chemical bonding can be associative, where a molecule is adsorbed from the gas phase without fragmentation, or dissociative where the adsorbate molecule breaks apart before the fragments chemisorb to the surface.

In comparison to chemisorption, physisorption is very weak and is associated with Van der Waals type interactions between molecules, arising from a redistribution of charge within the adsorbate and the adsorbent. The enthalpy of adsorption, ΔH^{o}_{ads}, for physisorption is generally between -2 and -30 kJ mol^{-1} compared to that of chemisorption which is usually more negative than -35 kJ mol^{-1}.

References

[1] A. J. Bard, L. R. Faulkner, *Electrochemical methods: fundamentals and applications*
2ed., J. Wiley and Sons inc., New York, **2001**.
[2] F. G. Will, C. F. Knorr, *Zeitschrift fur Elektrochemie* **1960**, *64*, 258.
[3] P. A. Christensen, A. Hamnett, *Techniques and mechanisms in electrochemistry*, Kluwer academic publishers, **1993**.
[4] B. E. Conway, G. Jerkiewicz, *Solid State Ionics* **2002**, *150*, 93.
[5] D. B. Hibbert, *Introduction to electrochemistry*, Macmillan Press Ltd., London, **1993**.
[6] S. Morin, H. Dumont, B. E. Conway, *Journal of Electroanalytical Chemistry* **1998**, *412*, 39.
[7] V. Horvat-Radosevic, K. Kvastek, *Electrochimica Acta* **2002**, *48*, 311.
[8] N. V. Krstajic, B. N. Grgur, N. S. Mladenovic, M. V. Vojnovic, M. M. Jaksiz, *Electrochimica Acta* **1997**, *42*, 323.
[9] R. D. Armstrong, M. Henderson, *Journal of Electroanalytical Chemistry* **1972**, *39*, 81.
[10] B. E. Conway, J. H. Barber, S. Morin, *Electrochimica Acta* **1998**, *44*, 1109.
[11] D. E. Smith, *Analytical Chemistry* **1976**, *48*, 221.
[12] D. E. Smith, *Analytical Chemistry* **1972**, *48*, 517.
[13] S. J. M. Rosvall, M. Sharp, A. Bond, *Journal of Electroanalytical Chemistry* **2002**, *536*, 161.
[14] M. Rosvall, *Electrochemistry Communications* **2000**, *2*, 791.
[15] S. J. M. Rosvall, M. Sharp, A. Bond, *Journal of Electroanalytical Chemistry* **2003**, *546*, 51.
[16] E. Wright, Exeter (Ph.D Thesis) **2004**.
[17] M. Rosvall, M. J. Honeychurch, D. M. Elton, A. Bond, *Journal of Electroanalytical Chemistry* **2001**, *515*, 8.
[18] D. J. Gavaghan, A. Bond, *Journal of Electroanalytical Chemistry* **2003**, *480*, 133.
[19] J. Hazi, D. M. Elton, *Journal of Electroanalytical Chemistry* **1997**, *437*, 1.
[20] M. J. Honeychurch, A. M. Bond, *Journal of Electroanalytical Chemistry* **2002**, *529*, 3.
[21] M. Rosvall, M. Sharp, *Electrochemistry Communications* **2000**, *2*, 338.
[22] J. Schiewe, J. Hazi, V. A. Vincente-Beckett, A. Bond, *Journal of Electroanalytical Chemistry* **1998**, *451*, 129.
[23] C. W. Bradford, M. J. Cleare, H.Middleton, Johnson Matthey & Co. Ltd.
[24] E. E. Farndon, D. Pletcher, A. Saraby-Reintjes, *Electrochimica Acta* **1997**, *42*, 1269.
[25] L. Nui, Q. Li, F. Wei, S. Wu, P. Liu, X. Cao, *Journal of Electroanalytical Chemistry* **2005**, *578*, 331.
[26] R. Jurczakowski, C. Hitz, A. Lasia, *Journal of Electroanalytical Chemistry* **2004**, *572*, 355.
[27] K. J. D. Mackenzie, N. Hadipour, *Thermochimica acta* **1980**, *35*, 227.
[28] L. Chen, D. Guay, F. H. Pollak, F. Levy, *Journal of Electroanalytical Chemistry* **1997**, *429*, 185.
[29] H. W. Ng, Z. Gan, *Finite elements in analysis and design* **2005**, *41*, 1235.
[30] L. Zhao, K. Seeman, A. Fischer, E. Lugscheider, *Surface coatings technology* **2003**, *168*, 186.

[31] C. R. Bickmore, K. F. Waldner, R. Baranwal, T. Hinklin, D. R. Treadwell, R. M. Laine, *Journal of the European Ceramic Society* **1998**, *18*, 287.
[32] L. Madler, A. Roessler, S. E. Pratsinis, T.Sahm, A. Gurlo, N. Barsan, U. Weimar, *Sensors and Actuators B* **2006**, *114*, 283.
[33] M. Mitov, A. Popov, I. Dragieva, *Colloids and Surfaces A; Physiochemical Engineering aspects* **1999**, *149*, 413.
[34] Y. Schacham-Diamand, *Thin Solid Films* **1995**, *262*, 93.
[35] Y. Schacham-Diamand, V. M. Dubin, *Microelectronic Engineering* **1997**, *33*, 47.
[36] F. J. Vidal-Iglesias, A.Al-Akl, D. J. Watson, G. A. Attard, *Electrochemistry Communications* **2006**, *8*, 1147.
[37] J. H. Barber, B. E. Conway, *Journal of Electroanalytical Chemistry* **1999**, *461*, 80.
[38] J. H. Barber, S. Morin, B. E. Conway, *Journal of Electroanalytical Chemistry* **1998**, *446*, 125.
[39] E. Herrero, J. M. Feliu, A. Wieckowski, J. Clavilier, *Surface Science* **1995**, *325*, 131.
[40] T. J. Schmidt, P. N. Ross, N. M. Markovic, *Journal of Electroanalytical Chemistry* **2002**, *524*, 252.
[41] N. M. Markovic, *Journal of The Chemical Society: Farday Transactions* **1996**, *92*, 3719.
[42] D. J. Watson, G. A. Attard, *Surface Science* **2002**, *515*, 87.
[43] R. Gomez, J. M. Feliu, A. Aldaz, *Electrochimica Acta* **1996**, *42*, 1675.
[44] R. Gomez, A. Fernandez-Vega, J. M. Feliu, A.Aldaz, *Journal of Physical Chemistry* **1993**, *97*, 4769.
[45] J. Clavilier, *Journal of Electroanalytical Chemistry* **1988**, *243*, 419.
[46] J. Clavilier, R. Faure, G. Guinet, R. Durand, *Journal of Electroanalytical Chemistry* **1980**, *107*, 205.
[47] G. Attard, C. Barnes, *Surfaces*, Oxford University Press, New York, **1998**.
[48] G. A. Attard, O. Hazzazi, A. Ahmadi, D. Jenkins, P. Wells, *ChemPhysChem* **2003**, *4*.
[49] O. A. Hazzazi, G. A. Attard, P. B. Wells, *Journal of Molecular Catalysis A: Chemical* **2004**, *216*, 247.
[50] A. J. Gellman, J. D. Horvath, M. T. Buelow, *Journal of Molecular Catalysis A: Chemical* **2001**, *167*, 3.
[51] N. Furuya, S. Koide, *Surface Science* **1989**, *220*, 18.
[52] H. L. F. V. Helmoltz, W. Abhandl, *Annalen der Physik* **1853**, *89*, 211.
[53] G. Gouy, *Journal de Physique et Le Radium* **1910**, *9*, 457.
[54] D. L. Chapman, *Philosophy Magazine* **1913**, *25*, 475.
[55] O. Stern, *Zeitschrift fur Elektrochemie* **1924**, *30*, 508.
[56] D. C. Grahame, *Chemical Reviews* **1947**, *41*, 508.
[57] T. M. Thomas, W. J. Thomas, *Introduction to the Principles of Heterogeneous Catalysis*, Academic Press, New York, **1967**.
[58] E. Bauer, *Zeitschrift fur Kristallographie* **1958**, *110*, 372.
[59] F. C. Frank, J. H. v. d. Merwe, *Proceedings of The Royal Society of London* **1949**, *198*, 205.
[60] F. C. Frank, J. H. v. d. Merwe, *Proceedings of The Royal Society of London* **1949**, *200*, 125.
[61] I. N. Stranski, L. Krastanow, *Akademie der Wissenschaften und Literatur Mainz, Mathematisch-Naturwissenschaftliche Klasse IIB* **1939**, *146*, 797.

[62] M. Volmer, A. Weber, *Zeitschrift fur Physikalische Chemie* **1926**, *119*, 277.
[63] A. Slygin, A. Frumkin, *Acta Physiochimica URSS* **1935**, *3*, 791.

Chapter 3
Experimental

3.1 Rotating disc electrode experiments

3.1.1 Hydrogen oxidation on Pt

Rotating disc electrode (RDE) hydrogen oxidation experiments were performed on polycrystalline Pt in 0.1 M $HClO_4$ (Analar) and 0.05 M H_2SO_4 (Analar).
The experiments were performed using a polycrystalline Pt working electrode (BAS, 3 mm diameter Pt rod encased in Nylon) in a three-electrode cell, with a Pt counter electrode and a Ag/AgCl in 3 M NaCl reference electrode (BAS, +0.262 V *vs.* RHE in 0.1 M $HClO_4$, +0.292 V *vs.* RHE in 0.05 M H_2SO_4, though the potential varied with concentration, all potentials quoted are converted to Pd/H or RHE where appropriate). A BAS standard cell (25ml) was used in conjunction with a BAS RDE-2 cell stand. The data was recorded using a BAS CV-50W potentiostat, which was connected to a PC running BAS 100W software. Fig 3.1.1 shows the rotating disc electrode apparatus used for these tests.

The working electrode was polished by hand using increasingly fine grade diamond paste (15 μm, 6 μm, 3 μm, 1 μm) until a mirror finish was achieved, it was rinsed with nanopure deionised water before each experiment.
Electrochemical cells were cleaned by washing with detergent and soaking in a mixture of 2:1 concentrated nitric acid:concentrated hydrochloric acid for approximately 2 hours to remove organic contaminants before rinsing with deionised water and drying in an oven (this cleaning procedure was abandoned when the project moved to single crystal work which is even more sensitive to contaminants as this treatment did not clean the glassware satisfactorily).

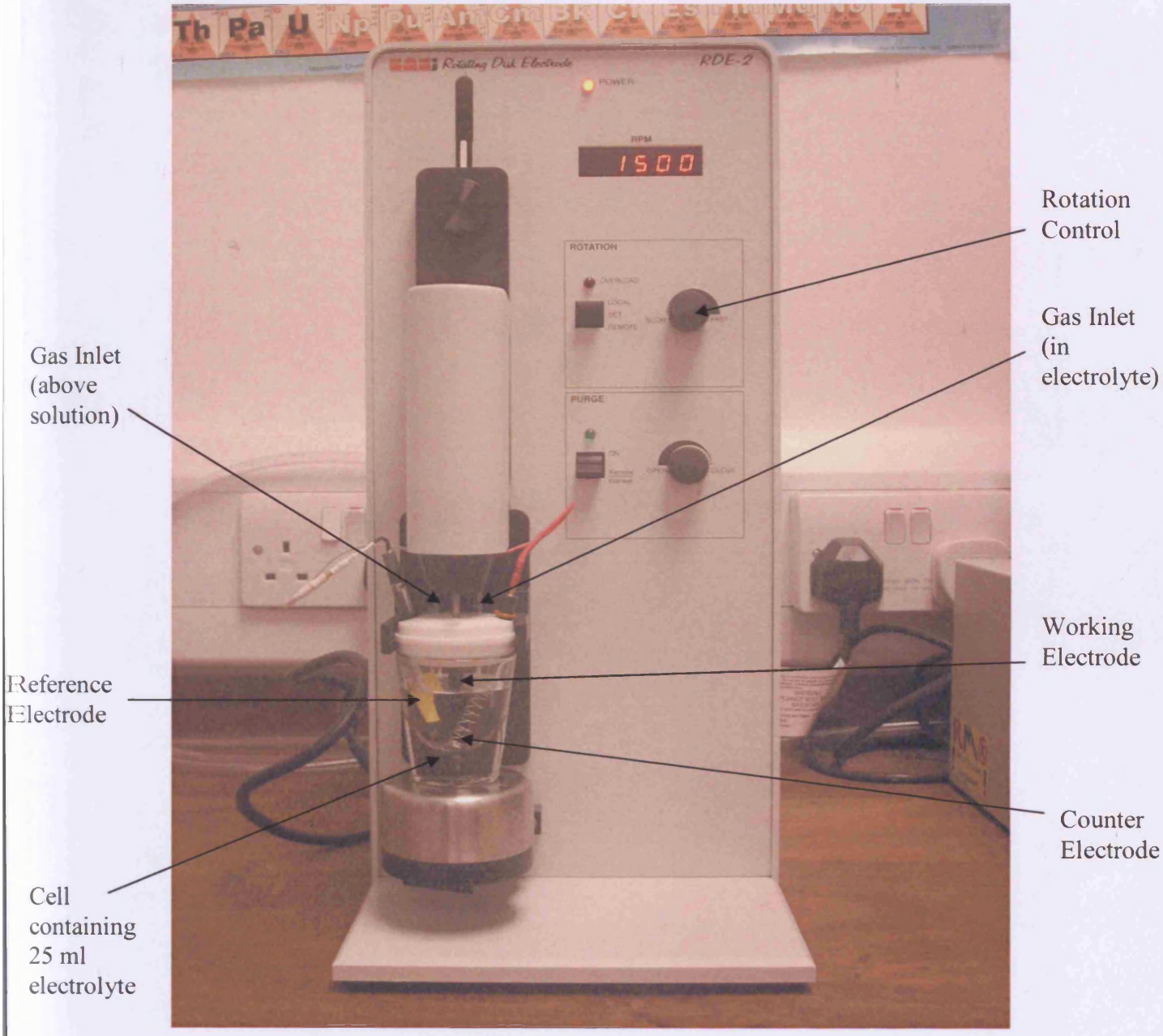

Fig 3.1.1 Rotating Disc Electrode apparatus.

The experimental setup described above (shown in fig. 3.1.1) was used with aqueous 0.1 M $HClO_4$ (Analar) as the electrolyte, purged with hydrogen and kept under a hydrogen atmosphere (blanket coverage of the solution, BOC gases 99.995%). A salt bridge was placed between the solution and the reference electrode to counteract any leaching of ions from the reference electrode into the electrolyte. The potential of the working electrode, relative to the reference, was swept in a positive direction (from −0.262 to −0.162 V *vs.* Ag/AgCl) from the rest potential (open circuit potential) to

study H_2 oxidation on the working electrode, for comparison with literature results[1]. Cyclic voltammograms (CVs) of the Pt surface were recorded after each RDE measurement to verify that the electrode surface had not been physically affected by the experiment. Current versus voltage (*I-E*) curves were taken for rotation rates between 500 - 4000 rpm at 500 rpm intervals. The experiment was repeated with 0.05 M H_2SO_4 as an electrolyte.

3.1.2 Hydrogen evolution

Hydrogen evolution tests were performed in 0.1 M H_2SO_4 using the same experimental configuration and techniques as described in section 3.1.1, with a negative-going potential sweep (from – 0.292 to – 0.492 V *vs.* Ag/AgCl). The electrode surfaces investigated were polished polycrystalline Pt (BAS, 3 mm diameter Pt rod encased in Nylon), polished polycrystalline Ir (workshop constructed, 3mm diameter Ir rod encased in Nylon) and Ru (electroplated onto the polished polycrystalline Pt electrode previously mentioned).

3.1.2.1 Electroplating Ru

A layer of Ru was successfully electroplated onto a polycrystalline Pt electrode. A plating bath (provided by Johnson-Matthey PLC) consisting of 10 g l^{-1} Ru from $K_3[Ru_2^{IV}NCl_8(H_2O)_2]$ (30.53% Ru) and 10 g l^{-1} HCO_2NH_4 dissolved in Millipure® H_2O was used[2]. The solution was heated to 70 °C and the pH adjusted to 1.3 using 0.5 M HCl, before a current of 6.219 mA cm^{-2} was passed through a Pt electrode for approximately 1 hour using Pt as a counter electrode. A complete surface coverage of Ru was achieved, which showed no visible defects under x 3 magnification. Attempts were also made to electroplate Ru onto Ni, Ti, Au and glassy carbon, in order to find a more inexpensive substrate electrode material. These attempts, however, proved unsuccessful as the deposited Ru layers either did not cover the substrate surface completely or they were insufficiently robust when rotated in RDE experiments.

3.2 Multi-Frequency AC Voltammetry (MFACV)

Multi-Frequency AC Voltammetry was performed using a three-electrode cell consisting of a working electrode (made from the metal under investigation), a reference electrode (Ag/AgCl in 3 M NaCl (BAS)) and a Pt counter electrode. The experiments were run in a BAS standard (25ml) cell on a BAS cell stand (see fig. 3.1.1), connected to a Solartron 1286, which was connected to a PC running Labview 5 software and a NI PCI-MOI-1-1E multifunction input output card with two digital-analogue converters as is shown in fig. 3.2.1.

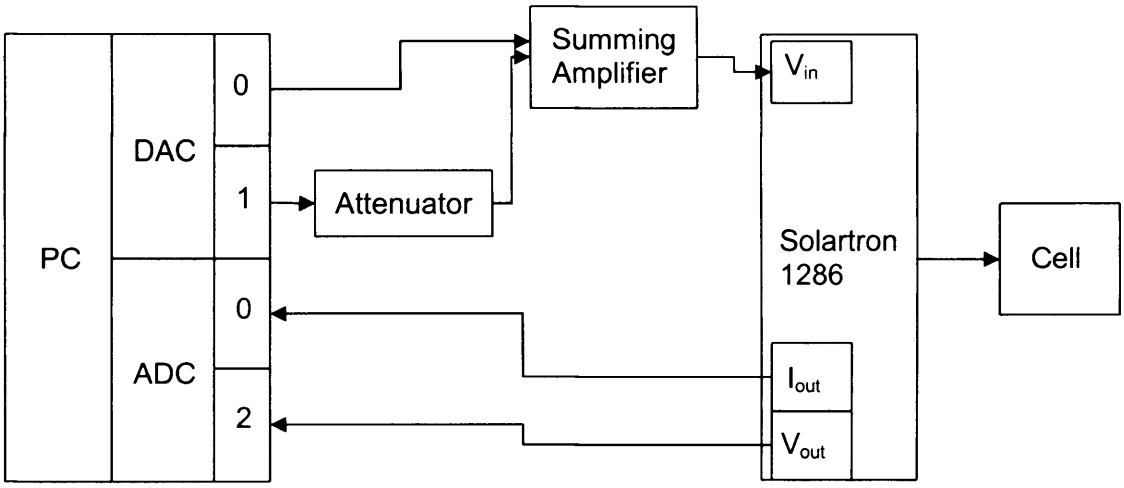

Fig. 3.2.1 Schematic diagram of Multi-Frequency AC Voltammetry apparatus.

MFACV was performed on a polished, polycrystalline Pt electrode (3 mm diameter rod encased in Nylon) in 0.05 M H_2SO_4, under N_2 atmosphere. The DC potential was swept from 0.30 to -0.38 V *vs.* Ag/AgCl at ~0.00125 V s^{-1}. The sweep rate was not controlled directly but by two separate parameters; the number of potential steps and sample time. The input parameters gave a resulting sweep rate of 0.005 V every 4 s (i.e. the DC potential varied in 0.005 V increments every 4 s). AC frequencies applied were between ~ 1 – 100 Hz with amplitude of ~ 2 mV. A frequency of 1.71 Hz was used as the base frequency in order that multiples of this frequency (which comprised the applied AC signal) did not correspond to electrical noise frequencies, which would interfere with the results. Variations on the above setup were employed for further investigation of the Pt surface; 0.25 M H_2SO_4 was used as an electrolyte to investigate the effect of H^+ ion concentration on HER. N_2 and H_2 were used to degas the system to investigate effects of overpressure of different gases on HER. Also tests were performed at various rotation rates (0 – 5000 rpm) and temperatures (5 – 45 °C).

3.3 Single crystal cyclic voltammetry

CV and MFACV tests were performed on basal plane single crystal surfaces and various stepped single crystal surfaces. In the latter case the effect of {111} steps on {100} terraces and of {100} steps on {111} terraces during HER was studied. Hence, the surfaces along one side of the stereographic triangle (from the {111} pole to the {100} pole) were studied in order to investigate the dependence of HER on single crystal surface structure. The manufacturing process for these single crystal electrodes is described in section 3.4.

All tests were performed in a customised three-electrode cell (fig. 3.3.1) with a Pt mesh counter electrode and a Pd/H reference electrode (+0.060 V *vs.* RHE). The cell was designed such that an overpressure of gas could be used to expel air from the system. This feature was extremely useful for single crystal results as it kept out airborne contaminants.

The Pd/H reference electrode had to be charged at the beginning of each day. This involved heating the Pd wire in a Bunsen flame (to eliminate contaminants) and partially submerging it in water in a cell with H_2 bubbling through it for 30 minutes (through gas inlet 1, see fig. 3.3.1). The Pd would absorb the hydrogen and hold its charge (and therefore its potential) for up to 10 hours.

Electrolytes were prepared in clean glassware using Aristar grade sulphuric acid and ultra-pure water.

The cell was degassed by bubbling with N_2 before each experiment (BOC gases (99.999%) through gas inlet 3, see Fig. 3.3.1) to expel oxygen or other airborne contaminants and held under a N_2 overpressure throughout (gas inlet 2).

CV data were recorded using a BAS C3 cell stand connected to a BAS 100 B potentiostat, which was, in turn, connected to a compatible PC with BAS 100 W software. The applied potential waveform is shown in fig. 3.3.2.

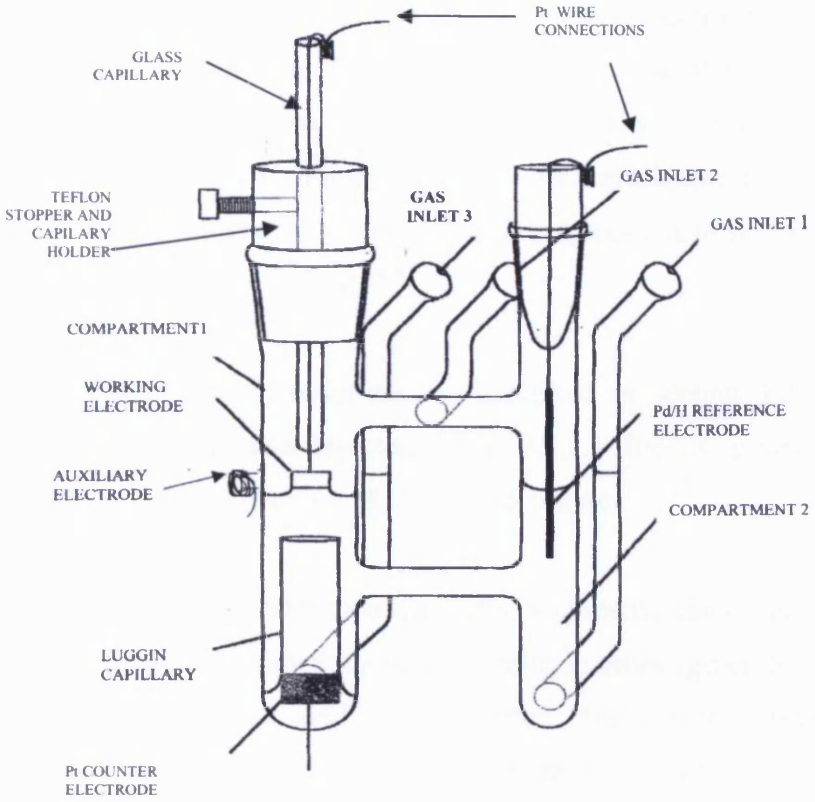

Fig. 3.3.1 Diagram of electrochemical cell used for single crystal measurements.

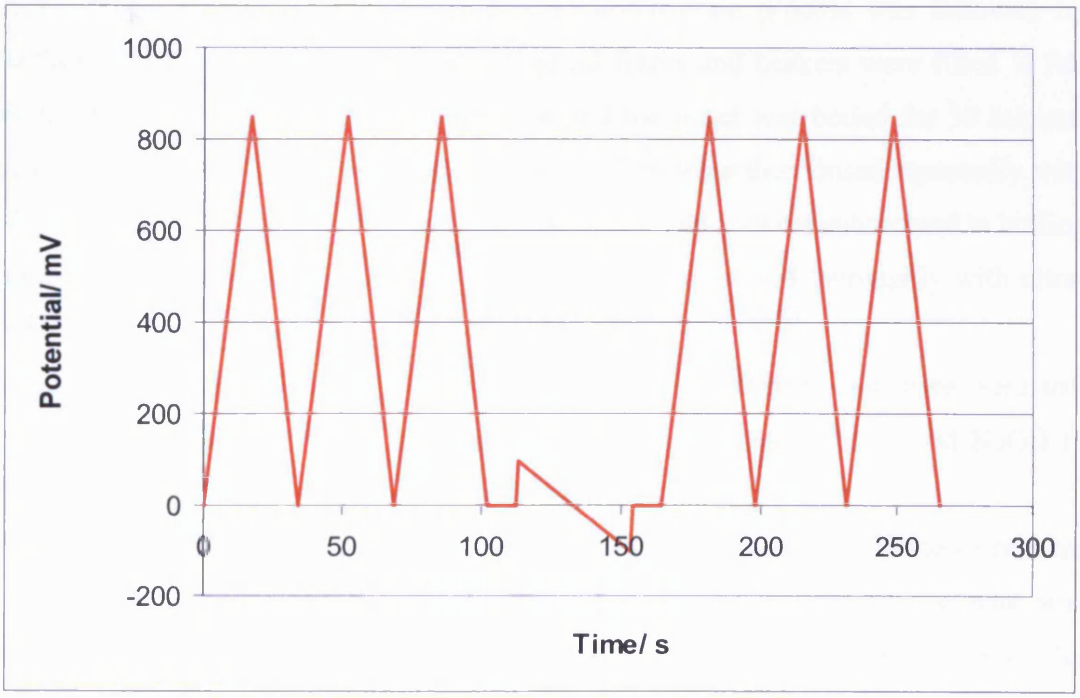

Fig. 3.3.2 Potential waveform for CV and HER experiments on Pt single crystals.

Before each CV was taken, single crystal electrodes were cleaned by flame annealing (in a Bunsen flame), cooled in H_2 and protected with a droplet of ultra-pure water (18.2 MΩ cm resistivity from Millipore Milli-RO/Milli-Q purifying system) to prevent contamination before immersion into the electrochemical cell, as described elsewhere[3]. It has been shown that this procedure gives rise to surface topographies reasonably close to the nominal ones[4, 5]

MFACV experiments were performed as described in section 3.2, but with the electrochemical cell apparatus depicted in fig. 3.3.1. The DC potential was swept from 0.1 to -0.19 V *vs.* Pd/H in 0.1 M H_2SO_4 electrolyte.

All glassware (including electrochemical cells, volumetric flasks, gas bubblers and associated stoppers) was cleaned by rinsing multiple times (generally 10 times) and soaking overnight in "green acid" (concentrated H_2SO_4 with a small amount of potassium permanganate dissolved into it, until apple green) to remove any organic contaminants. The glassware was again repeatedly rinsed with ultra-pure water, then large items (electrochemical cells and gas bubblers) were supported over a clean conical flask containing boiling ultra-pure water and steam-cleaned by the stream of steam produced (for 30 minutes). The steam-cleaning process was followed by further rinsing with ultra-pure water. Conical flasks and beakers were filled ¼ full with ultra-pure water, placed on a hotplate and the water was boiled for 30 minutes producing a flow of steam to clean the glass. They were then rinsed repeatedly with ultra-pure water. Small items such as stoppers and holders were submerged in boiling ultra-pure water in a clean beaker for 30 minutes, then rinsed thoroughly with ultra-pure water.

If the steam-cleaning/boiling process did not clean sufficiently, and there were still organic contaminants present, the glassware was soaked overnight in 3 M NaOH to etch the glass, before rinsing and steam cleaning as above.

The Pt wire connection for the working electrode was heated in a flame to remove organic contaminants and the glass capillary holder which supports the wire was thoroughly dried to avoid interference of electrical signals due to contact between the wire and water trapped in the glass capillary. Similarly the reference electrode and counter electrode connections were also dried.

3.4 Preparation of single crystal electrodes

Single crystal electrodes were prepared using the Clavilier bead method[6] . A small amount of Pt wire (5 cm, 0.2 mm diameter, 99.999% purity, Goodfellow Metals Ltd) was melted without vibration to form a molten bead and cooled slowly and steadily to form a single crystal (as described in section 2.2.6). The bead was then placed in a goniometer cradle on an optical bench (fig. 3.4.1) and aligned using a He-Ne Laser to determine the positions of the single crystal facets and calculate the angle required to achieve the desired surface orientation.

The single crystal bead of an fcc metal (Pt, Pd, Ag, and Au among others) may be oriented so that it may be cut to expose a specific single crystalline surface based on the diffraction of He-Ne laser light by the {111} and {100} facets. The {111} and {100} facets produced characteristic diffraction patterns which were used to orient the crystal bead to the desired cutting angle.

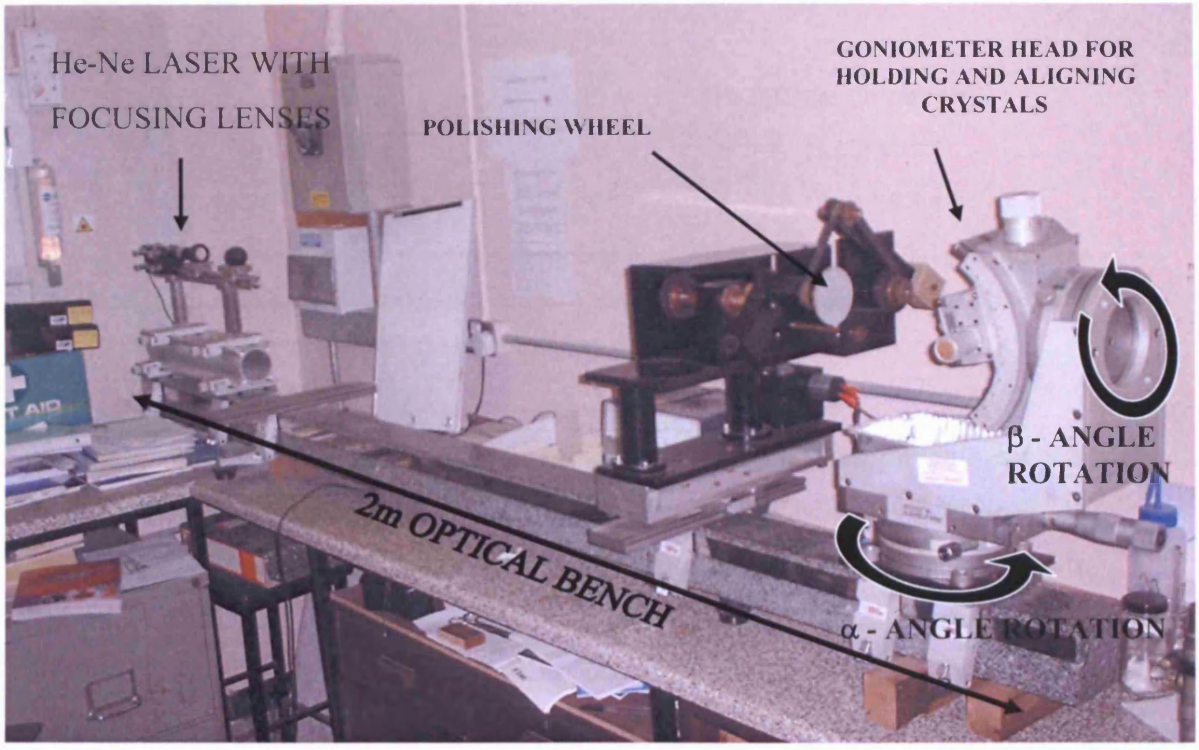

Fig. 3.4.1 The optical bench used for the manufacture of single crystal bead electrodes.

Measurement of the angles between the {111} and {100} diffraction patterns from surface crystal facets is also a useful tool in determining whether the bead is single crystalline or not. Fig. 3.4.2 is a schematic diagram showing the diffraction patterns from the facets on a single crystal bead and the angles between them. The diffraction from the {111} facets will appear as a set of sharp, concentric rings, whereas those of the {100} facets will be a similar shape but rather more diffuse (see fig. 3.4.2). Due to these reflections, the fcc {111} and {100} surfaces are the simplest to manufacture using the Clavilier method. For other orientations, the appropriate angle for polishing must be calculated from the geometry of the crystal structure.

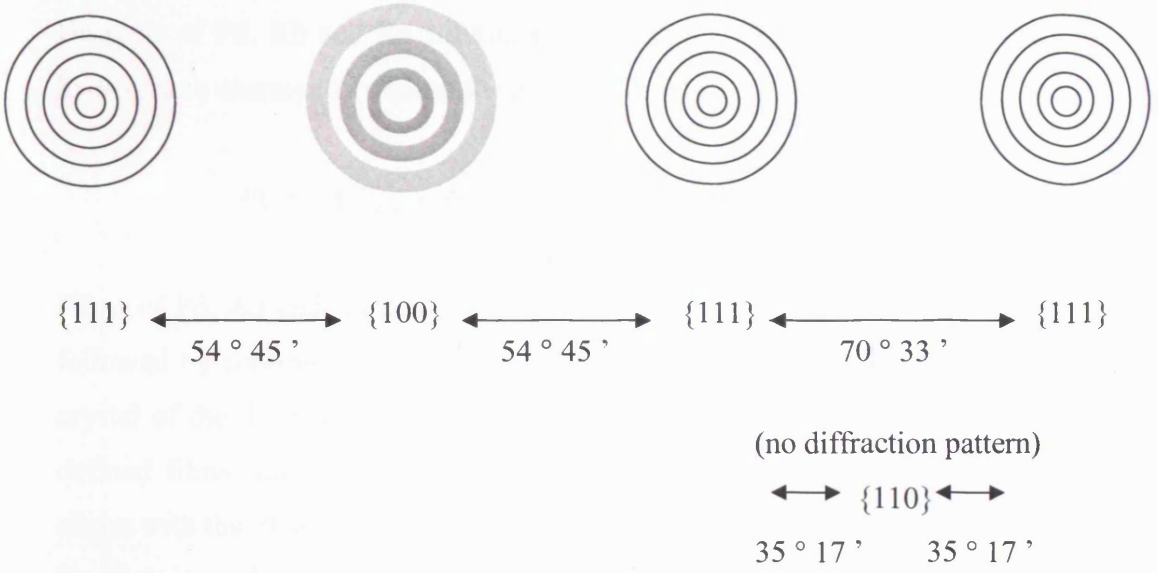

Fig. 3.4.2 Schematic representation of diffraction patterns produced by {111} and {100} planes from a single crystalline fcc bead. When aligned correctly, these facets will appear in the same plane of rotation, with the corresponding angles between them.

The crystal was set into position with epoxy resin. A grinding/polishing wheel, positioned perpendicular to the optical bench was used to grind the crystal bead to a hemispherical shape using carborundum paper with grades of decreasing roughness (600 grit ~1 hour, 1200 grit ~1 hour, and 2400 grit ~ 2 hours) with ultra-pure water as a lubricant. Once the hemisphere was reached, the crystal was polished to a mirror finish using the same polishing wheel, but with nylon polishing pads coated with fine grade diamond paste (3 μm ~2 hours, 1 μm ~2 hours and ¼ μm ~1 hour) using ethanol based lubricants. The remaining epoxy resin was removed by soaking overnight in dichloromethane. Once removed from the epoxy resin, the single crystal was heated

for two hours in a blue Bunsen flame in order to anneal the surface and remove impurities.

3.5 Deposition of metal films onto Pt single crystals

Metal films (Pd, Au, Rh, Ru, Ir) were deposited onto Pt electrodes. All of the metals were deposited from dilute chloride solutions ~10^{-6} mol dm^{-3} (K_2PdCl_4, $HAuCl_4$, $RhCl_3$, $RuCl_3$ and H_2IrCl_6 respectively) (Johnson Matthey).

Droplets of Pd, Rh and Ru solutions were attached to a Pt electrode in a stream of hydrogen to chemically deposit the metal from its ions following the general reaction:

$$Pt + M^{Z+}_{(aq)} + Z/2\ H_{2\,(g)} \rightarrow Pt\text{-}M_{(adsorbed)} + Z\ H^{+}_{(aq)} \qquad \textbf{(3.5.1)}$$

Films of Pd, Au and Rh could then be annealed by gentle heating in a Bunsen flame followed by cooling in hydrogen to give well ordered surfaces analogous to a single crystal of the deposited metal. This forced deposition procedure for preparing well-defined films has been reported previously[7]. These metal films could also form alloys with the Pt substrate under certain heating conditions.

Ru films were less easily annealed as volatile RuO_2 was readily formed in a Bunsen flame. Instead, the Ru film on Pt was resistively heated under nitrogen atmosphere by passing currents up to ~10 A through the electrode for ~20 s (enough to make the crystal bead glow orange).

Ir did not readily deposit onto Pt by hydrogen reduction and had to be "flash" reduced. The "flash" reducing method involves a droplet of the Ir solution being held on the Pt bead and evaporated quickly in a Bunsen flame to leave just the metal on the surface, followed by cooling in hydrogen. Bi was irreversibly deposited onto Pt electrodes by immersing the Pt electrode into a dilute $Bi(NO_3)$ solution.

3.6 CO and the hanging-meniscus and submerged-bead electrode configurations

In order to eliminate edge effects from crystal beads in the hanging meniscus conformation the following technique was employed. The crystal bead was flame annealed and cooled in hydrogen. A cyclic voltammogram of the surface was then taken in the hanging meniscus configuration to confirm the surface structure and system cleanliness. When a good quality surface had been achieved, the crystal bead was placed in a stream of CO which adsorbed strongly to the surface and tended not to interfere with surface structure. The bead was then transferred to the electrochemical cell and connected to the electrolyte with a hanging meniscus contact. A cyclic voltammogram was taken (0 – 0.85 V *vs.* Pd/H). The first (positive) potential sweep of this voltammogram would electrochemically remove CO from the electrode surface in contact with the electrolyte as CO is readily oxidised from Pt by electrochemically sweeping to moderately positive potentials (it starts to desorb from the surface at 0.4 V *vs.* Pd/H and is completely removed by 0.8 V *vs.* Pd/H). However, the CO on the hemisphere of the bead (not in contact with the electrolyte) was not affected. Subsequent potential sweeps would then give cyclic voltammograms of the Pt surface in the hanging meniscus configuration. If these did not match those of the flame annealed surface, the results were discarded and the experiment repeated.

The crystal electrode was kept under potential control (~ 0.001 V *vs.* Pd/H, low enough that CO would not be oxidised) and partially submerged into the electrolyte, such that the crystal edges were no longer in a hanging meniscus conformation (see fig. 3.6.1). Cyclic voltammograms were again taken (but only between 0 – 0.35 V *vs.* Pd/H so that no further CO was removed from the submerged bead surface) to confirm the surface had not changed and that the hemisphere of the electrode was still coated with CO. Hence the voltammogram showed no contributions from the hemisphere of the bead and matched the equivalent section of the voltammogram for the flame annealed crystal surface. If the voltammogram had changed, the result would be discarded and the experiment would be reattempted.

MFACV tests were then attempted on these partially submerged surfaces but, due to the length of time required to run each experiment, the CO would be displaced from the surface, hence the cyclic voltammetry was different at the start and the end of the experiment, rendering the results null and void.

However, it was possible to carry out DC tests as they have a much shorter experimental timescale. Linear sweep voltammograms were taken at steady state, sweeping negative into the hydrogen evolution region (between 0.1 and -0.1 V *vs.* Pd/H). The LSVs were performed firstly on the clean, flame annealed crystal surface in the hanging meniscus configuration, then, after the CO had been removed from the flat crystal surface in the hanging meniscus configuration followed by another on the partially submerged bead (still with CO on the bead hemisphere). Cyclic voltammograms were taken before and after each of these linear sweeps in order to ensure that the surface was not changing throughout the course of the experiment. If the CVs were different at any stage of the experiment, the result would be discarded.

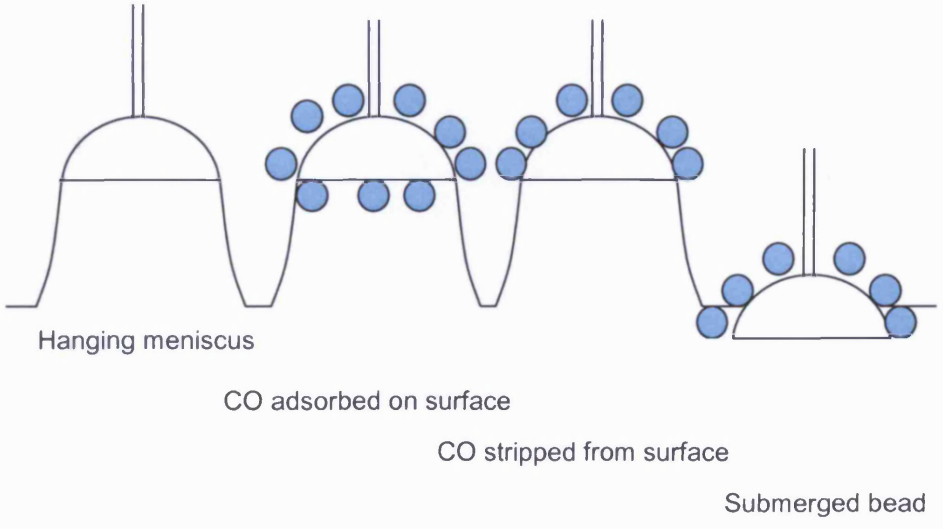

Fig. 3.6.1 schematic diagram to show the steps involved in CO coating experiments to eliminate crystal bead edge effects.

References

[1] J. Maruyama, M. Inaba, K. Katakura, Z. Ogumi, Z.-I. Takehara, *Journal of Electroanalytical Chemistry* **1998**, *447*, 201.

[2] C. W. Bradford, M. J. Cleare, H.Middleton, Johnson Matthey & Co. Ltd.

[3] A. Rodes, K. E. Achi, M. A. Zamakhchari, J. Clavilier, *Journal of Electroanalytical Chemistry* **1990**, *284*, 245.

[4] K. Domke, *Journal of Electroanalytical Chemistry* **2005**, *552*, 115.

[5] N. Garcia-Araez, *Surface Science* **2004**, *560*, 269.

[6] J. Clavilier, *Journal of Electroanalytical Chemistry* **1980**, *107*, 211.

[7] F. J. Vidal-Iglesias, A.Al-Akl, D. J. Watson, G. A. Attard, *Electrochemistry Communications* **2006**, *8*, 1147.

[8] Z.-Q. Tian, B. Ren, D.-Y. Wu, *Journal of Physical Chemistry B* **2002**, *106*, 9463.

Chapter 4
Results

4.1 Hydrogen evolution and hydrogen oxidation on polycrystalline Pt

4.1.1 Hydrogen electro-oxidation on polycrystalline Pt

Rotating disc electrode (RDE) hydrogen oxidation experiments were performed on polycrystalline Pt in 0.1 M $HClO_4$ and 0.05 M H_2SO_4. The Pt electrode gave rise to exchange current densities, j_0, of 2.45 and 0.89 mA cm^{-2} in 0.1 M $HClO_4$ and 0.05 M H_2SO_4 respectively, with transfer coefficients, α, of 0.65 and 0.68. The standard rate constants, k^0, for the perchloric and sulphuric acid electrolytes were found to be 2.46 x 10^{-4} and 1.10 x 10^{-4} cm s^{-1} respectively.

4.1.1.1 HOR on Pt in 0.1 M $HClO_4$

Rotating disc electrode experiments were performed as described in section 3.1.1, using 0.1 M $HClO_4$ as the electrolyte. The electrolyte was purged with hydrogen and kept under a hydrogen atmosphere (blanket coverage of the solution). Cyclic voltammograms (CVs) of the Pt surface were recorded between each rotating disk measurement (fig. 4.1.1). Current versus voltage (*I-E*) curves were taken for rotation rates between 500 - 4000 rpm at 500 rpm intervals (fig. 4.1.2).

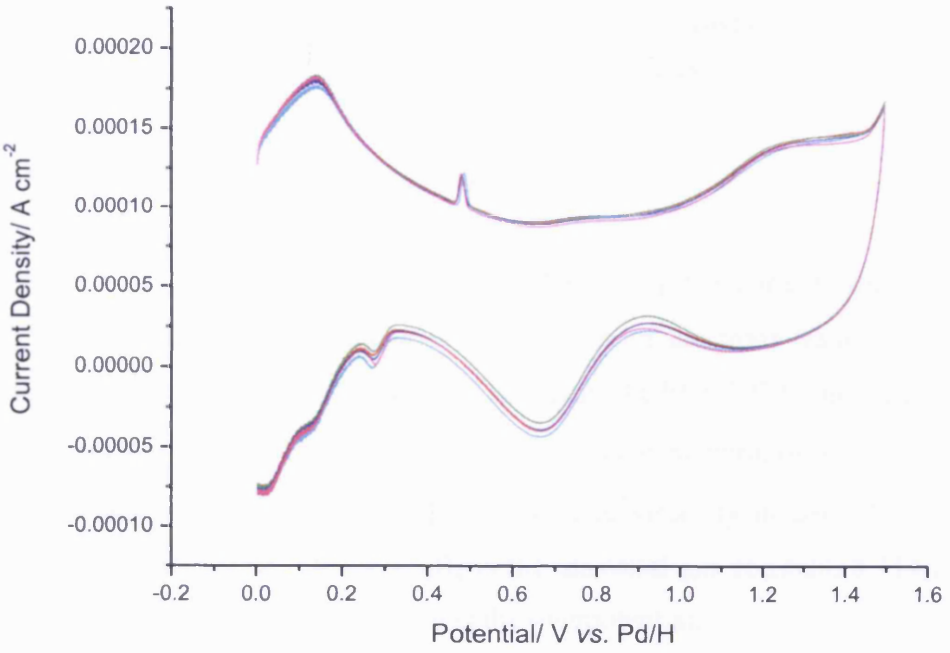

Fig. 4.1.1 CVs of Pt in 0.1 M $HClO_4$ under a hydrogen atmosphere taken before and after RDE experiments. Potential sweep rate 0.1 V s^{-1}. Pd/H reference electrode.

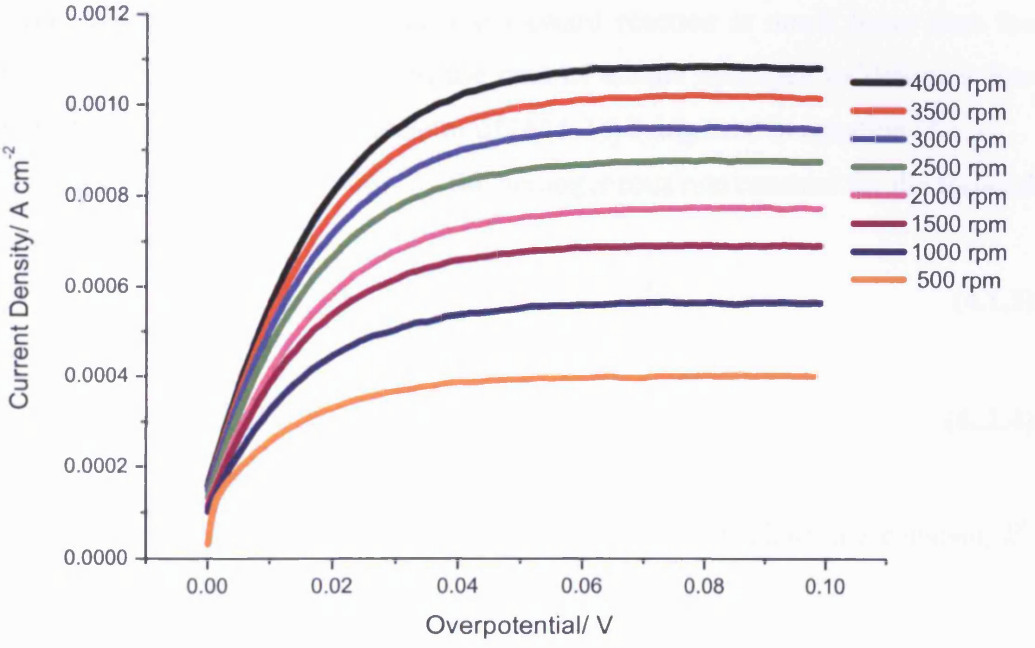

Fig. 4.1.2 Rotating disc electrode data for Pt in 0.1 M $HClO_4$, for rotation rates between 500 - 4000 rpm.

A modified version of the Koutecky-Levich equation was used to analyse the data in the same manner as in published work from Maruyama *et al*[1]

$$\frac{1}{j} = \frac{b}{(b-1)}\left(\frac{1}{j_k} + \frac{1}{0.62nFD_o^{2/3}C_o^*\gamma^{-1/6}\omega^{1/2}}\right) \qquad \textbf{(4.1.1)}$$

where $b = e^{\frac{nF}{R_gT}\eta}$, j is the measured current density, j_k the current density in the absence of mass transport effects, n is the number of electrons transferred in the reaction (2 in this case) F is the Faraday constant, 9.649 x 10^4 C mol^{-1}, D_o is the diffusion coefficient for the system, C_o^* is the bulk concentration of the oxidised species in solution (H_2 in this case), γ is kinematic viscosity in cm^2 s^{-1}, ω is the frequency of rotation of the electrode, R_g is the universal gas constant, 8.314 J mol^{-1} K^{-1}, T is the temperature in Kelvin and η is the overpotential.

A graph of $1/j$ versus $1/\omega^{1/2}$ was plotted (fig. 4.1.3 (a)) and a value of j_k found from the $1/j$ axis intercept for each rotation rate.

The general Koutecky-Levich equation for rotating disk electrodes is[2]:

$$\frac{1}{j} = \frac{1}{j_k} + \frac{1}{0.620nFD_o^{2/3}C_o^*\gamma^{1/6}\omega^{1/2}} \qquad \textbf{(4.1.2)}$$

However, this equation assumes that the forward reaction is much faster than the reverse reaction, which is not true in the case of anodic hydrogen oxidation at low overpotentials, leading to the extra factor of $[b/(b\text{-}1)]$ being used in equation (4.1.1).

The j_k values were then used to find k_f, the homogeneous rate constant for the forward reaction, from the equations:

$$j_k = nFk_fC_o^* = j_0e^{\{(1-\alpha)nF\eta/R_gT\}} \qquad \textbf{(4.1.3)}$$

and

$$j_0 = nFk^0C_o^* \qquad \textbf{(4..1.4)}$$

$\ln k_f$ was then plotted against overpotential, η, to find the standard rate constant, k^0, from the relation:

$$\ln k_f = \ln k^0 + \frac{(1-\alpha)nF\eta}{R_gT} \qquad \textbf{(4.1.5)}$$

Similarly $\ln j_k$ was plotted against overpotential, η, (fig. 4.1.3 (b)) to find the exchange current density, j_0 (taking the active electrode area as 0.265 cm^{-2} for the Pt

electrode used, calculated from charge under the cyclic voltammogram assuming a charge density of 220 μC cm^{-2} for polycrystalline Pt), and transfer coefficient, α, using the relation

$$\ln j_k = \ln j_0 + (1-\alpha) nf\eta \qquad \textbf{(4.1.6)}$$

where f is F/R_gT.

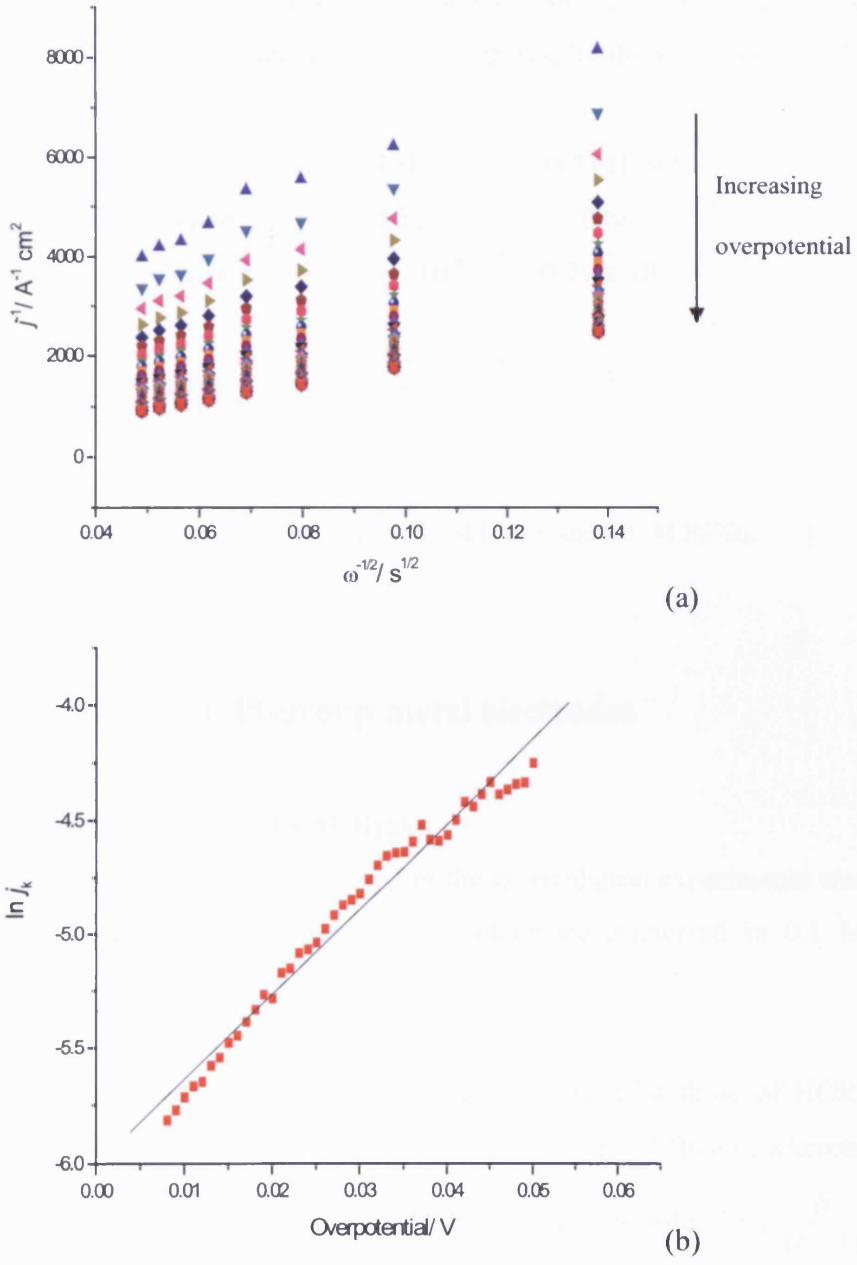

Fig. 4.1.3 (a) Koutecky-Levich plots at overpotentials between 0 and - 0.1 V and (b) ln j_k versus overpotential for Pt in 0.1 M $HClO_4$ using Maruyama's modified version of the Koutecky-Levich equation.

The results obtained were found to lie in a similar range as those found by Maruyama et al.[1] shown in table 4.1.1.

4.1.1.2 Pt in 0.05 M H_2SO_4

The same experimental conditions were used as in section 4.1.1.1, but with 0.05 M H_2SO_4 as the electrolyte solution instead of 0.1 M $HClO_4$. Similarly, the quantitative analysis was the same as that used in section 4.1.1.1, with results shown in table 4.1.1.

	0.1 M $HClO_4$	0.05 M H_2SO_4
Transfer coefficient	0.52	0.68
Standard Rate constant/ cm s^{-1}	1.26×10^{-4}	0.79×10^{-4}
Exchange Current Density/ mA cm^{-2}	2.42	0.89

Table 4.1.1 Data for hydrogen oxidation on Pt in 0.1 M $HClO_4$ and 0.05 M H_2SO_4.

4.1.2 Hydrogen evolution on Pt-group metal electrodes

4.1.2.1 Hydrogen evolution on Pt in 0.1 M H_2SO_4

The same experimental arrangement as was used in the H_2 oxidation experiments was used for hydrogen evolution, with the Pt working electrode immersed in 0.1 M H_2SO_4, under a hydrogen atmosphere.

The Koutecky-Levich calculations for HER are slightly different for those of HOR. HOR is controlled by the reverse reaction rate as well as hydrogen diffusion whereas for HER current density, the reverse reaction plays an insignificant role. The $\frac{b}{(b-1)}$ factor[1] in equation (4.1.1) from the modified Koutecky-Levich equation can therefore be neglected for HER analysis, which thus reverts to the original form of the equation (equation (4.1.2)).

Also, as hydrogen evolution is concerned with the opposite branch of the Tafel curve compared to hydrogen oxidation, wherever (1 - α) is used for hydrogen oxidation calculations, it is replaced by (-α) for hydrogen evolution calculations. Thus, equations (4.1.5) and (4.1.6) become (4.1.7) and (4.1.8) respectively.

$$\ln k_f = \ln k^0 - \frac{\alpha n F \eta}{R_g T} \qquad \textbf{(4.1.7)}$$

$$\ln j_k = \ln j_0 - \alpha n f \eta \qquad \textbf{(4.1.8)}$$

Results of this treatment are shown in fig. 4.1.4, fig. 4.1.5 and table 4.1.2.

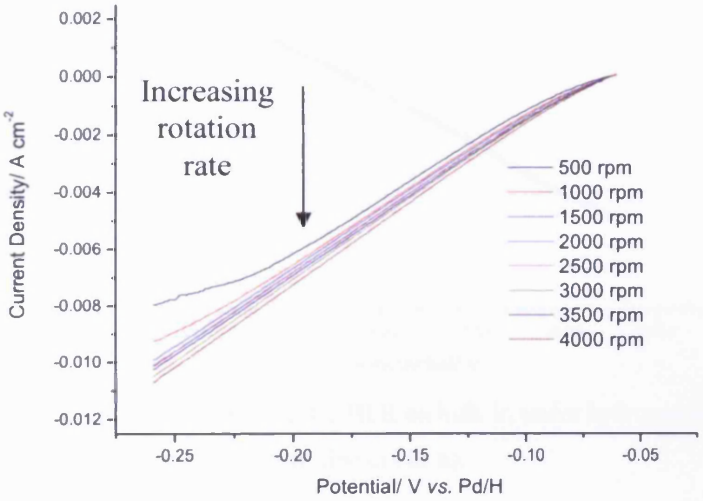

Fig. 4.1.4 Rotating Disk Electrode results for HER on Pt in 0.1 M H_2SO_4 under hydrogen atmosphere.

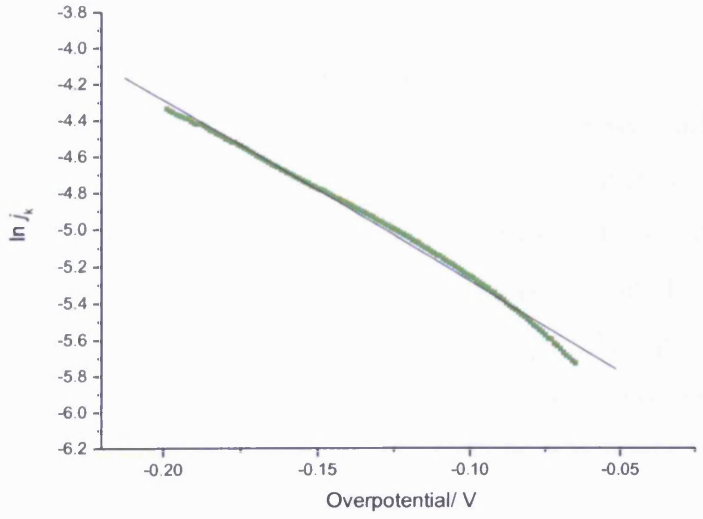

Fig. 4.1.5 Graph of $\ln j_k$ versus overpotential for HER on Pt, under hydrogen atmosphere (with best fit line in black).

4.1.2.2 Hydrogen evolution on Ir in 0.1 M H_2SO_4

Polycrystalline Ir was used as the working electrode and examined in the same manner as Pt described in section 4.1.2.1. Fig. 4.1.6 shows a plot of ln j_k versus overpotential. It is linear over the potential range plotted and exchange current density, j_0, could be estimated from the intercept on the y-axis. The resultant data is displayed in table 4.1.2.

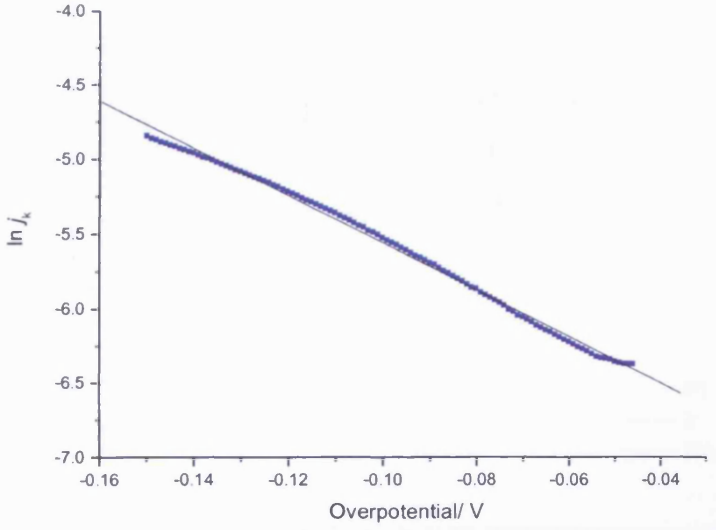

Fig. 4.1.6 Graph of ln j_k versus overpotential for HER on bulk Ir, under hydrogen atmosphere (with best fit line in black).

4.1.2.3 Hydrogen evolution on Ru plated on Pt

Attempts were made to electroplate Ru onto Ni, Ti, Au and glassy carbon, in order to produce a more cost effective electrode consisting of a layer of electrocatalytic material on an inexpensive, less noble metal substrate. These attempts proved unsuccessful. However, a layer of Ru was successfully plated onto Pt. A plating bath (provided by Johnson-Matthey Ltd.) consisting of 10 g l^{-1} Ru from $K_3[Ru_2^{IV}NCl_8(H_2O)_2]$ (30.53% Ru) and 10 g l^{-1} HCO_2NH_4 dissolved in deionised H_2O (18.2 MΩ cm resistivity) was used[3]. The solution was heated to 70°C and the pH adjusted to 1.3 using 0.5 M HCl, before 6.219 mA cm^{-2} was passed through the Pt electrode for approximately 1 hour. The Pt electrode was plated with Ru and showed

no visible defects under 3 x magnification (the cyclic voltammogram of the surface is shown, along with those of Ir and Pt, in fig. 4.1.7).

The same experimental procedure was performed on the Ru-plated Pt electrode as with the Ir and Pt electrodes. The Ru-plated Pt results gave significantly lower exchange current density and standard rate constant values compared to those of Pt and Ir. The results are displayed in table 4.1.2.

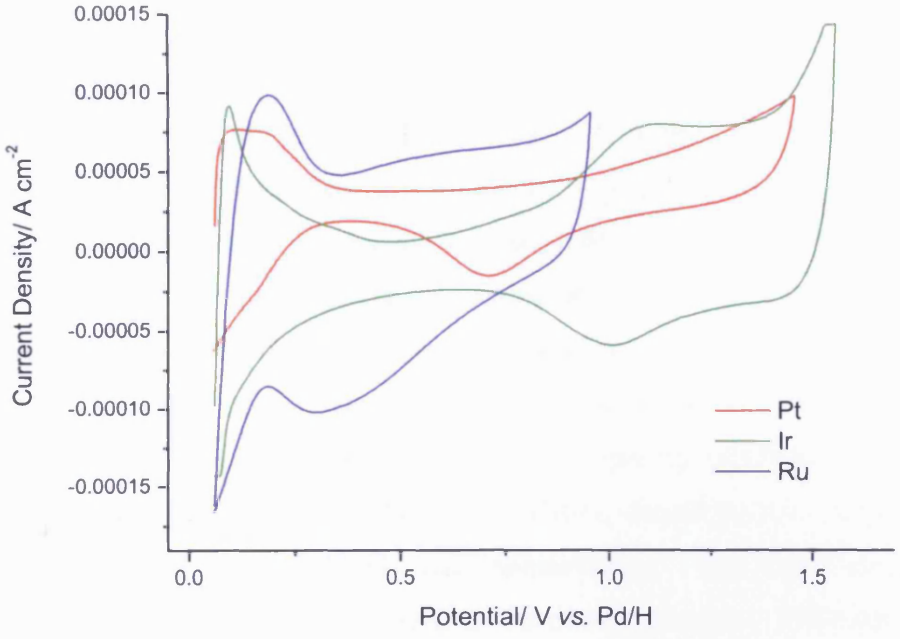

Fig. 4.1.7 Cyclic voltammograms of Pt, Ru and Ir in 0.1 M H_2SO_4.

	Pt	Ru on Pt	Ir
Transfer Coefficient	0.13	0.17 - 0.20	0.19
Standard rate Constant/ cm s^{-1}	0.94 x 10^{-4}	0.11 – 0.13 x 10^{-4}	0.24 x 10^{-4}
Exchange Current Density/ mA cm^{-2}	1.88	0.24 - 0.27	0.50

Table 4.1.2 Data obtained from hydrogen evolution experiments on Pt, Ir and Ru (plated onto Pt) surfaces in 0.1 M H_2SO_4.

4.2 Multi-Frequency AC Voltammetry

Multi-Frequency AC Voltammetry (MFACV) experiments were performed on a Pt electrode in dilute H_2SO_4. The effects of a range of system parameters were investigated, including the aqueous acidic electrolyte concentration, rotation rate, temperature and gaseous atmosphere.

4.2.1 Varying acid strength

MFACV was performed on Pt in 0.05 M and 0.25 M H_2SO_4, using the same experimental apparatus as described in section 3.2, with a DC potential sweep between 0.20 and -0.32 V *vs.* Ag/AgCl for the 0.25 M electrolyte (0.38 and -0.14 V *vs.* Pd/H) and 0.30 to -0.38 V *vs.* Ag/AgCl for the 0.05 M electrolyte (0.53 to -0.15 V *vs.* Pd/H). The voltammograms in the two electrolytes give very similar shapes when plotted on scales normalised to their maximum admittance densities, confirming that the reaction is the same in both systems. When plotted on the same absolute scale (as shown in fig. 4.2.1) it can be seen that the limiting admittance density is approximately five times greater in the 0.25 M H_2SO_4 electrolyte than in the 0.05 M solution (1.20 Ω^{-1} cm^{-2} and 0.25 Ω^{-1} cm^{-2} respectively). This figure corresponds directly to the ratio of acid concentrations in the two experiments. Note that the AC frequency ranges for the two tests are different (8 – 180 Hz and 40 – 400 Hz for the 0.05 M and 0.25 M H_2SO_4 electrolytes respectively). However, this will not affect the frequency-independent magnitude of the limiting admittance density.

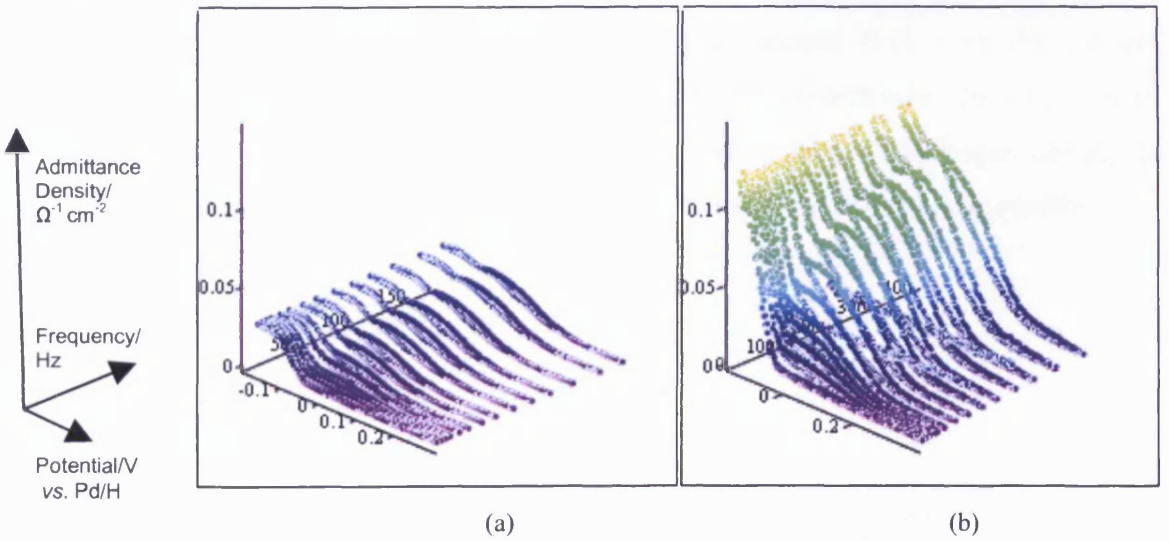

(a) (b)

Fig. 4.2.1 Multi-Frequency AC Voltammograms of Pt in (a) 0.05M and (b) 0.25M H_2SO_4.

4.2.2 Varying the H_2 overpressure

Multi-frequency AC voltammograms were obtained for Pt using the setup described in section 3.2, over an AC frequency range of 40 – 400 Hz. The system used 0.25 M H_2SO_4 as the electrolyte, degassed with N_2 for the first run and performed under a nitrogen atmosphere. The measurement was then repeated with H_2 as the background gas.

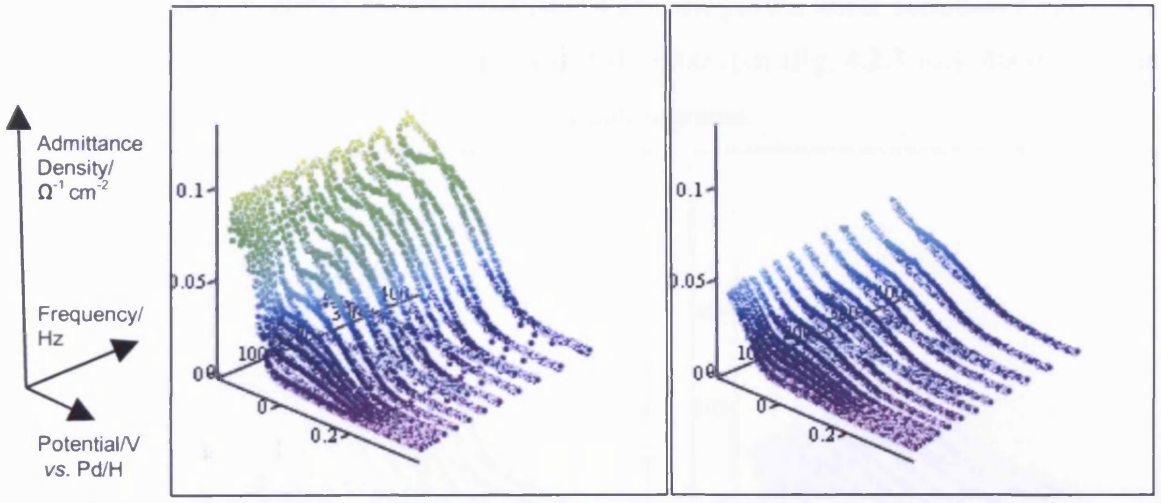

Fig. 4.2.2 Multi-Frequency AC Voltammograms of Pt in 0.25 M H_2SO_4 degassed with (a) N_2 and (b) H_2.

It can be seen from fig. 4.2.2 that the peaks are strongly affected by the hydrogen in solution. The frequency independent OPD-H peak around -0.18 V *vs.* Pd/H is not visible with hydrogen atmosphere, implying that the H_2 evolution has been suppressed by the purging. This may be expected since if there is more hydrogen already in solution, further production of hydrogen would be expected to occur less readily.

4.2.3 Rotating Disk MFACV

Multi-Frequency AC Voltammetry experiments were performed using a rotating Pt working electrode in 0.25 M H_2SO_4 (degassed with N_2) over an AC frequency range of 8 – 180 Hz. The potential was swept between 0.20 and −0.32 V *vs.* Ag/AgCl (0.38 and -0.14 V *vs.* Pd/H).

It was found that rotating the electrode at 1000 rpm gave a MFACV with significantly lower admittance than the same test at a stationary electrode (figs. 4.2.3 (a) and (b)). Rotating the electrode at 2000 rpm (fig. 4.2.3 (c)) gave a lower admittance again and all subsequent, higher, rotation rates tested (3000 rpm (fig. 4.2.3 (d)), 4000 rpm and 5000 rpm) gave essentially identical voltammograms.

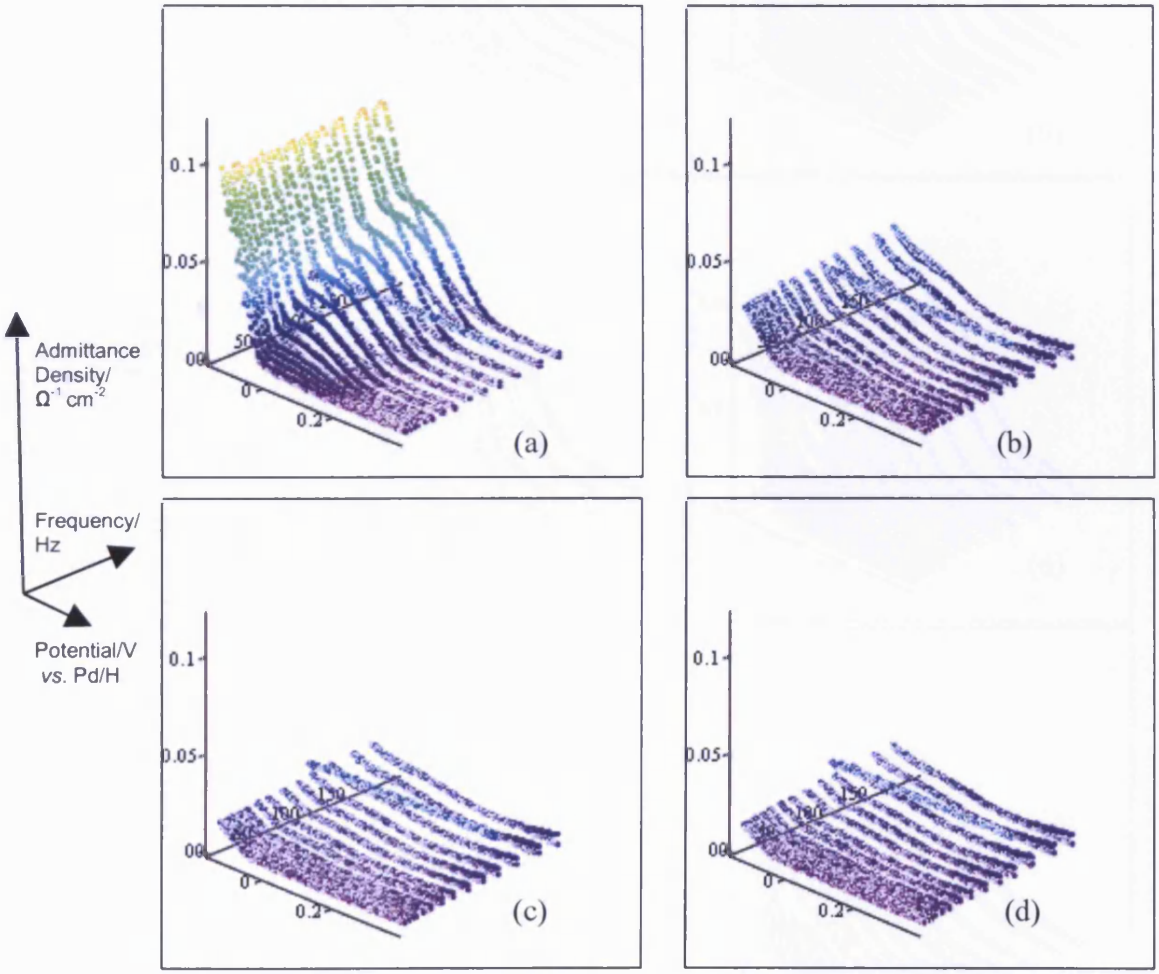

Fig. 4.2.3 Multi-Frequency AC Voltammograms of Pt in 0.25 M H_2SO_4 with the electrode (a) stationary and rotating at (b) 1000 (c) 2000 (d) 3000 rpm.

4.2.4 Temperature dependence of MFACV

MFACV tests were performed on Pt in 0.25 M H_2SO_4 at temperatures from 278 - 318 K (5 - 45 °C), over an AC frequency range of 40 – 400 Hz, degassed with N_2. The results show that the admittance of the system increased with temperature (fig. 4.2.4 (a)-(d)), however, at 313 K and above (fig. 4.2.4 (e)(f)), it decreased. This happened on repeating the experiment (running at 278, 283, 288, 298, 308, 313, and 318 K).

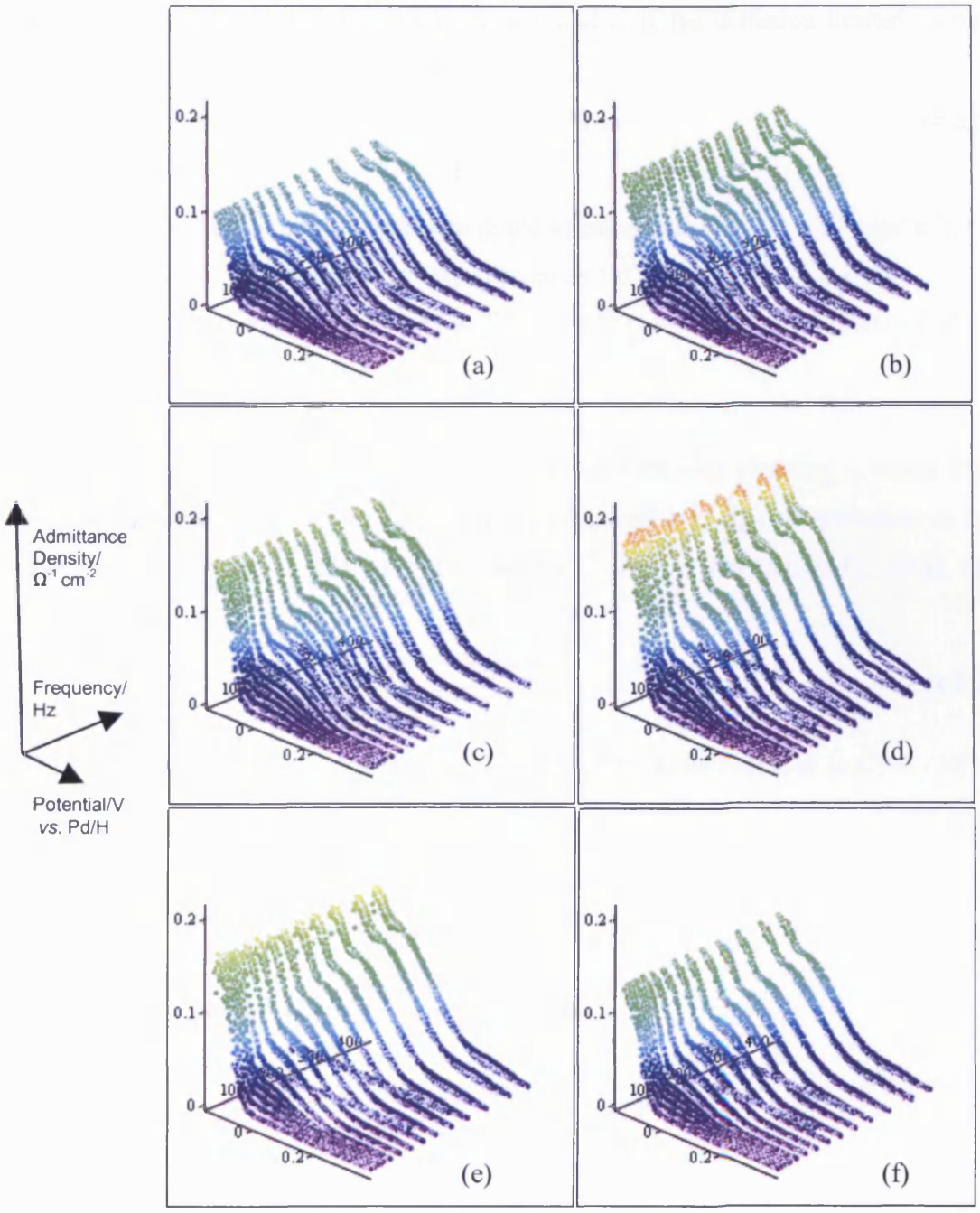

Fig. 4.2.4 Multi-Frequency AC Voltammograms of Pt in 0.25 M H_2SO_4; varying temperature (a) 278 K (b) 288 K (c) 295 K (atmospheric temperature) (d) 308 K (e) 313 K (f) 318 K.

4.2.5 DC temperature dependence measurements of the HER

Tafel data (positive potential sweep at 0.01 V s^{-1}) was taken for Pt in 0.05 M H_2SO_4 rotating at 900 rpm, purged with N_2 and varying the temperature between 273 - 323 K.

Tafel plots of log $[j_d j/(j_d - j)]$ versus overpotential were produced to find values of log j_0. Where j is the measured current density and j_d is the diffusion limited current density, calculated from the equation:

$$j_d = 0.62nFD_H^{2/3}\gamma^{-1/6}s_0\omega^{1/2} \qquad \textbf{(4.2.1)}$$

where D_H is the diffusivity of hydrogen in the solution (taken as 3.7 x 10^{-5} cm^2 s^{-1}), γ is the kinematic viscosity of the solution (taken as 1.07 x 10^{-2} cm^2 s^{-1}) s_0 is the solubility of H_2 in the solution (taken as 7.14 x 10^{-3} M) and ω is the rotation rate in Hz.

The Tafel data (fig. 4.2.5) produced a good linear Arrhenius plot (log j_0 versus $1/T$) (fig. 4.2.6) which gave an activation energy (apparent enthalpy of activation at the reversible potential) of $\Delta H^{0\#}$ = 17.91 kJ mol^{-1} for polycrystalline Pt, using the equation:

$$\frac{d\log j_0}{d(1/T)} = -\frac{\Delta H^{0\#}}{2.3R_g} \qquad \textbf{(4.2.2)}$$

The result was in good agreement with the findings by Markovic *et al* (c.f. 9.5 - 18 kJ mol^{-1} for single crystal faces[4]).

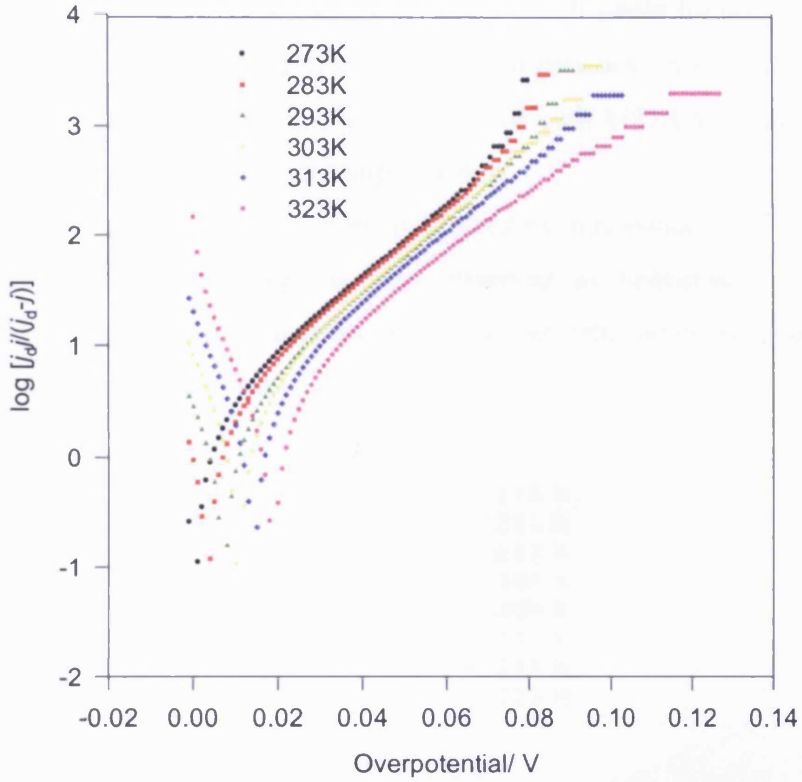

Fig. 4.2.5 Tafel plots of log [$j_d j/(j_d - j)$] for temperatures between 273 - 323 K as shown in the legend.

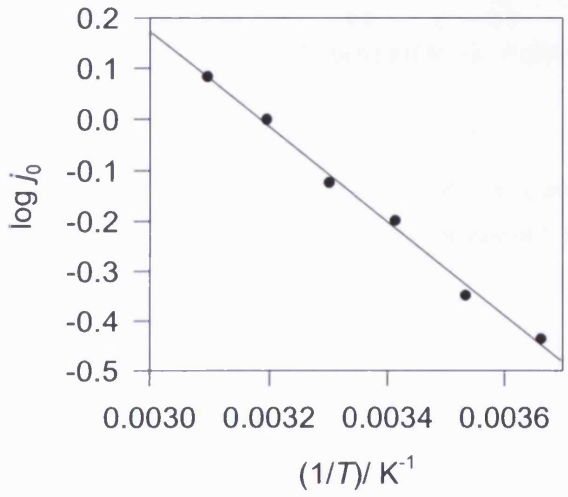

Fig. 4.2.6 Arrhenius plot of log j_0 versus $1/T$ to find activation energy from gradient.

The cyclic voltammetry also yielded some consistent trends for increasing temperature (fig. 4.2.7). Most clearly visible are the Pt oxide forming and stripping peaks, both of which increase significantly with temperature. A reversal of this trend was not observed at 313 K and above as was seen with MFACV. The slope of the voltammograms also increases with temperature.

Similar experiments have recently been published by Jerkiewicz *et al*[5] in which an increased oxide thickness/charge is also observed as temperature is increased. Jerkiewicz did not observe an increase in CV slope with increasing temperature as was observed in the present study.

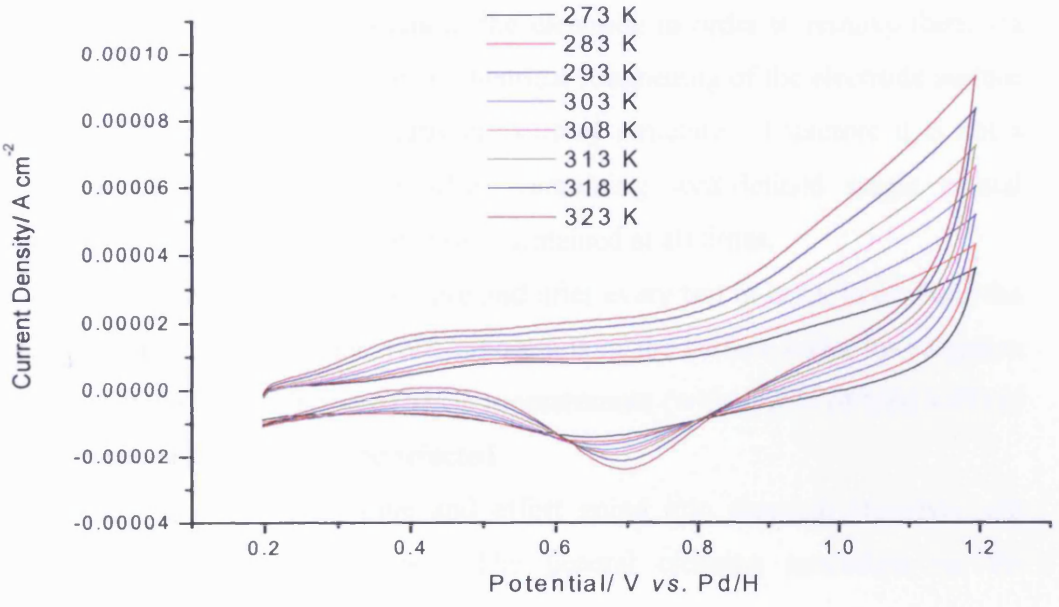

Fig. 4.2.7 CV showing temperature dependence of Pt in 0.05 M H_2SO_4, rotating at 900 rpm, N_2 degassed, between 273 - 323 K at potential sweep rate of 0.1 V s^{-1}.

4.3 Single crystal electrode studies

4.3.1 Cyclic voltammetry and MFACV studies

Cyclic voltammetry and MFACV tests were performed on the basal plane single crystal Pt electrode surfaces together with various stepped surfaces between the {111} and {100} zones of the stereographic triangle (see section 2.3) in order to investigate possible relationships between surface structure and HER rate.

Single crystal experiments are highly sensitive to contamination. Organic molecules are particularly troublesome as they block the crystal surface and require the application of high positive potentials to the electrode in order to remove them via electro-oxidation. This results in electrochemical roughening of the electrode surface due to oxide formation which perturbs the surface structure. Therefore it is not a viable option of surface cleaning when examining well-defined single crystal surfaces. Hence, clean conditions must be maintained at all times.

Cyclic voltammograms were taken before and after every test in order to evaluate the cleanliness of the solution. If the voltammograms of the surface under investigation did not match before and after each HER measurement (with ± 2 % of total UPD-H charge), the measurement would be rejected.

This led to a large amount of time and effort going into cleaning processes and investigating contamination sources. The general cleaning procedure for the glassware is described in section 3.3.

Good voltammetric data was observed for the three basal plane Pt single crystal surfaces ({111}, {100}, {110}) as depicted in fig. 4.3.1 and a range of stepped surfaces between Pt{111} and {100} (fig. 4.3.2).

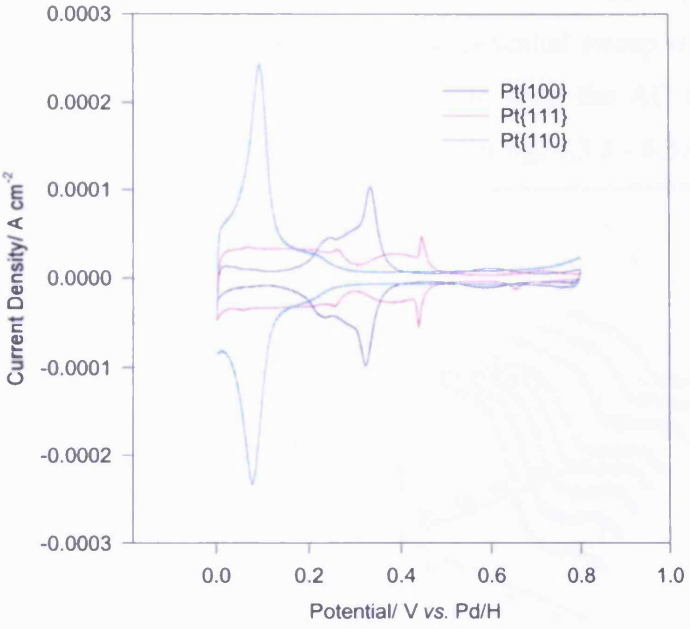

Fig. 4.3.1 Cyclic voltammograms of Pt{111}, Pt{110} and Pt{100} in 0.1 M H_2SO_4, sweep rate 0.05 V s^{-1}.

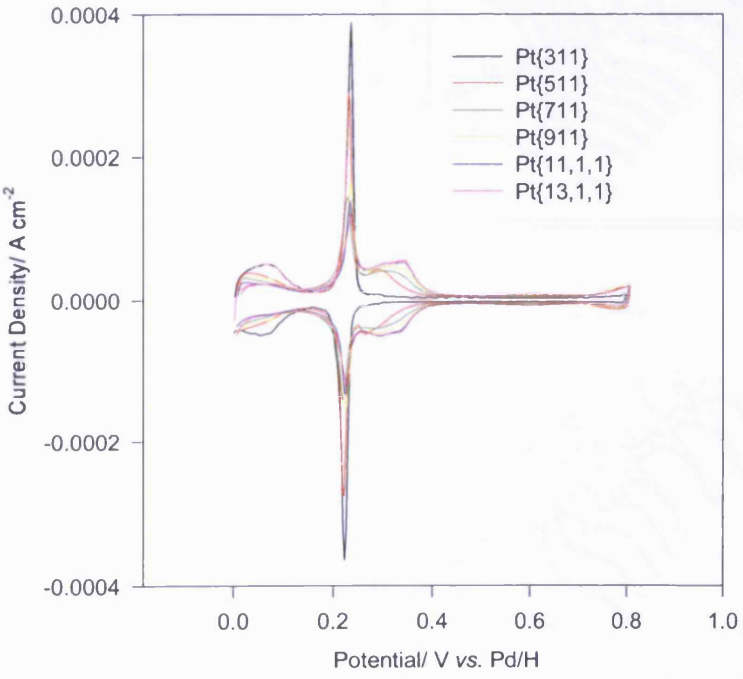

Fig. 4.3.2 Cyclic voltammograms of Pt{211}, Pt{311}, Pt{511}, Pt{711}, Pt{911}, Pt{11,1,1} and Pt{13,1,1} in 0.1 M H_2SO_4, sweep rate 0.05 V s^{-1}.

After cyclic voltammetry had confirmed cleanliness and reproducibility of the single crystal surfaces under investigation, multi-frequency AC voltammetry was performed on each of the surfaces in 0.1 M H_2SO_4. The DC potential sweep was between 0.10 and -0.19 V *vs.* Pd/H at 0.00125 V s^{-1} sweep rate with the AC frequency range between 10 – 100 Hz. The data obtained are shown in fig. 4.3.3 - 4.3.4.

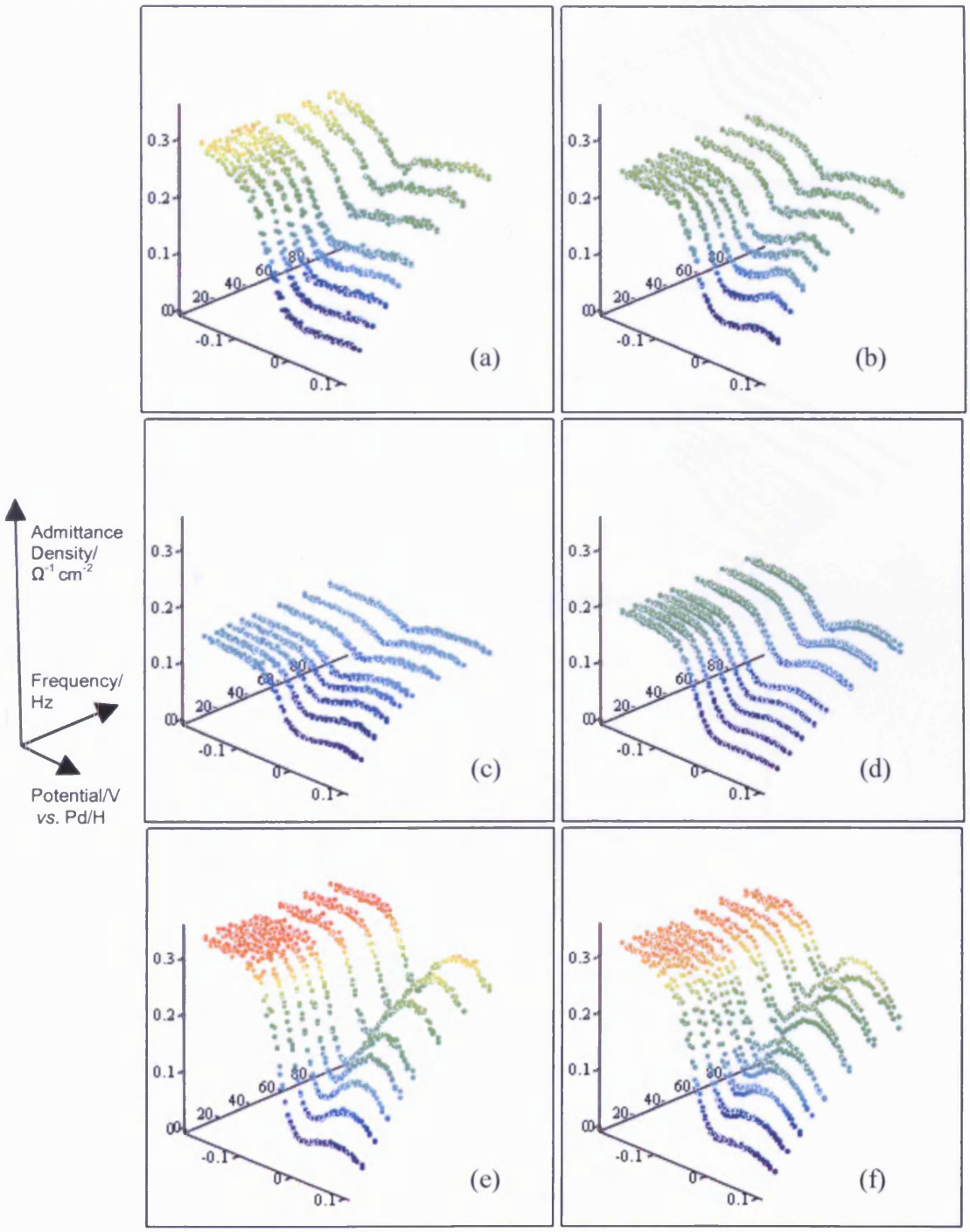

Fig. 4.3.3 MFACVs for Pt single crystal surfaces (a) {111} (b) {755} (c) {533} (d) {211} (e) {311} (f) {511} in 0.1 M H_2SO_4.

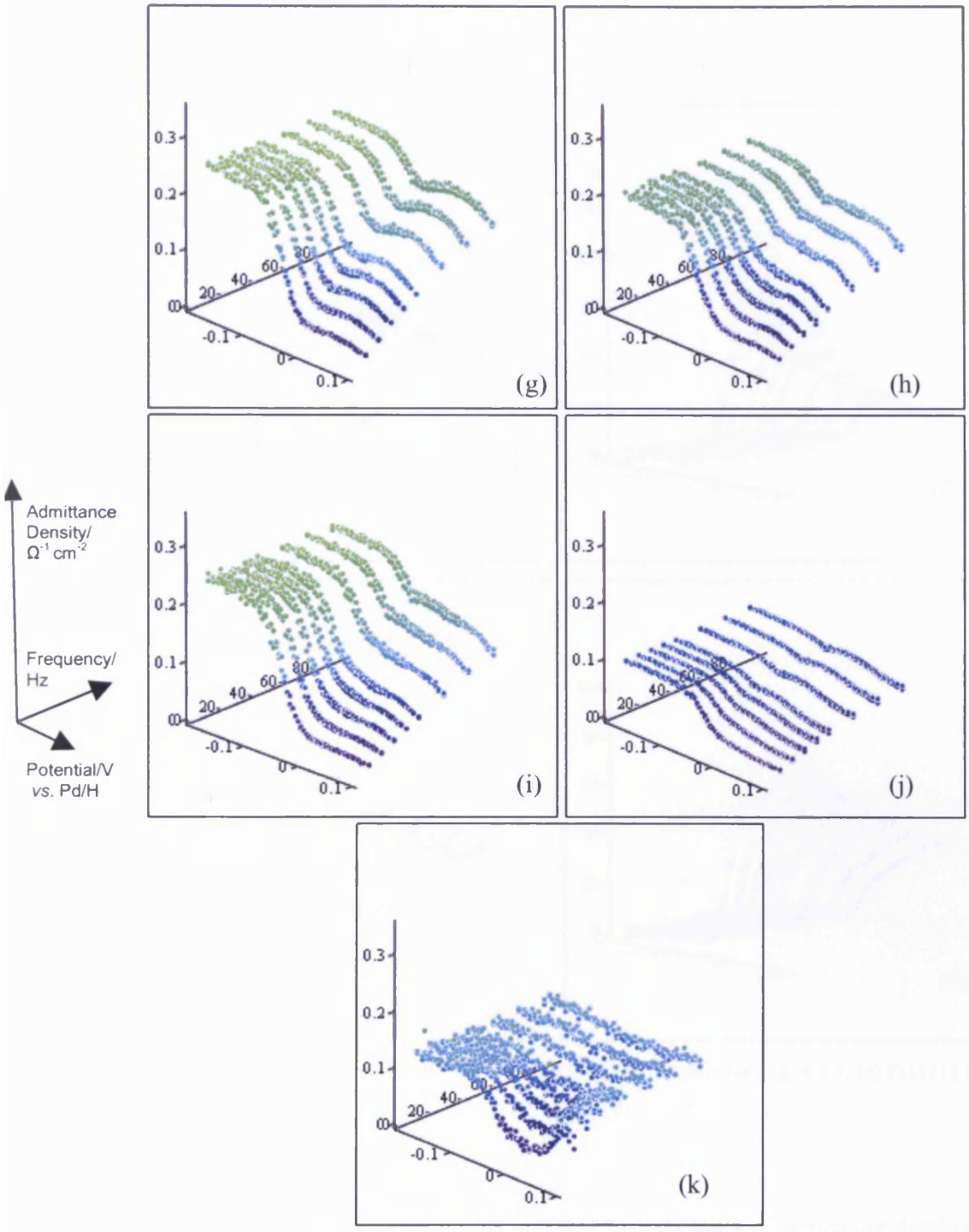

Fig. 4.3.4 MFACVs for Pt single crystal surfaces (g) {711} (h) {911} (i) {11,1,1} (j) {13,1,1} (k) {100}, in 0.1 M H_2SO_4.

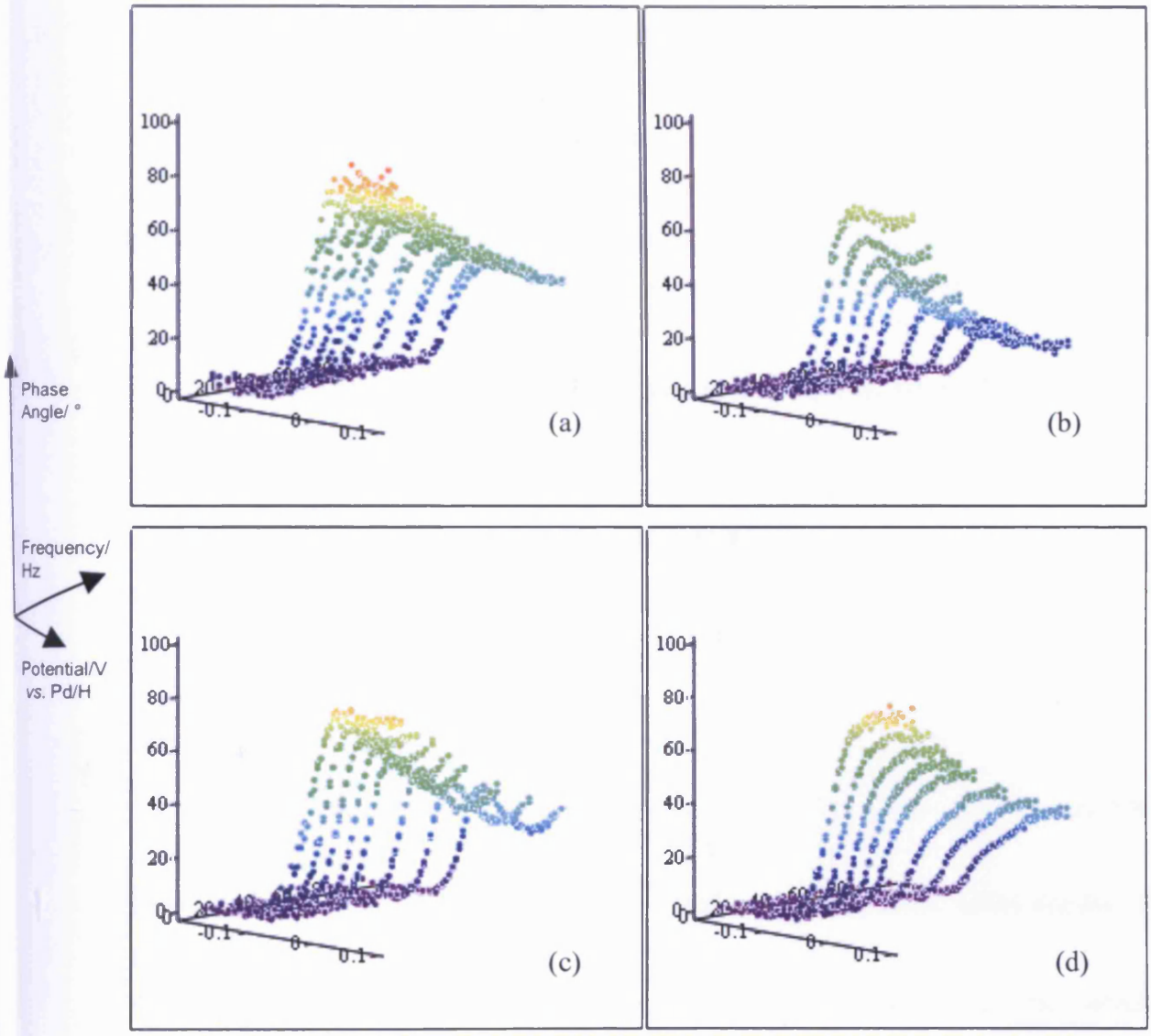

Fig. 4.3.5 Phase plots for selected MFACV voltammograms shown in fig. 4.3.4. (a) Pt{111} (b) Pt{533} (c) Pt{311} (d) Pt{100}.

The phase plots for the single crystal surfaces tested (some of which are displayed in fig. 4.3.5) show a frequency dependent anion region between 0 and 0.1 V, becoming frequency independent in the hydrogen evolution region. The phase angle decreases to zero on all of the Pt single crystal surfaces tested (at potentials negative of ~0.02 V *vs.* Pd/H). No hysteresis is observed between the forward and reverse potential sweeps.

Initial HER activity comparisons can be taken from the limiting admittance density; i.e. the point on the MFACV plot ($1/Z$ versus ω versus V) at which the admittance density reaches a plateau.

A graph of limiting admittance density versus crystal step density (i.e. density of {111}x{100} or {100}x{111} steps per cm^2 crystal electrode area) was plotted (fig. 4.3.6) to investigate any structural dependence for the HER rate.

The step densities were calculated using two equations for the two investigated regions of the stereographic triangle (from {111} to the turning point and from the turning point to {100}, excluding the planar surfaces, which we assume have zero step density).

For the region between {111} and the turning point at {311}, where the surface has the general microfacet notation:

Pt(s)[n{111}x{100}]

and adopts the Miller index form:

$$\{h,k,l\} = (n+1,n-1,n-1) \qquad \textbf{(4.3.1)}$$

step density, N, is calculated from[6]:

$$N_{SD} = \frac{2}{\sqrt{3}.d_{Pt}} \cdot \frac{1}{n-1_3} \qquad \textbf{(4.3.2)}$$

where d_{Pt} is the Pt atomic diameter (2.78 Å) and n is the associated series number of the crystal.

Similarly, for the surfaces in the region between the turning point and {100} which have the general microfacet notation:

Pt(s)[n{100}x{111}]

with the Miller index formula:

$$\{h,k,l\} = (2n-1,1,1) \qquad \textbf{(4.3.3)}$$

step density can be calculated from the formula[6]:

$$N_{SD} = \frac{1}{d_{Pt}} \cdot \frac{1}{n-1_2} \qquad \textbf{(4.3.4)}$$

The step densities are displayed in table 4.3.1.

Pt fcc {*hkl*} surface	*n*	Step density/ 10^6 cm^{-2}
{111}	∞	0
{755}	6	7.33
{533}	4	11.33
{211} (≡ {422})	3	15.57
{311}	2\\2	24.45
{511}	3	14.39
{711}	4	10.28
{911}	5	7.99
{11,1,1}	6	6.54
{13,1,1}	7	5.53
{100}	∞	0

Table 4.3.1 Step densities for the single crystal surfaces under investigation.

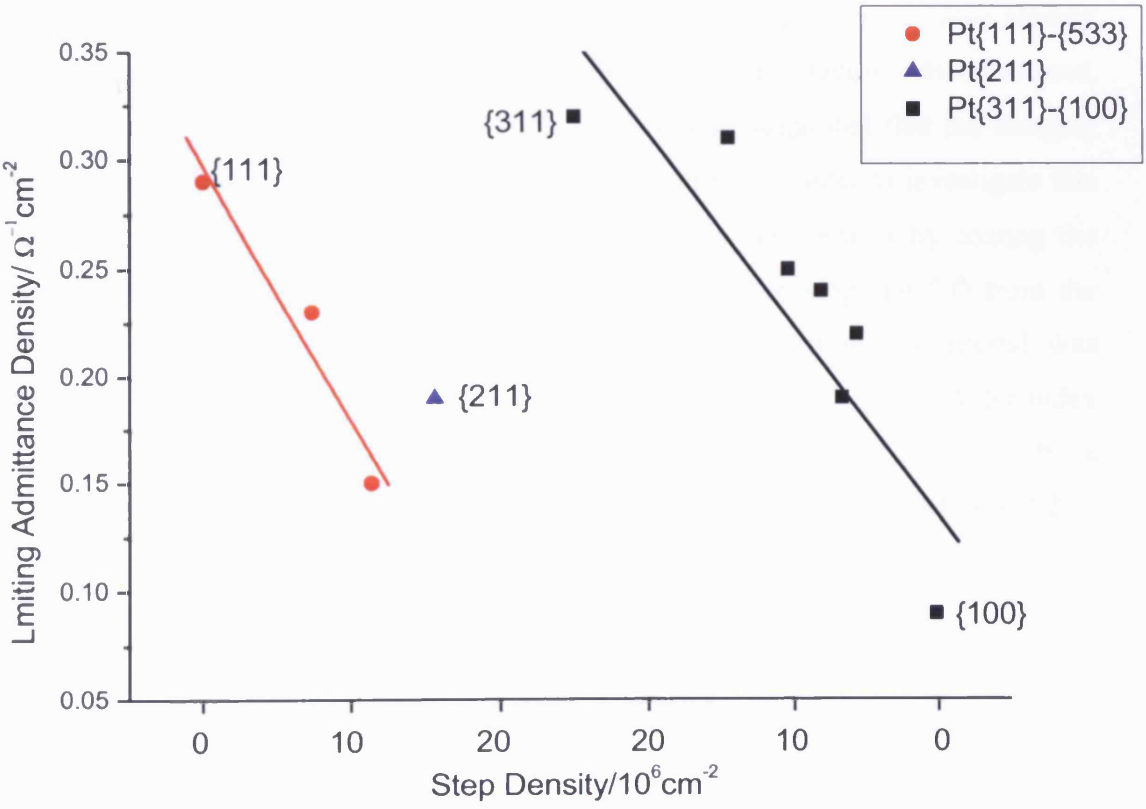

Fig. 4.3.6 Graphs of limiting admittance density taken from MFACV in 0.1 M H_2SO_4 versus Pt crystal structure for surfaces between {111} - {100}.

Observing the data displayed in fig. 4.3.6, it is seen that the plot may be split into two separate data sets, those relating to the crystal surfaces with larger {111} terrace width and those with larger {100} terrace width. As the plot moves from {111} towards {311}, there is a trend of decreasing limiting admittance density until it reaches the turning point on the stereographic triangle, {311}, (where there is equal {111} and {100} character). The {211} surface is the point on the graph which reverses the decreasing trend, which then increases to a maximum at {311}. The trend between {311} and {100} is then seen to exhibit a general decrease in limiting admittance density. The above analysis would imply a structure dependence for the HER, enhanced by {111} terraces and by {111}x{100} steps.

It was noted, however, that the crystals tested were of differing surface area, and more specifically, that the largest crystals were giving rise to the smallest limiting admittance density. Consequently, a graph of limiting admittance density versus the reciprocal of the crystal area was plotted in order to test this relationship (fig. 4.3.7). It was found that there was a positive correlation, showing that there was an inverse dependence of HER on electrode area, despite the absolute admittance value already being normalised to area. This implies that there is another factor, related to area, which is playing a significant role in HER rate. It was suggested that the hanging meniscus was playing a role in this behaviour. Therefore, in order to investigate this possibility, an experiment was devised to eliminate any edge effects by coating the crystal bead with CO (see experimental section 3.6). After stripping CO from the surface of the electrode in the hanging meniscus configuration, the crystal was submerged below the level of the electrolyte, thereby exposing only the Miller index plane to the electrolyte whilst the rest of the bead electrode was protected by a chemisorbed CO layer. This experiment is discussed in more detail in section 4.3.2.

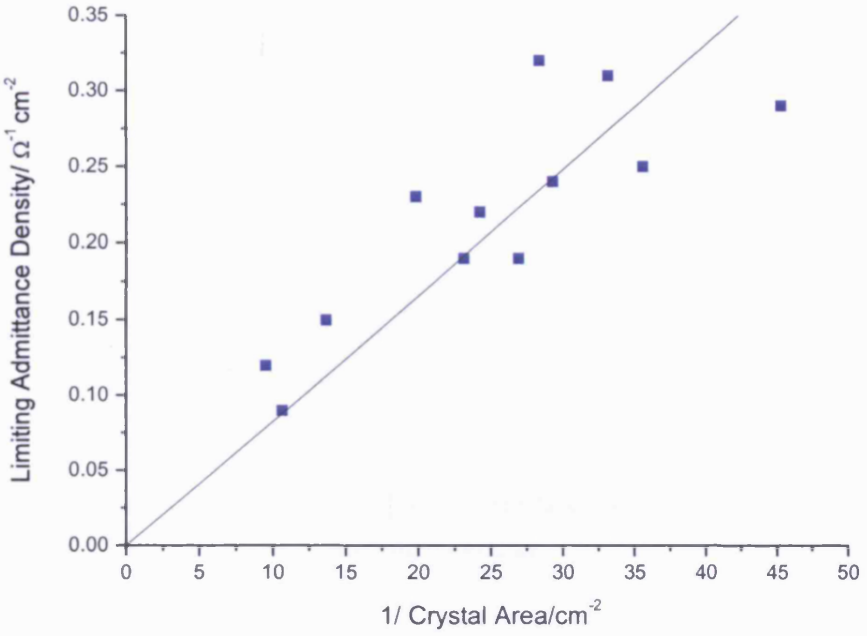

Fig. 4.3.7 Graph of limiting admittance density versus reciprocal of crystal surface area.

4.3.1.1 Model circuit analysis of MFACV data

As explained in section 2.1.2.1, electrochemical cells may be modelled as a circuit consisting of contributions from an arrangement resistors and capacitors representing the various elements within the cell. Ideally, the MFACV data should be modelled using the circuit depicted in fig. 4.3.8. This circuit separates the pure, charge transfer resistance and a theoretical, frequency dependent impedance, the Warburg impedance, which represents mass transport effects within the solution.

The frequency independence of the MFACV data over the range studied, however renders it impossible to define a Warburg impedance term as there is no possibility of separating resistances in series without additional information. Thus the equivalent circuit must be reduced to a potential dependent charge-transfer resistance, R_{CT} and a series resistance term, R_S, which includes the solution resistance (which may vary with electrode area) and all other resistance terms which could influence the admittance. The double layer capacitance also becomes impossible to fit in the plateau region of the MFACV, due to the frequency independence of the admittance. The circuit therefore reduces simply to that shown in fig. 4.3.9.

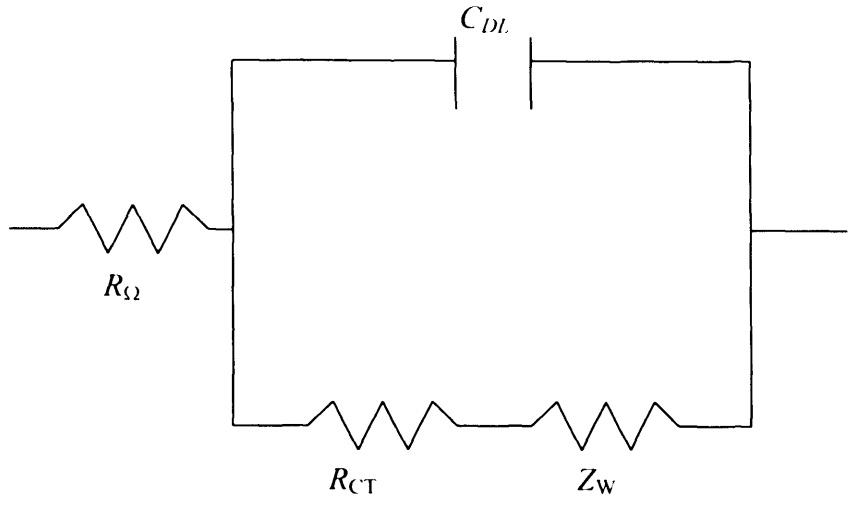

Fig. 4.3.8 Model circuit example, separating Fardaic impedance into charge transfer resistance and Warburg impedance.

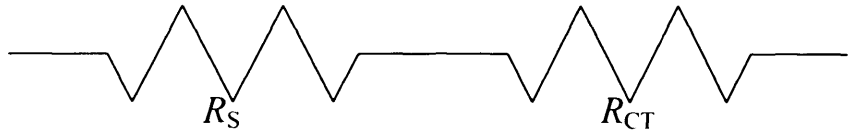

Fig. 4.3.9 The equivalent circuit which had to be used for the MFACV analysis due to the frequency independent nature of the data in the OPD-H region.

For the analysis of the single crystal MFACV data, it was assumed that any frequency dependence observed on the MFACVs (figs. 4.3.3 and 4.3.4) was related to the desorption of species positive of 0 V *vs.* RHE and was independent of the hydrogen evolution reaction on the Pt surfaces. Each MFACV was then simulated using equations (4.3.4) – (4.3.6)

$$Y = \frac{1}{ZA} \qquad \textbf{(4.3.4)}$$

where Y is the admittance density in Ω^{-1} cm^{-2}, A is the electrode area in cm^2 and Z is the electrochemical impedance in Ω, given by:

$$Z = R_S + R_{CT} \qquad \textbf{(4.3.5)}$$

where:

$$R_{CT} = R_0 \exp(\frac{\alpha n F}{R_g T} E) \qquad \textbf{(4.3.6)}$$

where R_0 is simply the pre-exponential factor in the charge transfer resistance.

The simulated MFACVs were generated by modelling the lowest frequency MFACV data (admittance density versus potential at approximately 8 Hz, see fig. 4.3.10) for each surface by manipulation of R_0, R_S and α until a good fit was achieved. The simulation was then expanded over the experimental frequency range to produce a MFACV (which is valid as it has been assumed that any frequency effect observed in the real data is due to anion desorption effects and not hydrogen evolution).

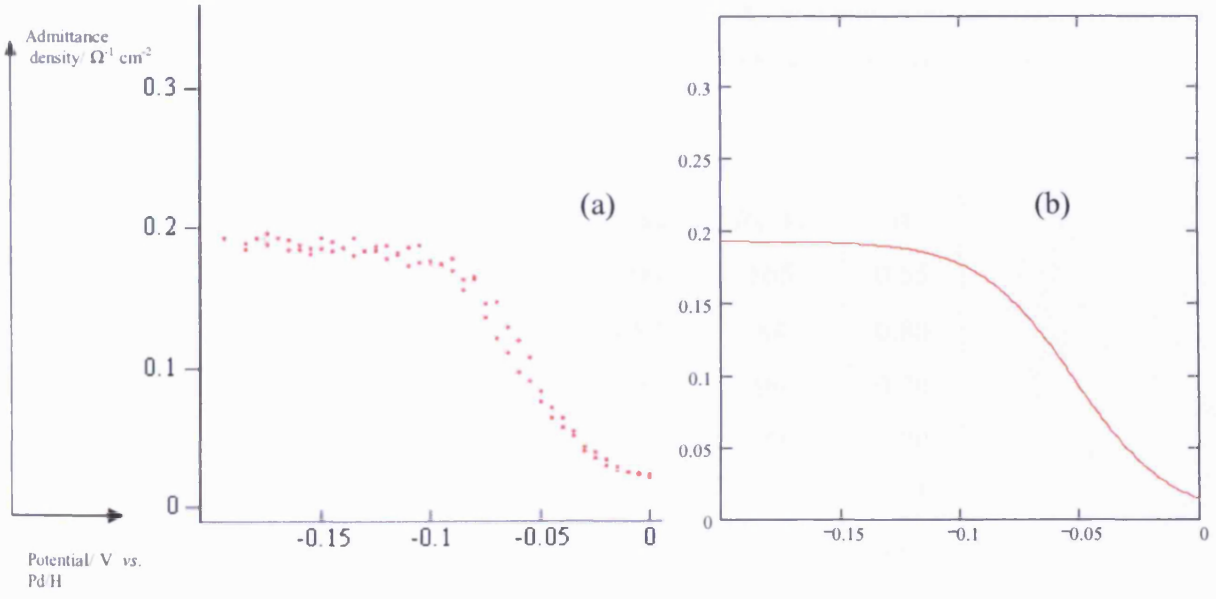

Fig. 4.3.10 (a) Real and (b) simulated admittance density versus potential curves at low frequency (8.07 Hz) for Pt{11,1,1} electrode surface in 0.5 M H_2SO_4. The simulated curve takes the values of R_0 = 1600 Ω, R_S = 120 Ω, α = 0.64.

An example of a simulated MFACV in comparison to the experimentally recorded data (for the Pt{11,1,1} electrode) is shown in fig. 4.3.11. The data used to simulate each MFACV (R_0, R_S and α) is presented in table 4.3.2.

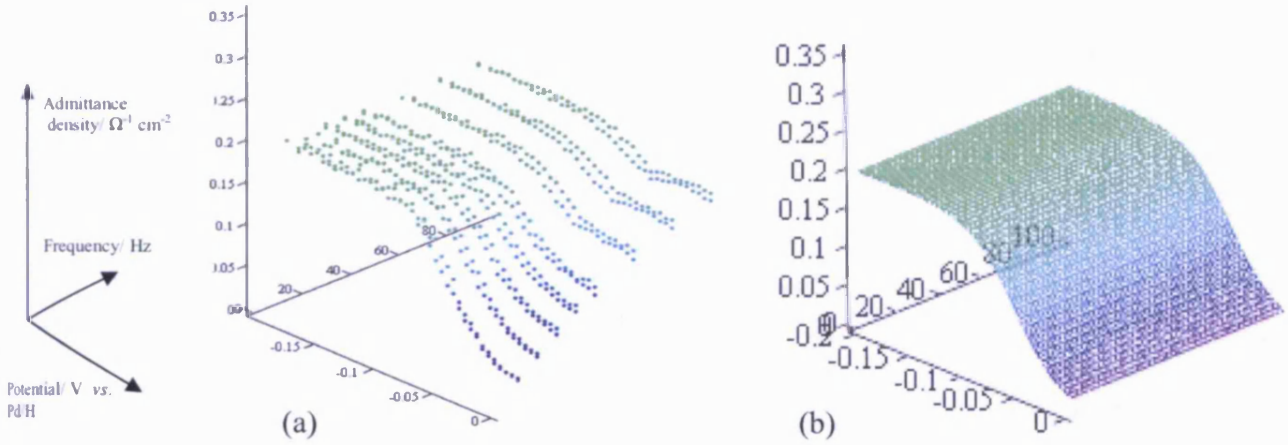

Fig. 4.3.11 (a) Real and (b) simulated multi-frequency AC voltammograms for Pt{11,1,1} single crystal electrode in 0.5 M H_2SO_4. R_0 = 1600 Ω, R_S = 120 Ω, α = 0.64.

Crystal	R_0/ Ω	R_S/ Ω	α
Pt{111}	3500	165	0.55
Pt{755}	1050	84	0.80
Pt{533}	1000	99	0.70
Pt{211}	1500	159	0.70
Pt{311}	2700	88	0.75
Pt{511}	2300	106	0.60
Pt{711}	2000	143	0.64
Pt{911}	2200	122	0.64
Pt{11,1,1}	1600	120	0.64
Pt{13,1,1}	1900	103	0.64
Pt{100}	350	120	0.60

Table 4.3.2. Data used to simulate single crystal MFACVs.

R_0 was found to vary linearly with limiting admittance density and 1/area (see fig. 4.3.12), whilst the graph of R_0 versus crystal step density showed the same relationship as that observed with the plot of limiting admittance density versus crystal step density. The transfer coefficient showed no systematic variation with limiting admittance density, 1/area or crystal step density. Similarly, the series resistance showed no significant dependence on any of the three factors investigated.

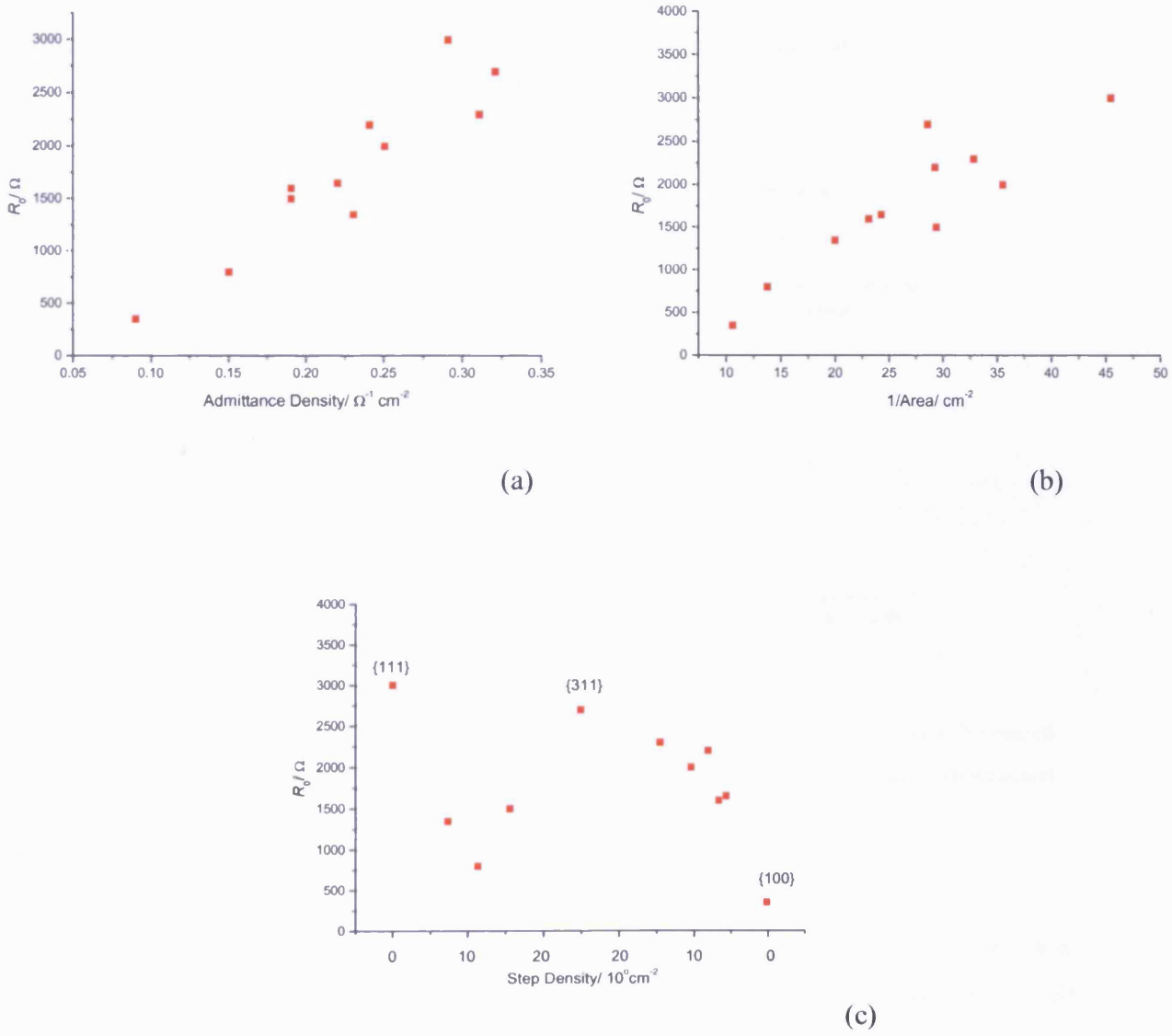

Fig. 4.3.12 Plots of R_0 versus (a) limiting admittance density (b) 1/area and (c) crystal step density.

4.3.2 CO blocking experiments

It proved unreliable to perform the CO blocking tests with MFACV techniques due to the length of time required to run each experiment. The MFACV measurements took approximately 10 minutes to obtain good, steady state data with little noise. During this time, the CO would be displaced from the crystal bead hemisphere, resulting in an increase in electrode area during the course of the measurement (as shown by cyclic voltammetry in fig. 4.3.13), hence the signal being measured consisted of other contributions in addition to the Pt{*hkl*} plane. This would mean that the HER would no longer be originating from the desired single crystal electrode plane, but would also be produced from the sides of the crystal.

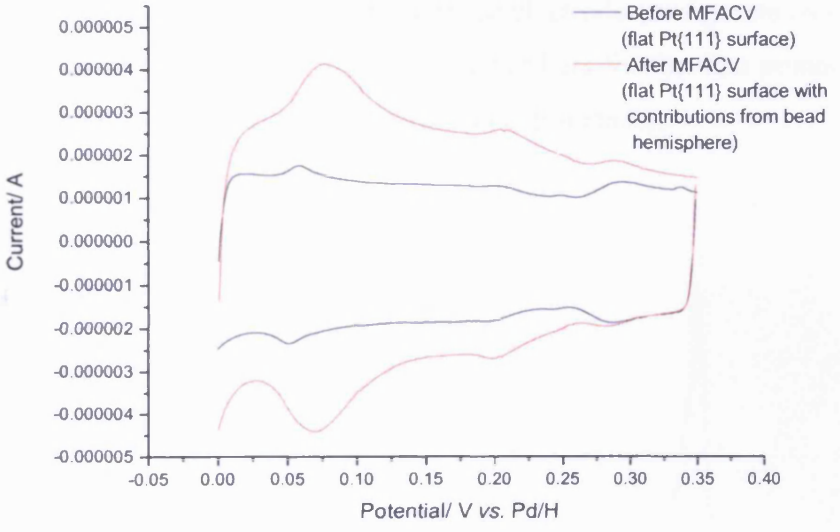

Fig. 4.3.13 Cyclic voltammograms taken before and after a MFACV measurement on a CO-coated Pt{111} electrode submerged blow the electrolyte surface, showing that the CO had been removed over the time period of the experiment, rendering the result invalid.

Therefore, an equivalent DC test was undertaken. A single crystal electrode was flame annealed and cooled in hydrogen, a cyclic voltammogram was taken (0 – 0.85 V, 0.05 V s^{-1}) in a normal hanging-meniscus configuration, followed by linear sweep voltammetry (LSV) (0.1 to – 0.1 V, at a sweep rate of 0.005 V s^{-1}). A CV was taken to confirm both the cleanliness of the system after the LSV measurement. The single crystal electrode surface was then blocked using chemisorbed CO and a CV taken (0 –

0.85 V, 0.05 V s^{-1}) to remove CO from the flat electrode surface. After a further LSV, the CV was repeated to confirm that no adsorption sites had been exposed (by displacement of CO) in addition to those in the Pt{*hkl*} plane. The bead was then partially submerged in the electrolyte. A cyclic voltammogram was run (0 – 0.35 V, 0.05 V s^{-1}), the maximum potential being the most positive potential the system could be swept to without affecting/removing CO from the bead hemisphere, yet still providing a Pt{111} cyclic voltammogram response for cleanliness/reproducibility comparisons. A linear sweep voltammogram into the HER potential region was then performed, followed by a final CV to check once again for changes in CV response after HER. If all cyclic voltammograms did not match within a reasonable error throughout the test, the results would be discarded (see fig. 4.3.14).

Exchange current density was plotted against single crystal step density and also reciprocal of electrode area for each of the three electrode configurations tested. The results are shown in figs. 4.3.15 - 4.3.20 (the error bars for the data points arise from variation in j_0 from multiple tests performed on each surface).

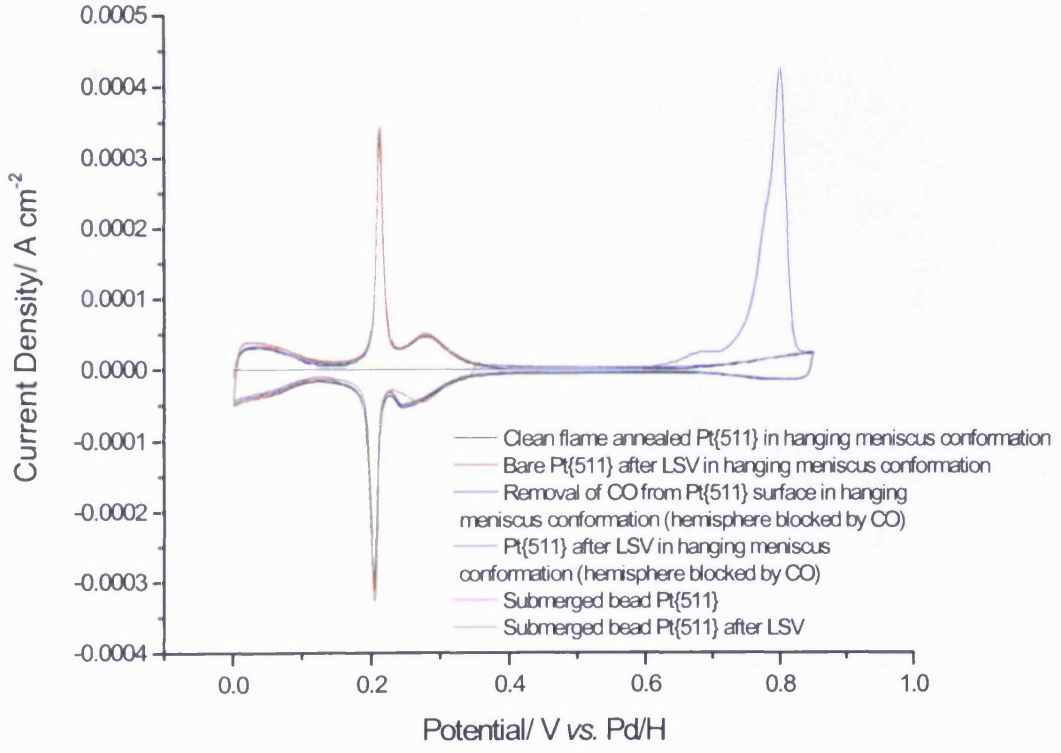

Fig. 4.3.14 CVs of Pt{511} at various stages throughout the CO blocking experiment.

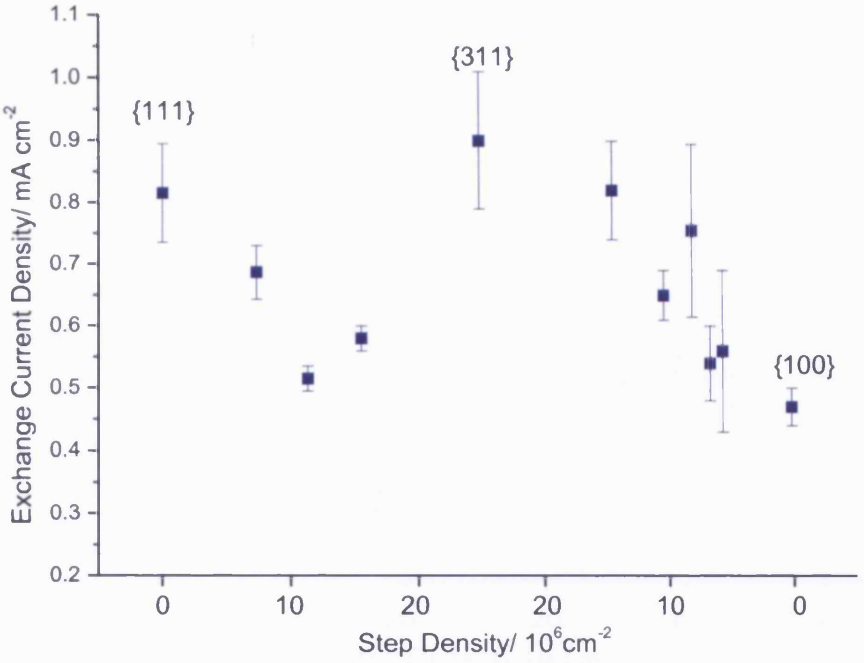

Fig. 4.3.15 Graph of exchange current density versus single crystal step density for annealed Pt single crystal electrodes in hanging meniscus configuration. Taken from Tafel slopes of LSVs performed in 0.5 M H_2SO_4, 0.005 V s^{-1}.

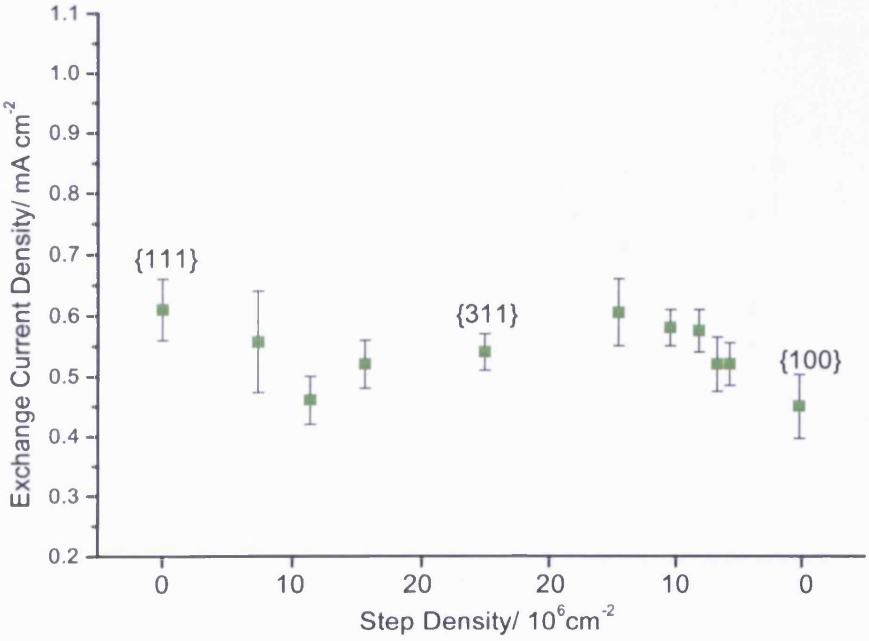

Fig. 4.3.16 Graph of exchange current density versus single crystal step density for Pt single crystal electrodes in hanging meniscus configuration after being coated with CO (which had been stripped from the crystal face). Taken from Tafel slopes of LSVs performed in 0.5 M H_2SO_4, 0.005 V s^{-1}.

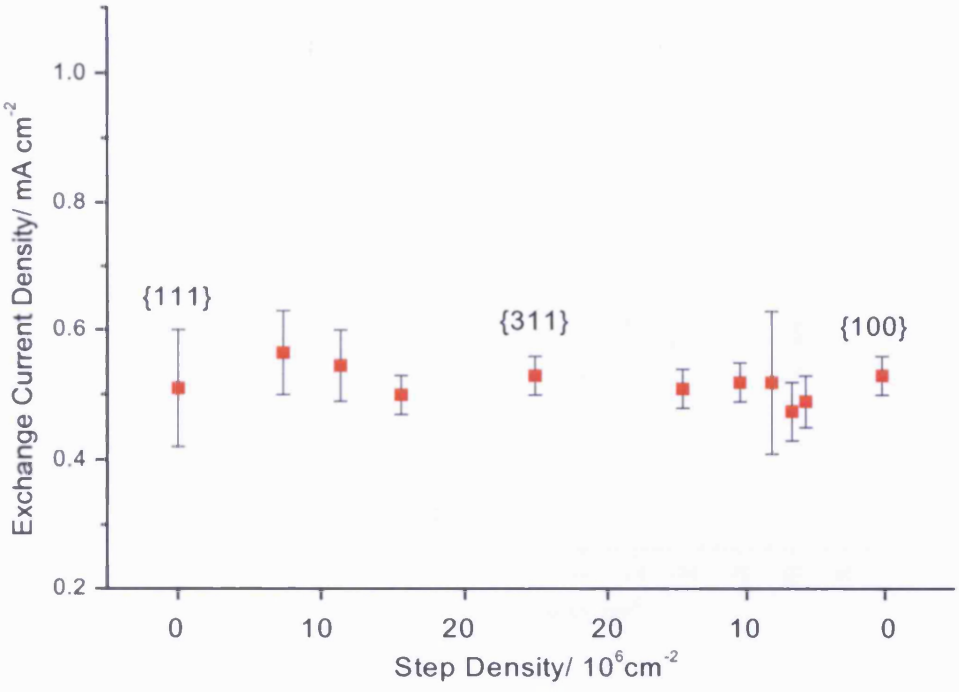

Fig. 4.3.17 Graph of exchange current density versus single crystal step density for Pt single crystal electrodes, partially submerged in the electrolyte with bead hemisphere coated with CO. Taken from Tafel slopes of LSVs performed in 0.5 M H_2SO_4, 0.005 V s^{-1}.

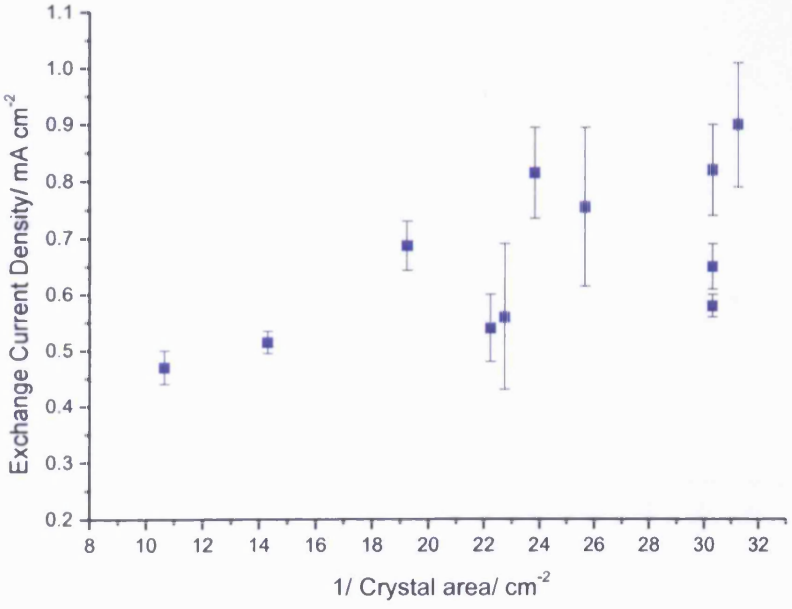

Fig. 4.3.18 Graph of exchange current density versus reciprocal of crystal area for annealed Pt single crystal electrodes in hanging meniscus configuration. Taken from Tafel slopes of LSVs performed in 0.5 M H_2SO_4, 0.005 V s^{-1}.

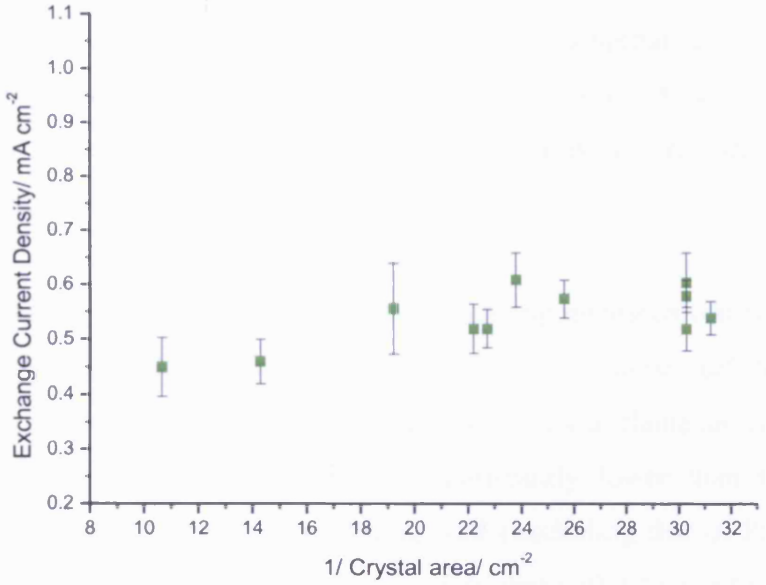

Fig. 4.3.19 Graph of exchange current density versus reciprocal of crystal area for Pt single crystal electrodes in hanging meniscus configuration after being coated with CO (which had been stripped from the crystal face). Taken from Tafel slopes of LSVs performed in 0.5 M H_2SO_4, 0.005 V s^{-1}.

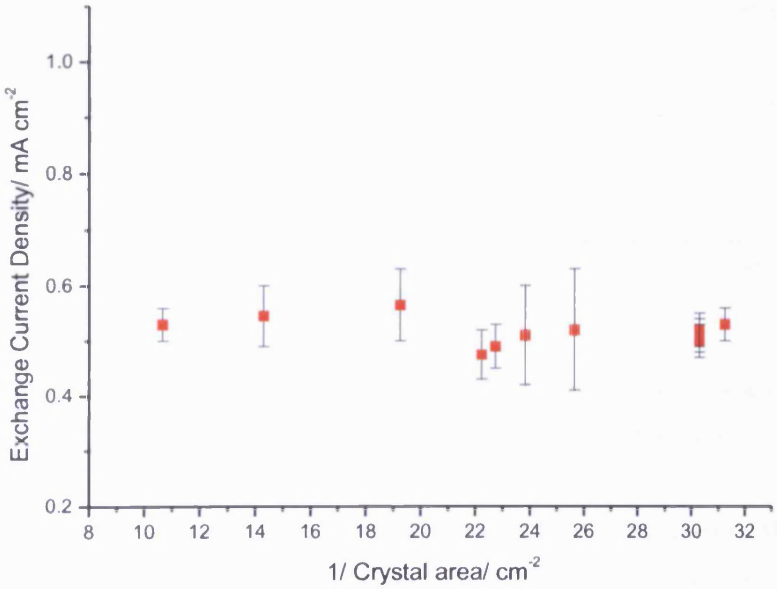

Fig. 4.3.20 Graph of exchange current density versus reciprocal of crystal area for Pt single crystal electrodes, partially submerged in the electrolyte with bead hemisphere coated with CO. Taken from Tafel slopes of LSVs performed in 0.5 M H_2SO_4, 0.005 V s^{-1}.

A plot of current density versus crystal step density ({111}x{100} and {100}x{111} steps) for the clean, flame annealed, single crystal working electrodes (fig. 4.3.15 - 4.3.17) showed a very similar trend to that seen when admittance density from the MFACV results was plotted in the same manner (fig. 4.3.6). A positive correlation was also seen when current density was plotted against the reciprocal of crystal surface area (fig. 4.3.18 - 4.3.20).

The data for the single crystal electrodes in the hanging meniscus configuration, after being coated in CO (which had been stripped from the planar surface by electro-oxidation) (fig. 4.3.16) followed a similar trend to the clean flame annealed surfaces. The absolute current density values were significantly lower than those for the annealed surfaces, despite the CVs matching well (excluding that of Pt{311} which invariably reconstructed significantly after being coated with CO, see fig. 4.3.21).

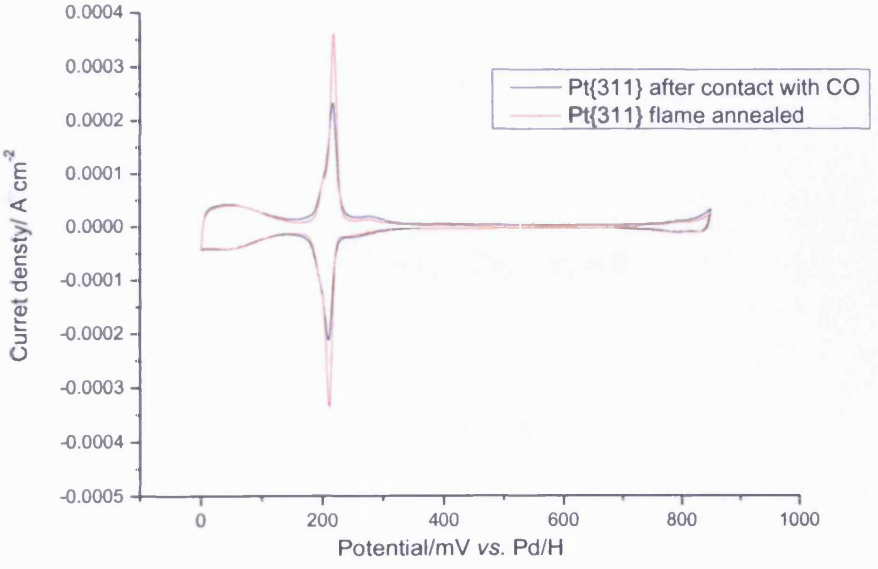

Fig. 4.3.21 Pt{311} in hanging meniscus configuration (0.5 M H_2SO_4, 0.05 V s^{-1}) when flame annealed (red line) and reconstruction after coating with CO (black line).

When the crystal bead was partially submerged into the solution (still with CO coating the hemisphere), no significant trend was observed for current density versus step density or 1/area, i.e. current density was found to be independent of both of these parameters in this configuration.

4.3.2.1 Fitting rate constants to single crystal Tafel data

A fitting routine (using a prewritten routine in MatLab, shown in appendix I) was applied to the Tafel data for each of the stepped single crystal electrodes tested in sections 4.3.1 and 4.3.2. The program adjusted the rate constants for the forward and backward reactions associated with the appropriate HER mechanism (from initially inputted figures); i.e. the Volmer-Tafel mechanism for Pt (giving k_1 and k_{-1} from equation (4.3.7) and k_2 and k_{-2} from equation (4.3.8)). Using equations (4.3.7) – (4.3.9),

$$\text{Volmer: } v_1 = k_1 C^*_{H^+}(1-\theta_H)e^{-\alpha f\eta} - k_{-1}\theta_H e^{(1-\alpha)f\eta} \quad \text{(I)} \quad \textbf{(4.3.7)}$$

$$\text{Tafel: } v_2 = k_2\theta_H^{\,2} - k_{-2}(C^{\sigma}_{H_2}/C^*_{H_2})(1-\theta_H)^2 \quad \text{(II)} \quad \textbf{(4.3.8)}$$

$$\text{Heyrovsky: } v_3 = C^*_{H^+}\theta_H e^{-\alpha f\eta} - k_{-3}(C^{\sigma}_{H_2}/C^*_{H_2})(1-\theta_H)e^{(1-\alpha)f\eta} \quad \text{(III)} \quad \textbf{(4.3.9)}$$

where the parameters are defined in section 1.2.

At steady state:

$$\frac{\partial\theta_H}{\partial t} = v_1 - 2v_2 - v_3 = 0 \qquad \textbf{(4.3.10)}$$

$$\frac{dC_{H_2}}{dt} = v_2 + v_3 = 0 \qquad \textbf{(4.3.11)}$$

Combining (4.3.10) and (4.3.11) gives:

$$v_1 - v_2 = 0 \qquad \textbf{(4.3.12)}$$

Substituting in (4.3.7) and (4.3.8) for v_1 and v_2 gives:

$$C^*_{H^+}k_1(1-\theta_H)\exp\left[\frac{-\alpha nF}{R_gT}E\right] - k_{-1}\theta_H\exp\left[\frac{(1-\alpha)nF}{R_gT}E\right] = k_2\theta_H^{\,2} - k_{-2}(1-\theta_H)^2(C^{\sigma}_{H_2}/C^*_{H_2}) \qquad \textbf{(4.3.13)}$$

which can be rearranged to give a quadratic in terms of θ_H:

$$a\theta_H^{\ 2} + b\theta_H + c = 0 \qquad \textbf{(4.3.14)}$$

where:

$$a = k_{-2}(C^{\sigma}_{H_2} / C^{*}_{H_2}) - k_2 \qquad \textbf{(4.3.15)}$$

$$b = \left\{ C^{*}_{H^+} k_1 \exp\left[\frac{-\alpha n F}{R_g T} E \right] + 2k_{-2}(C^{\sigma}_{H_2} / C^{*}_{H_2}) \right\} \qquad \textbf{(4.3.16)}$$

$$c = C^{*}_{H^+} K_1 \exp\left[\frac{-\alpha n F}{R_g T} E \right] + k_{-2}(C^{\sigma}_{H_2} / C^{*}_{H_2}) \qquad \textbf{(4.3.17)}$$

Solving this quadratic and inputting the relevant parameters, the isotherm in fig. 4.3.22 is achieved.

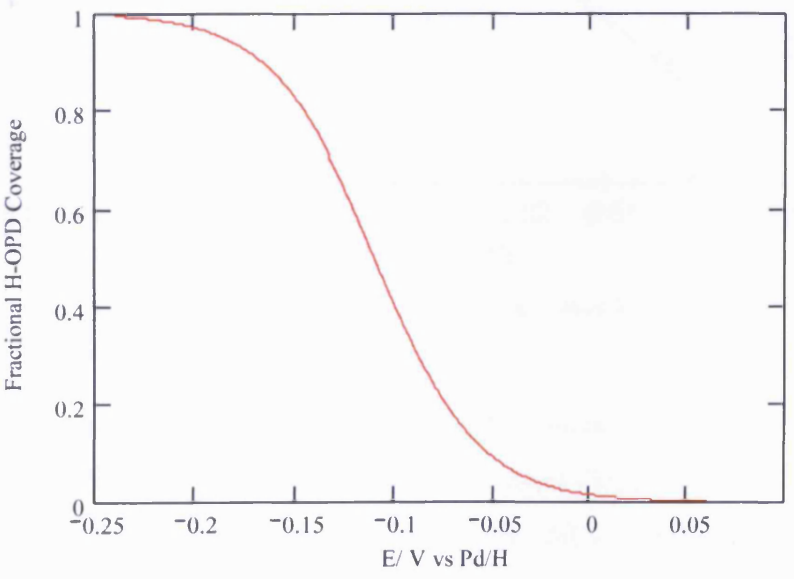

Fig. 4.3.22 Simulated isotherm for OPD-H surface coverage as a function of potential on a Pt electrode in 0.5 M H_2SO_4, using parameters; $\alpha = 0.5$, $k_1 = 1.3 \times 10^{-3}$, $k_{-1} = 5.4 \times 10^{-4}$, $k_2 = 1.59 \times 10^{-8}$, $k_{-2} = 7.42 \times 10^{-21}$ and $(C^{\sigma}_{H_2} / C^{*}_{H_2}) = 1$.

The quality of the Tafel data fitting for hydrogen evolution on a Pt surface is shown in fig. 4.3.23, the fit result converging to the actual data in the hydrogen evolution region. The Volmer-Tafel-Heyrovsky fitting routine also converged well to the Pt data but gave unreasonably high Heyrovsky values implying that the Heyrovsky kinetics dominate the rate of the reaction which is not true for Pt. Simply inputting low values for the Heyrovsky term in this fitting routine would not allow the fit to converge to the actual data, hence the Heyrovsky term had to be completely omitted (by using the Volmer-Tafel fitting routine) to obtain a reasonable result.

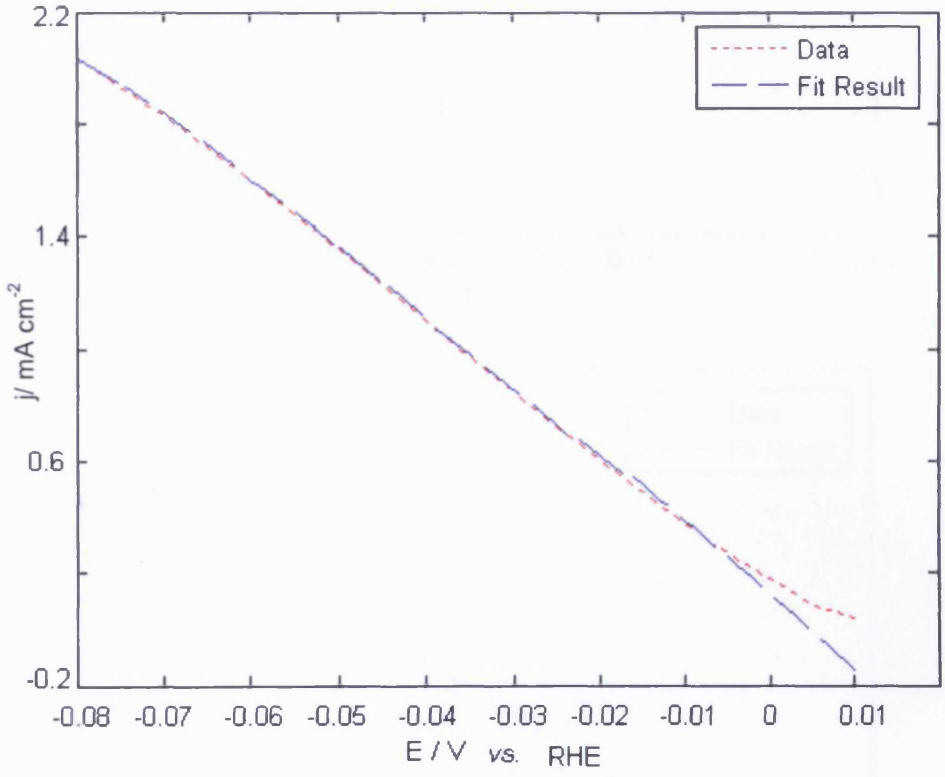

Fig. 4.3.23 Volmer-Tafel fitting routine for hydrogen evolution on Pt in 0.5 M H_2SO_4.

Similarly, the Volmer-Tafel and Volmer-Tafel-Heyrovsky fitting routines were both applied to Au (which is known to follow the Volmer-Heyrovsky mechanism). Fig. 4.3.24 shows (a) the Volmer-Tafel routine, which did not converge well to the Au surface data (and would therefore not be used for results purposes) and (b) the Volmer-Tafel-Heyrovsky routine which gave a very good fit.

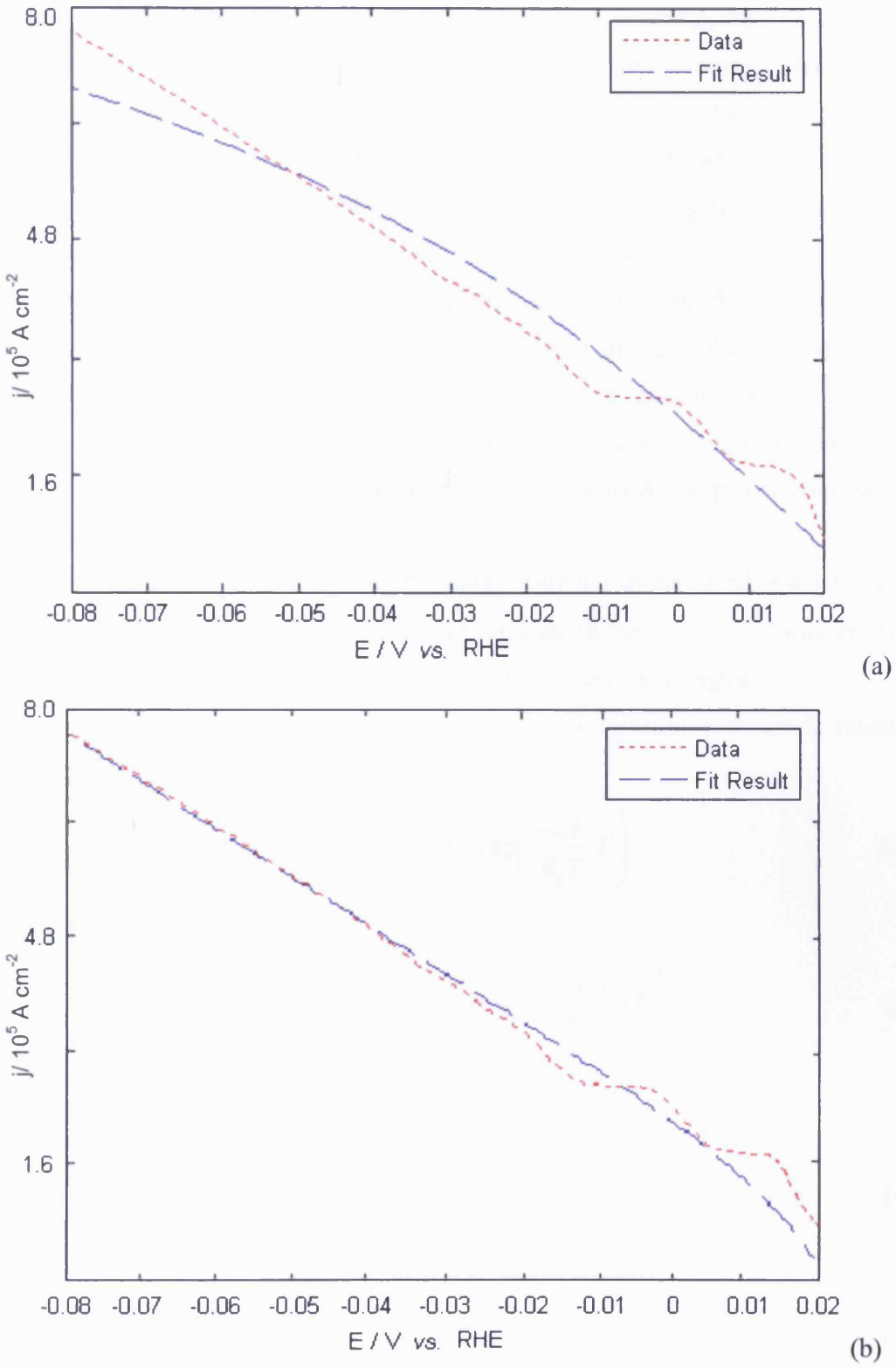

Fig. 4.3.24 Data fitting for hydrogen evolution (current density versus RHE potential) on a Au surface (which is known to adopt the Volmer-Heyrovsky mechanism) in 0.5 M H_2SO_4, using (a) Volmer-Tafel and (b) Volmer-Tafel-Heyrovsky fitting routines.

The OPD-H surface coverage plot, as a function of potential, may be automatically generated from the rate constants calculated from the fitting routine. Hence, it can act as an indicator as to whether the fitting routine has yielded credible values. Therefore a high value of Heyrovsky rate constant, k_3, may give data which fits well with the linear sweep voltammograms, yet the surface hydrogen coverage may be inappropriately low (< 0.3 monolayers). This would lead to the result being discarded and a different set of initial rate constant figures entered into the routine. The initial rate constant figures inputted may lead to different fitting of the data, so the OPD-H surface coverage is a useful tool in the deduction of genuinely acceptable rate constant values. In the case of the Pt stepped single crystals, which are known to adopt the Volmer-Tafel HER mechanism, the Heyrovsky step was eliminated from the fitting routine.

The figures for k_1, k_{-1} and k_2 from the data fitting are shown in table 4.3.3 – 4.3.5, k_{-2} has not been displayed in these tables (or throughout this thesis) as it was so small that it was effectively zero, hence the absolute values were meaningless.

The ratio of k_1 and k_{-1} gives the Volmer reaction equilibrium constant K_1 (assuming α is approximately 0.5) as:

$$k_1 = k_1^0 \exp\left(\frac{-\alpha F}{R_g T} E\right) \qquad \textbf{(4.3.18)}$$

and

$$k_{-1} = k_{-1}^0 \exp\left(\frac{(1-\alpha) F}{R_g T} E\right) \qquad \textbf{(4.3.19)}$$

Therefore, when K is defined as:

$$K_1 = \frac{k_1^0}{k_{-1}^0} \qquad \textbf{(4.3.20)}$$

If $\alpha = 0.5$, it is fair to assume that at any given potential:

$$K_1 = \frac{k_1}{k_{-1}} \qquad \textbf{(4.3.21)}$$

Similar ratios of the Tafel and Volmer rate constants give equilibrium constants K_2 and K_3 respectively.

	k_1/ 10^{-3} cm s^{-1}	k_{-1}/ 10^{-4} mol cm^{-2} s^{-1}	k_2/ 10^{-8} cm s^{-1}
Pt{111}	1.31	5.44	1.59
Pt{755}	1.52	4.78	1.31
Pt{533}	1.18	4.35	1.81
Pt{211}	0.06	0.32	1.76
Pt{311}	0.07	0.29	1.26
Pt{511}	0.42	1.19	1.10
Pt{711}	1.49	4.35	1.60
Pt{911}	1.40	5.00	1.33
Pt{11,1,1}	1.36	4.95	1.55
Pt{13,1,1}	0.71	2.43	1.44
Pt{100}	1.61	3.54	1.06

Table 4.3.3 Volmer-Tafel data for stepped single crystal electrodes, flame annealed and held in the hanging meniscus configuration in 0.5 M H_2SO_4.

	k_1/ 10^{-2} cm s^{-1}	k_{-1}/ 10^{-2} mol cm^{-2} s^{-1}	k_2/ 10^{-8} cm s^{-1}
Pt{111}	2.07	1.09	2.23
Pt{755}	2.21	1.03	2.28
Pt{533}	2.74	0.74	1.10
Pt{211}	2.61	1.70	2.56
Pt{311}	2.60	1.68	2.60
Pt{511}	2.63	1.61	2.63
Pt{711}	2.37	0.83	1.14
Pt{911}	2.12	0.92	1.65
Pt{11,1,1}	2.22	1.09	2.38
Pt{13,1,1}	2.22	1.12	2.27
Pt{100}	3.25	0.89	1.32

Table 4.3.4 Volmer-Tafel data for stepped single crystal electrodes, CO coated and stripped, held in the hanging meniscus configuration in 0.5 M H_2SO_4.

	k_1/ 10^{-3} cm s^{-1}	k_{-1}/ 10^{-3} mol cm^{-2} s^{-1}	k_2/ 10^{-8} cm s^{-1}
Pt{111}	0.35	0.19	1.94
Pt{755}	30.62	12.8	2.08
Pt{533}	0.18	0.06	1.07
Pt{211}	0.12	0.07	1.62
Pt{311}	0.20	1.12	2.05
Pt{511}	0.16	0.09	1.84
Pt{711}	31.75	5.72	0.35
Pt{911}	24.81	14.24	2.12
Pt{11,1,1}	5.42	3.21	2.66
Pt{13,1,1}	5.07	3.15	2.99
Pt{100}	0.53	0.19	2.47

Table 4.3.5 Volmer-Tafel data for stepped single crystal electrodes, with CO coated hemisphere, submerged below the electrolyte surface in 0.5 M H_2SO_4.

The rate constants for the forward and backward Volmer reactions were plotted against exchange current density, the reciprocal of the surface area and the crystal step density for the three electrode configurations. The same was done for the forward Tafel rate constants. None of the plots showed a significant positive correlation.

4.3.3 Pt{111} crystals of different sizes

A simple experiment was performed to investigate whether the exchange current density on Pt single crystal electrodes was related to crystal structure or electrode area. A second, larger, Pt{111} crystal was manufactured (section 3.4) and tested in the same way as previously stated (section 3.6). It was found that the larger crystal gave significantly lower exchange current density than the smaller one used throughout the rest of section 4.3.

Pt{111} Crystal Area/ cm^2	Crystal Circumference/ cm	Circumference/Area Ratio/ cm^{-1}	Exchange Current Density/ mA cm^{-2}
0.029	0.60	20.8	0.82
0.049	0.74	17.1	0.59

Table 4.3.6 Comparing data for two Pt{111} crystals, clean, flame annealed in 0.5 M H_2SO_4.

Referring to table 4.3.6, it can be seen how the crystal exchange current density is affected by edge/area ratio for two clean, flame annealed Pt{111} electrodes. The smaller electrode has an edge/area ratio 1.22 times greater than the larger electrode and j_0 value 1.39 times greater.

4.3.4 Pt{110} and different cooling methods

Previous work from Lipkowski[7] and Feliu[8] proposed that there is no crystallographic structural dependence for the HER. However, the Feliu group quote values of exchange current density on Pt{110} higher than those on Pt{111} and Pt{100} (0.97 mA cm^{-2} c.f. 0.84 mA cm^{-2} and 0.84 mA cm^{-2} respectively) despite not declaring it in relation to a structure sensitivity for HER.

Incidentally, other works which have discovered a dependence for HER on single crystal surface structure[4, 9] , also quote the Pt{110} surface as the fastest for HER

under acidic conditions (as well as HOR in acid[10] and both HER and HOR in alkaline solutions[11]). One explanation for this may be different cooling methods used after flame annealing. This is particularly relevant to the Pt{110} surface as different cooling methods may result in different reconstructed phases of the surface. When heated in a Bunsen flame and cooled in CO the Pt{110} electrode will give a (1x1) surface; whereas if cooled in H_2 it will reconstruct in a (1x2) configuration[12]. In light of this, a Pt{110} crystal bead was tested in the same manner as those above (in hanging meniscus, CO stripped hanging meniscus and CO coated submerged bead). The crystal was flame annealed and cooled in CO and H_2 to test the difference in (1x1) and (1x2) reconstruction.

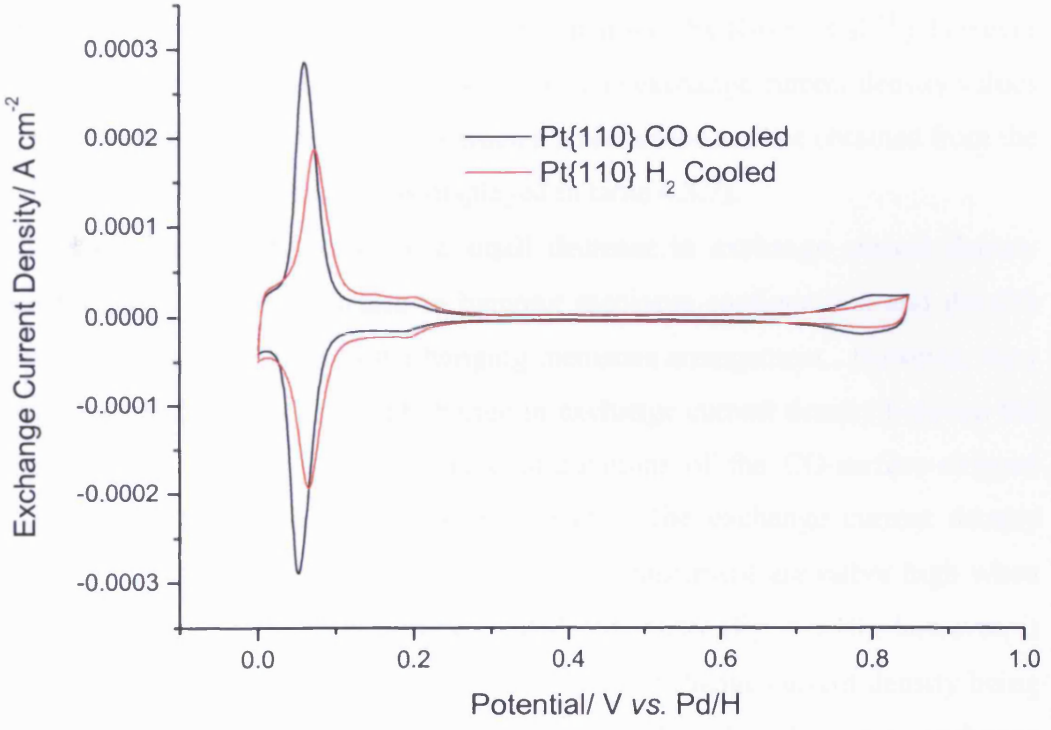

Fig. 4.3.25 CVs of Pt{110} crystal (0.098 cm^2) cooled in CO and H_2. 0.5 M H_2SO_4, 0.05 V s^{-1}.

	Exchange Current Density/ mA cm^{-2}		
Crystal Area/ Cooling Method	Hanging Meniscus	CO stripped Hanging Meniscus	CO coated Submerged Bead
0.098/CO	0.58	0.52	0.52
0.098/H_2	0.58	0.52	0.51

Table 4.3.7 Exchange current densities relating to Pt{110} with different cooling techniques and held in different conformations in 0.5 M H_2SO_4.

The CO cooling approach did not give a perfect (1x1) surface, nor did the H_2 cooled give a perfect (1x2) reconstruction (compared to that seen by Kibler et al[13]), however the two CVs were clearly different (fig. 4.3.25). The exchange current density values were not affected by the different reconstructed states of the surface obtained from the different cooling methods (the data is displayed in table 4.3.7).

Both structures of the crystal show a small decrease in exchange current density between the clean annealed surface in hanging meniscus configuration and the CO blocked-surface stripped bead in the hanging meniscus arrangement. However, they also both show little or insignificant change in exchange current density between the hanging meniscus and submerged bead configurations of the CO-surface-stripped electrode (with hemisphere still blocked by CO). The exchange current density values for the electrode in the hanging meniscus arrangement are rather high when compared to the single crystal electrodes tested previously (fig. 4.3.18), however, it could be easily argued that they support the trend of exchange current density being inversely proportional to electrode area. The submerged bead configuration exchange current density value fits well with the previous single crystal work in section 4.3.2.

The absolute exchange current density values were low with respect to those quoted in the literature; Markovic quotes a value of 0.98 mA cm^{-2} [4] (303 K), Feliu *et al.* quote 0.97 mA cm^{-2} [14].

4.4 Surface modified Pt{*hkl*} electrodes

4.4.1 Epitaxial single crystal metal films

Thick films of Rh, Pd and Ru were deposited onto a Pt{111} electrode as described in section 3.5. When annealed, they gave CVs analogous to the equivalent metal {111} surface ({0001} in the case of hcp Ru) (fig. 4.4.1), in good agreement with those seen in the literature[8, 15-19] (fig. 4.4.2). It can be seen that the Pd surface is more similar to a semi-thick film deposited on Pt from Markovic *et al*[16] (fig. 4.4.2 (b)) than bulk Pd{111} (fig. 4.4.2 (c)).

Linear sweep voltammetry (LSV) was then performed on these films (fig. 4.4.3) to give a qualitative trend as to which gave the fastest kinetics for the HER. The tests were performed using fast sweep rates to avoid contamination, sweeping the potential to -0.4 V *vs.* Pd/H at 0.5 V s^{-1}. In addition to Rh, Pd and Ru, Bi was also deposited onto Pt{111} (as described in section 3.5) and tested for HER in the same manner.

Bare Pt and Ru on Pt gave the steepest current density versus potential slopes with Pd on Pt exhibiting a significantly lower activity. The Bi and Rh covered surfaces then gave a quite different shaped plot compared to the others; the HER was forced to more negative potentials and the rate of HER rate was significantly reduced. It can also be seen that the region just positive of hydrogen evolution is a much shallower curve for Bi/Pt{111} (less so for Rh{111}) than that of the other Pt-like metals.

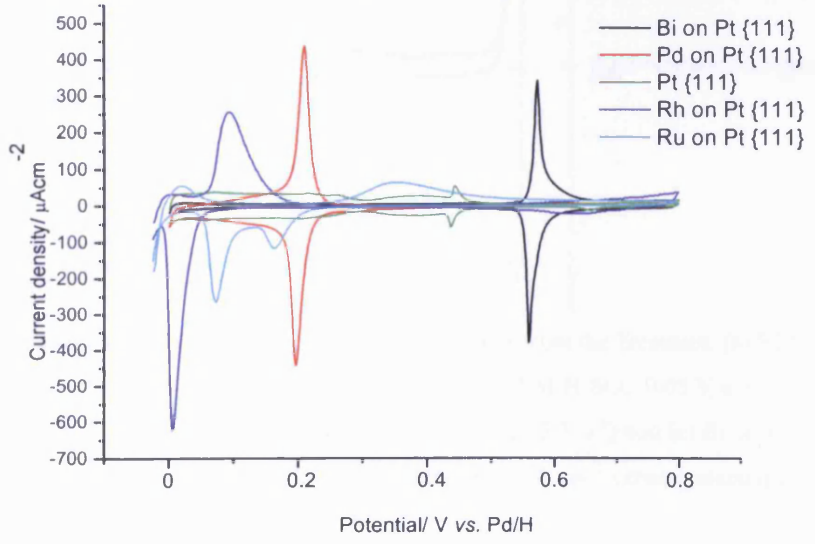

Fig. 4.4.1 CVs of bare Pt{111} and Pt{111} coated with films of Ru, Rh, Bi and Pd. In 0.1 M H_2SO_4 at a sweep rate of 0.05 V s^{-1}.

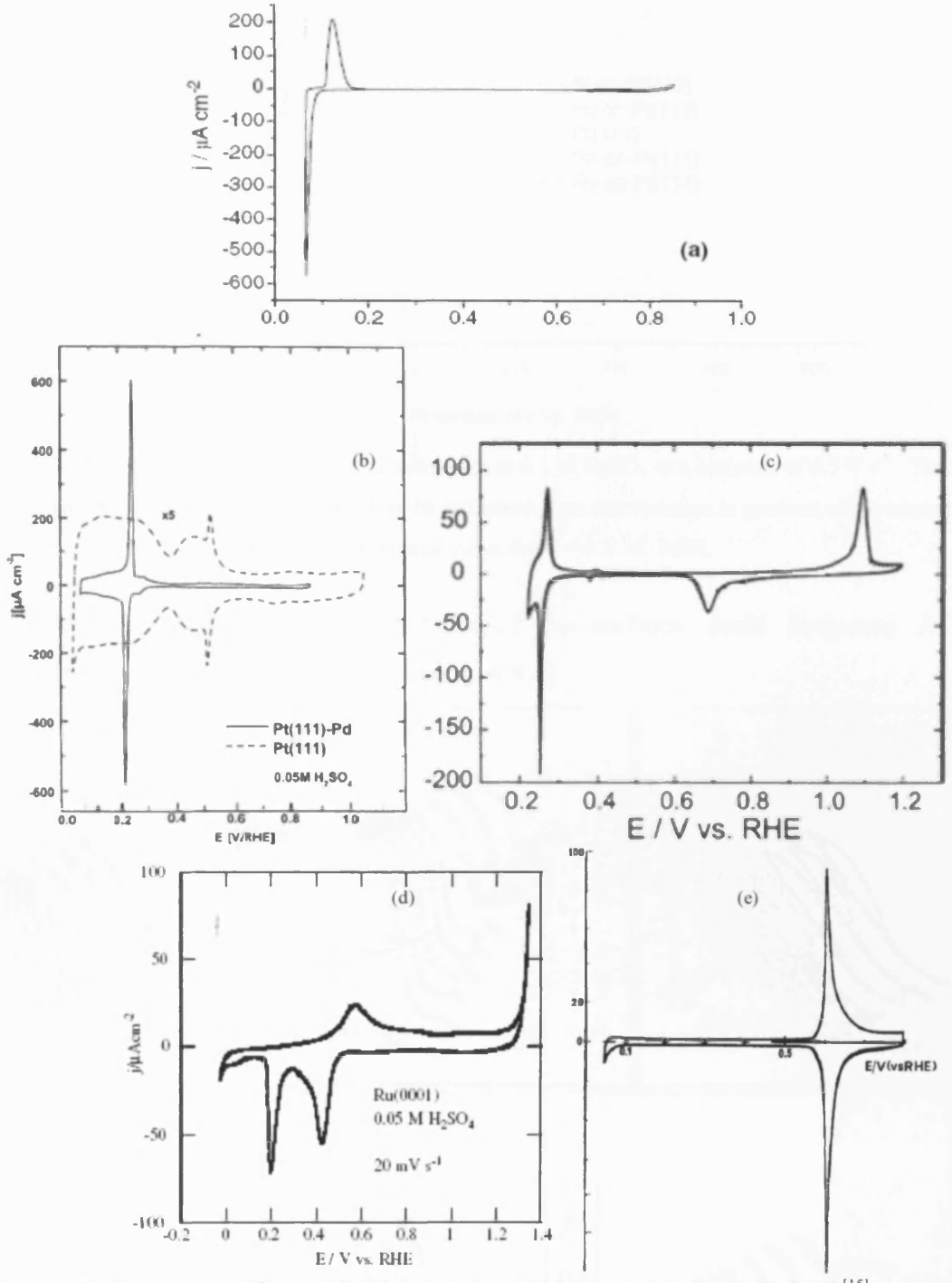

Fig. 4.4.2 Examples of CVs from well-defined electrodes from the literature. (a) Rh{111}[15] (0.5 M H_2SO_4, 0.02 V s^{-1}), (b) Pt{111} and Pd on Pt{111}[16] (0.05 M H_2SO_4, 0.05 V s^{-1}), (c) Pd{111}[19] (0.1 M H_2SO_4, 0.01 V s^{-1}) (d) Ru{0001}[17] (0.05 M H_2SO_4, 0.02 V s^{-1}) and (e) Bi on Pt{111}[18] (0.5 M H_2SO_4, 0.02 V s^{-1}). All figures plot current density in μA cm^{-2} versus potential in V *vs.* RHE.

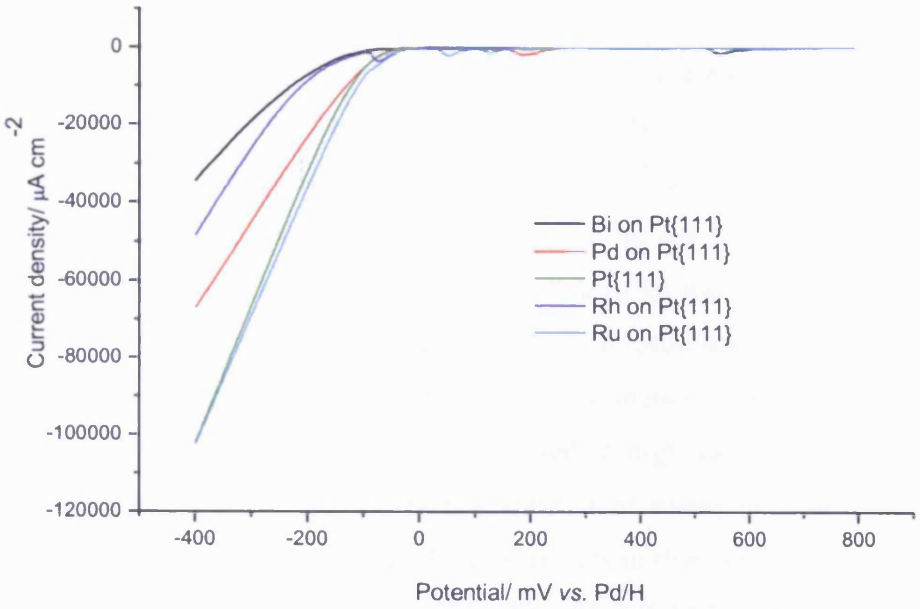

Fig. 4.4.3 LSVs for the various surfaces investigated, in 0.1 M H_2SO_4 at a scan rate of 0.5 V s^{-1}. The relative rate of the HER for each surface may be estimated from the variation in gradient of the current density versus potential curve for E < 0 V *vs.* Pd/H.

After obtaining good CV data for each of the surfaces, multi frequency AC voltammograms (MFACVs) were taken (fig. 4.4.4).

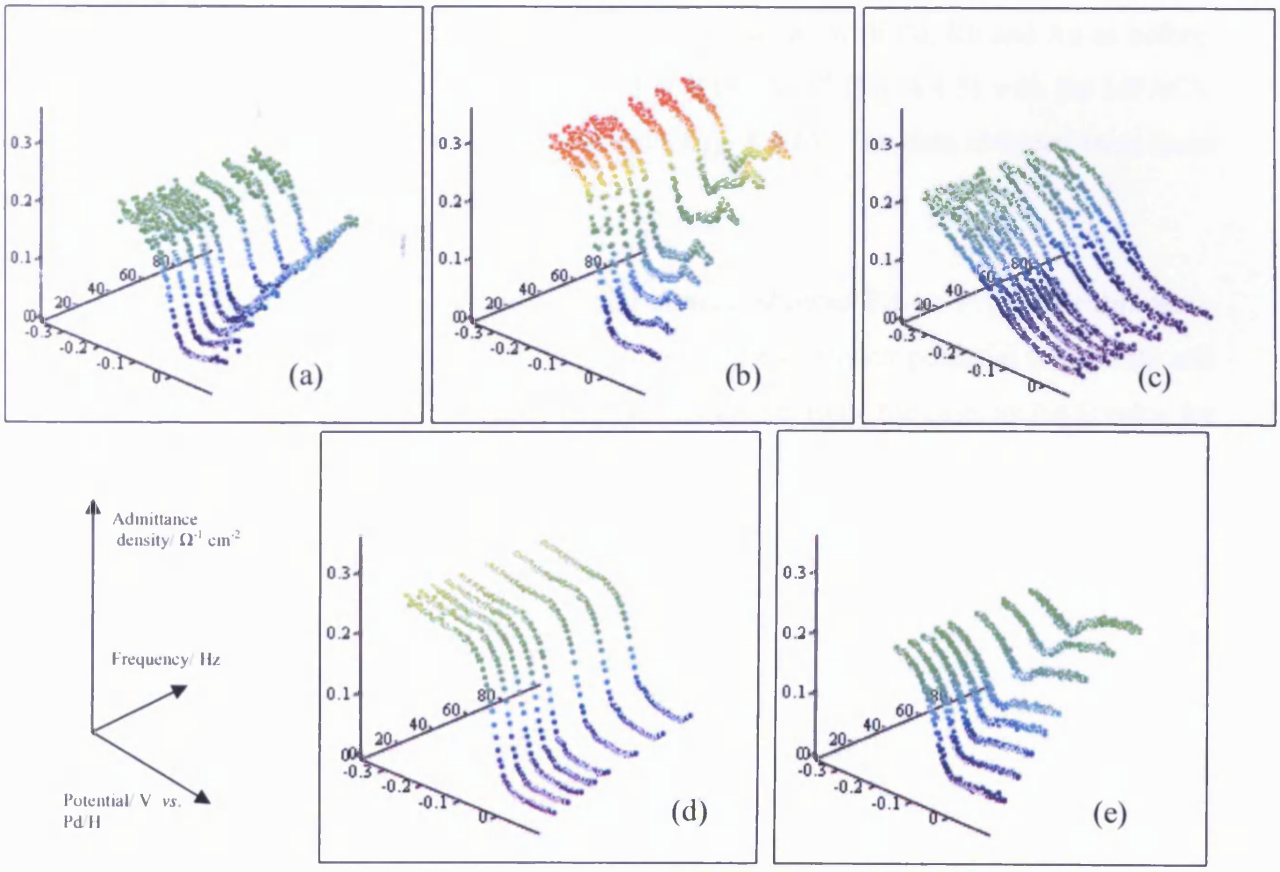

Fig. 4.4.4 MFACVs performed on (a) Pd on Pt{111}, (b) bare Pt{111}, (c) Rh on Pt{111}, (d) Ru on Pt{111} and (e) Bi on Pt{111}.

was intermediate between the Bi and Ru limiting admittance density values. It should be remembered that the LSV data were collected at high sweep rates, whereas the MFACVs were not (0.00125 V s^{-1}). Hence, the role of anions in controlling electron transfer rate is also highlighted in the MFACV results in that at lower sweep rates, the LSV data do not correlate with MFACV. The Rh MFACV gave a very different shape to that of the other surfaces as it had to be swept to very negative potentials before it reached a "plateau". In fact, only the Rh film could be taken as negative as -0.3 V. When the other electrodes are swept to -0.3 V *vs.* Pd/H, too much hydrogen is produced, leading to blocking of the electrode surface, due to gas bubbles forming.

The results in 0.5 M H_2SO_4, under steady state conditions proved to be somewhat different. In this test, Pt{111} was coated once again with Pd, Rh and Au as before. However, the LSV was now carried out at 0.005 V s^{-1} (fig. 4.4.5) with the MFACV data carried out under the usual conditions (fig. 4.4.6). The data obtained from these experiments is shown in table 4.4.1.

The data in fig. 4.4.3, though not quantitative, showed Pd on Pt{111} exhibited a faster HER rate than Rh on Pt{111}. However, with slower potential sweep rate and higher electrolyte concentration, this does not appear to be the case, as the j_0 value for Rh is twice that for Pd.

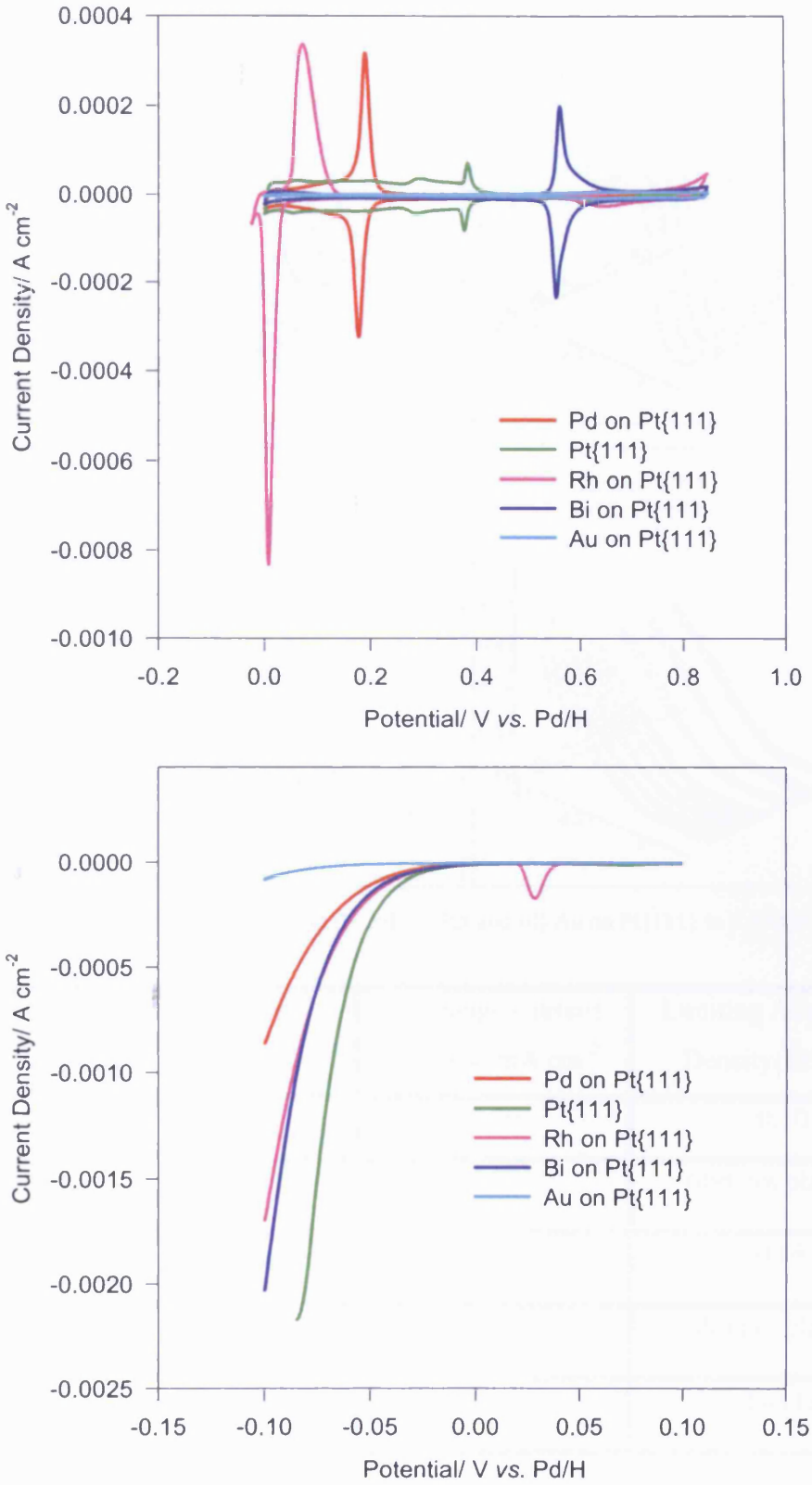

Fig. 4.4.5 CVs and LSVs of Pt{111} and Pd, Rh and Au on Pt{111} in 0.5 M H_2SO_4. The potential sweep rates of the CVs and LSVs were 0.05 V s^{-1} and 0.05 V s^{-1} respectively.

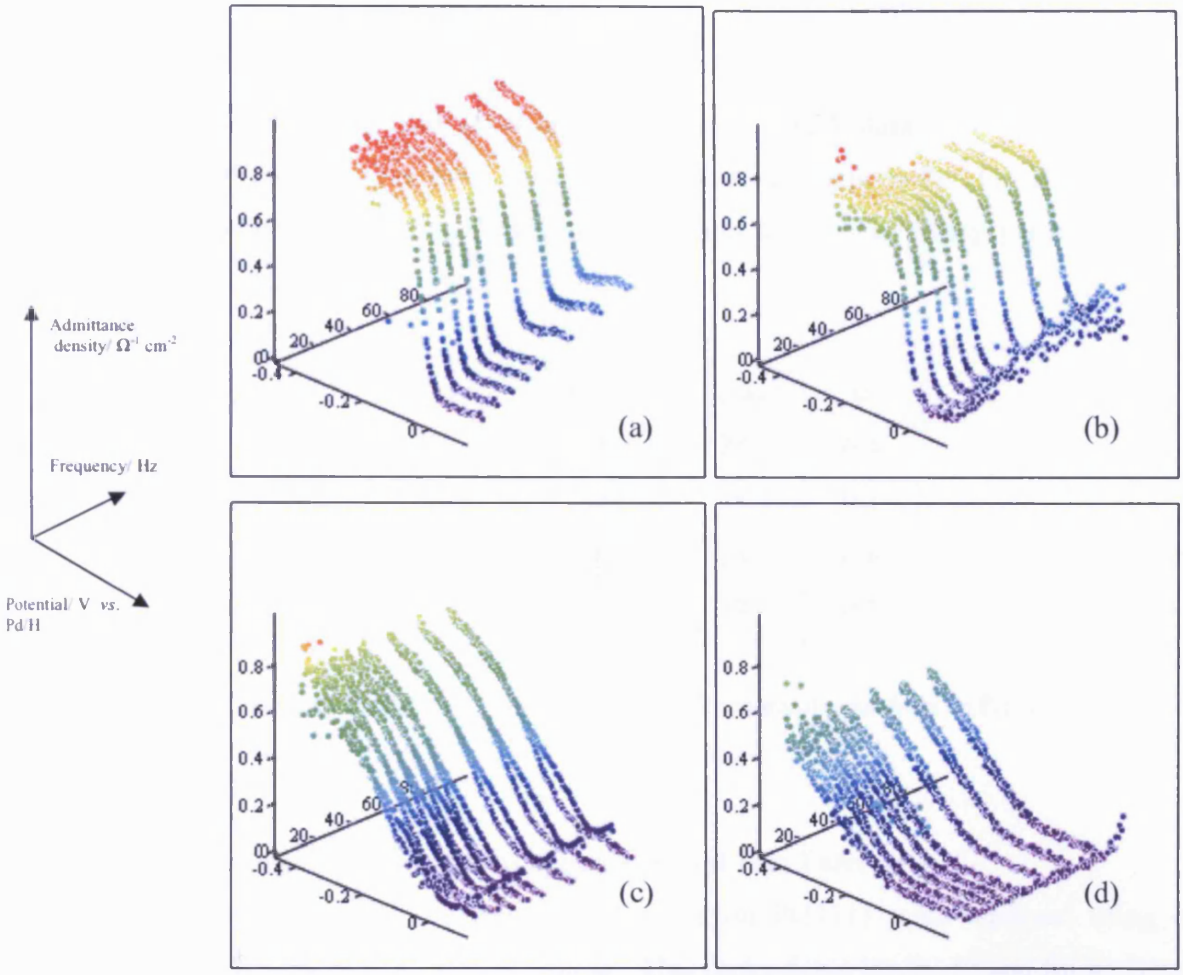

Fig. 4.4.6 MFACV of (a) Pt{111} and (b) Pd, (c) Rh and (d) Au on Pt{111} in 0.5 M H_2SO_4.

	Tafel Slope/ mV/dec	Exchange Current Density/ mA cm^{-2}	Limiting Admittance Density/ Ω^{-1} cm^{-2}
Pt{111}	31.5	0.59	0.10
Au on Pt{111}	45.4	0.03	(did not plateau)
Pd on Pt{111}	44.4	0.14	0.08
Rh on Pt{111}	35.5	0.28	(did not plateau)
Bi on Pt{111}	33.4	0.28	(no data taken)

Table 4.4.1 Showing HER data for films on Pt{111} under steady state conditions.

4.4.1.1 Model circuit analysis of epitaxial films MFACV data

The model circuits were fitted for the epitaxial metal films on Pt{111} as described for the stepped single crystal surfaces in section 4.3.1. The fitting parameters are shown in table 4.4.2.

	R_0/ Ω	R_s/ Ω	α
Pt	2080	23	0.4
Rh	200	25	0.1
Pd	2000	28	0.6
Au	4000	37	0.2

Table 4.4.2 Model circuit fitting parameters for epitaxial metal films on Pt{111}.

4.4.1.2 Fitting rate constants to epitaxial metal film Tafel data

The Tafel data for the epitaxial metal films on Pt{111} were analysed using a Volmer-Tafel-Heyrovsky fitting routine. This broke down for the Pt and Rh surfaces (giving a low H-surface coverage isotherm), so they were refitted using a Volmer-Tafel routine with no Heyrovsky component. The data obtained is shown in table 4.4.3.

	k_1/ cm s^{-1}	k_{-1}/ mol cm^{-2} s^{-1}	k_2/ cm s^{-1}	k_3/ cm s^{-1}
Au on Pt{111}	1.12×10^{-6}	2.56×10^{-7}	1.08×10^{-16}	4.66×10^{-6}
Pd on Pt{111}	4.08×10^{-5}	9.33×10^{-6}	8.50×10^{-7}	5.24×10^{-5}
Pt{111}	2.03×10^{-2}	6.48×10^{-3}	2.38×10^{-7}	--
Rh on Pt{111}	1.68×10^{-2}	1.79×10^{-3}	2.32×10^{-8}	--

Table 4.4.3 Volmer-Tafel-Heyrovsky data for epitaxial films on Pt{111} in 0.5 M H_2SO_4 at 0.005 V s^{-1}.

4.4.2 Ir deposited onto Pt{111}

Ir proved difficult to deposit onto Pt using the hydrogen reduction (forced deposition) method. Consequently, a droplet of aqueous H_2IrCl_6 was contacted with the crystal bead and "flash" reduced onto the surface by exposure to a Bunsen flame (section 3.5). This gave a very rough, Ir deposit (single crystalline Ir CV responses could not be achieved with further annealing or resistive heating in N_2). These Ir deposits gave fast HER rates (well above any expected increase due to a small increase in area). As Ir was removed by heating gently in the Bunsen flame and cooling in H_2, the HER rate did not decrease systematically. CVs of the Ir on Pt{111} surfaces are shown in fig. 4.4.7, whilst the associated LSVs are shown in fig. 4.4.8.

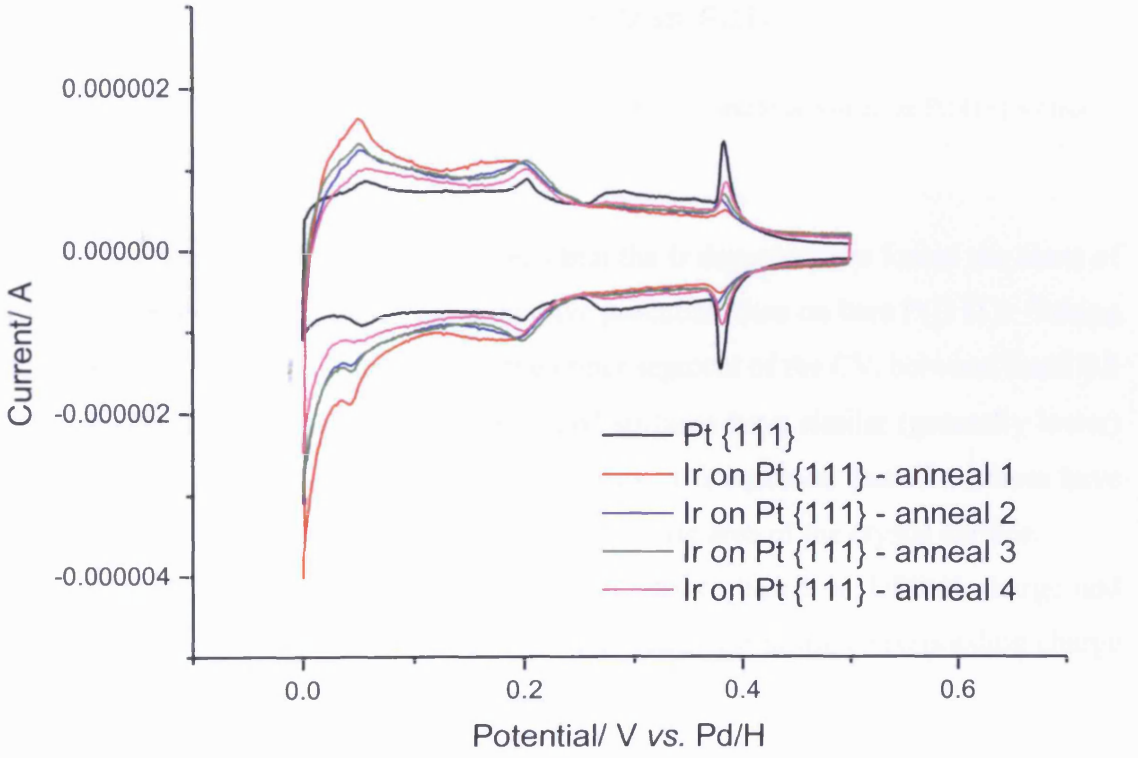

Fig. 4.4.7 CVs of Pt{111} and Ir deposits on Pt{111} in decreasing amounts due to removal by flaming gently. 0.5 M H_2SO_4, 0.05 V s^{-1}.

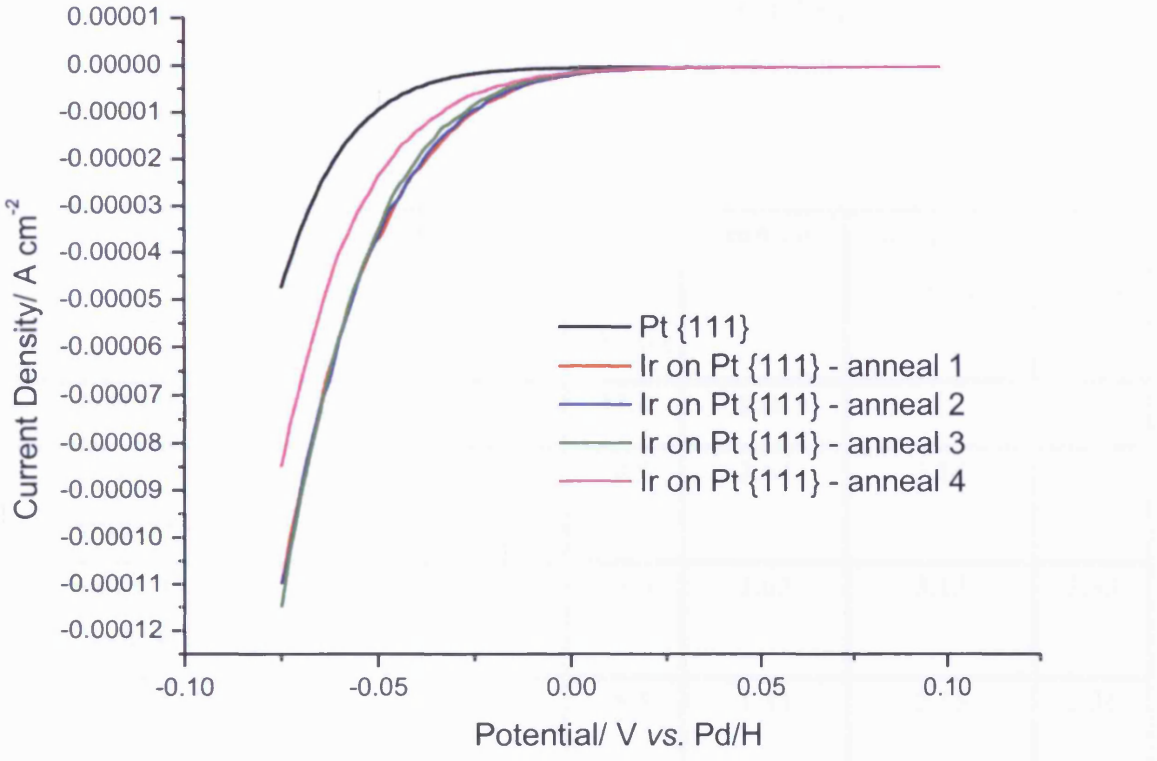

Fig. 4.4.8 LSV into hydrogen evolution region for bare Pt{111} and Ir deposited on Pt{111} surfaces. 0.5 M H_2SO_4, 0.005 V s^{-1}.

From the CVs in fig. 4.4.7, it can be seen that the Ir deposits have forced the onset of hydrogen evolution to occur at more positive potentials than on bare Pt{111}. Taking the charge under the CV graph (using the upper segment of the CV, between 0 and 0.5 V *vs.* Pd/H) it can be seen that the Ir coated surfaces have similar (generally lower) charge than bare Pt, so for further data analysis, it is assumed that all surfaces have the same area, which has been taken as the geometric area of the crystal surface.

Charge densities, σ, were calculated for each surface based on UPD-H charge and geometrical surface area of the electrode. The ratio of σ to the corresponding charge density on Pt{111}, $\sigma_{Pt\{111\}}$, was defined as

$$\frac{\sigma}{\sigma_{Pt\{111\}}} = A_{\sigma} \qquad \textbf{(4.4.1)}$$

In a similar manner, the exchange current density, j_0, for each surface was evaluated based on the geometrical area of the electrode. The ratio of j_0 to the exchange current density from Pt{111}, $j_{0Pt\{111\}}$ was evaluated as

$$\frac{j_0}{j_{0Pt\{111\}}} = B_j \qquad \textbf{(4.4.2)}$$

Hence, the ratio of B_j to A_σ allowed a simple comparison of the intrinsic capability of the Ir surfaces to promote HER over and above that of clean Pt{111}. This data analysis is presented in table 4.4.4.

	σ/ μC cm^{-2}	$\sigma/\sigma_{Pt\{111\}} = (A_\sigma)$	Tafel Slope/ mV/dec	j_0/ mA cm^{-2}	$j_0/j_{0Pt\{111\}} = (B_j)$	B_j/A_σ ratio
Pt{111}	**241**	**1**	**33.6**	**0.84**	**1**	**1**
Ir on Pt{111} –anneal 1	**267**	**1.11**	**34.9**	**2.64**	**3.14**	**2.82**
Ir on Pt{111} – anneal 2	**220**	**0.91**	**36.0**	**2.63**	**3.13**	**3.43**
Ir on Pt{111} – anneal 3	**220**	**0.91**	**35.5**	**1.81**	**2.15**	**2.36**
Ir on Pt{111} – anneal 4	**208**	**0.86**	**37.0**	**1.05**	**1.25**	**1.45**

Table 4.4.4 Data for Ir deposited onto Pt{111}.

The data in table 4.4.4 shows an increase in HER over and above that directly related to area for Ir/Pt{111} electrodes..

4.4.2.2 Fitting rate constants to Ir modified Pt Tafel data

Rate constants for the Volmer-Tafel HER mechanism were fitted to the Ir on Pt data in a similar manner to that described for the Pt single crystal surfaces in section 4.3.2.1 (shown in table 4.4.5). It was observed that the Tafel rate constant did not vary significantly with the exchange current density of the five surfaces (the backward Tafel rate constant was insignificantly small). The Volmer forward and backward rate constants showed an interesting trend in that those for the Ir modified Pt surfaces increased quite linearly with exchange current density. However k_1 and k_{-1} for the bare Pt{111} surface do not fit with the trend as the values (for both forward and backward rate constant) are higher than on the Ir surfaces (fig. 4.4.9).

	k_1/ 10^{-3} cm s^{-1}	k_{-1}/ 10^{-4} mol cm^{-2} s^{-1}	k_2/ 10^{-9} cm s^{-1}
Pt{111}	2.34	3.37	3.07
Ir on Pt{111} –anneal 1	2.04	1.15	2.35
Ir on Pt{111} – anneal 2	2.00	1.18	2.42
Ir on Pt{111} – anneal 3	1.58	1.12	2.91
Ir on Pt{111} – anneal 4	0.95	0.72	2.24

Table 4.4.5 Volmer-Tafel data for Ir deposited on Pt{111} in 0.5 M H_2SO_4.

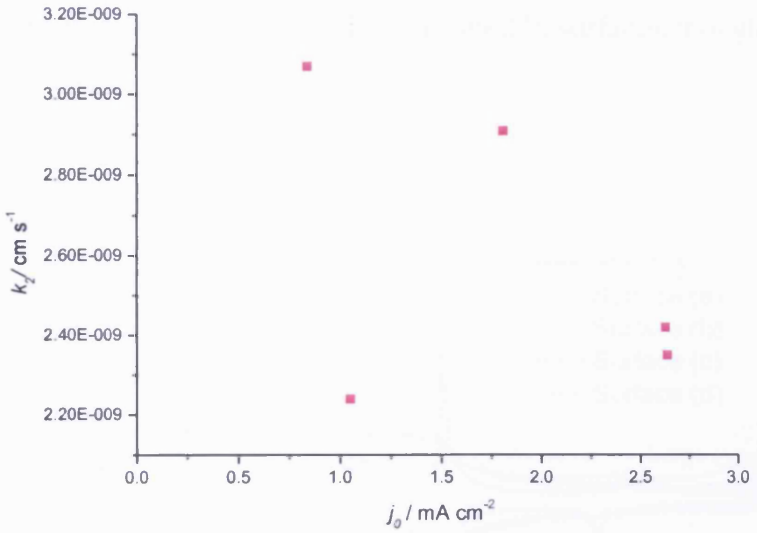

(a)

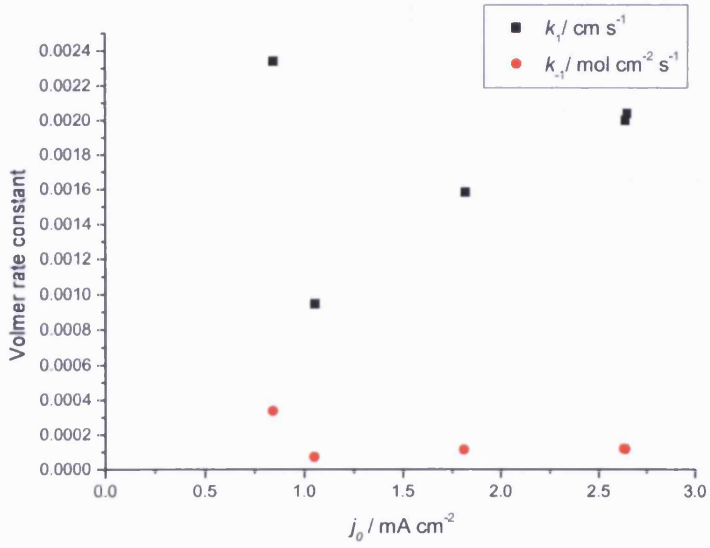

(b)

Fig. 4.4.9 Graphs of (a) k_2 and (b) k_1 and k_{-1} versus exchange current density for Ir modified Pt surfaces.

4.4.3 Pt deposited onto Pt{111}

In order to investigate the origin of the Ir HER rate enhancement and whether it is related to structure or is a genuine catalytic effect, the Ir deposition experiment was repeated by depositing Pt onto Pt{111}. A Pt{111} electrode was dipped into a solution of H_2PtCl_6 and held in a Bunsen flame momentarily and cooled in H_2 to reduce Pt onto the surface. The electrode was repeatedly exposed to a Bunsen flame to anneal Pt in order to investigate variations in Pt surface roughness. The CVs of these surfaces are shown in fig. 4.4.10 and the associated LSVs are shown in fig. 4.4.11. The data from these experiments is displayed in table 4.4.6.

A rate enhancement was observed on the deposited Pt surfaces, though not as great as when Ir was the deposited metal.

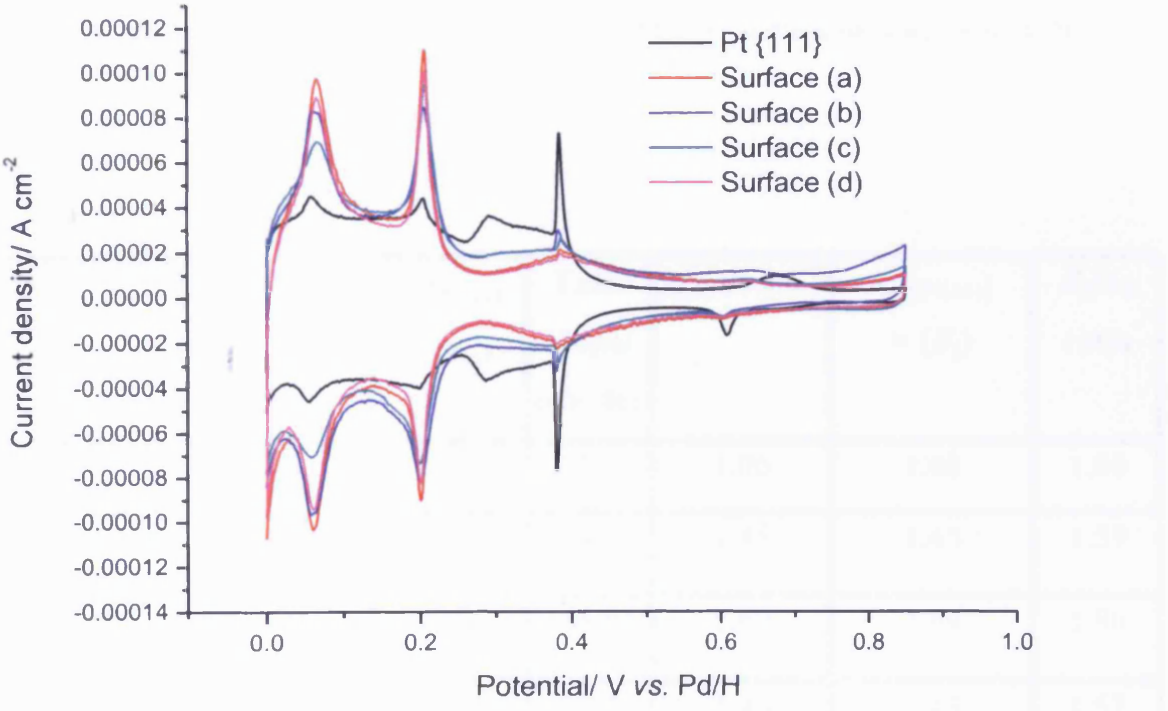

Fig. 4.4.10 CVs of Pt deposits on Pt{111}. Surface roughness was varied by repeated flame annealing. 0.5 M H_2SO_4, 0.05 V s^{-1}.

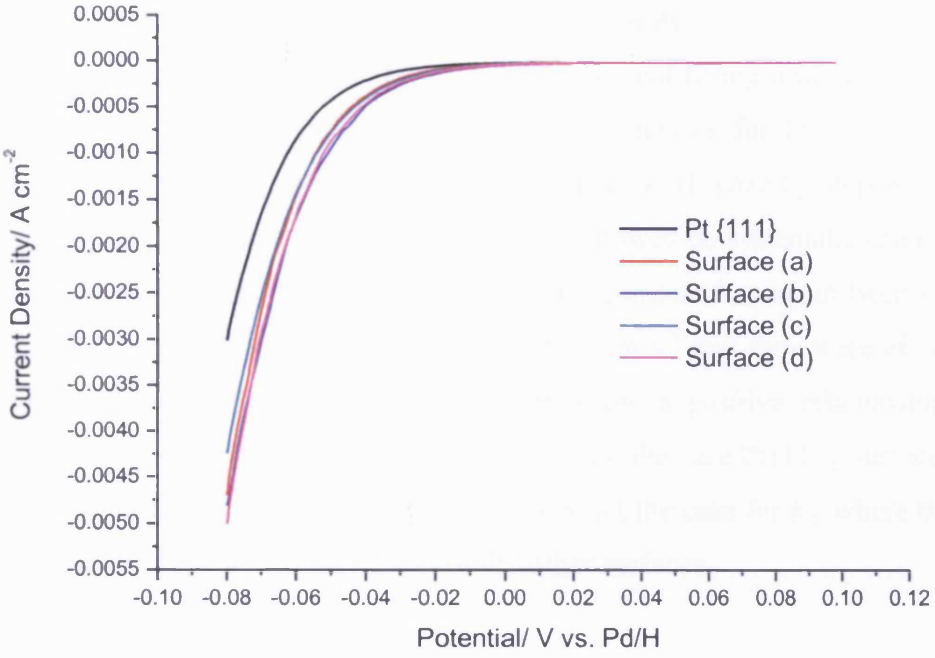

Fig. 4.4.11 LSV into hydrogen evolution region for the Pt on Pt{111} surfaces showing enhanced HER rate. 0.5 M H_2SO_4, 0.005 V s^{-1}.

	σ/ μC cm^{-2}	$\sigma/\sigma_{Pt\{111\}} = (A_\sigma)$	Tafel Slope/ mV/dec	j_0/ mA cm^{-2}	$j_0/j_{0Pt\{111\}} = (B_j)$	B_j/A_σ ratio
Pt{111}	**241**	**1.00**	**32.6**	**1.00**	**1.00**	**1.00**
Surface (a)	**220**	**0.91**	**34.2**	**1.45**	**1.45**	**1.59**
Surface (b)	**220**	**0.91**	**35.0**	**1.69**	**1.69**	**1.86**
Surface (c)	**220**	**0.91**	**32.7**	**1.43**	**1.43**	**1.57**
Surface (d)	**220**	**0.91**	**34.7**	**1.74**	**1.74**	**1.91**

Table 4.4.6 Tafel and surface area data for Pt deposited on Pt{111}.

4.4.3.1 Fitting rate constants to Tafel data from Pt on Pt

As with the Ir deposited onto Pt surfaces, a computational fitting routine was used to find the rate constants for the Volmer and Tafel reactions for Pt deposited onto Pt{111} (see table 4.4.7). It was again assumed that no Heyrovsky step was active for these surfaces. The forward Tafel rate constant showed no systematic change with exchange current density (the backward Tafel rate constant has again been omitted from table 4.4.7 as the values were so low, ~ 10^{-20} cm s^{-1} that they were effectively meaningless). The Volmer rate constants both show a positive relationship with exchange current density for the Pt deposited surfaces, the bare Pt{111} surface value even agrees with the trend for k_1. However, this is not the case for k_{-1}, where the bare Pt{111} value does not fit with the data for the other surfaces.

	k_1/ 10^{-3} cm s^{-1}	k_{-1}/ 10^{-4} mol cm^{-2} s^{-1}	k_2/ 10^{-9} cm s^{-1}
Pt{111}	1.65	4.99	7.05
Surface (a)	1.48	3.35	7.51
Surface (b)	2.44	3.20	4.91
Surface (c)	2.20	3.38	5.11
Surface (d)	2.76	4.60	5.92

Table 4.4.7 Volmer-Tafel data for Pt deposited on Pt{111} in 0.5 M H_2SO_4.

4.4.4 Pd films on Pt

Pd films were deposited on Pt{111} (area = 0.022 cm^2) using the "forced deposition" method (as described in section 3.5). The Pd films were deposited in small increments up to a maximum of ~2 monolayers. It was observed that submonolayer amounts of Pd had little effect on the HER rate, which remained fairly constant. Above one monolayer the HER activity began to decrease (Tafel slope increased, exchange current density decreased) but settled with subsequent deposits. As the Pd coverage approached a second monolayer, the HER rate became slower again. The exchange current density and Tafel slope values for each of the coverages tested are shown in table 4.4.8. The results can be seen graphically in fig. 4.4.14. Cyclic voltammograms and linear sweep voltammograms of the surfaces are shown in fig. 4.4.12 and 4.4.13 respectively.

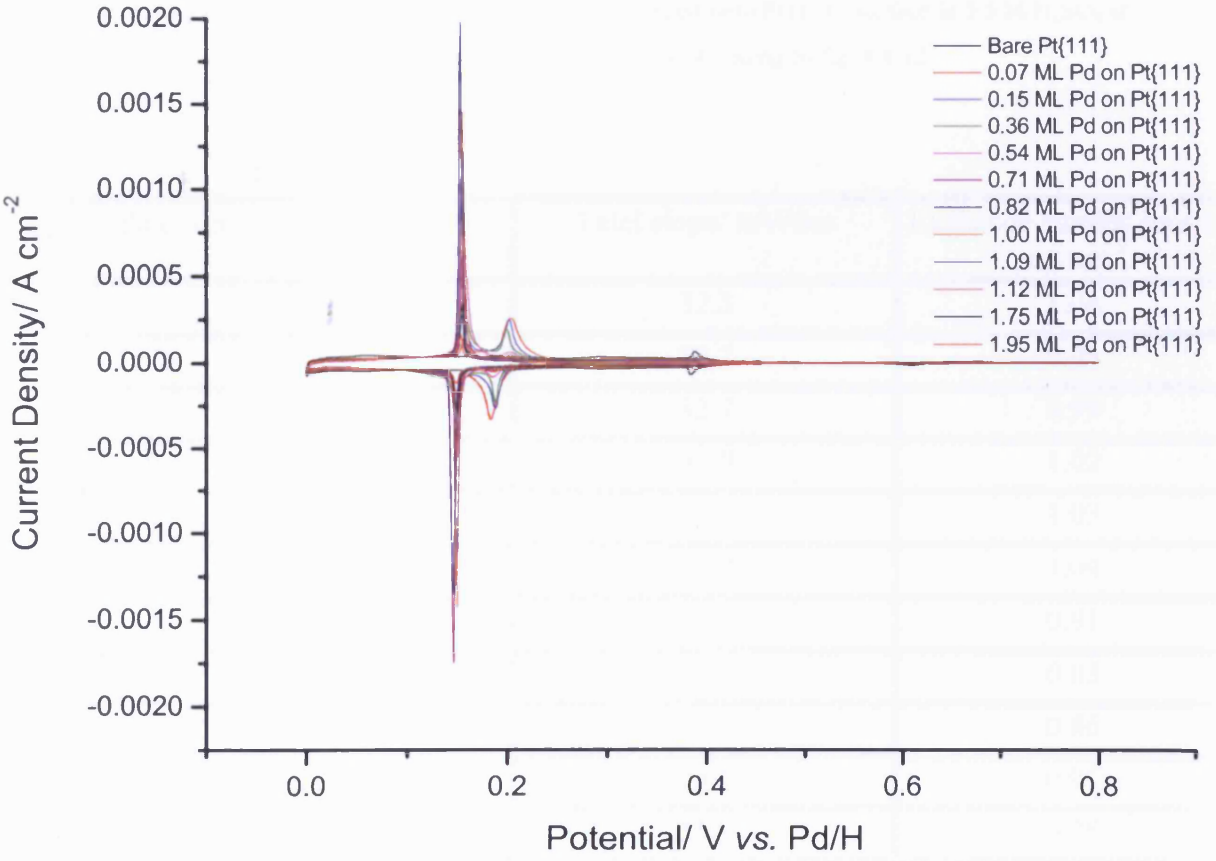

Fig. 4.4.12 Cyclic Voltammograms of Pd deposited onto Pt{111} surface in 0.5 M H_2SO_4 at potential sweep rate 0.05 V s^{-1}.

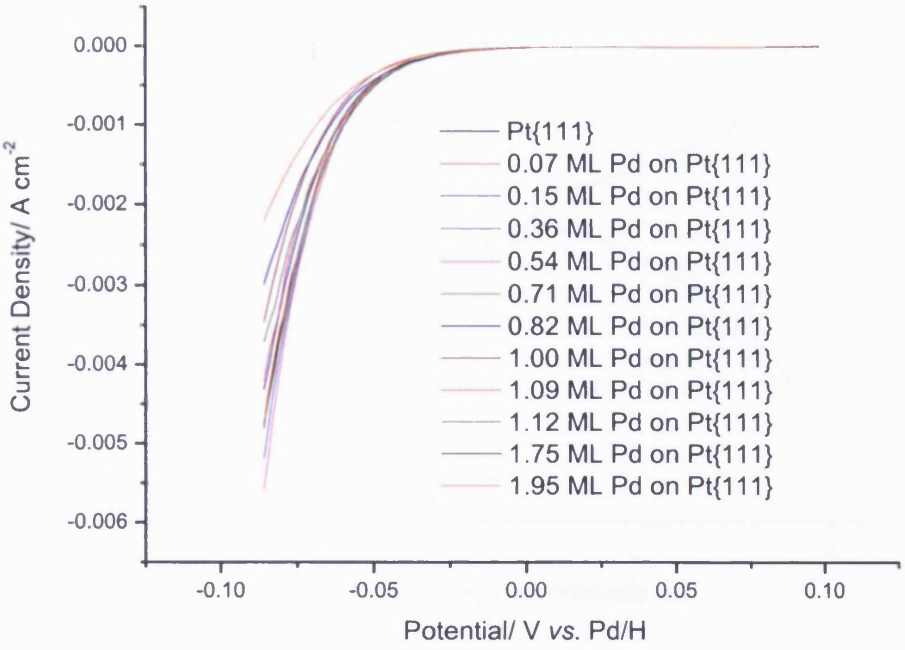

Fig. 4.4.13 Linear sweep voltammograms of Pd deposited onto Pt{111} surface in 0.5 M H_2SO_4 at potential sweep rate 0.005 V s^{-1}, corresponding to fig. 4.4.12.

Pd coverage/ monolayers	Tafel slope/ mV/dec	Exchange current density/ mA cm^{-2}
0	32.3	1.04
0.07	32.2	0.95
0.15	32.7	0.99
0.36	31.9	1.02
0.54	31.7	1.03
0.71	31.9	1.04
0.82	32.5	0.91
1.00	32.5	0.83
1.07	32.7	0.86
1.12	34.1	0.91
1.75	35.9	0.78
1.95	39.2	0.63

Table 4.4.8 Tafel slopes and exchange current densities for Pd films on Pt{111}.

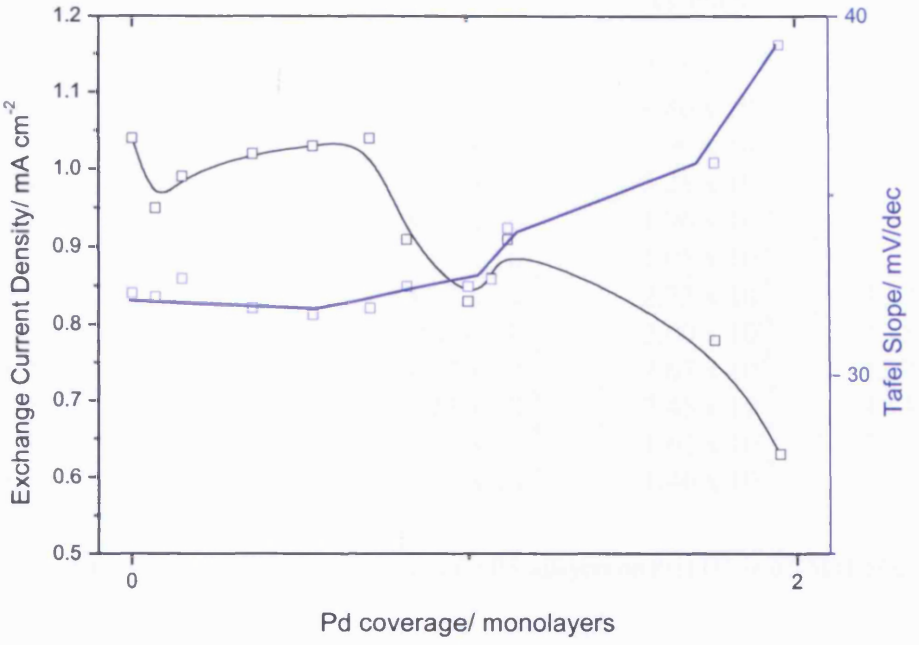

Fig. 4.4.14 Graph showing the change of Tafel slope and exchange current density with Pd coverage.

4.4.4.1 Fitting rate constants to Tafel data from Pd films on Pt

Volmer, Tafel and Heyrovsky rate constants were found for the Pd adlayer surfaces on Pt{111}. The Heyrovsky component was detrimental to the fitting on the surfaces with Pd coverage below 1 monolayer, so the data was also fitted using a Volmer-Tafel fitting routine, omitting the Heyrovsky analysis. At certain Pd coverages (0.82 – 1.12 Pd monolayers), both fitting routines (Volmer-Tafel and Volmer-Tafel-Heyrovsky) worked well. This gives an ambiguity as to which mechanism is dominating, or if there are significant contributions from each of the mechanisms, due to the reaction occurring separately on both the Pd and Pt surfaces. The results are displayed in table 4.4.9.

Pd coverage/ monolayers	k_1/ cm s^{-1}	k_{-1}/ mol cm^{-2} s^{-1}	k_2/ cm s^{-1}	k_3/ cm s^{-1}
0	1.34×10^{-3}	3.63×10^{-4}	7.45×10^{-9}	--
0.07	2.64×10^{-1}	8.60×10^{-2}	4.86×10^{-7}	--
0.15	3.45×10^{-1}	9.44×10^{-2}	3.90×10^{-7}	--
0.36	2.86×10^{-1}	9.38×10^{-2}	5.28×10^{-7}	--
0.54	8.69×10^{-5}	3.82×10^{-5}	1.96×10^{-8}	--
0.71	1.03×10^{-4}	3.17×10^{-5}	1.05×10^{-8}	--
0.82	3.23×10^{-5}	3.12×10^{-5}	2.73×10^{-6}	4.20×10^{-6}
1.00	2.48×10^{-5}	2.1×10^{-5}	2.00×10^{-6}	3.15×10^{-6}
1.07	1.94×10^{-5}	1.77×10^{-5}	2.67×10^{-6}	4.29×10^{-6}
1.12	2.41×10^{-5}	1.23×10^{-5}	7.45×10^{-7}	4.44×10^{-6}
1.75	4.59×10^{-5}	1.12×10^{-5}	1.62×10^{-7}	2.27×10^{-6}
1.95	5.43×10^{-6}	2.29×10^{-6}	1.46×10^{-7}	7.06×10^{-6}

Table 4.4.9 Volmer-Tafel-Heyrovsky data for Pd adlayers on Pt{111} in 0.5 M H_2SO_4.

4.4.5 Pd-Pt alloys

Pd-Pt surface alloys were prepared by gently flame annealing bulk deposits of Pd on a Pt{111} surface, such that the two metals form an alloy within the surface of the crystal. Pd can be removed subsequently by heating in a Bunsen flame at 1500 K.

The percentages of Pd in the surface layer were calculated using previous measurements carried out within the Cardiff Electrochemical Surface Science group[20]. The cyclic voltammograms of these surfaces are shown in fig. 4.4.15 and the linear sweep voltammetry into the hydrogen evolution region is shown in fig. 4.4.16.

It was found that there was little deviation from the exchange current density and mechanism for bare Pt{111} as a function of Pd composition. This implies that Pd shows no significant influence on the reaction rate when there is Pt present at the electrode surface. The results can be seen in table 4.4.10.

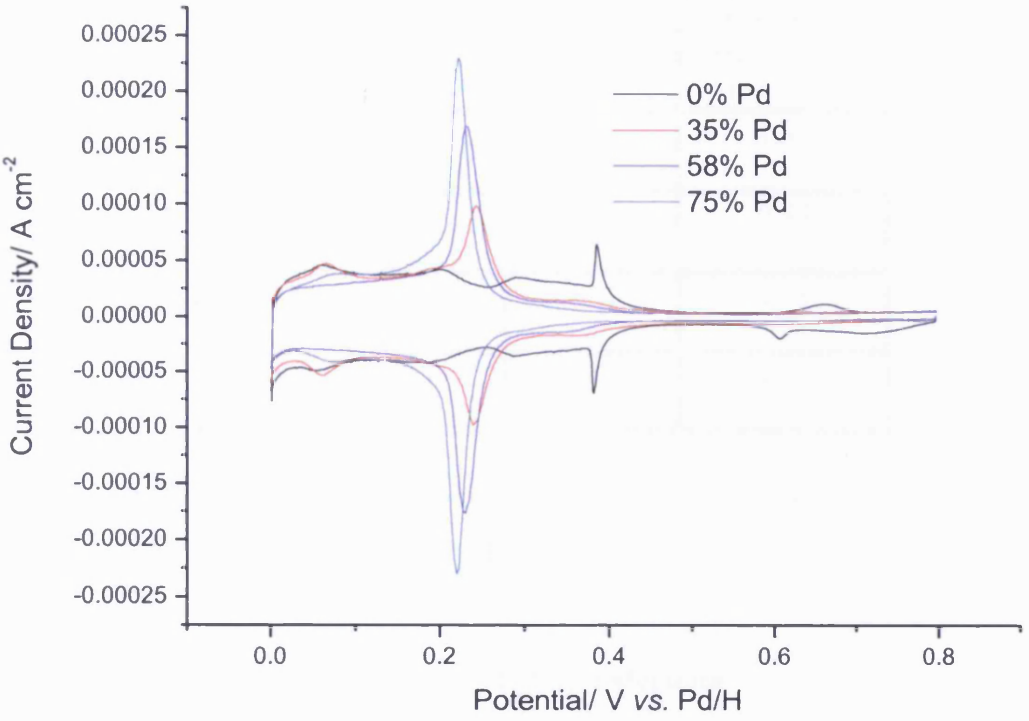

Fig. 4.4.15 Cyclic Voltammograms of Pd-Pt surface alloys, showing variation as a function of Pd surface composition in 0.5 M H_2SO_4 at potential sweep rate 0.05 V s^{-1}.

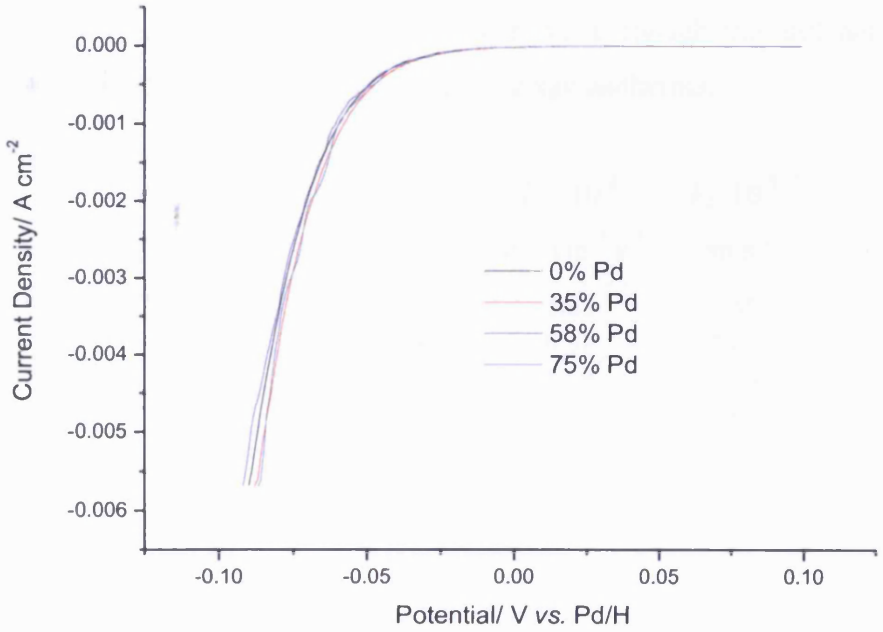

Fig. 4.4.16 Linear sweep voltammograms of Pd-Pt surface alloys, in 0.5 M H_2SO_4 at potential sweep rate 0.005 V s^{-1}, corresponding to fig. 4.4.16.

Pd in surface layer/ %	Tafel slope/ mV/dec	Exchange current density/ mA cm^{-2}
75	32.4	1.03
58	33.5	0.94
35	33.1	1.08
Bare Pt{111}	32.8	1.02

Table 4.4.10 Tafel data and exchange current densities for Pd-Pt alloys.

4.4.5.1 Fitting rate constants to Pd-Pt alloy Tafel data

The Volmer and Tafel rate constants for the hydrogen evolution reaction on the Pd-Pt alloys from the previous section were found using a computational fitting routine and are shown in table 4.4.11. The fitting was also attempted using a fitting routine including an element for the Heyrovsky mechanism, though this did not fit well, giving unrealistically low hydrogen surface coverage isotherms.

Pd in surface layer/ %	k_1/ 10^{-3} cm s^{-1}	k_{-1}/ 10^{-4} mol cm^{-2} s^{-1}	k_2/ 10^{-9} cm s^{-1}
Bare Pt{111}	1.34	3.63	7.45
35	2.56	6.37	7.27
58	2.61	6.18	5.79
75	1.31	3.74	8.81

Table 4.4.11 Volmer-Tafel-Heyrovsky data for Pd-Pt alloys in 0.5 M H_2SO_4.

4.4.6 Bi overlayers on Pt single crystals

Pt{111}, {110} and {100} were repeatedly dipped into a solution of $Bi(NO_3)_3$ to test the effect of covering active hydrogen evolution sites with an inert site-blocker, which should inhibit the Pt atoms below them from taking part in the HER.

The graphs of exchange current density versus fractional Bi coverage (fig. 4.4.17, where $\Phi_{Bi} = 1$ represents a complete coverage of the Pt surface with Bi) were of similar shape to those reported by Feliu and Gomez[8, 21]. Each graph gave a similar shape. There was a large decrease in electrode activity (exchange current density) at low fractional Bi coverages ($\Phi_{Bi} < 0.2$) with little further decrease in exchange current density until relatively high Bi coverages were achieved and the activity decreased more rapidly once again.

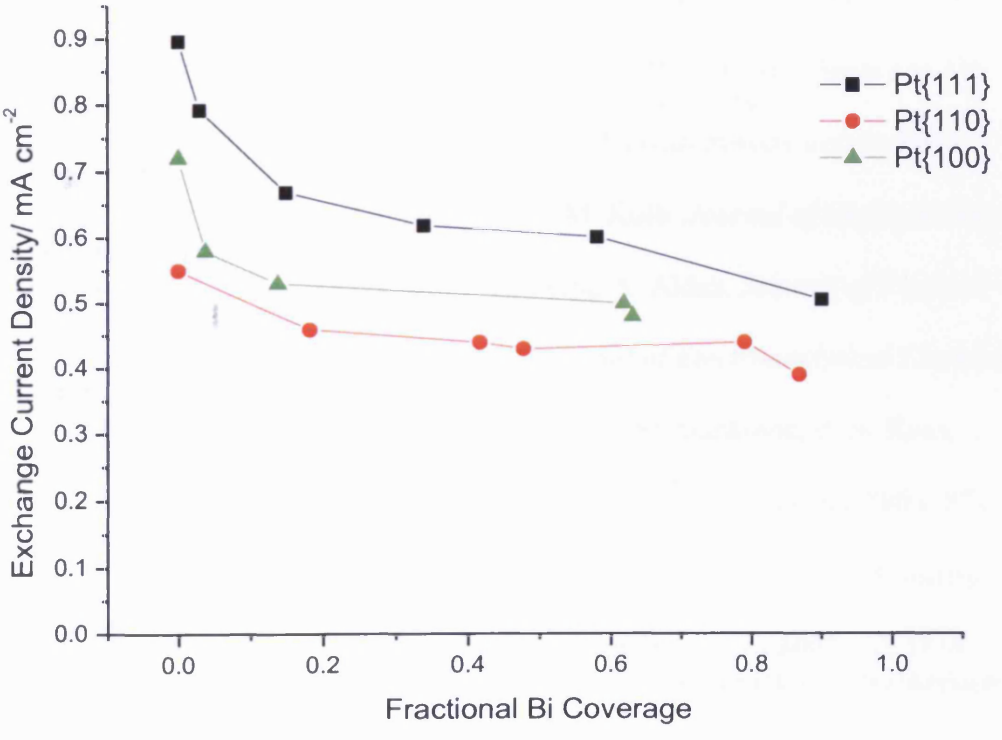

Fig. 4.4.17 Graph of exchange current density versus fractional Bi coverage (calculated from proportion of UPD-H sites blocked) on Pt{111}, Pt{110} and Pt{100}.

References

[1] J. Maruyama, M. Inaba, K. Katakura, Z. Ogumi, Z.-I. Takehara, *Journal of Electroanalytical Chemistry* **1998**, *447*, 201.

[2] A. J. Bard, L. R. Faulkner, *Electrochemical methods: fundamentals and applications*
2ed., J. Wiley and Sons inc., New York, **2001**.

[3] C. W. Bradford, M. J. Cleare, H.Middleton, Johnson Matthey & Co. Ltd.

[4] N. M. Markovic, B. N. Grgur, P. N. Ross, *Journal of Physical Chemistry B* **1997**, *101*, 5405.

[5] M. Alsabet, M. Grden, G. Jerkiewicz, *Journal of Electroanalytical Chemistry* **2006**, *589*, 120.

[6] N. Garcia-Araez, V. Climent, E. Herrero, J. M. Feliu, *Surface Science* **2004**, *560*, 269.

[7] K. Seto, A. Ianelli, B. Love, J.Lipkowski, *Journal of Electroanalytical Chemistry* **1987**, *226*, 351.

[8] R. Gomez, A. Fernandez-Vega, J. M. Feliu, A.Aldaz, *Journal of Physical Chemistry* **1993**, *97*, 4769.

[9] J. Barber, S. Morin, B. E. Conway, *Journal of Electroanalytical Chemistry* **1998**, *446*, 125.

[10] N. M. Markovic, H. A. Gasteiger, P. N. R. Jr., *Journal of Physical Chemistry* **1995**, *99*, 3411.

[11] N. M. Markovic, S. T. Sarraf, H. A. Gasteiger, P. N. R. Jr., *Journal of The Faraday Society, Faraday Transactions,* **1996**, *92*, 3719.

[12] C. A. Lucas, N. M. Markovic, P. N. Ross, *Physical Review Letters* **1996**, *77*, 4922.

[13] L. A. Kibler, A. Cuesta, M. Kleinert, D. M. Kolb, *Journal of Electroanalytical Chemistry* **2000**, *484*, 73.

[14] R. Gomez, A. Fernandez-Vega, J. M. Feliu, A. Aldaz, *Journal of Physical Chemistry B* **1993**, *97*, 4769.

[15] T. H. M. Housmans, M. T. M. Koper, *Journal of Electroanalytical Chemistry* **2005**, *575*, 39.

[16] N. M. Markovic, C. A. Lucas, V. Climent, V. Stamankovic, P. N. Ross, *Surface Science* **2000**, *465*, 103.

[17] M. B. Vukmirovic, R. L. Sabatini, R. R. Adzic, *Surface Science* **2004**, *572*, 269.

[18] J. Clavilier, J. M. Feliu, A. Aldaz, *Journal of Electroanalytical Chemistry* **1988**, *243*, 419.

[19] M. Hara, U. Linke, T. Wandlowski, *Electrochimica Acta* **2007**, *52*, 5733.

[20] F. J. Vidal-Iglesias, A. Al-Akl, D. J. Watson, G. A. Attard, *Electrochemistry Communications* **2006**, *8*, 1147.

[21] R. Gomez, J. M. Feliu, A. Aldaz, *Electrochimica Acta* **1997**, *42*, 1675.

[22] Z.-Q. Tian, B. Ren, D.-Y. Wu, *Journal of Physical Chemistry B* **2002**, *106*, 9463.

[23] R. J. Nichols, A. Bewick, *Journal of Electroanalytical Chemistry* **1988**, *243*, 445.

Chapter 5
Discussion

5.1 Hydrogen evolution and hydrogen oxidation on polycrystalline Pt

5.1.1 Hydrogen electro-oxidation on polycrystalline Pt

5.1.1.1 HOR on Pt in 0.1 M $HClO_4$

Cyclic Voltammetry of polished polycrystalline Pt in 0.1 M $HClO_4$ was reproducible, although it has since been noted that the system was not completely free of contaminants. Despite this, data was obtained which was in agreement with work from Maruyama *et al*[1]. The general shape of the current density versus overpotential plots at varying rotation rates matched the reported figures well. However the upper current density values at fast rotation rates (ω > 3000 rpm) were not as high as those given by Maruyama *et al.* The upper j value obtained experimentally at 3500 rpm is 1.05 mA cm^{-2} compared to that shown in the literature for 3600 rpm of 1.54 mA cm^{-2} in the same electrolyte. Thus, the Koutecky-Levich plots of j^{-1} versus $\omega^{-1/2}$ over the potential range (0 – 0.1 V overpotential) were also very close to the reported findings except at high rotation rates. This discrepancy should not affect the values obtained for j_k (from the intercept on the j^{-1} axis) as the slope will be largely defined by the data at lower rotation rates. It must be noted that, as in Murayama's work, the magnitude of the gradients of the Koutecky-Levich plots decreased with overpotential. Hence, j_k values were calculated in the same manner as described in Maruyama's paper from the modified version of the Koutecky-Levich equation which includes an additional term representing the influence of the backward reaction rate on the kinetics (it is thought that this influence is the reason for high exchange current density during hydrogen oxidation). Subsequently the graph of $\ln j_k$ versus η was effectively linear over the same potential range as in Maruyama's work (0 – 0.06 V overpotential). In contrast, the graph plotted from j_k values taken from the general Koutecky-Levich equation (equation (4.1.2)) was curved. These two graphs and the equivalent from Maruyama's paper are shown in fig. 5.1.1, plotted on the same scales for a more direct comparison to the published work. The data from the modified Koutecky-Levich equation was used in subsequent analysis as it matched Maruyama's data more

closely than that found using the unmodified version. Although the graph in fig. 5.1.1 (a) is similarly linear in shape to the published graph (shown in fig. 5.1.1 (c)), the absolute kinetic current density values are quite different (higher at low overpotentials and lower at high overpotentials). Hence, the slope obtained is much shallower and the resulting exchange current density is significantly higher than Maruyama's results, 2.42 mA cm^{-2} compared to 1.35 mA cm^{-2}.

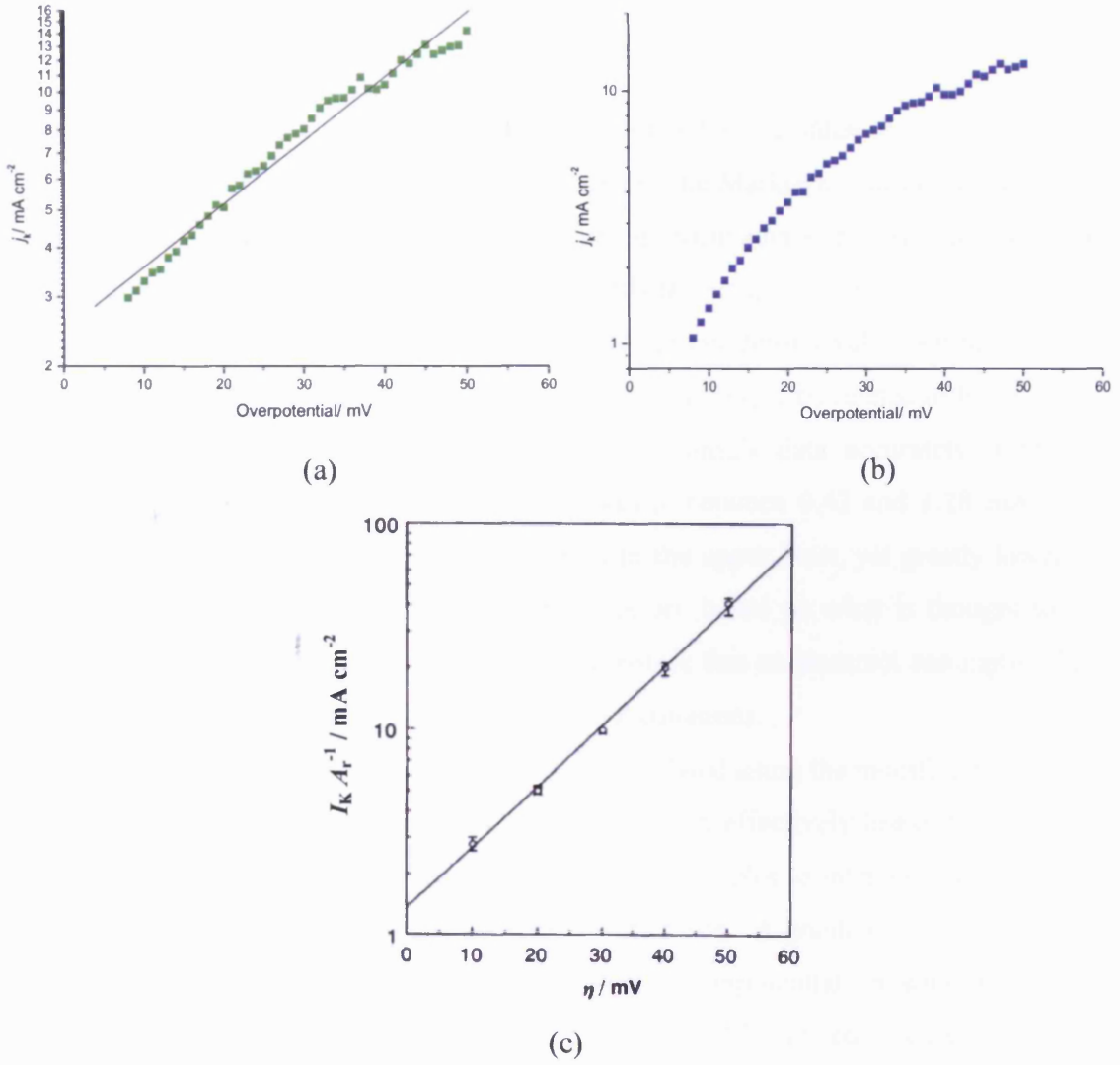

Fig. 5.1.1. Logarithmic plots of j_k versus η using (a) modified version and (b) generally accepted version of the Koutecky-Levich equation and (c) the equivalent plot from Maruyama *et al.*[1]

The j_o values obtained in the present study and in Maruyama's work are both high relative to figures quoted by Markovic *et al*[2] and Feliu *et al*[3] whilst conducting hydrogen evolution experiments (0.45 – 0.98 mA cm^{-2} in 0.1 M H_2SO_4 using single crystal electrodes). There are a wide range of factors which may be influential here. Feliu's experiments were performed on stationary electrodes and therefore analysed with a simple Tafel-slope model (where j_0 is found from the intercept of a plot of $\log j$ versus overpotential). Markovic's approach is different again, assuming that for rotating disc electrode measurements, at low overpotentials (< ± 0.01 V):

$$j = j_0 \frac{\eta F}{R_g T} \qquad \textbf{(5.1.1)}$$

Applying equation (5.1.1) to the data from section 4.1.1.1, a value of j_0 = 1.48 – 1.54 mA cm^{-2} is found, which is still high compared to the Markovic and Feliu values but significantly lower than the value obtained using Maruyama's analysis method. The result found using Markovic's analysis method is in fact quite similar to Murayama's result. Maruyama states that the high exchange current density value is related to the reverse reaction occurring at the electrode, but it may simply be related to his analysis technique. It is very difficult to analyse Maruyama's data accurately from the published figures[1]. A rough calculation gives j_0 between 0.42 and 1.28 mA cm^{-2} which is very close to the original calculation in the upper limit, yet greatly lower in the lower limit. All of the analysis techniques are based on what is thought to be sound theoretical calculations, yet it may be possible that an incorrect assumption has been made at some point in the derivation of the equations.

It can be seen from the plot of $\ln j_k$ versus η (calculated using the modified version of the Koutecky-Levich equation, fig. 4.1.3) that, though effectively linear, the linearity begins to break down around 0.04 V. This causes the plot to intercept the $\ln j_k$ axis slightly higher than if the more linear region were taken. A graph of $\ln j_k$ versus η for the more linear portion of the data (0.007 – 0.038 V overpotential, shown in fig. 5.1.2) gives a j_0 value of 2.12 mA cm^{-2}. This value is 0.3 mA cm^{-2} lower than that calculated from the original data (which covers a wider potential range) though still significantly higher than Maruyama's result.

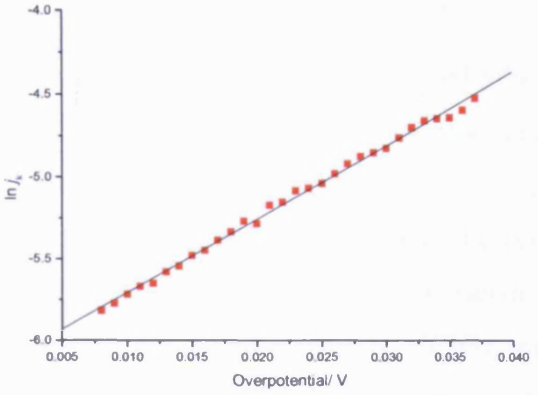

Fig. 5.1.2 Plot of ln j_k versus η using the same data as in fig. 4.1.3 (b) but over a narrower potential range, giving a more linear fit.

It is surprising that the results from this section yield a high value of exchange current density as it has since been discovered that the electrochemical cell probably contained significant amounts of contaminants. The cell was made of soda glass, which, though cleaned by soaking in a mixture of 2:1 concentrated nitric:hydrochloric acid to remove organic molecules, contains lead-based impurities. This was unknown at the time of the experiment. Similarly, the electrolytes were prepared from Analar grade as opposed to Aristar or better. The reference electrode used was Ag/AgCl in 3 M NaCl. However, to avoid chloride ions diffusing into the electrolyte, a salt bridge was placed between the reference electrode and the electrolyte solution. The cell was not well sealed so, although the solution was degassed with H_2 and held under a H_2 atmosphere, it may have been possible for air and airborne contaminants to enter the solution if the gaseous overpressure was not great enough. The platinum working electrode was coated in nylon, which may also have introduced contamination. Despite all of these potential contamination factors, the cyclic voltammograms were reproducible (fig. 4.1.1), though not as good (in terms of UPD-H peak definition) as previous published figures[1]. As the raw data matched well with Maruyama's published work, it was assumed that the system was clean. As mentioned earlier in this section, there is a discrepancy in the results at the higher rotation rates compared to Maruyama's work. This can now be assigned to small levels of contaminants within the solution being drawn to the electrode surface. The contamination effect will be more significant at higher rotation rates as the flux of material to the electrode is higher. Hence, more contaminants, will be drawn to the electrode and adsorb on it, blocking electroactive sites and therefore lowering electrochemical activity.

5.1.1.2 Pt in 0.05 M H_2SO_4

The aim of this experiment was to compare the activity of hydrogen oxidation on Pt in two different acid electrolytes. Aqueous sulphuric acid dissociates to form bisulphate anions which are known to adsorb strongly to the Pt surface relative to the more weakly adsorbed perchlorate anions from aqueous perchloric acid.

The results in table 4.1.1 show an increased value of transfer coefficient, α, when using H_2SO_4 as the electrolyte, compared to that of $HClO_4$, with values of 0.68 and 0.52 respectively. These values were calculated from the gradients of the respective graphs of $\ln j_k$ versus η. It is commonly assumed that $\alpha = 0.5$. It is thought that the deviation in the values of α seen in the present results is not greatly significant and that a variation such as this does not correspond to a difference in reaction mechanism. However, it has been found using charge displacement and FTIR measurements that all anions should be desorbed from Pt electrodes at HER potentials[4, 5]. Therefore the difference in transfer coefficient in the different electrolytes is unusual.

The exchange current density value is significantly lower in H_2SO_4 electrolyte than in $HClO_4$. However, an important factor here is one which could be related to the acid concentration rather than the electrolyte itself since, unfortunately, the solutions used were not of equivalent proton concentrations. 0.05 M H_2SO_4 was used, assuming that the nature of the electrolyte was dibasic, such that two H^+ ions would fully dissociate from the sulphuric acid molecule giving an H^+ concentration of 0.1 mol dm^{-3}. This assumption was not correct and in fact an effective H^+ concentration of only 0.0585 mol dm^{-3} was reached in this experiment. This concentration value was calculated from the pK_a values for the two dissociation steps where pK_a = -3 for the first/complete H^+ dissociation and 1.92 for the second/partial dissociation step. This should not yield drastically different results to those from 0.1 M H_2SO_4 and can be compared with the results for $HClO_4$. Markovic's equivalent studies were performed in 0.05 M H_2SO_4[2] (though single crystal electrodes were used), allowing an almost direct comparison with published works. As it stands, the present results are in good agreement with Markovic's work on hydrogen oxidation (and hydrogen evolution which will give the same value for exchange current density) on Pt single crystal electrodes (0.45 – 0.98 mA cm^{-2}). An interesting point to note is that Markovic's work shows that there is a dependence upon Pt single crystal structure for the three basal planes. Hence, a polycrystalline electrode with structural contributions from

each of these planes should give an exchange current density value which lies in the range of these single crystal values. The results from this project on polycrystalline Pt lie within this range, matching the prediction.

Similarly, the present result lies within the range of values for exchange current densities on the basal plane single crystals found by Gomez *et al*[3] (0.84 – 0.97 mA cm^{-2}), though, according to these authors, these findings are not thought to be related to electrode structure. Hence, polycrystalline Pt is likely to give an exchange current density within the same range. Gomez's experiments were conducted in 0.5 M H_2SO_4, whilst the present study used 0.05 M H_2SO_4 as the electrolyte. This difference in concentration would be expected to lead to a large difference in exchange current density. Equation (4.1.3) shows explicitly the relationship between the exchange current density and proton concentration. Comparison of Gomez's results with those from this project and those of Markovic *et al*[2] imply that there is no dependence of exchange current density on acid concentration, contradicting equation (4.1.3). However the comparison with Markovic's results implies that results collected in this project correspond to clean electrodes, free from contaminants (at least over the duration of these experiments). This leads back to the matter of why the result in $HClO_4$ electrolyte gave such a high value for exchange current density. The published value for j_0 for HER/HOR in $HClO_4$ of 1.35 mA cm^{-2} (from Maruyama *et al*[1]) is higher than that reported for H_2SO_4 of 0.45 – 0.98 mA cm^{-2} (from Markovic *et al*[2]). Though these values are not directly comparable, again due to the different electrolyte concentrations, it is thought that this discrepancy in concentration should account for the difference in exchange current density. This assumption would imply that there is little effect due to the different electrolytes used.

The standard rate constants, k^0, evaluated in the present study show a relatively small variation, with electrolyte, giving values of 1.26×10^{-4} cm s^{-1} in $HClO_4$ and 0.79×10^{-4} cm s^{-1} in H_2SO_4, compared to the much greater discrepancy between the j_0 values. Unfortunately no literature values for k^0 could be found for comparison.

5.1.2 Hydrogen evolution on Pt-group metal electrodes

5.1.2.1 Hydrogen evolution on Pt in 0.1 M H_2SO_4

The hydrogen evolution experiments were performed in a similar manner to the hydrogen oxidation experiments on a polycrystalline Pt electrode, but the potential was swept in the opposite sense, from 0 V to -0.200 V *vs.* RHE (-0.292 V to -0.492 V *vs.* Ag/AgCl).

The experimental results afforded an exchange current density value of 1.88 mA cm^{-2}, which is high compared to the literature value of 1.00 mA cm^{-2} reported by Bockris *et al*[6]. The j_0 value from the present study is roughly twice as high as the value obtained from the hydrogen oxidation experiments in section 5.1.1 in 0.05 M H_2SO_4. This implies a direct proportionality between concentration and exchange current density, which is in agreement with the relationship:

$$nFk_f C_o^* = j_0 e^{-\alpha n f \eta} \qquad \textbf{(5.1.2)}$$

(all symbols are defined in section 4.1.1.1) which shows the direct proportionality between j_0 and C_o^*. However, this then contradicts the comparison of Markovic *et al*[2] and Gomez *et al*[3], where similar j_0 values are found but in different concentrations of H_2SO_4 (0.05 mol dm^{-3} and 0.5 mol dm^{-3} respectively). There must therefore be a further factor involved which is possibly related to the rotation of the electrode. The results in the present project have been taken at varying rotation rates and analysed in the appropriate manner using the Koutecky-Levich equations. Similarly Markovic's work was performed over a range of rotation rates. Gomez's data was collected using stationary electrodes. For a fixed proton concentration, the exchange current density should not differ between the two techniques. However, the difference between the Gomez *et al* and Markovic *et al* studies appears to be attributable to the difference in experimental setup (if j_0 is proportional to electrolyte concentration).

The 0.1 M H_2SO_4 j_0 value is closer to the 0.1 M $HClO_4$ value (section 5.1.1) than the value from the HOR experiments in 0.05 M H_2SO_4 (1.88 mA cm^{-2}, 2.42 mA cm^{-2} and 0.89 mA cm^{-2} respectively). This may be expected as the more concentrated sulphuric acid is closer to the perchloric acid in terms of proton concentration than the less concentrated sulphuric acid. The discrepancy in j_0 can therefore be largely attributed to anion adsorption effects. The bisulphate anions should be

electrochemically desorbed from the Pt electrode at hydrogen evolving potentials, yet there is a strong case to suggest that they do have an effect. Literature comparisons may be argued as supporting this concept, i.e. comparison of the Maruyama[1] and Bockris[6] works. Maruyama finds an exchange current density of 1.35 mA cm^{-2} in 0.1 M $HClO_4$, whereas Bockris *et al* find a value of 1.00 mA cm^{-2} in a H_2SO_4 solution of the same concentration.

5.1.2.2 Hydrogen evolution on Ir in 0.1 M H_2SO_4

Polycrystalline Ir was tested in the same manner as Pt as outlined in section 5.1.2.1. Ir gave an exchange current density of 0.50 mA cm^{-2}, much lower than that found on polycrystalline Pt, showing that Ir is less active for the HER than Pt. Similarly, the standard rate constant for Ir was less than that for Pt and the transfer coefficient was in the same range (see table 4.1.2). A point to note about the transfer coefficient for hydrogen evolution is that the sum of the transfer coefficient for hydrogen evolution and that for hydrogen oxidation should be 1, i.e.

$$\alpha_{HER} + \alpha_{HOR} = 1 \qquad \textbf{(5.1.3)}$$

Yet, the α_{HER} values for Ir (and the other metals tested) seem particularly low, given that the α_{HOR} values for Pt in H_2SO_4 did not stray too far from 0.5, which is typical for a reversible system and is often assumed to be the figure for use in equations when the real value is unknown. The α_{HER} values are found to be lower than 0.2, hence it would not be fair to assume a value of 0.5 in this case.

Unfortunately, no previously reported data could be found for the transfer coefficient or the standard rate constant for HER on Ir in H_2SO_4, though the exchange current density was found for a 0.5 M H_2SO_4 electrolyte. It would be expected that the experimental value found in 0.1 M H_2SO_4 would be lower than that in 0.5 M H_2SO_4. However, this was not the case as the present work was found to give a value of 0.50 mA cm^{-2} compared to the literature values of 0.20 – 0.40 mA cm^{-2}[7, 8] in 0.5 M H_2SO_4. The present Ir j_0 value is in a similar range to these literature values, but it seems to be fairly consistent with the experimental results in this section that the exchange current density figures are generally higher than those quoted in published works. This again shows that a difference is observed when measuring exchange current densities on effectively similar systems when using forced convection or

stationary electrodes. However, there should be no difference between the two methods under steady state conditions.

5.1.2.3 Hydrogen evolution on Ru plated on Pt

Ru was plated onto the Pt electrode used in earlier experiments to assess the hydrogen evolution reaction on a thick Ru film in order to mimic the behaviour of a bulk electrode of the metal. It is difficult to procure a pure solid Ru electrode. The plating proved difficult and a range of electrolysis parameters were investigated, varying the current applied to the electrode, the temperature of the plating bath and the length of electrolysis time amongst other factors. The final experimental parameters are detailed in section 3.1.2.1. Visually, the plated electrode was found to be less shiny than the un-plated electrode, with the full Pt surface being covered by Ru and no visible cracks observable in the Ru layer. A major experimental difficulty with this electrode was that it could not be polished since the plated Ru would be removed. Similarly, the electrode could not be electrochemically cleaned since soluble RuO_2 forms when the potential is swept positive of ~0.9 V *vs.* RHE. Hence, the surface was rough, despite being plated onto highly polished, mirror finish Pt. The cyclic voltammogram (fig. 4.1.7) reflects this. It can be seen that the Ru surface has a very high double layer capacitance which is typical of rough Ru surfaces[9]. The area of the Ru surface was calculated through comparison of similar eletrodeposited Ru cyclic voltammograms from Rand and Woods[9]. The area was found to be 1.475 cm^2, which is much higher than the values for Pt and Ir (0.265 and 0.294 cm^2 respectively).

The values of exchange current density for HER were fairly constant (0.24 – 0.27 mA cm^{-2}), but all were much lower than those for Pt and Ir. This shows that this surface is very inactive for the HER. It is thought that this may be due to the stability of RuO_2 or RuO phases present under HER conditions and hence hindering the HER in the cases of the lower potential limit. However, the values are greater than those found by Inoue *et al*[10], who performed hydrogen oxidation experiments on Ru{0001} and Ru{1010} single crystal electrodes in 0.05 M H_2SO_4, reporting exchange current density values of 0.13 and 0.16 mA cm^{-2} respectively. This would support the effect of doubling concentration causing a doubling of exchange current density (assuming

that there is no significant difference between j_0 values on single crystal Ru surfaces and polycrystalline Ru). A twofold increase in Inoue's results would give a range of 0.26 – 0.32 mA cm^{-2} (for a hypothetical 0.1 M H_2SO_4 electrolyte) which corresponds well to the values of 0.24 – 0.27 mA cm^{-2} found in this project using 0.1 M H_2SO_4.

An interpretation of the high exchange current densities found throughout this section of the project may be through a discrepancy in the determination of the electrode areas as a result of contamination. It was assumed that the polycrystalline Pt electrode and the electrolytes were clean as reproducible CVs were obtained. It was therefore also assumed that the charge on the surface was measurable from the area of the UPD-H charge on the CV (as explained in section 2.1.1.2) and the UPD-H charge density was assumed to be approximately 210 μC cm^{-2} for a polycrystalline surface. However, if there were contaminants present and the surface was partially blocked, the charge density would be lower than the assumed value and hence the real electrode area would be higher than the calculated value (from equation (2.1.13)) which would give lower exchange current density values than those previously reported in section 4.1.

The transfer coefficients on all of the Ru surfaces tested lie within a narrow range and are in agreement with those for Pt and Ir.

The Ru standard rate constants are very low in comparison to the other two materials. The standard rate constant values are fairly consistent between the three Ru surfaces tested, giving a range of 0.11 – 0.13 x 10^{-4} cm s^{-1}. The narrow data range shows that the Ru surfaces are fairly reproducible using the preparation method described in section 3.1.2.1 (this is in agreement with the findings from the other two parameters, α and j_0, which also lie within a relatively narrow range). However the HER activity of the plated Ru surfaces is relatively low. This low activity of the Ru electrode is thought to arise due to ruthenium oxides on the surface.

5.2 Multi-Frequency AC Voltammetry

5.2.1 Varying acid concentration

Multi-frequency AC voltammetry was performed on polycrystalline platinum to investigate how hydrogen evolution on Pt varied with frequency. Other parameters were also changed (electrolyte concentration, H_2 overpressure, rotation rate and temperature) and their influence on the frequency response monitored. The Pt electrode was tested in 0.05 and 0.25 mol dm^{-3} H_2SO_4. The voltammograms in both instances gave very similar shapes (and looked alike when plotted on their relative scales) which shows that the same process is occurring in both systems. Yet, it can be seen that the magnitude of the MFACV in the more concentrated solution (fig. 4.2.1 (b)) is much greater than the less concentrated solution (fig. 4.2.1 (a)). This highlights the direct effect of concentration on electrochemical rate, especially when considering the magnitude of the admittance density in the hydrogen evolution region. The electrode in 0.05 M H_2SO_4 reaches a maximum value of 0.025 Ω^{-1} cm^{-2} on the admittance density axis, whilst in 0.25 M H_2SO_4, a value of 1.20 Ω^{-1} cm^{-2} is reached. This shows directly a fivefold increase in concentration leading to a fivefold increase in admittance density. It can be seen that at the most negative potentials, the admittance density of the MFACV in 0.05 M H_2SO_4 reaches a plateau where it does not increase further. This was not investigated in more depth at the time, but was later found to occur on Pt single crystal surfaces and is discussed in more detail in section 5.3.1.

There is a small hysteresis on the voltammograms, which is more visible on the 0.25 M H_2SO_4 voltammogram (due to the scale) (fig. 4.2.1 (b)). This is a result of hydrogen bubbles forming at the electrode surface at the negative potentials of roughly -0.09 V *vs.* RHE (-0.38 V *vs.* Ag/AgCl, -0.15 V *vs.* Pd/H).

5.2.2 Varying the H_2 overpressure

The gas used to degas the system (Pt in 0.25 M H_2SO_4) was varied, using N_2 and H_2. The gas was then used as a blanket atmosphere in both cases to keep oxygen and any airborne contaminants from entering the solution. Fig. 4.2.2 shows the two voltammograms taken under each of these conditions. There is a strong variation in the shape of the voltammograms, which seems to show a suppression of the hydrogen evolution under hydrogen atmosphere as the two systems are swept to the same potential, yet only a very small amount of hydrogen is evolved under a hydrogen atmosphere compared to that measured under a nitrogen atmosphere. This may be rationalised as a consequence of the solution being already saturated with hydrogen. Hence, it becomes more difficult to introduce more hydrogen (evolved from the working electrode) into the solution. Therefore, an increased driving potential is required, i.e. the potential must be swept further negative before hydrogen is evolved.

5.2.3 Rotating Disk MFACV

The working electrode was rotated and the rotation rate varied to study the effect of this variation on the multi-frequency AC voltammetry. Fig. 4.2.3 shows some of the voltammograms taken, on the stationary electrode and at rotation rates of 1000 – 3000 rpm. Subsequent runs at higher rotation rates (up to 5000 rpm) showed no change in the voltammetry and for that reason have not been presented in fig. 4.2.3. It can be seen that hydrogen evolution is suppressed as rotation rate is increased, to the point where virtually no activity is observed at all. Unfortunately this is not thought to be an effect directly related to rotation rates, but more a feature of contaminants within the electrolyte. The faster the working electrode is rotated, the more contaminants are drawn to the electrode surface, which adsorb thus decreasing the activity. Even if the solution appears to be very clean, with insignificant contamination effects under stationary conditions, this is unlikely to be the case when rotated, particularly at high rotation rates. This was also observed when rotating disk experiments were performed on clean single crystal electrodes. Though they are highly susceptible to contamination, the stationary electrodes gave good clean DC cyclic voltammograms,

but the peaks diminished in magnitude when rotated. This would suggest that the rotating results taken in section 4.1 should be the result of contamination. It may be that the timescale of the MFACV experiments is relatively long compared to the DC measurements (approximately 20 minutes and 30 seconds respectively). Hence, the MFACV experiments contaminate over the timescale of the test, whilst the faster linear sweep voltammetry does not.

5.2.4 Temperature dependence of MFACV

Multi-frequency AC voltammograms were taken on Pt in 0.25 M H_2SO_4 at a range of temperatures between 278 and 318 K (5 – 45 °C). An interesting trend was noted and was reproducible on repeat runs. The measurements were taken over the same potential range, between 0.30 and -0.38 V *vs.* Ag/AgCl (0.53 to -0.15 V *vs.* Pd/H as shown in fig. 4.2.4, or 0.59 to -0.09 V *vs.* RHE), under N_2 atmosphere. Initially, the temperature was varied in increments of roughly 10 K (278, 288, 295 (atmospheric temperature), 308, 313 and 318 K) as shown in fig. 4.2.4. It can be seen that the hydrogen evolution activity increased with temperature, reaching a limit around 308 K then decreasing with subsequent runs at higher temperatures. Average values of admittance at each temperature have been plotted in fig. 5.2.1. A linear increase of admittance density is observed up to 308 K, which is followed by a sharp decrease in admittance density as the temperature is raised further.

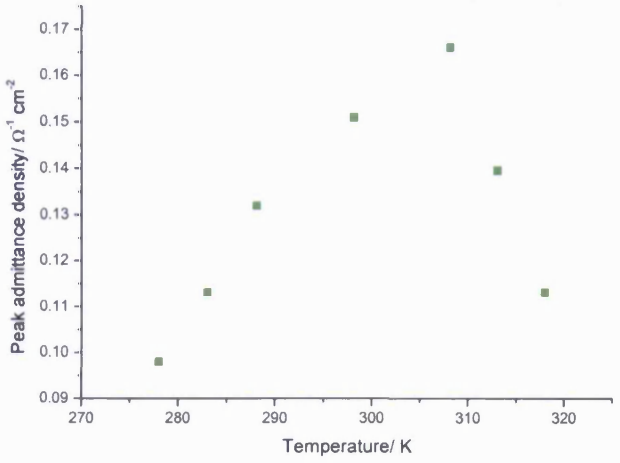

Fig. 5.2.1 Graph showing the relationship between temperature and peak admittance density in MFACV studies on Pt in 0.25 M H_2SO_4.

This trend is thought to be related to contaminants as opposed to a genuine kinetic effect of the activity of the electrode decreasing at temperatures above 308 K. It may be that the mobility of any contaminants within the solution is enhanced at higher temperatures. This would result in more contaminants colliding with and adsorbing to the electrode surface, causing a decrease in activity and therefore a lower admittance density peak in the hydrogen evolution region. However, it is noted that it is unlikely that there is a particular temperature at which the contaminant mobility is suddenly increased. It is more likely that a constant increase throughout the temperature range investigated is to be expected. DC temperature dependent measurements were performed to investigate this phenomenon further.

5.2.5 DC temperature dependence measurements

Tafel data was taken for Pt in 0.05 M H_2SO_4, purged with H_2 and varying the temperature between 273 - 323 K, specifically at 273, 283, 293, 303, 313 and 323 K. The Tafel data was taken using a rotating disk electrode, rotating at 900 rpm for direct comparison with temperature dependent studies by Markovic *et al*[2]. The results were analysed using the same method as in Markovic's paper, as described in section 4.2.5. The Tafel plots gave exchange current densities similar to those found by Markovic *et al*[2]. The data are shown in table 5.2.1. It can be seen that the experimentally obtained exchange current density values for polycrystalline Pt all lie within the range of those seen by Markovic for single crystal electrodes. At low temperatures the polycrystalline results agree closely with the published results for Pt{100} whilst at higher temperatures they tend more towards the Pt{110} values. Nonetheless, no peak in the value of j_0 as a function of T was found in the DC measurements. Rather, j_0 was found to increase continuously with T, a normal aspect of electrochemical rate data. The logarithm of exchange current density was plotted against the reciprocal of the temperature (fig. 4.2.6), giving a linear Arrhenius plot which is in good agreement with Markovic's results for single crystal Pt electrodes. This shows that the results are consistent with previously published data[2].

Temperature/ K	Exchange current density/ mA cm^{-2}			
	Experimental value	Literature values[2]		
	Polycrystalline Pt	Pt{111}	Pt{100}	Pt{110}
274	0.37 (273 K)	0.21	0.36	0.65
283	0.45	0.25	0.38	0.72
293	0.63	0.36	0.46	0.84
303	0.75	0.45	0.60	0.98
313	1.00	0.53	0.67	1.07
323	1.21	0.74	0.71	1.24

Table 5.2.1 Exchange current density values at various temperatures.

The gradient of the arrhenius plot gives the activation energy for the hydrogen oxidation reaction (and hydrogen evolution reaction), i.e. the apparent enthalpy of activation at the reversible potential, $\Delta H^{0\#}$, where

$$\frac{\partial \log j_0}{\partial (1/T)} = -\frac{\Delta H^{0\#}}{2.3R_g} \qquad \textbf{(5.2.1)}$$

The value found from the present results is 19.1 kJ mol^{-1}, which is in the same range as that found by Markovic on a Pt{111} electrode (18 kJ mol^{-1}). Markovic also found lower values for $\Delta H^{0\#}$ for the other two basal plane single crystal surfaces (9.5 kJ mol^{-1} and 12 kJ mol^{-1} for Pt{110} and Pt{100} respectively), though they are still within the same ranges as the values determined in this study.

Cyclic voltammograms were also recorded on polycrystalline Pt under the same conditions as employed for the Tafel data, but using N_2 for degassing the electrolyte/overpressure and at a greater number of temperatures, particularly in the range 303 – 323 K where the MFACV showed that the electrode was decreasing in its HER activity.

The cyclic voltammetry (fig. 4.2.7) showed an interesting trend with temperature. The charge under the oxide forming and stripping regions of the voltammogram increased with temperature, i.e. the oxide layer is more readily adsorbed (and hence is thicker, with more oxide adsorbing to the electrode). This trend was also recently observed in a similar experiment conducted by Jerkiewicz *et al*[11], though more quantitatively with cleaner voltammetry.

The DC measurements, both Tafel measurements and cyclic voltammograms show a continual increasing trend as temperature increases. Tafel data show exchange current density increasing with temperature whilst CVs show an increasing oxide region area. This implies that the relationship between admittance density and temperature shown in fig. 5.2.1 (i.e. the HER activity decreasing above approximately 308 K) is solely related to the MFACV method. However, closer inspection of the DC results may offer an explanation. It can be seen that the potential of the CVs is shifting negative with increasing temperature. This translates to the reference electrode being affected by the temperature either through an increase in the mobility of Na^+/Cl^- ions within the electrode or the variation of pH of the electrolyte. This feature can also be observed on the Tafel slopes in fig. 4.2.5 as the overpotential of the exchange current is shifting positive with increasing temperature (this was taken into account when calculating j_0 and therefore the calculated value of $\Delta H^{0\#}$ will not be affected). The potential shift in the DC measurements can then be used to rationalise the apparent trend in the MFACV data. The admittance density increases with temperature and at temperatures below ~ 308 K the reference potential shift is small enough that the admittance density increase is still observable. Whereas, at temperatures above 308 K the potential has shifted far enough that the admittance peak is significantly negative of the lowest potential in the sweep parameters. Thus, the assumed admittance peak is actually at a potential more positive of the actual peak, making it appear as thought the limiting admittance density is decreasing when in reality it is likely to be increasing.

5.3 Single crystal electrode studies

The conditions and experimental arrangements for the remainder of the investigation were very different to those in the previous sections. Single crystal electrodes are highly susceptible to the adsorption of contaminants. Contaminants impact more significantly on the voltammetry of single crystals due to the sharpness of the voltammetric peaks, arising from the highly ordered nature of the surface. Small concentrations of contaminants will noticeably reduce the intensity of such well defined voltammetric peaks due to adsorption to the single crystal electrode surface, leading to blocking of sites for hydrogen adsorption. The experimental setup employed for single crystal studies was described in section 3.3. The main alterations to the system in relation to the earlier studies included the cell (fig. 3.3.1) which was fitted with gas inlets and stoppers in order to keep out air and maintain an overpressure of inert gas. The electrolytes were all prepared from concentrated Aristar grade sulphuric acid, diluted with ultrapure water (18 MΩ cm) in clean glassware (cleaned as described in section 3.3) and hence contained minimal contaminants. This was supported by the cleanliness of the cyclic voltammograms. A Pd/H reference electrode was used (instead of Ag/AgCl) as it may be cleaned by heating in a Bunsen flame. There is also no chance that it will leach chloride ions into the solution as may occur with Ag/AgCl reference electrodes.

This led to a large amount of time being spent on ensuring the cleanliness of the system, which often consisted of multiple cleaning attempts using cleaning methods which regularly required soaking in strong oxidising acids over long periods of time.

5.3.1 Cyclic voltammetry and MFACV studies

Good cyclic voltammetric data was obtained for the three basal plane single crystal Pt surfaces ({111}, {100}, {110}) and various stepped Pt surfaces between {111} and {100} on the stereographic triangle ({755}, {533}, {211}, {311}, {511}, {711}, {911}, {11,1,1} and {13,1,1}). The reproducibility of these voltammograms and their similarity to the accepted voltammetric profiles[12] shows that the cell and electrolyte were clean, hence further tests could be reliably conducted on the surfaces.

Multi-frequency AC voltammetry was then performed in the hydrogen evolution region on each of these surfaces in order to investigate any structure specificity. As explained previously, there has been much debate between groups as to whether the hydrogen evolution reaction is dependent upon single crystal surface structure[2, 13] or not[3, 14, 15]. Hence, the issue is not fully resolved. These experiments on single crystal electrodes hope to shed some light on the issue.

HER activity comparisons were taken from the limiting admittance density; i.e. the point on the MFACV plot ($1/Z$ versus ω versus E) at which the admittance density reaches a plateau. The greater this value, the faster the HER rate.

A graph of limiting admittance density versus crystal step density (i.e. number of {111}x{100} or {100}x{111} steps per cm^2 of electrode area) was plotted (fig. 4.3.6) to investigate a structural dependence for the reaction rate.

It was noted from this graph that Pt{111} had a relatively high admittance density plateau, which decreased with decreasing {111} terrace width/ increasing {100}x{111} step density, until the structure approached the turning point on the relevant side of the stereographic triangle. From {211}, approaching the turning point, {311}, where step density is a maximum, the admittance density increased and reached a maximum at {311}. The Pt{511} surface, which is close to {311} on the stereographic triangle (on the branch of decreasing {111}x{100} step density between the turning point and {100}) also gave a relatively high admittance density plateau. The admittance density plateau then decreased with decreasing {111}x{100} step density/ increasing {100} terrace width.

This implies a structure sensitivity for HER rate on Pt, which decreases with increasing surface density of {100}x{111} steps for Pt(s)[n{111}x{100}] crystals and

increases with decreasing surface density of {111}x{100} steps for Pt(s)[n{100}x{111}] crystals. However, both of these trends break down near the turning point {311} where the HER rate increases to a maximum.

Subsequently, it was then noted that, despite the data already being normalised to surface area, there appeared to be a trend relating decreasing admittance density with single crystal electrode area. A graph of admittance density plateau versus reciprocal crystal area was therefore plotted (fig. 4.3.7) which confirmed this trend.

Hence, there is a further factor relating to electrode area which is affecting the HER rate on Pt. It is proposed that this relates to the edge sites of the electrode. The smaller the circular electrode surface, the greater the ratio of edge sites to surface plane sites, (simply an argument of geometry). If these edge sites are more active for HER, the rate will be faster on small electrodes even after normalisation to surface area.

It is suggested the edge effects may be crucial as a consequence of the electrode/electrolyte/gas interface in a hanging meniscus configuration. If H_2 is able to diffuse away from the electrode surface into the gas phase more quickly at the edge compared to when desorbing from the electrode surface into the electrolyte, then the faster H_2 can be evolved.

MFACV experiments also record data besides potential, frequency and admittance. Phase angle, time and the real and imaginary components of impedance are also recorded. Phase plots (phase angle versus frequency versus potential) for some of the single crystal surfaces investigated in this chapter are shown in fig. 4.3.5. They show a frequency dependence in the UPD hydrogen region (which is also observed on the admittance magnitude plots) but no frequency dependence in the hydrogen evolution region, where the phase angle also drops away to zero on each of the surfaces. The zero phase angle is generally associated with a pure resistor, hence there is no capacitative effect at these frequencies in the hydrogen evolution region. Phase plots can be useful when a hysteresis is seen on the admittance plots, as the hysteresis relates to the process occurring in a different manner on the forward and reverse potential sweeps. The phase plots are independent of electrode area and will only show the hysteresis of the admittance plots if the surface has chemically changed. If the hysteresis is related to a decrease in area due to contaminants deactivating sites or hydrogen bubbles forming on the surface, this will not be observed in the phase plot.

Fortunately none of these single crystal MFACVs show hysteresis on the admittance plots and the electrodes/electrolytes were tested for cleanliness before and after each experiment using cyclic voltammetry.

The single crystal electrodes show similar MFACVs to those on polycrystalline Pt in the less clean configuration used in the earlier part of the project, though the admittance is significantly higher for the single crystal electrodes when considering the concentrations of the sulphuric acid electrolytes (0.1 M for the single crystal electrodes, 0.25 M for the polycrystalline electrode). A plateau is observed for the limiting admittance density of the single crystal electrodes when the potential is swept sufficiently negative into the hydrogen evolution region. The plateau region was also observed on a roughened (polycrystalline) single crystal Pt surface (fig. 5.3.1).

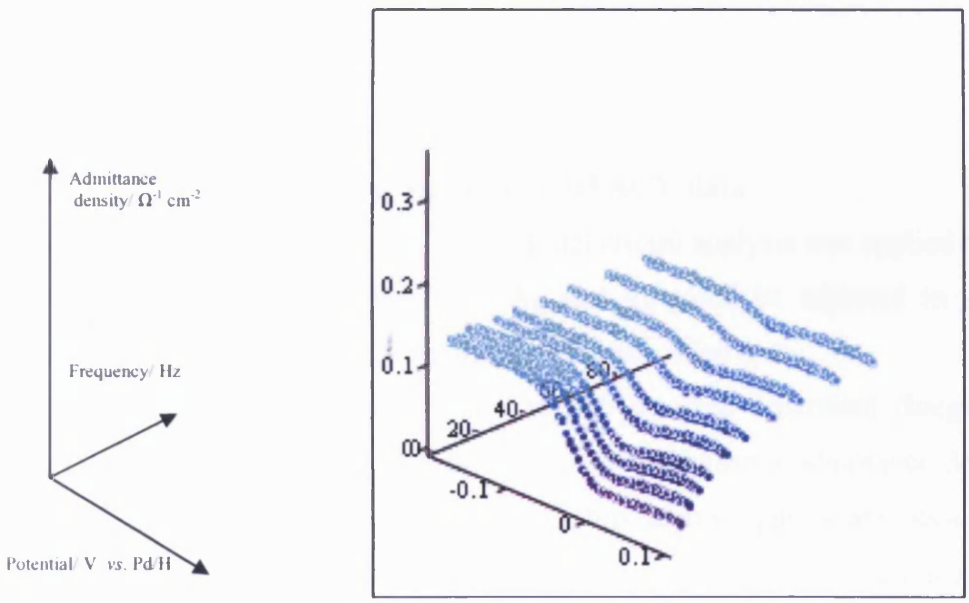

Fig. 5.3.1 MFACV of roughened Pt{111} in 0.1 M H_2SO_4.

The MFACV of roughened single crystal Pt showed a similar shape to those observed for the single crystal electrodes, with an admittance density plateau of 0.13 Ω^{-1} cm^{-2}. This value does not agree well with the results taken for the single crystal electrodes in comparison with graph 4.3.7 (admittance density plateau versus 1/area) as the high electrode area of 0.139 cm^2 should give an even lower admittance density plateau (approximately 0.07 according to graph 4.3.7), though it is in a similar range.

In comparison with the previous polycrystalline data (section 4.2.1, fig. 4.2.1(a)), it is observed that the admittance definitely does show a plateau on the polycrystalline Pt electrode at potentials negative of -0.10 V *vs.* Pd/H. The polycrystalline data from

section 4.2.1 also showed the plateau around – 0.1 V *vs.* Pd/H. It is therefore surprising to see such a difference in the admittance density plateaus in the two electrolytes, 0.03 Ω^{-1} cm^{-2} and 0.13 Ω^{-1} cm^{-2} in 0.05 M H_2SO_4 and 0.10 M H_2SO_4 respectively. It may be possible that this is related to the different electrode configurations. In the earlier setup using a polycrystalline Pt electrode encased in nylon, only the flat Pt surface was exposed and submerged in the electrolyte. The use of a hemispherical bead electrode in meniscus contact with the solution is thought to lead to an enhancing effect on the HER due to the electrode/electrolyte/gas interface (as described earlier in this section and discussed in further detail in section 5.3.2), though this is unlikely to cause such a dramatic effect as that seen here. This implies that, for the 0.05 M H_2SO_4 result, there may also be an effect due to contaminants deactivating Pt sites without affecting the HER mechanism, which are not present in the cleaner solution.

5.3.1.1 Model circuit analysis of MFACV data

As shown in section 4.3.1.1, a model circuit analysis was applied to the MFACV data, where three parameters (R_0, R_S and α) could be adjusted in order to simulate a MFACV plot of the same shape as the recorded data.

R_0, the pre-exponential factor in the potential-dependent charge-transfer resistance term, was found to vary linearly with the limiting admittance density value and the reciprocal of area. This relationship seems appropriate because as surface area increases, the charge transfer resistance decreases and since it has been shown that there is a linear relationship between limiting admittance density and 1/surface area, there should also be a linearity between limiting admittance density and charge transfer resistance. It can also be seen that the region over which the charge transfer resistance is influential (i.e. the region between the onset of hydrogen evolution and the admittance density plateau) ranges over approximately the same potential region for each of the surfaces (between 0 and -0.1 V). Hence, the rate of increase of R_{CT} (and therefore R_0) will depend upon the limiting admittance density. There was no systematic variation of R_0 with the crystallographic step density, implying there is no dependence of HER on surface structure.

The series resistance in the model circuit analysis, R_S, is a more complicated term as it may represent many resistances in the electrochemical system which may not be

separated from each other due to the frequency independence of the recorded data. Referring back to the simulation equations (4.3.4) – (4.3.6) it can be seen that at the limiting admittance potentials

$$R_S = Z \tag{5.3.1}$$

Hence, the limiting admittance density is given by

$$Y_{lim} = \frac{1}{R_S A} \tag{5.3.2}$$

Therefore $1/R_S A$ should vary linearly with limiting admittance density. This linear relationship is shown in fig. 5.3.2, which is effectively the raw limiting admittance value versus $1/R_S$. The good linear fit shows that the simulated R_S values are essentially the same as the limiting impedance values from the experimental data.

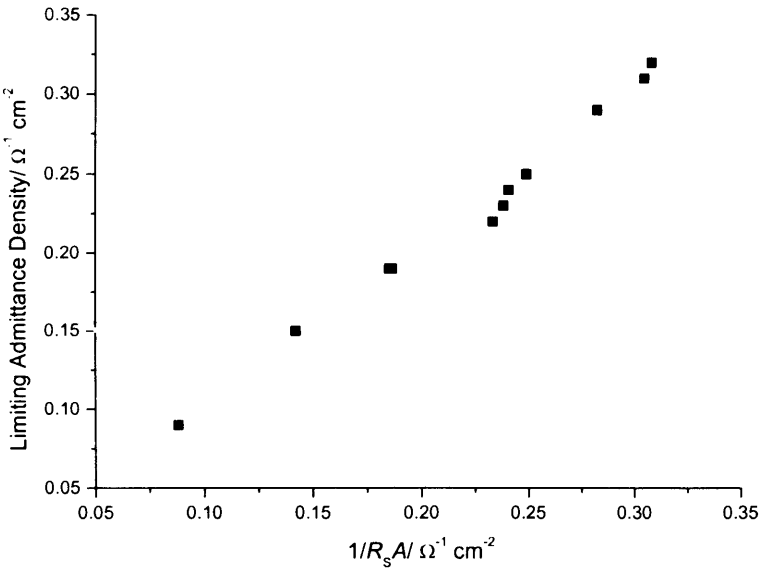

Fig. 5.3.2 Graph of limiting admittance density versus $(R_S A)^{-1}$.

The transfer coefficient, α, showed little significant variation when plotted against any of the three factors investigated (limiting admittance density, 1/area and crystal step density) and any variation observed was not linked to these factors.

5.3.2 CO blocking experiments

In order to investigate the influence of the hanging meniscus electrode configuration (specifically the effect of the crystal edge/electrolyte/gas interface) in relation to HER an experiment was devised to eliminate these effects. Experimental details are explained in sections 3.6 and 4.3.2. The general premise of this experiment is that CO blocks the edge sites of the electrode being tested, such that a measurement which is independent of these sites may be taken.

As explained in section 4.3.2, the timescale for multi-frequency AC voltammetry experiments was relatively long (approximately 10 minutes) during which time the CO was gradually removed from of the electrode (as shown in fig. 4.3.13) rendering the results invalid. Therefore the tests were performed under DC, steady state conditions (potential swept between 0.1 and -0.1 V with a sweep rate of 0.005 $V s^{-1}$, in 0.5 M H_2SO_4, such that the conditions were similar to published work by Gomez *et al*[3]). This allowed the tests to be conducted on a much faster time-scale, such that CO was still adsorbed on the electrode surface at the end of the experiment. The cyclic voltammetric data did not change throughout each test.

A number of important data sets were collected for each electrode in the three electrode configurations involved in the experiment:

(i) the clean annealed single crystal in the hanging meniscus position,

(ii) the CO coated crystal in the hanging meniscus position with CO electrochemically stripped from the surface,

(iii) the partially submerged electrode with the flat surface exposed to the electrolyte but with its hemisphere still blocked by CO.

Exchange current density was plotted as a function of step density and reciprocal of electrode area for each of these electrode configurations. The cyclic voltammograms obtained are shown in fig. 4.3.14, whilst plots of the exchange current densities versus atomic Pt step density and 1/area are shown in figs. 4.3.15 – 4.3.20.

The exchange current density values obtained from the DC experiments for each annealed single crystal in the hanging meniscus conformation followed the same trend as the MFACV data taken previously. The shape of the exchange current density versus step density graph (fig. 4.3.15) matched well with the limiting admittance density versus step density graph (fig. 4.3.6). Similarly, the DC graph of exchange

current density versus reciprocal electrode area (fig. 4.3.18) showed a trend which agreed with that seen for the AC graph of limiting admittance density versus reciprocal electrode area (fig. 4.3.7).

The data for the CO coated electrode in the hanging meniscus configuration showed a similar trend, although it was much less pronounced and all exchange current densities were lower than their annealed equivalents, despite cyclic voltammetry data matching well. This shows that the edge sites must be partially deactivated by the CO. The nature of this deactivation is uncertain; one notion could be that CO physically hinders the diffusion of H_2 into the gas phase, thereby slowing the rate of evolution of hydrogen. However it is unlikely that such a significant decrease in rate would be observed as a result of such behaviour.

Interpretation of the clean, annealed and CO-coated beads in the hanging meniscus configuration is facilitated by use of a model in which atomic hydrogen is mobile over Pt surfaces[16]. As hydrogen is evolved rapidly via the Volmer mechanism, faster than it can recombine via the Tafel mechanism (which is the rate determining step for the HER on Pt, see section 1.2) at the electrode/electrolyte interface, the concentration gradient becomes so great that hydrogen is forced to migrate onto the hemisphere of the electrode. Here it can recombine outside of the solution and desorb as H_2. Hence, when the hemisphere of the electrode bead is covered with adsorbed CO, the mobility of H over the hemisphere surface is hindered, lowering the rate at which hydrogen may be evolved from the surface in the close proximity of the electrolyte. If the entire hemisphere was involved in the process, the larger electrodes would show a greater rate enhancement for the clean annealed surface as the hemisphere area is approximately equal to $2\pi r^2$ (where r is the radius of the electrode). HER rate would therefore increase directly with surface area, πr^2. This is not found to be the case, as it can be seen that the HER rate is enhanced more on the smaller electrodes than the larger ones. Therefore only a small area of the hemisphere is involved in this process, which is likely to be a similar area for all the bead sizes (since it is governed by diffusion rate not total size) and so will have a greater effect on small crystals. It is therefore only a small, localised region of the hemisphere, close to the electrolyte over which the hydrogen is able to migrate (fig. 5.3.3).

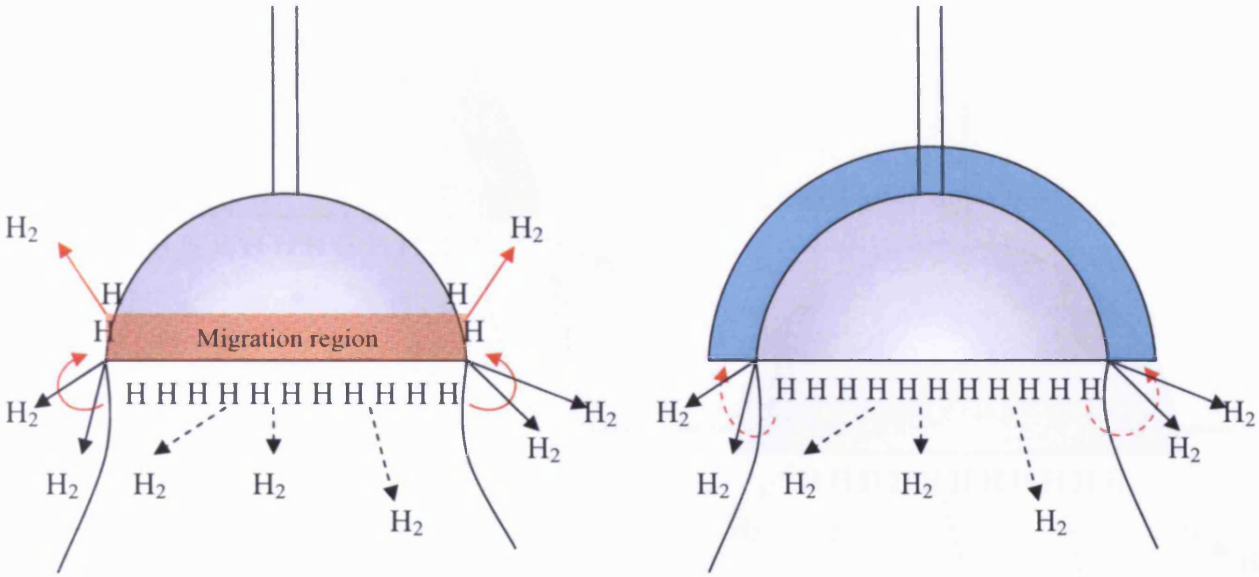

Fig. 5.3.3 Two-dimensional schematic diagram showing H migration across Pt surface (represented by red arrows) and blocking by CO adsorbed to the surface (the blue region represents CO adsorbed on the hemisphere of the electrode).

Comparison of the CO coated bead in the hanging meniscus and partially submerged bead configurations also showed a discrepancy in exchange current density values. The data for the partially submerged electrode showed no significant trends for exchange current density with respect to step density or crystal area (fig. 4.3.17 and 4.3.20). This shows that there must be a further effect which is slowing the hydrogen evolution between the CO blocked hanging meniscus and partially submerged bead configurations. It is highly likely that this is related to the electrode/electrolyte/gas interface and the ability of H_2 to diffuse away from the electrode more readily into the gas phase than into the electrolyte. The decrease in j_0 on the CO coated bead is relatively small between the hanging meniscus and submerged electrode configurations. This decrease is related to area in a similar manner as the larger decrease observed between the annealed and CO coated beads in the hanging meniscus configuration. The smallest electrodes show a greater j_0 decrease than the larger ones. This is represented schematically in fig. 5.3.4.

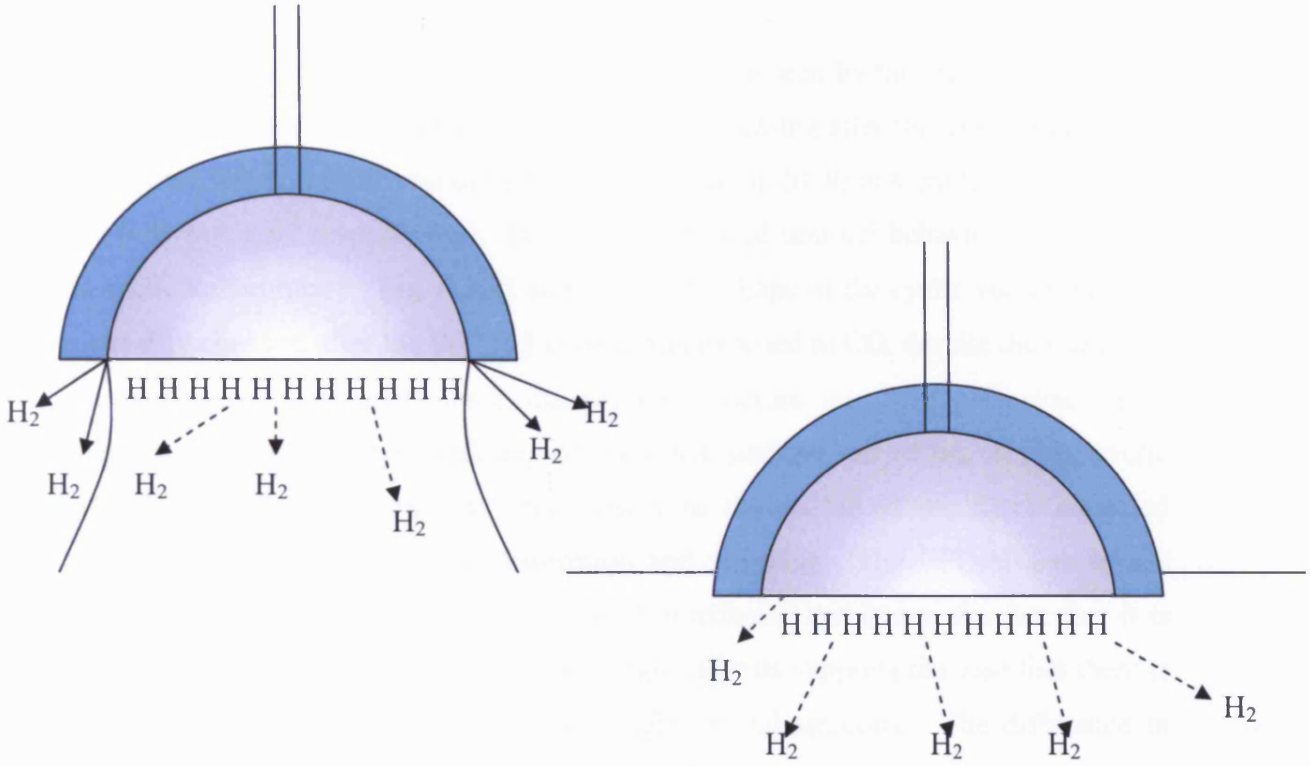

Fig. 5.3.4 Two-dimensional schematic diagram, highlighting the enhanced hydrogen evolution from edges at the electrode/electrolyte/gas interface comparing CO coated electrode hemispheres in the hanging meniscus and submerged bead configurations.

The exchange current density values for the submerged electrode are considerably lower than those found by Gomez *et al*[3] using single crystal electrodes in the same electrolyte (0.48 – 0.56 mA cm^{-2} compared to 0.84 – 0.97 mA cm^{-2}). Gomez *et al* also use single crystals manufactured by the Clavilier bead method with just the planar faces exposed (as seen by cyclic voltammograms[17]) and with no holder or resin delimiting the electrode from the electrolyte[18], in the hanging meniscus configuration. It is speculated that Gomez *et al* would also find a similar decrease in j_0 if they were to eliminate the hanging meniscus effect. Comparing the data from this project for the exchange current density values in the hanging meniscus configuration, it is the relatively small electrodes which show values similar to those of Gomez's work. Thus it is predicted that the electrodes used by Gomez *et al* are of surface areas in the range of 0.028 – 0.038 cm^2.

The Pt{311} single crystal electrode obeyed the trend seen by the other single crystal electrodes in terms of exchange current density decreasing after the CO treatment and again after being partially submerged into the solution (0.90 mA cm^{-2}, 0.54 mA cm^{-2} and 0.53 mA cm^{-2} respectively). However, it showed unusual behaviour in terms of its cyclic voltammetry. Fig. 4.3.21 shows that the shape of the cyclic voltammogram invariably changed after the Pt{311} crystal was exposed to CO, despite the CO being electrochemically stripped, hence the surface structure was being affected. This phenomenon was not seen with any of the other surfaces, all of which gave cyclic voltammograms which matched very closely to the profile of the flame annealed crystal before and after the CO adsorption and stripping. The UPD-H area of the cyclic voltammogram of Pt{311} has not been affected and hence, the fact that it is still showing the same trend as the other single crystals supports the case that there is no dependence of the HER activity on single crystal structure. The difference in exchange current density values between individual single crystal electrodes is related to the crystal area (more specifically the edge seffects).

5.3.2.1 Fitting rate constants to single crystal Tafel data

The Volmer and Tafel rate constants were found for a range of stepped single crystal Pt electrodes in the three electrode configurations described in section 5.3.2 using a computational fitting routine. The data is displayed in tables 4.3.3 – 4.3.5. No prominent trends are observed when plotting the Volmer or Tafel rate constants against exchange current density, the reciprocal of crystal area or even crystal step density. This is consistent with little structural dependence of HER rate.

5.3.3 Pt{111} crystals of different sizes

A further test was constructed to investigate the findings relating to exchange current density dependence on area as opposed to single crystal structure. Two similar, flame annealed Pt{111} crystals of different sizes were tested in the hanging meniscus configuration and measured for exchange current densities. The results can be seen in table 4.3.6. It can be seen that the smaller crystal gave a significantly higher exchange current density than the larger one, supporting the present findings that hydrogen evolution is dependent upon single crystal electrode area (specifically related to edge sites) as opposed to surface structure. Both values are in good agreement with data taken in the hanging meniscus configuration for the experiments in section 4.3.2, and would fit well on the graph of exchange current density versus reciprocal electrode area (fig. 4.3.18). Of course the larger crystal would not support the hypothetical trend relating to structure dependence of hydrogen evolution detailed in section 4.3.1 (fig. 4.3.6). The cyclic voltammograms of the two Pt{111} surfaces are shown in fig. 5.3.5.

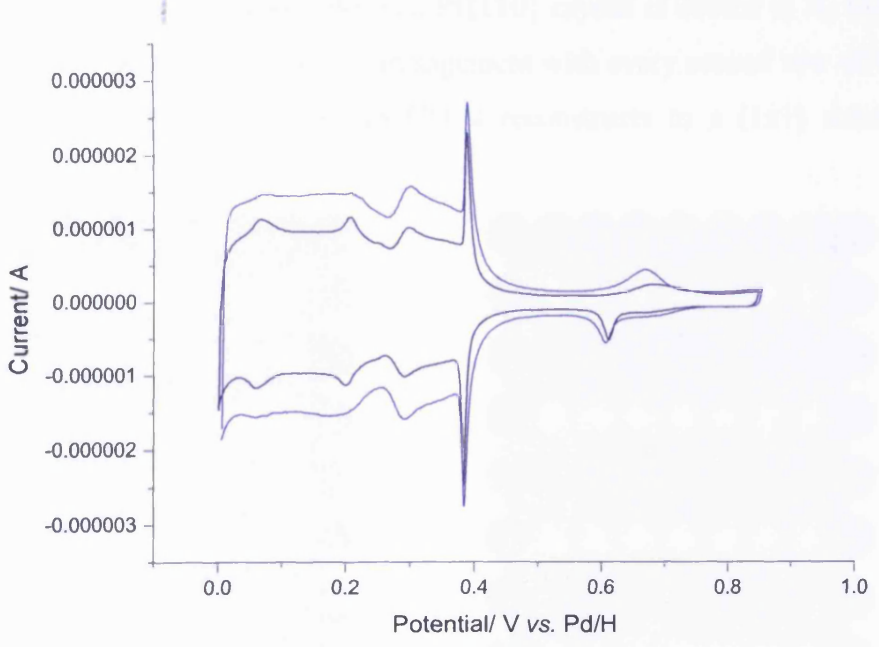

Fig. 5.3.5 Cyclic voltammograms of the two Pt{111} crystals under investigation in section 4.3.3, in 0.5 M H_2SO_4 at potential sweep rate 0.05 V s^{-1}.

5.3.4 Pt{110} and different cooling methods

At this point, we have seen that there is no dependence of hydrogen evolution rate on Pt single crystal surfaces between {111} and {100} on the stereographic triangle once edge effects are eliminated. This is in agreement with previous work by the Lipkowski[15] and Feliu[3] groups. However, looking at Feliu's exchange current density values, it can be seen that Pt{111} and {100} give the same value, 0.84 mA cm^{-2}, whilst the figure quoted for Pt{110} is significantly higher at 0.97 mA cm^{-2}. This is overlooked in terms of a structural dependence and is said to be within error. Coincidentally, the works by Conway[13] and Markovic[2] which support the structure sensitivity of HER on Pt single crystals also quote Pt{110} as having the fastest rate for HER in acid.

It was therefore thought to be important to address Pt{110} as the structural dependence analysis so far in this project has been based on single crystal surfaces lying between {111} and {100} on the stereographic triangle.

An interesting phenomenon associated with the Pt{110} surface which has been exploited in this test was the formation of two different structures of the surface when cooled in different atmospheres. When a Pt{110} crystal is cooled in H_2 the surface reconstructs in a partial (1x2) atomic arrangement with every second row of top layer atoms absent[19], but when cooled in CO it reconstructs to a (1x1) arrangement, (shown schematically in fig. 5.3.6).

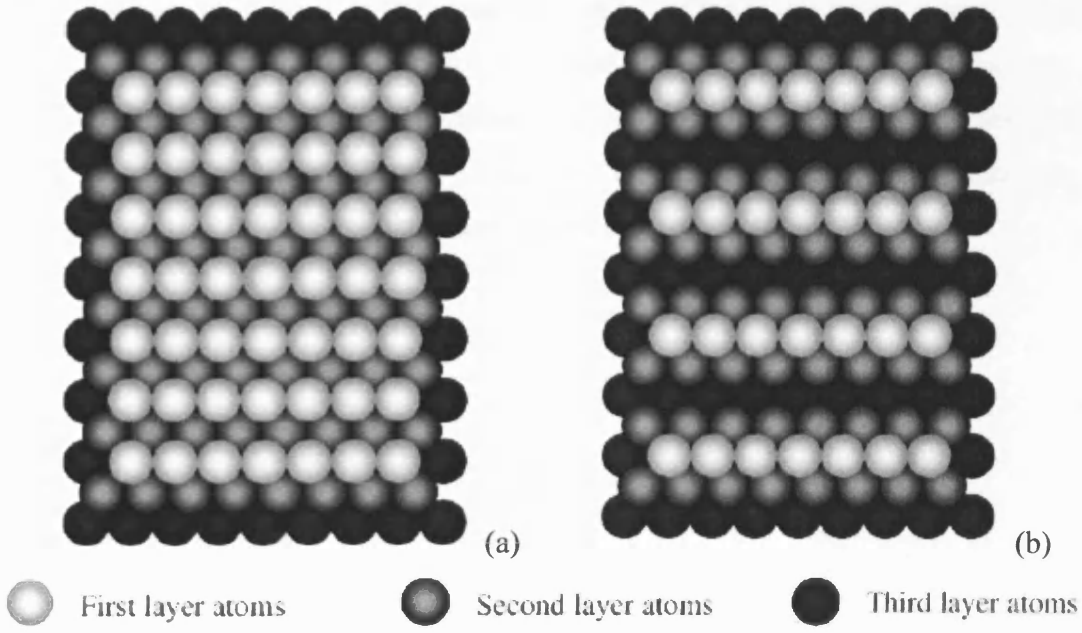

Fig. 5.3.6 Schematic diagram of Pt{110} in (a) 1x1 and (b) 1x2 reconstruction[20].

The cyclic voltammograms in fig. 4.3.25 show that the different cooling methods have resulted in different surface reconstructions of the Pt{110} electrode, yet neither a perfect {1x1} or {1x2} reconstruction was achieved. Instead two intermediate surfaces were achieved. However, they were sufficiently different to warrant further investigation. Hence, the CO coating/electrode submersion experiment was performed as with the single crystal surfaces (as described in section 3.6).

As can be seen in table 4.3.7 the exchange current density values of the flame annealed crystal are relatively low, as expected due to the large electrode area (0.098 cm^2). There is a small decrease in j_0 when the crystal bead is coated in CO and little or no significant change when the electrode is partially submerged. The data for the two surface reconstructions agree very closely, showing no significant dependence upon surface structure at all. The figures also fit with the exchange current density versus 1/area graphs for the previously tested single crystal electrodes in the three investigated electrode configurations (figs. 4.3.18 – 4.3.20). This, then contradicts the findings of Conway *et al*[13] and Markovic *et al*[2]. Rather, in the present study at least, there is no dependence of exchange current density on single crystal structure.

The structural dependence observed by Markovic and Conway must therefore be related to the experimental processes used. Markovic's work utilises cylindrical Pt electrodes with single crystal surfaces, flame annealed, cooled in H_2 and mounted in a rotating ring disk electrode holder[21]. The high exchange current densities observed must therefore be related to the rotation of the electrode. However it is not known precisely why the Markovic group see a variation of j_0 with surface structure. It would be useful if, in future, systematic measurements could be performed in the Markovic configuration. Then it may be expected that systematic changes in exchange current density as a function of step density would be observed.

5.4 Surface Modified Pt{*hkl*} electrodes

5.4.1 Epitaxial single crystal metal films

Thick films of Pd, Rh and Ru were deposited onto a Pt{111} single crystal electrode (0.022 cm^2) and annealed to give the equivalent single crystal surface (i.e. Pd{111}, Rh{111} and Ru{0001}) using the forced deposition technique described in section 3.5. Fig. 4.4.1 shows the cyclic voltammograms of these surfaces and fig. 4.4.2 shows the bulk metal equivalents from literature sources. It can be seen that the shapes of the appropriate voltammograms are in good agreement with each other, showing that the deposition was successful and yielded metallic layers analogous to their bulk single crystal surfaces. This technique has a range of advantages. It is much cheaper than manufacturing the individual single crystal surfaces as it only requires a small amount of the metal to be studied in a solution and only one single crystal electrode template is required as a substrate for the investigation of a number of different metals. A further advantage in the present study is that any edge effects would be "constant" throughout the experiment. However, it can be difficult to anneal the surface to the correct point, particularly when annealing in a Bunsen flame, such that the surface becomes single crystalline without removing too much of the deposited metal (as a volatile oxide). This was found to be particularly problematic in the case of Ru, which subsequently had to be resistively heated by the passage of up to 11 A of current through the electrode for 1 – 2 minutes, whilst under a N_2 atmosphere (i.e. no oxygen present). The surfaces are therefore not ideally suited for flame annealing, though this may become easier as the technique is refined. A further drawback associated with the technique is that small amounts of the deposited metal may alloy with the bulk substrate electrode, which can be difficult to remove and can require prolonged periods of flame annealing or electrochemical cycling to regenerate the pristine Pt surface.

Initial linear sweep measurements were taken on the surfaces described above in 0.1 M H_2SO_4 (fig. 4.4.3), but not under steady state conditions (with a sweep rate of 0.5 V s^{-1} over a wider potential range than is generally used for HER, 0.8 to -0.4 V). These initial results are therefore merely qualitative indicators of relative catalytic activity. Hence, exchange current density figures could not be taken from these plots. Pt and

Ru appear to give the highest HER activity based on the magnitude of the HER currents generated. Bi gave the lowest activity. Since Bi blocks HER active Pt sites and hydrogen evolution still occurred despite all UPD-H sites being blocked, it is concluded that UPD-H is not involved in the HER as reported previously by Gomez[3, 22]. The Rh surface gave rise to a similarly shaped LSV to the Bi surface, in that the onset of hydrogen evolution started at more negative potentials than for the other three surfaces, though the HER on Rh did appear faster than on Bi. The Pd linear sweep voltammogram resided roughly midway between the Ru and Rh voltammograms.

Multi-frequency AC voltammograms were also taken on the five surfaces in 0.1 M H_2SO_4 (see fig. 4.4.4). They were performed at steady state (0.00125 V s^{-1}) and should therefore be reliable in comparison with the linear sweep voltammograms above. It can be seen that bare Pt and Ru give the highest limiting admittance density values at 0.32 and 0.28 Ω^{-1} cm^{-2} respectively, which is expected from the linear sweep voltammetry. Pd gave a lower value of 0.21 Ω^{-1} cm^{-2}. The Bi and Rh surfaces give the lowest admittances, with admittance on the Bi covered Pt surface reaching a plateau at 0.18 Ω^{-1} cm^{-2}, whilst that for Rh did not reach a plateau. The Rh surface gave quite a distinct shape and did not reach a limiting admittance (at 0.20 Ω^{-1} cm^{-2}) density until swept to very negative potentials (-0.35 V *vs.* Pd/H) compared to the other surfaces which all reached a constant admittance value before -0.19 V *vs.* Pd/H. The Rh voltammogram also shows a large hysteresis which is not observed on the other surfaces. Although on Pt, FTIR shows that HSO_4^- anions are already desorbed from the surface at HER potentials[5], this may not necessarily be the case for Rh. This strong UPD-H adsorption is even observed at very low sweep rates and is therefore an intrinsic property of HSO_4^- anions on the surface. It may be that this strong irreversibility in anion adsorption and desorption just prior to UPD-H may be causing the hysteresis effect observed for the Rh surface in the MFACV measurements. Thus the strongly adsorbed HSO_4^- is present on the negative-going MFACV potential sweep and desorbs at negative potentials, forcing hydrogen evolution to occur at potentials negative of this. However the anions are not present on the return (positive) potential excursion, hence the difference in surface, giving rise to the hysteresis on the MFACV. The phase plot for the Rh surface (fig. 5.4.1) is very "noisy" between 0 and -0.1 V *vs.* Pd/H, showing that the nature of the surface is changing in this region, which is likely to be due to the adsorption/desorption of

HSO_4^- anions. At more negative potentials the phase plot shows no hysteresis, implying that the hysteresis observed on the admittance plot is related to a change in available surface area (as phase plots are independent of area). The admittance plot hysteresis is therefore likely to be due to hydrogen bubbles formed on the surface as a result of the high negative potential to which the system must be driven to in order to desorb the anions before hydrogen is evolved.

The cyclic voltammograms of each surface taken before and after the MFACV (fig. 5.4.2), show a small change, though not significant.

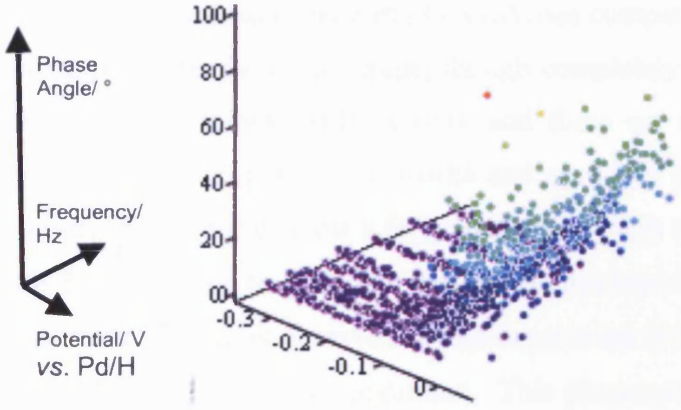

Fig. 5.4.1 Phase plot for deposited Rh on Pt{111} in 0.1 M H_2SO_4, corresponding to the admittance plot in fig. 4.4.4 (c).

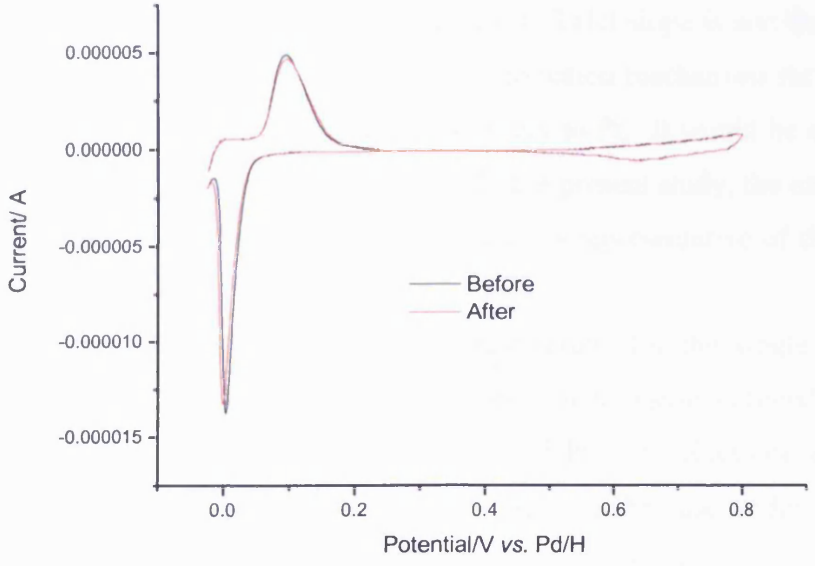

Fig. 5.4.2 Cyclic voltammograms of Rh on Pt{111} before and after MFACV experiments were performed on the surface.

The Rh, Pd and Bi coated Pt surfaces were reproduced and tested using linear sweep voltammetry under steady state conditions, in 0.5 M H_2SO_4, at potential sweep rate 0.005 V s^{-1}. A Au{111} surface was also prepared using the same method as that for the other films. However a Ru surface of similar quality proved difficult to reproduce and was subsequently not included in this set of results.

The linear sweep voltammograms were recorded over a significantly shorter potential range than the non-steady state tests above (0.1 to -0.1 V *vs.* Pd/H) and showed different trends. Bare Pt is again the most active surface giving a (relatively low) j_0 value of 0.59 mA cm^{-2} (see table 4.4.1). Bi gives a lower exchange current density value as expected, though the HER mechanism is not changing, as the Tafel slope does not vary far from that of bare Pt (33.4 mV/dec compared to 31.5 mV/dec on bare Pt). This implies that the Bi coverage, though completely blocking UPD-H activity, does not completely block HER activity and there are still Pt sites available for hydrogen evolution. Experimental works and proposed models by Gomez *et al*[22] deduce similar findings, yet show a far greater decrease in HER activity (0.85 mA cm^{-2} on bare Pt decreasing to 0.12 mA cm^{-2} at approximately full Bi coverage of the Pt{111} surface[22]) than is observed in this experiment (0.59 mA cm^{-2}, decreasing to 0.28 mA cm^{-2}) under the same conditions. This phenomenon is discussed further in section 5.4.6.

Rh displays a very similar linear sweep voltammogram to that of Bi on Pt, with a slightly higher Tafel slope (35.5 mV/dec), but the same value for exchange current density as Bi on Pt (0.28 mA cm^{-2}). The increase in Tafel slope is surprisingly large for Rh which is reported to adopt the Tafel recombination mechanism for HER[23, 24] (with the Tafel step being rate determining) similarly to Pt. It would be expected to give a Tafel slope in the region of 29 mV/dec. In the present study, the experimental value is approaching the value of 42 mV/dec which is representative of the Volmer-Heyrovsky mechanism.

A significant difference between the steady state results for the single crystalline metallic overlayers on Pt compared to the non-steady state results is found for Pd. It is somewhat less active for HER than the Bi coated Pt{111} electrode and the Rh layer when under steady state conditions. This was not the case under non-steady state conditions. It can be seen from the Tafel data in table 4.4.1 that Pd adopts the Volmer-Heyrovsky mechanism for hydrogen evolution (where the Heyrovsky step is rate determining) as the Tafel slope is 44.4 mV/dec. The Pd surface is therefore likely

to be less active for HER than other surfaces which evolve hydrogen via the Volmer-Tafel mechanism.

The Au{111} surface then gives the lowest exchange current density value of 0.03 mA cm^{-2}, making it almost inactive for hydrogen evolution. The small amount of hydrogen which is produced is via the Volmer-Heyrovsky mechanism as the Tafel slope is not dissimilar to that on Pd (45.4 mV/dec compared to 44.4 mV/dec) despite the relatively large difference in j_0 (0.03 mA cm^{-2} for Au compared to 0.14 mA cm^{-2} for Pd).

Multi-frequency AC voltammograms were taken on the metallic surfaces in 0.5 M H_2SO_4 and showed some intriguing results when compared to the DC measurements. Unsurprisingly, the bare Pt surface was the most active, giving a limiting admittance density of 0.10 Ω^{-1} cm^{-2}, yet Pd was the next most active surface for HER as it gave a limiting admittance density of 0.08 Ω^{-1} cm^{-2}. As was observed with the MFACVs of the surfaces in the earlier experiment using 0.1 M H_2SO_4 as the electrolyte, the Rh surface could be swept to relatively high negative potentials before the admittance density reached a plateau (in this case it had not even reached a plateau at -0.45 V *vs.* Pd/H). This is thought to be a consequence of the strong adsorption of HSO_4^- anions as described above. Hence, as the electrolyte concentration is greater in this experiment than that used previously (0.5 M H_2SO_4 compared to 0.1 M H_2SO_4 used in the previous experiment), the anion adsorption/desorption effect is so strong that the hydrogen evolution reaction kinetics are still not dominant over the anion desorption even at -0.45 V *vs.* Pd/H and no plateau is observed. Similarly, the highly inactive Au layer did not reach an admittance density plateau despite being swept to -0.45 V *vs.* Pd/H, compared to the Pd and Pt surfaces were only be swept to -0.29 V *vs.* Pd/H.

An intriguing point of note is the discrepancy between the Rh and Pd surfaces when using multi-frequency AC voltammetry and linear sweep voltammetry. The exchange current density data from the linear sweep voltammetry indicates that Rh on Pt{111} is more active for the HER than Pd on Pt{111}, yet the opposite is shown by the multi-frequency AC voltammetry. It is unclear why this should be, as both experiments were done on the same respective surfaces and under the same conditions. Both features appear to be genuine. Pd is known to produce hydrogen via the Volmer-Heyrovsky mechanism[25] and should therefore yield a linear sweep voltammogram with a Tafel slope close to 42 mV/dec which is observed in the

present study. Also the feature of the MFACVs, whereby Pd produces a plateau and Rh does not, was observed both in 0.5 M H_2SO_4 and in 0.1 M H_2SO_4 electrolyte, both of which were performed under steady state conditions.

5.4.1.1 Model circuit analysis of epitaxial films MFACV data

The model circuit data in table 4.4.2 shows the variation in R_0, R_S and α for the epitaxial metal films. It can be seen that the two surfaces which give multi-frequency AC voltammograms which do not plateau (i.e. the Au and Rh films) both have very low transfer coefficient values of 0.1 and low R_0 values of 200 Ω and 400 Ω for Rh and Au respectively compared to 2080 Ω and 2000 Ω for Pt and Pd respectively. An interesting point of note is that R_S shows very little variation between the four surfaces with a range of just 23 – 29 Ω. This supports the findings from the stepped single crystal Pt electrodes as it shows that external resistance effects (such as those which may arise from variations in solution concentration, edge effects, electrode shape or changes in meniscus configuration) do not vary significantly between different metals if the shape and size of the electrode surface does not change. The absolute R_S figures for these surfaces are much lower than those seen on the stepped single crystal Pt electrodes due to the concentration of the electrolyte used in each case, 0.5 M H_2SO_4 for the epitaxial films and 0.1 M H_2SO_4 for the stepped single crystals, i.e. the higher the acid concentration, the lower the resistance within the solution.

5.4.1.2 Fitting rate constants to epitaxial metal film Tafel data

The rate constants of the films on Pt support the accepted HER mechanisms. The Volmer-Tafel-Heyrovsky fitting routine broke down for the surfaces which are known to adopt the Volmer-Tafel mechanism[23] (Pt and Rh) yet it fitted well for the surfaces which are known to adopt the Volmer-Heyrovsky mechanism (Pd[26] and Au[24]). The different possible mechanisms make comparisons of rate constants between surfaces difficult as only the Pt and Rh surfaces have meaningful Tafel rate constants, whilst only the Pd and Au surfaces have meaningful Heyrovsky rate constants. The Volmer forward and backward rate constants show an increase with exchange current density. However, due to the small number of surfaces tested, it is not reliable to deduce if the

trend is linear or if another dependence is present. A point of note is that the forward Tafel rate constant on Pd is much higher than that for the Au surface (8.5×10^{-7} and 1.08×10^{-16} cm s^{-1} on Pd and Au respectively). It is even higher than that for Pt and Rh (2.38×10^{-7} and 2.32×10^{-7} cm s^{-1} respectively). Thus the kinetics of the HER on Pd are being affected by the Tafel reaction, which could be due to the recombination reaction occurring on Pt below the Pd surface due to absorbed hydrogen within the Pd. The Pd film is reasonably thick, though it is not quite bulk-like. Hence, it may be possible for the kinetics of the HER on the subsurface Pt to be influencing the rate constants. However, the Tafel slope does not appear to be affected by the Tafel mechanism as it takes a value of 44.4 mV/dec. This Tafel slope is representative of Volmer-Heyrovsky kinetics (where the Tafel slope is approximately 42 mV/dec[27]), suggesting that the Tafel reaction is not involved in the HER on Pd. It is therefore suggested that the Heyrovsky step is the rate determining step, whilst the extent of the Tafel reaction occurring in this instance may be real, but not great enough to influence the kinetics of the HER to any considerable degree.

5.4.2 Ir deposited onto Pt{111}

Ir was found to be difficult to deposit onto Pt using the forced deposition method and therefore the method of using a Bunsen flame to "flash reduce" a droplet of Ir(III) solution onto the electrode (as described in section 3.5) was employed. This resulted in a rough Ir deposit which did not give rise to a single crystalline structure[28] upon gentle flame annealing or even by resistively heating under a N_2 atmosphere. A high Ir coverage could be achieved by the flash deposition method, whilst linear sweep voltammetry and cyclic voltammetry were used to study the surface. The Ir modified Pt electrode was heated in a Bunsen flame (to systematically remove small amounts of Ir) and subsequently cooled in H_2, in order to study the effect of Ir loading on the hydrogen evolution activity. The CVs and LSVs of these various Ir covered surfaces are shown in fig. 4.4.7 and fig. 4.4.8 respectively. It can be seen from the cyclic voltammetry that the Ir-modified surfaces cause hydrogen evolution to occur at less negative potentials as a significant amount is evolved at potentials positive of 0 V *vs.*

Pd/H. The Tafel slopes for the Ir surfaces are slightly larger than that for the bare Pt{111} surface, although it is not thought that this increase is great enough to represent a change in HER mechanism. The cyclic voltammetry also shows that the Ir surface area decreases with annealing as more Ir is removed. However, the decrease in activity shown by the linear sweep voltammetry does not correlate directly to the decrease in Ir area. This correlation was quantified by normalising the charge density of each surface to that of the bare Pt{111} surface and similarly normalising the exchange current density value from each surface to that of Pt{111}. The ratio of these two figures then corresponds to the relative activity of each surface compared to the bare Pt surface. It can then be seen from the data in table 4.4.4 (taken from fig. 4.4.7 and fig. 4.4.8) that the increase in HER activity is a genuine observation which must be related either to Ir being either a more effective catalytic material or to some geometric feature associated with the roughness of the deposit. It was observed earlier in the project (section 4.1.2.2) that bulk Ir is a less effective catalyst for the HER than Pt, hence it was suspected that the increased hydrogen evolution activity observed for Ir deposited onto Pt{111} was related either to surface alloying or to the geometry of the deposits. However, recent density functional theory calculations from Nørskov *et al*[29-31] suggest that Pt-Ir alloys would not be significantly more active for hydrogen evolution than Pt. Hence, in section 4.4.3, an experiment was designed to test whether or not the enhanced HER activity observed on the Ir surfaces is related to the morphology of the Ir film. This is discussed further in section 5.4.3.

5.4.2.2 Fitting rate constants to Ir modified Pt Tafel data

The HER responses of the Ir on Pt surfaces were all fitted to find Volmer and Tafel rate constants (omitting any Heyrovsky term). The results are displayed in table 4.4.5. The fitting routine broke down when the Heyrovsky step was modelled, showing that the HER on the Ir surfaces is occurring via a Volmer-Tafel mechanism. The low Tafel rate constant values with respect to the Volmer rate constants shows that the Tafel step is rate determining. The individual rate constants were plotted against exchange current density in order to see if any meaningful trends could be seen (fig. 4.4.9). The Ir surfaces showed that k_1 and k_{-1} increased linearly with j_0, though the Pt{111} surface did not fit with the trend. k_2 showed a general decrease with j_0, though one of the Ir surfaces (anneal 4) did not fit the trend. If there was a

genuine relationship between k_2 and j_0 it would be expected that hydrogen evolution activity (and therefore j_0) should increase with rate (and therefore the limiting rate constant, k_2). It was therefore deduced that plotting the individual rate constants against exchange current density was not meaningful and they were not plotted in subsequent experiments. However, the fitting routines were still applied to subsequent results as they indicate the HER mechanism on the surface under investigation.

5.4.3 Pt deposited onto Pt{111}

In a similar experiment to that performed in the previous section with Ir, a solution of Pt(IV) was flash reduced onto a Pt{111} surface to give a rough Pt layer. The results were also analysed in a similar manner to those from section 4.4.2. Cyclic voltammograms were taken of the surfaces from a large bulk-like Pt deposit, decreasing the surface area of the overlayer in small increments by gentle heating in a Bunsen flame until a well-ordered Pt{111} surface was obtained. Cyclic voltammograms of the rough Pt deposits again show the onset of hydrogen evolution beginning at more positive potentials relative to the smooth Pt{111} surface (as was also observed with the Ir deposits). As with Ir, as small amounts of Pt were removed from the surface, the exchange current density (taken from the linear sweep voltammograms in fig. 4.4.11) did not decrease accordingly. The Tafel slopes increased slightly on the deposited Pt surfaces, yet not significantly. The quantitative data shown in table 4.4.6 shows that all of the deposited Pt surfaces have slightly lower UPD-H charge than bare Pt (and therefore charge density also, as it has been assumed that the surface area is the same as the geometric area on all of the surfaces, 0.022 cm^{-2}). The comparison of the exchange current density/charge density ratio relative to bare Pt shows an increase in HER activity, though not as significant as that observed with Ir (1.44 – 1.91 for deposited Pt compared to 1.45 - 3.43 with Ir).
This then indicates that the increased HER rate is a result of the arrangement of the deposited atoms as opposed to a genuine electrochemical catalytic effect from the material (which may have been an explanation for the effect with deposited Ir). Here,

a model is proposed for the arrangement, to explain the results. It is suggested that small islands/mountains form under the "flash" deposition conditions, which cause an increased radial diffusion to and from the electrode[32]. These deposits act as microelectrodes (or even nanoelectrodes) and are separated such that the collective diffusion domains which they enclose is greater than that of a planar Pt{111} electrode. Diffusion domain theory has been investigated in depth by Compton and Davies[32-34]. Fig. 5.4.3 is a schematic diagram from Davies and Compton[33] showing the diffusion profiles for various types of diffusion on an array of microelectrodes embedded in an insulator. It shows the cases for (1) small linear diffusion, (2) small non-linear diffusion, (3) overlapping (or large) non-linear diffusion layers and (4) large, overlapping linear diffusion. The nature of the diffusion domains overlapping results in a deactivation of diffusion to the surface overall. However, when the domains are sufficiently far apart that there is no overlap, the gap between the diffusion domains leaves a region with no diffusion. Hence, there is an optimum spacing between microelectrodes at which the total diffusion area enclosed is a maximum. This spacing should be equal to $2r$, where r is the radius of the spherical diffusion domain associated with each microelectrode (assuming they are of equal size).

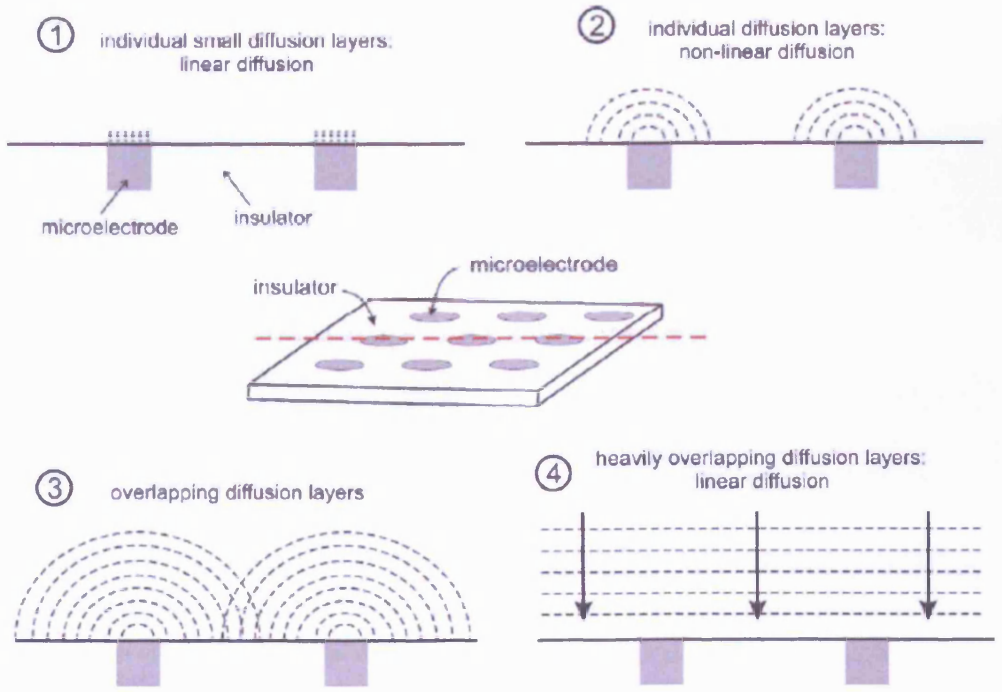

Fig. 5.4.3 Schematic diagram presenting different possible diffusion profiles for an array of microelectrodes within an insulating material. Reproduced from Davies and Compton[33].

If it is assumed that the diffusion to the surface of the flash deposited metal is similar to that at microdisc electrodes as seen in fig. 5.4.3 (2) or (3), with non-linear diffusion (greater than the linear diffusion on the planar Pt{111} substrate electrode) then a version of Davies and Compton's model may be applied to the system. The different annealed states of the surface give rise to different overlapping interactions of the diffusion domains. When the inter-island spacing is so small that there is a strong diffusion domain overlap, the diffusion becomes effectively linear and akin to that of the bulk surface. Therefore, the surfaces which give rise to the greatest enhancement for the HER are speculated to have average island spacing closest to the optimum value. This is shown schematically in fig. 5.4.4. The possible drawback with this model is that the area of the electrode is increasing in proportion to the diffusion domain, yet the cyclic voltammograms of Ir on Pt and Pt on Pt show little or no increase in charge, implying that there is a small or insignificant increase in area. This suggests that the diffusion domains associated with the islands of deposited metal must be much greater than that of the planar Pt substrate, so much so that they are highly dispersed and do not relate to a significant increase in electrode area. Looking specifically at the cyclic voltammograms of Ir deposited onto Pt{111} (fig. 4.4.7), it is clear that the surface is very close to Pt{111} in nature and that only a small amount of Ir must be present on the surface. This supports the speculation that there is a large spacing between islands.

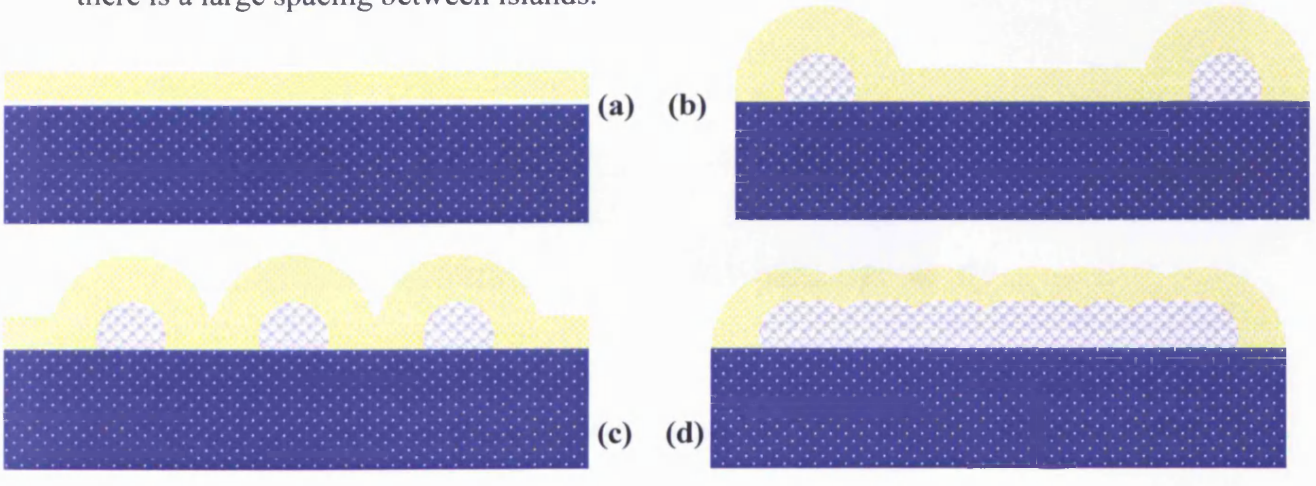

Fig. 5.4.4. Two-dimensional schematic diagram showing how the island spacing affects the net diffusion domain (yellow) of the islands (grey) deposited on a surface (blue) with (a) linear diffusion domain of a flat electrode, (b) radial diffusion domains of highly dispersed islands, (c) radial diffusion domains of islands close to the optimal spacing and (d) strongly overlapping diffusion domains of close islands, approaching linear diffusion.

Cyclic voltammograms of the Pt deposited on Pt{111} surface show less long range {111} order than those of Ir deposited on Pt{111}. Thus the deposited Pt islands cover a greater proportion of the surface than the Ir islands. This may arise from either Pt islands being much wider and flatter than the Ir islands (and therefore covering a greater surface area) or they may simply be more numerous, breaking up the long-range order. However, a high number of islands is unlikely in these cases as no significant area increase is observed, which would be expected with many small islands as the simulated surface is effectively rough. The suggested island arrangements for the Ir and Pt islands are shown in fig. 5.4.5.

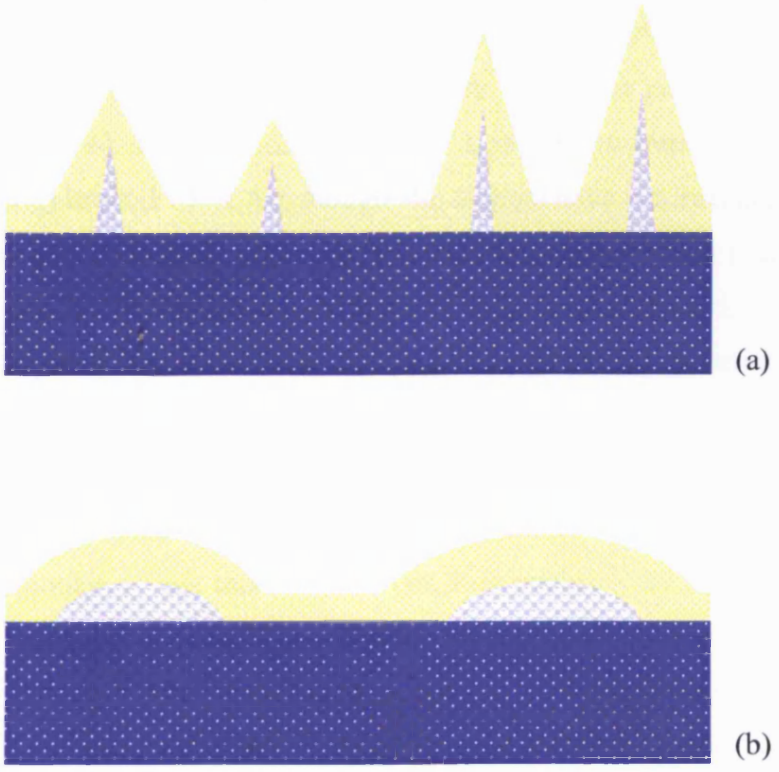

Fig. 5.4.5 Schematic diagram showing possible arrangements of (a) Ir and (b) Pt islands deposited onto Pt{111}.

A further suggestion relating HER enhancement to enhanced radial diffusion at the monoatomic high edge sites of islands was disregarded because such small atomic structures causing enhanced HER effects is unlikely considering there is no discrepancy between HER rate on different single crystal surface structures.

Pandelov and Stimming reported a similar enhanced HER rate for Pd islands deposited on Au{111} surfaces[35]. They find that for submonolayer coverages of Pd, the smaller the Pd deposits, the greater the HER enhancement. This is partially in agreement with the proposed model for Ir on Pt{111} in the present study where diffusion to and from islands allows for augmented HER kinetics. However, the suggestion of HER rate decreasing with increasing island deposits can only apply for surfaces where the diffusion domains of the islands overlap. It can be seen from Pandelov's graph of exchange current density versus the percentage of gold in the surface (fig. 5.4.6) that one could interpret a maximum (representing the optimum island spacing) around 95 % Au, though the authors have not assumed this. This is in agreement with the present study as it shows that the optimum island spacing may arise at a very low coverage, which appears to be true of the Ir islands. Pandelov's proposed model is that the Volmer discharge step is the rate-determining step for the HER and occurs quickly on Pd islands. The adsorbed intermediate hydrogen is then able to move relatively freely over the Au surface (spillover) where it recombines (which also occurs on the Pd surface), leaving Pd sites free for the Volmer process to continue. Though, if this model is correct, it is unclear why the same enhancement should not be observed for all Pd coverages up to one monolayer. Further arguments arise with this spillover model as it is known that the Volmer step is not rate-determining on either Au or Pd[24], rather it is the Heyrovsky desorption step on both materials. Thus the mention of recombination of hydrogen (i.e. Tafel step) by Pandelov and Stimming[35] creates a flaw, though it is thought that the description would also apply to the actual mechanism (including the Heyrovsky step).

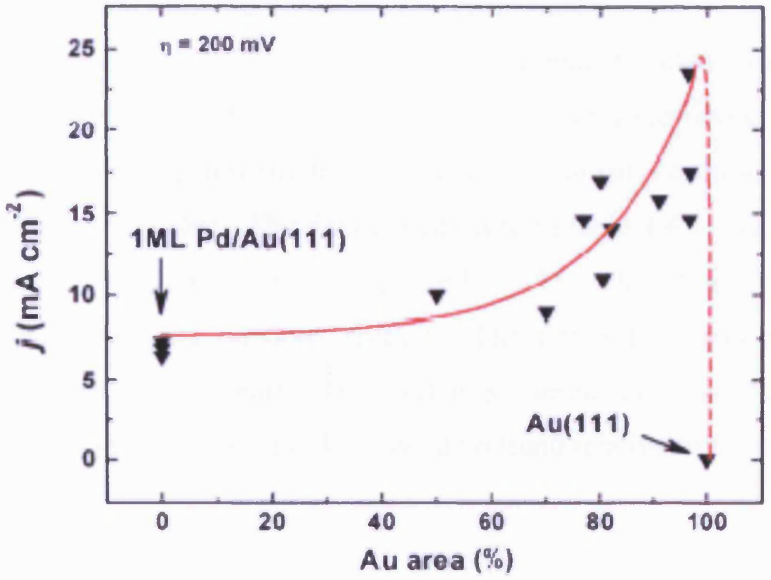

Fig. 5.4.6 Plot of exchange current density versus percentage of Au in surface for Pd islands deposited on Au{111}[35].

It has been suggested that the spillover model[35] could offer an explanation for the HER enhancement observed in the present study. This could apply by way of mobile adsorbed hydrogen being evolved at the Pt surface and spilling over onto Ir islands where it can recombine and leave the surface more readily than on the Pt-electrode surface as the M-H bond strength on Ir is lower than on Pt. However, Trasatti's volcano curve[36] (fig.1.3.1 (b)) the M-H bond strength is actually very slightly stronger on Ir than on Pt. Also, this is not supported by the enhanced HER observed from depositing Pt on Pt{111}.

A means of rationalising the enhanced HER rate on both Pt and Ir modified Pt{111} surfaces would be to suggest that the shape of the deposits facilitates the spillover effect. This would relate to an optimum enhancement as a balance between the structural spillover effect and the deactivation of hydrogen evolution due to the less active deposited material blocking more active Pt sites. Thus, the Pt on Pt{111} goes against the theory once again as an optimum HER enhancement would relate to a very rough surface and therefore an increase in area, which is not observed. Therefore, it is thought that the spillover model may be disregarded in favour of the diffusion model for the present study.

5.4.3.1 Fitting rate constants to Tafel data from Pt on Pt

The Pt deposited onto Pt{111} surfaces gave rate constants fitted using a Volmer-Tafel fitting routine. An attempt to model the data using a Heyrovsky-based fitting routine did not work well, showing that the HER mechanism on these surfaces does not involve a Heyrovsky step. The data is displayed in table 4.4.7. The Pt-modified surface rate constants fit more closely with the Pt{111} surface than those on the Ir-modified surfaces from the previous section. The forward Volmer rate constants appeared to increase fairly linearly with exchange current density, though this was assumed to be coincidental as k_{-1} and k_2 showed no trend relating to j_0.

5.4.4 Pd films on Pt

As well as depositing a relatively thick film of Pd onto Pt{111} to obtain a model, near bulk-like Pd{111} surface (section 5.4.1), very small amounts of Pd were added in increments, up to a coverage of two monolayers using the forced deposition method described in section 3.5. The figures in section 4.4.4 illustrate the results. Table 4.4.8 shows the data, in terms of monolayer fractional coverage, Tafel slope and exchange current density. The Tafel slope and exchange current density are plotted against fractional Pd coverage in fig. 4.4.14. This graph indicates that the Tafel slope shows little change below one monolayer Pd coverage. It begins to increase when the Pd coverage is greater than one monolayer but does not quite reach 42 mV/dec as is observed on bulk Pd surfaces where the HER mechanism tends to the Volmer-Heyrovsky as opposed to the Volmer-Tafel mechanism (which occurs on Pt). Similarly, the exchange current density at Pd coverages below one monolayer does not vary far from the figure on bare Pt. As the coverage approaches one monolayer, there is a small but significant, decrease in j_0. This value remains fairly constant until the Pd coverage approaches two monolayers. The surface behaviour then becomes more Pd-like with further significant decreases in exchange current density accompanied by a simultaneous increase in Tafel slope.

The results show that depositing small amounts of Pd onto a Pt surface has little effect on the HER activity below a monolayer coverage, with the surface behaving as

though there were no Pd present. It is not until the Pd coverage is close to a full monolayer that an effect is observed, though this partial change in mechanism is not great enough to show that the HER is taking place solely via the Volmer-Heyrovsky mechanism. This suggests that Pt is still actively catalysing the HER despite being covered by Pd. Pt actually appears to be more influential on the hydrogen evolution mechanism at one monolayer Pd coverage than Pd, as the Tafel slope and exchange current density figures match more closely to those on bulk Pt than on bulk Pd. Even at two monolayers of Pd deposited onto the Pt electrode, the Pt still has a strong influence on the hydrogen evolution as the HER mechanism is still not representative of bulk Pd.

In similar experiments conducted by Markovic *et al*[26] (at 278 K in 0.05 M H_2SO_4 using a rotating disc electrode) it was found that the deposition of a monolayer of Pd resulted in a change in mechanism to the Volmer-Heyrovsky mechanism and that the HER rate actually increased with Pd coverage up to one monolayer. Markovic attributes this to small defects or steps within the Pd layer. He also shows that the Pd is adopting the Pt structure pseudomorphically, where HER enhancement may arise from the induced lattice strain within the Pd layer (where the lattice constants for Pd and Pt are 3.89 Å and 3.92 Å respectively). The results are not in agreement with the present study either mechanistically (the present study suggests that there will not be such a significant change in mechanism at one monolayer Pd) or kinetically (there should not be increased HER kinetics with Pd deposited on Pt). It is thought that the differing results must arise due to the different experimental approaches between the groups, yet the present study suggests it unlikely that monolayer coverage of Pd on Pt should give an enhanced HER rate.

5.4.4.1 Fitting rate constants to Tafel data from Pd films on Pt

Two different fitting routines were used in the analysis of the Pd films on Pt. This was because the HER mechanism was not the same over all surfaces. Similar to the results seen for the exchange current density altering with Pd coverage, there were three distinguishable regions which applied for the fitting routines. At low Pd coverages (< 0.82 monolayers), the Volmer-Tafel fitting routine was applied, whilst at high coverages (approaching two monolayers) this broke down and the Volmer-Tafel-Heyrovsky fitting routine was applied. The intermediate surfaces could be fitted

reliably with both fitting routines (those using the Volmer-Tafel-Heyrovsky routine were shown in the results section, table 4.4.9).

An important point to note is that, whilst applying the Volmer-Heyrovsky model to the Pd adlayers data, the Tafel reaction rate constant is significantly large for all of the surfaces, even at the higher Pd coverages. A similar point was also observed for the semi-thick Pd layer on Pt{111} discussed in section 5.4.1.2. Hence, in the case of these thin Pd films it appears that the Tafel reaction is influential to a degree on all of the surfaces as the forward Tafel rate constants are in the same range as the forward Heyrovsky rate constants as can be seen in table 4.4.9. This is also supported by the change in Tafel slope with increasing Pd coverage, as the slope does not reach the figure of 42 mV/dec (the accepted figure for the Tafel slope of HER occurring via the Volmer-Heyrovsky mechanism[27]) which is due to the influence of the Tafel kinetics. Throughout the present study, it has been observed that the Tafel reaction is occurring on Pd on Pt{111}. It is also observed that the HER mechanism tends towards Volmer-Heyrovsky kinetics as Pd film thickness increases. This is to be expected if it is assumed that the Tafel reaction is occurring on the Pt substrate and the Heyrovsky reaction is occurring on the Pd surface. The thicker the Pd layer, the less absorbed hydrogen will be seen at the Pt surface and therefore the less hydrogen will be evolved via the Tafel mechanism, whilst more hydrogen will be evolved via the Heyrovsky mechanism occurring on the Pd. In addition to this point, at low Pd coverages (i.e. below one monolayer) the Pd atomic arrangement is likely to be closer to that of Pt (and the Pd may adopt more Pt-like properties) than a similar Pd layer in a bulk Pd structure. Hence, the more deposited Pd layers, the more the nature of the surface will become like bulk Pd.

It can be seen from table 4.4.9 that k_2 and k_3 do not vary linearly with Pd coverage (nor do they vary linearly with each other), though it can be seen that in general the Heyrovsky kinetics become more influential at the higher Pd coverages, whilst the Tafel kinetics become less influential.

The data in table 4.4.9 from the Volmer-Tafel fitting routine shows that k_1 and k_2 have no dependence on Pd coverage. Rather, the values vary non-systematically over a wide range (8.9×10^{-5} – 0.34 cm s^{-1} for k_1 and 7.45×10^{-9} – 5.28×10^{-7} cm s^{-1} for k_2). The data taken using the Volmer-Tafel-Heyrovsky mechanism seem much more consistent, yet they still do not show any definitive trends between rate constants and Pd surface coverage. The forward Volmer rate constant appears to show a general

decrease with Pd coverage, though the value at 1.75 monolayers appears to be an outlier. Similarly with k_3, one outlying point (in this case that at 1.95 monolayers) skews the plot so that a genuine trend can not be observed. The Tafel rate constant appears to decrease with Pd coverage but again it is not acceptable to assign a definite trend with so few data points.

5.4.5 Pd-Pt alloys

When a thick layer Pd deposited on a Pt surface is heated gently in a Bunsen flame, some Pd will be removed as the volatile palladium oxide, whilst a small residue can remain to form a surface alloy with Pt. This procedure was followed and gave rise to three Pt-Pd alloys with different proportions of the two metals (35, 58 and 75 % Pd). The cyclic voltammograms of these surfaces are shown in fig. 4.4.15 and the linear sweep voltammograms are presented in fig. 4.4.16. The Tafel slopes and exchange current density data are presented in table 4.4.10.

The results show a very interesting finding that, over the range of alloys tested, there is no significant change in exchange current density, which takes values in the range 0.94 – 1.08 mA cm^{-2}, with no trend relating to alloy composition. The figure remains relatively close to that found on the bare Pt{111} surface, 1.02 mA cm^{-2}. There is also no significant variation in Tafel slope (32.4 – 33.5 mV/dec). Thus showing that there is no change in HER mechanism at all throughout the range of alloys in this experiment, as the Tafel slope is representative of the Volmer-Tafel HER mechanism, typical of a pure Pt electrode. It is noted that the Tafel slopes are slightly high compared to the accepted values for the Volmer-Tafel mechanism, but this has been the case throughout the project. The typical value observed in these experiments is roughly 31.5 – 33.5 mV/dec compared to the accepted value of 29 mV/dec when the Tafel step is rate determining[37]. A similar finding is also noted when the Volmer-Heyrovsky mechanism is thought to be occurring on a surface. The theoretical value should be 42 mV/dec[27] yet the results from section 4.4.1 for semi-thick Pd and Au films show figures between 44 and 46 mV/dec.

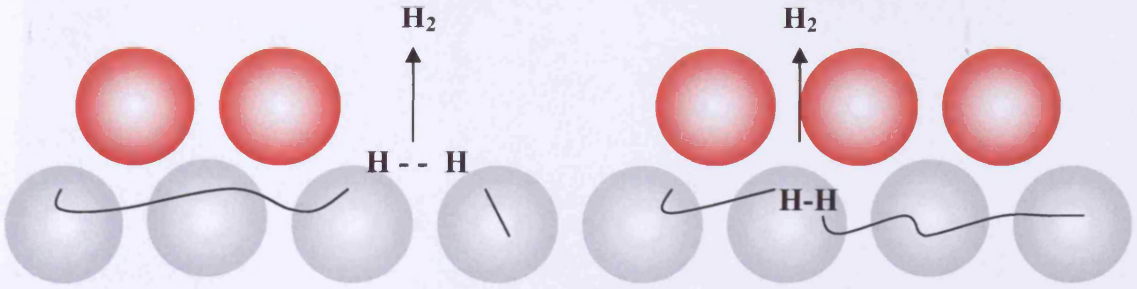

Fig. 5.4.7 Diagram showing that Pd (red) adsorbed to Pt (grey) in submonolayer amounts does not hinder hydrogen evolution.

The Pd-Pt alloys therefore show little or no effect of Pd on the hydrogen evolution reaction even with 75 % Pd present in the alloy. This is a highly surprising result as such a high proportion of Pd would be expected to affect the HER activity. This result can be compared to that observed with the submonolayer Pd film coverages on Pt from section 4.4.4 which showed a similar, negligible effect providing there was still Pt in the surface layer (shown schematically in fig. 5.4.7). This is significant and has not previously been reported. One explanation for this observation is that the catalytic effect of Pt is so great in comparison to Pd that even a small amount of Pt in the surface layer will dominate the mechanism. However, if this were the case Pd would block Pt sites as observed in the cyclic voltammetry and would therefore presumably deactivate the hydrogen evolution to some extent. The HER must therefore still be occurring as normal on Pt atoms despite the Pd adsorbed on the surface/alloyed within the surface layer. The surface layer Pd coverage may be easier to explain as hydrogen atoms could still diffuse relatively freely about the Pt surface. However, such diffusion processes are probably more complicated when the Pd is alloyed in the surface layer. It may be that the alloyed Pd in the surface absorbs hydrogen atoms produced from the Volmer reaction on the surface atoms (as is known to occur on bulk Pd[38]) which then undergo Tafel recombination on subsurface Pt sites as normal (fig. 5.4.8 (a)). However, this seems unlikely as the Pd would surely hinder the evolution of hydrogen if there were extra absorption and desorption steps involved in the process.

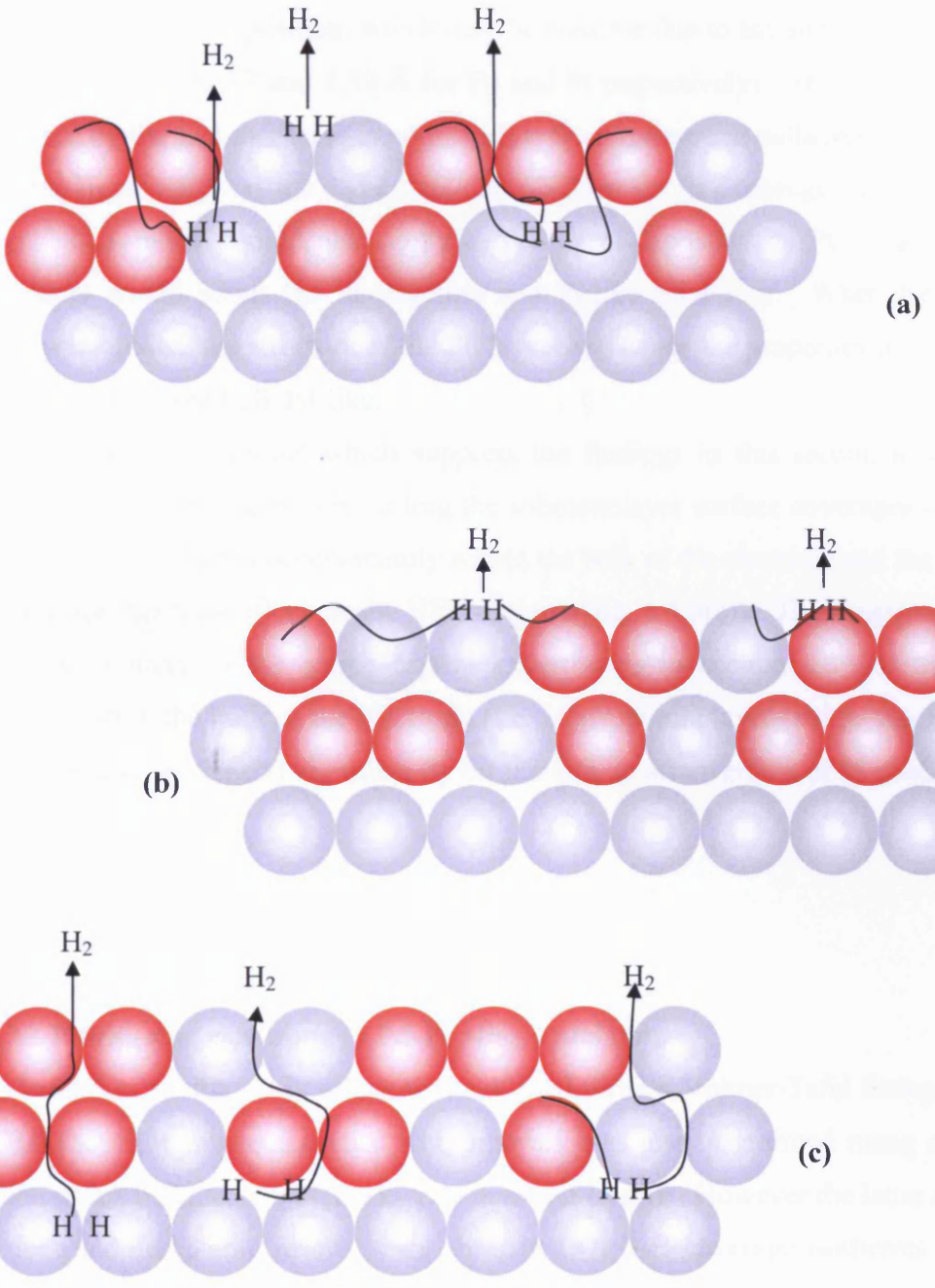

Fig. 5.4.8 Two dimensional schematic diagrams showing three possible explanations for the insignificant variation in HER activity between Pt-Pd surface alloys (a) Pd absorbing atomic H, which recombines on subsurface Pt, (b) Pd adopting Pt mechanism, (c) HER occurring mainly on Pt in the bulk of the electrode.

Another suggestion is that Pd adopts the role of Pt when within the Pt lattice (fig. 5.4.8 (b)). The alloy structure must then match the bulk Pt structure, even with relatively high Pd composition, which may be possible due to the similar atomic radii of the two metals (1.37 and 1.39 Å for Pd and Pt respectively). This explanation is supported by the fact that there is no influence from the typical palladium mechanism (Volmer-Heyrovsky) on the Tafel data and no decrease in exchange current density either. This model would also apply to Pd layers deposited on Pt. The first Pd monolayer would adopt the Pt structure and Pt-like behaviour. When further Pd layers were added, the structure of the Pd layer (and hence the properties of the layer) would become more bulk Pd-like.

A further suggested model which supports the findings in this section along with those in the previous section regarding the submonolayer surface coverages of Pd, is that hydrogen evolution occurs mainly within the bulk of the electrode and the surface composition has little effect on the HER activity (fig. 5.4.8(c)). This suggestion may also link strongly to the single crystal experiments in section 4.3. If the HER occurred within the bulk of the electrode (i.e. a few atomic layers below the surface), the rate would not depend significantly on the atomic arrangement of Pt atoms in the surface layer.

5.4.5.1 Fitting rate constants to Pd-Pt alloy Tafel data

The Tafel data for the Pd-Pt alloys was analysed using a Volmer-Tafel fitting routine to find the HER rate constants. The analysis was also performed using a fitting routine which included a Heyrovsky rate constant feature. However the latter analysis did not yield acceptable results since simulated OPD-H coverage isotherms showed that for the Heyrovsky step to be influential in the HER kinetics, the OPD-H surface coverage would be unrealistically low. Hence, it can be noted that the Pd (which is known to evolve hydrogen via a Volmer-Heyrovsky mechanism) is not significantly influencing the HER kinetics over Pt even when the alloy consists of a ratio of 75:25 Pd:Pt. This directly supports the results seen in the analysis of the exchange current density figures from the same data in section 5.4.5. Quantitative trends between rate constants and exchange current density (or Pd fraction) could not be drawn confidently due to the lack of data points.

5.4.6 Bismuth overlayers

Bi was deposited onto three Pt single crystal surfaces (Pt{111}, {100} and {110}) in order to investigate a structural dependence on the adsorption on the HER. The experiments were conducted solely in the hanging meniscus electrode configuration. The results can be compared to similar experiments conducted by Feliu and Gomez [3, 22] on Pt{111} and Pt{100}. Feliu and Gomez plot the exchange current density against bismuth adatom coverage, θ_{Bi}, which is related to the fractional bismuth coverage (Φ_{Bi} as used in the present study) by the relationship

$$\Phi_{Bi} = n_{Pt}\theta_{Bi} \qquad \textbf{(5.4.1)}$$

where n_{Pt} is the number of Pt sites blocked (in the UPD-H region) by each Bi atom, generally accepted to be 2 – 3[22], with Φ_{Bi} taking the value of unity when all Pt UPD-H sites are blocked. The cyclic voltammograms are shown in fig. 5.4.9 and are on a similar scale to those of Gomez *et al*[3, 22].

The graph of exchange current density versus fractional bismuth coverage on Pt{111} in fig. 4.4.17 gives a shape very similar to that of Gomez *et al*[22], in that the initial decrease in j_0 activity is relatively sharp, with just a small amount of Bi on the surface. The plot then continues on a shallower negative gradient until the Bi coverage approaches a full monolayer when the activity decreases more sharply again. The absolute values of exchange current density for Pt{111} are quite different between the present study and Gomez's results[22]. Both sets give an initial value (i.e. for bare Pt{111}) of approximately 0.9 mA cm^{-2}, yet Gomez's data diminishes to below 0.2 mA cm^{-2} with only 1/3 of the surface blocked by Bi. However, the j_0 values in this project do not go lower than 0.5 mA cm^{-2} even when the Pt{111} surface is almost fully blocked by Bi. Comparison of the results for the Pt{100} surface show that the present study and Gomez's results[3] are in good agreement over the range of Bi coverage tested in this project. However, Gomez managed to achieve very high Bi coverages by the use of high Bi concentrations in H_2SO_4 solution. The high Bi coverages in Gomez's work lead to the exchange current density decreasing rapidly, though it does not reach zero.

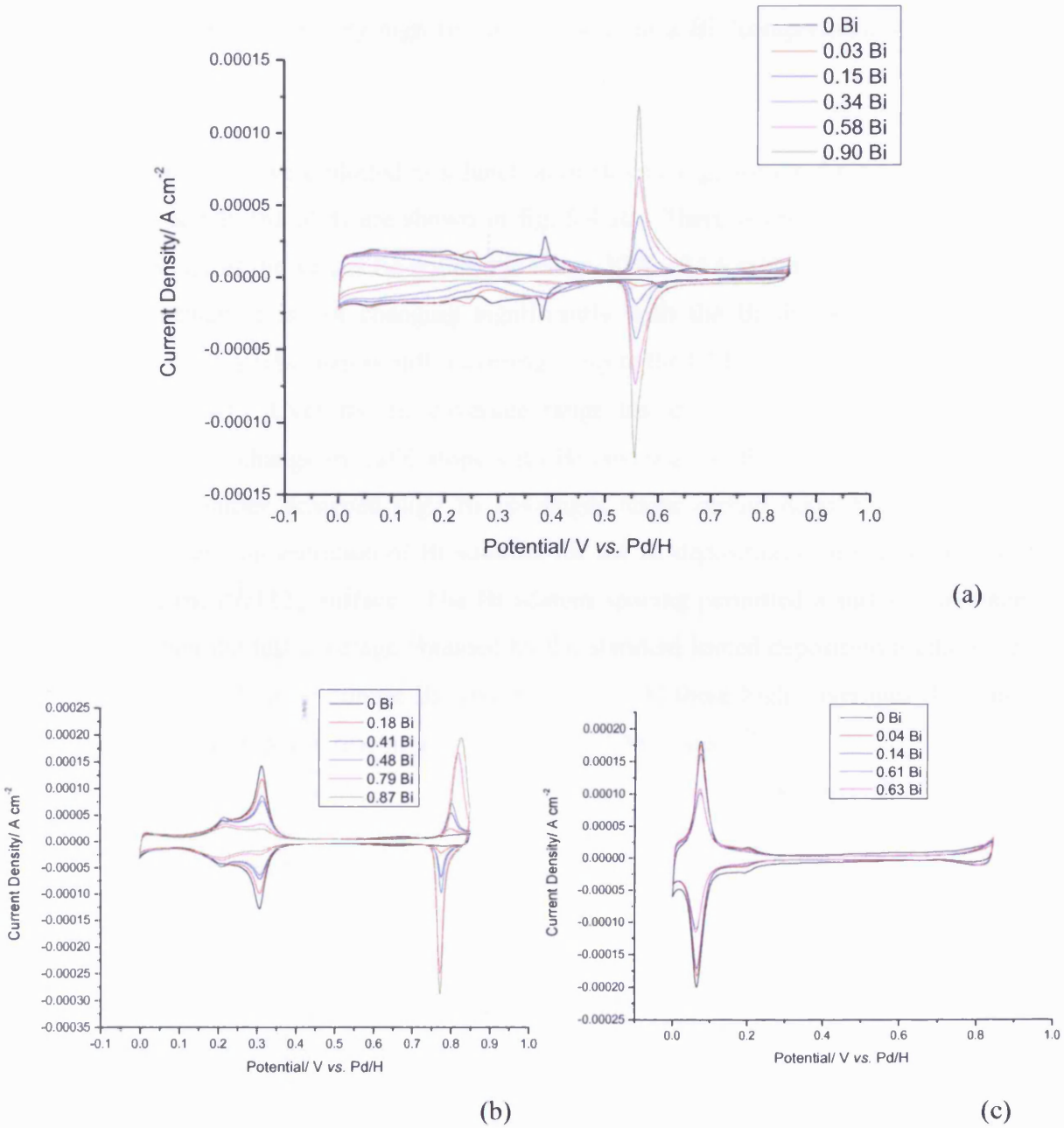

Fig. 5.4.9 Cyclic voltammograms of Bi deposited on (a) Pt{111} (b) Pt{100} and (c) Pt{110}.

All of the results from the present study and from Gomez's work are in agreement that hydrogen evolution is still occurring despite UPD-H sites being blocked. Thus, UPD-H is not related to the intermediate H in the HER.

These findings may be in agreement with those of the previous section which imply that hydrogen evolution is occurring on subsurface sites as well as on the electrode surface. Hence, even though the surface sites may be deactivated and blocked for

UPD-H, HER may still be occurring below the surface layer. The hydrogen evolution is then suppressed at very high Bi coverages when a Bi "compression structure" is formed[22].

The Tafel slopes were plotted as a function of Bi coverage for the three single crystal surfaces tested, the plots are shown in fig. 5.4.10. There is little variation of Tafel slope and all of the values lie within the range 30.8 – 34.6 mV/dec, showing that the HER mechanism is not changing significantly with the Bi deposits. Hence, the Volmer-Tafel mechanism is still occurring, despite the UPD-H sites on the Pt surface being blocked. Over the Bi coverage range tested in this project, Gomez also observes little change in Tafel slope with Bi coverage on Pt{111}[22] or Pt{100}[3]. However, Gomez achieved high Bi coverages under certain deposition conditions (using a high concentration of Bi solution for the Bi deposition or a long deposition time) on the Pt{111} surface. The Bi adatom spacing permitted a surface coverage greater then the full coverage obtained by the standard forced deposition method, i.e. where $\theta_{Bi} > 1/3$ (or fractional Bi coverage > 1). At these high coverages the Tafel slope increases rapidly, reaching figures around 60 mV/dec[22].

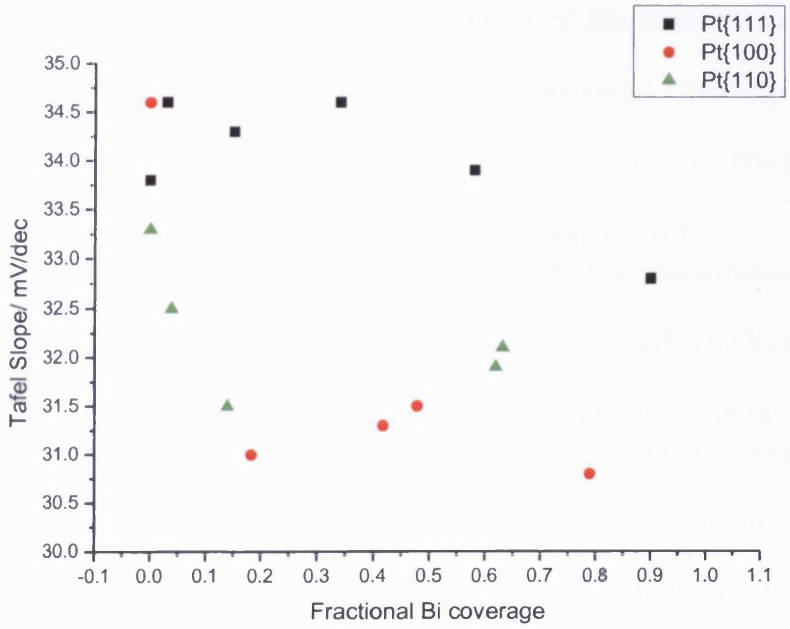

Fig. 5.4.10 Plots of Tafel slope against fractional Bi coverage for the three basal plane single crystal surfaces.

References

[1] J. Maruyama, M. Inaba, K. Katakura, Z. Ogumi, Z.-I. Takehara, *Journal of Electroanalytical Chemistry* **1998**, *447*, 201.

[2] N. M. Markovic, B. N. Grgur, P. N. Ross, *Journal Of Physical Chemistry B* **1997**, *101*, 5405.

[3] R. Gomez, A. Fernandez-Vega, J. M. Feliu, A.Aldaz, *Journal Of Physical Chemistry* **1993**, *97*, 4769.

[4] J. M. Orts, R. Gomez, J. M. Feliu, A. Aldaz, J. Clavilier, *Electrochimica Acta* **1994**, *39*, 1519.

[5] K. Domke, E. Herrero, A. Rodes, J. M. Feliu, *Journal of Electroanalytical Chemistry* **2003**, *552*, 115.

[6] J. O. M. Bockris, I. A. Ammar, A. K. M. S. Huq, *Journal Of Physical Chemistry* **1961**, 879.

[7] R. Mannan, University of Pennsylvania **1967**.

[8] D. B. Matthews, University of Pennsylvania **1965**.

[9] D. Michell, D. A. J. Rand, R. Woods, *Journal of Electroanalytical Chemistry* **1978**, *89*, 11.

[10] H.Inoue, J. X. Wang, K.Sasaki, R. R. Adzic, *J. Electroanal. Chem.* **2003**, *554-555*, 77.

[11] M. Alsabet, M. Grden, G. Jerkiewicz, *Journal of Electroanalytical Chemistry* **2006**, *589*, 120.

[12] N. Furuya, S. Koide, *Surface Science* **1989**, *220*, 18.

[13] J. Barber, S. Morin, B. E. Conway, *Journal of Electroanalytical Chemistry* **1998**, *446*, 125.

[14] H. Kita, S. Ye, Y. Gao, *Journal of Electroanalytical Chemistry* **1992**, *334*, 351.

[15] K. Seto, A. Ianelli, B. Love, J.Lipkowski, *Journal of Electroanalytical Chemistry* **1987**, *226*, 351.

[16] S. Shibata, M. Sumino, *Electrochimica Acta* **1986**, *31*, 217.

[17] J. Clavilier, J. M. Feliu, A. Aldaz, *Journal of Electroanalytical Chemistry* **1988**, *243*, 419.

[18] J. Clavilier, R. Faure, G. Guinet, R. Durand, *Journal of Electroanalytical Chemistry* **1980**, *107*, 205.

[19] G. A. Attard, C. Barnes, *Surfaces*, Oxford University Press, **1998**.

[20] J.-M. Zhang, H.-Y. Li, K.-W. Xu, *Journal of Physics and Chemistry of Solids* **2006**, *67*, 1623.

[21] N. M. Markovic, H. A. Gasteiger, P. N. Ross, *Journal Of Physical Chemistry* **1995**, *99*, 3411.

[22] R. Gomez, J. M. Feliu, A.Aldaz, *Electrochimica Acta* **1997**, *42*, 1675.

[23] J. O. M. Bockris, S. Srinivasan, *Electrochimica Acta* **1964**, *9*, 31.

[24] D. B. Hibbert, *Introduction To Electrochemistry*, Macmillan Press Ltd., London, **1993**.

[25] A. Saraby-Reintjes, *Electrochimica Acta* **1986**, *31*, 251.

[26] N. M. Markovic, C. A. Lucas, V. Climent, V. Stamenkovic, P. N. Ross, *Surface Science* **2000**, *465*, 103.

[27] B. E. Conway, B. V. Tilak, *Electrochimica Acta* **2002**, *47*, 3571.

[28] S. Motoo, N. Furuya, *Journal of Electroanalytical Chemistry* **1984**, *167*, 309.

[29] J. Greeley, T. F. Jaramillo, J. Bonde, I. Chorkendorff, J. K. Norskov, *Nature Materials* **2006**, *5*, 909.
[30] J. Greeley, J. K. Norskov, *Surface Science* **2007**, *601*, 1590.
[31] J. Greeley, J. K. Norskov, L. A. Kibler, A. M. El-Aziz, D. M. Kolb, *Chem Phys Chem* **2006**, *7*, 1032.
[32] T. J. Davies, R. R. Moore, C. E. Banks, R. G. Compton, *Journal of Electroanalytical Chemistry* **2004**.
[33] T. J. Davies, R. G. Compton, *Journal of Electroanalytical Chemistry* **2005**, *585*, 63.
[34] T. J. Davies, S. Ward-Jones, C. E. Banks, J. D. Campo, R. Mas, F. X. Munoz, R. G. Compton, *Journal of Electroanalytical Chemistry* **2005**, *585*, 51.
[35] S. Pandelov, U. Stimming, *Electrochimica Acta* **2007**, *52*, 5548.
[36] S. Trasatti, *Journal of Electroanalytical Chemistry* **1972**, *39*, 163.
[37] B. E. Conway, B. V. Tilak, *Electrochimica Acta* **2002**, *47*, 3571.
[38] U. Muschiol, P. K. Schmidt, K. Christmann, *Surface Science* **1998**, *395*, 182.

Chapter 6
Summary and Conclusions

The present study was intended to investigate the hydrogen evolution reaction on Pt and Pt-group metal (PGM) surfaces. The exploration into the most active surfaces for catalysing the reaction was important, with a view to increasing the efficiency and reducing the cost of electrocatalytic hydrogen production for use as a fuel, either in proton-exchange membrane fuel cells (PEMFCs) or hydrogen based internal combustion engines (ICE-H_2) as an alternative to the combustion of fossil fuels.
The project aims outlined in section 1.7 give a more insightful view as to the specific intentions of the work and will be discussed in this section.

The initial experimental aspect of the project was concerned with the HER and HOR on polycrystalline Pt and the HER on other PGM surfaces (specifically Ir and Ru). The results for HOR were conducted partly as a test to calibrate the system in order to determine if the experimental setup used could reproduce published results by Maruyama *et al*[1] for polycrystalline Pt in 0.1 M $HClO_4$. The exchange current density figures were found to lie in the same range as the published works but the absolute values were considerably higher (2.42 mA cm^{-2} compared to 1.35 mA cm^{-2} found by Maruyama). This result was considered acceptable and subsequently the same tests were performed in 0.05 M H_2SO_4 which gave j_0 values which were directly comparable to figures found by Markovic *et al*[2] (0.89 mA cm^{-2} compared to 0.45 – 0.98 mA cm^{-2} found in the published work).

The second section of the project involved the application of multi-frequency AC voltammetry (MFACV) to the polycrystalline Pt electrode. It was noted that the UPD-H activity was frequency dependent over the frequency range tested, whilst OPD-H activity was frequency independent. A number of parameters within the experiment were varied to monitor the effect on hydrogen evolution. It was observed that variation in acid concentration was directly linked to the admittance signal of the MFACV as a fivefold increase in acid concentration resulted in a fivefold increase in admittance.

H_2 and N_2 were both used to degas the electrolyte solution (and subsequently for atmospheric overpressure) and it was found that hydrogen evolved less readily when under a hydrogen atmosphere.
MFACV was combined with rotation of the electrode to investigate the effect of rotation rate. However, it was found that the rotation forced contaminants to the electrode surface, blocking sites and hindering hydrogen evolution activity.
The temperature of the system was varied between 278 – 318 K. The admittance increased linearly with temperature up to 308 K, though above this temperature, the admittance decreased sharply. This was not observed with DC Tafel measurements taken over the same temperature range.

As the project advanced, the experimental setup was refined dramatically in order to increase the reproducibility and reliability of results by using more rigorous cleaning methods and higher grade reagents. This facilitated the investigation of single crystal electrode surfaces which are highly susceptible to contaminants.

The third section of the project involved the investigation of stepped single crystal Pt electrodes. This yielded one of the most important findings of the study, showing the structural independence of the hydrogen evolution reaction on stepped single crystal surfaces. This finding adds fuel to the debate surrounding this topic. Whilst it supports the findings of Feliu *et al*[3] along with earlier work from Lipkowski *et al*[4] and Kita *et al*[5], it disagrees with research by Markovic *et al*[2, 6] and Conway *et al*[7] who believe that the rate of HER does vary with Pt single crystal structure. The early stages of the single crystal investigations in the present study indicated that different stepped Pt surfaces were giving rise to a range of exchange current density values and limiting admittance density values (in the MFACV experiments). This indicated that the HER was occurring at different rates on each surface and that the reaction was therefore dependent upon the single crystal surface structure. On further investigation it was noted that the larger crystal beads gave rise to the lower exchange current density values and the smallest crystal beads gave the higher values. Thus, there was a proportionality between the exchange current density and the reciprocal of the electrode area (despite all voltammograms being normalised to electrode area). Numerous experiments were then constructed to deduce the nature of this discrepancy. Linear sweep voltammetry was performed on two Pt{111} crystals of

different size which yielded j_0 figures supporting the observations (i.e. the larger electrode gave the lower exchange current density figure). The same test was performed on a Pt{110} crystal which, depending on the cooling method after annealing, reconstructed in different surface morphologies. It was observed that cooling the crystal in CO or H_2 gave differently shaped cyclic voltammograms, yet the linear sweep measurements on the two reconstructions gave very closely matching j_0 values, showing that the discrepancies in exchange current density previously observed were not related to structural differences. However, the most significant experiment involved the range of stepped single crystals and repeating the experiment in three different configurations in relation to the electrolyte. The electrode was (i) annealed and held in the hanging meniscus configuration. It was then (ii) coated in CO and held in the hanging meniscus configuration, and (iii) partially submerged into the electrolyte with the hemisphere of the bead still coated with CO (shown schematically in fig.3.6.1). This experiment eliminated the hanging meniscus and any enhanced diffusion which may occur at electrode edge sites. The stepped single crystals in configuration (i) showed a linear relationship between exchange current density and area. This was also visible to an extent in configuration (ii), though it was much less pronounced. No such trend could be seen in when the electrode was partially submerged. The difference in j_0 between configurations (i) and (ii) represents the effect of the electrode hemisphere being blocked by CO, deactivating the Pt sites and thereby inhibiting the mobility of H atoms over the Pt surface. The discrepancy between the exchange current density is greater for the smaller electrodes, showing that the recombination of hydrogen on the hemisphere of the bead adjacent to the planar surface is more significant for these electrodes. The smaller the electrode, the greater the ratio of "active" hemisphere area to planar surface area hence the more significant the decrease in exchange current density will be when the hemisphere is deactivated. The difference in j_0 between electrode configurations (ii) and (iii) therefore represents the (less significant) effect of diffusion at the edge sites at the gas/electrode/electrolyte interface, which does not occur when the bead is partially submerged in the electrolyte. Thus with these effects eliminated, it can be seen that there is no significant change in the exchange current density across all of the stepped Pt single crystal surfaces tested, and hence there is no structural effect on the hydrogen evolution reaction.

Thick metal films of Rh, Au and Pd were deposited onto a Pt{111} electrode surface using the "forced-deposition" method[8, 9] and annealed to give single crystalline surfaces comparable to published bulk electrode equivalents[10-12]. The aim was to investigate whether strain within the lattice of the deposited film resulted in an enhanced hydrogen evolution rate. It was found that none of the thick single crystal films were more effective at evolving hydrogen than the bare Pt{111} surface. Tafel slopes on each of the surfaces were similar to the accepted values for the bulk metals.

Attempts were made to form a bulk Ir electrode in the same manner as the other single crystal thick films, though it was found that Ir would not deposit via the "forced-deposition" method. Subsequently, Ir was deposited via the contact of a droplet of H_2IrCl_6 with the electrode and momentary exposure of this to a Bunsen flame. However, the deposit was not single crystalline and formed a rough Ir surface. This surface was annealed in an attempt to rearrange the Ir to form a single crystalline structure, though this proved unsuccessful. Instead, a dispersed array of Ir islands was speculated to form. This surface gave an enhanced hydrogen evolution rate, with exchange current density greater than that on bare Pt. In order to determine whether this effect was related to the arrangement of the deposit or a genuine catalytic effect from the Ir, the test was repeated by depositing Pt onto the Pt{111} electrode using the same deposition method. This produced a similarly rough Pt surface which also gave enhanced hydrogen evolution activity (though not as great as that observed with the Ir deposits). The cyclic voltammetry of the Pt and Ir deposited surfaces showed no increase in surface charge, implying that the area of the electrode was not increased as a result of the deposition. It was concluded that the Ir deposits were highly dispersed and sharp, covering very little of the electrode surface (as the cyclic voltammograms showed the surfaces to have significant Pt{111} structure), giving rise to a net diffusion domain greater than that that of the planar electrode surface without a significant increase in electrode area. The Pt deposits were assumed to be much wider and flatter, covering a greater surface area (though not significantly increasing the surface area) since the cyclic voltammograms showed less Pt{111} long-range order than those on the Ir deposited surface.

Pd was deposited onto a Pt{111} electrode in submonolayer increments and the hydrogen evolution activity was monitored accordingly. It was observed that the Pd

coverage had little effect on the HER kinetics until almost a full monolayer coverage was reached. As further Pd was added, the surface began to adopt more Pd-like characteristics, i.e. the Tafel slope increased from 32.3 mV/dec on bare Pt{111} to 39.2 mV/dec at Pd coverage of almost two monolayers (compared to accepted figures of 29 mV/dec on Pt[13] and 42 mV/dec on Pd[13]). Fitting rate constants to the data using a computational fitting routine showed that the Pt surface was still influencing the HER at this Pd coverage (hence why the Tafel slope was not as high as 42 mV/dec). When the fitting routine was applied to the bulk single crystal Pt surface, it was also observed that the Tafel rate constant (for the HER occurring on Pt) was high, yet it was not influencing the overall kinetics in this case as the Heyrovsky rate constant (for the HER on Pd) dominated.

Pd-Pt surface alloys were created by gently heating large Pd deposits on a Pt{111} electrode in a Bunsen flame. It was found that the Pd within the surface layer had no significant effect on the HER as the exchange current density and Tafel slope were unaffected even at 75 % Pd in the surface alloy. These results are both new and intriguing. In order to rationalise the independence of the HER on Pt{*hkl*} electrodes and on model thin films, it is suggested that a large proportion of the HER kinetics may be occurring within the electrode surface rather than at the surface. Hence the surface composition and atomic structure do not greatly influence the overall hydrogen evolution kinetics.

Bi was deposited onto Pt{111}, Pt{100} surfaces as in experiments conducted by Gomez and Feliu[3, 14] as well as Pt{110}. It was found that hydrogen was still evolved at a significant rate when all UPD-H Pt sites were blocked by Bi adsorbed on the surface. Gomez and Feliu found that the exchange current density diminished below 0.1 mA cm^{-2} on Pt{111}[14], whilst in the present study the figure was found to go no lower than 0.51 mA cm^{-2}. The Pt{100} results were in good agreement with Gomez's results over a similar Bi coverage range[3], although the very high surface coverages achieved by Gomez could not be reproduced here. The Bi on Pt{110} results showed similar trends to the Pt{111} and Pt{100} surfaces tested. All of the results confirm previous findings that UPD-H appears to play no role in HER kinetics.

Reviewing these results in light of the project aims, this work has been successful in the broadness of the study, despite many experimental problems and drawbacks.

- Hydrogen evolution has been studied on a wide range of surfaces, bringing clarity to the area by combining many results together, facilitating comparisons between the activity, rates and mechanisms for the reaction.
- Polycrystalline Pt and a range of stepped single crystal Pt electrodes were studied (using cyclic voltammetry, linear sweep voltammetry and multi-frequency AC voltammetry) and it was determined that there was no dependence of the HER on the structure of the planar Pt surfaces. It was however observed that electrode configuration does have a strong influence over the rate of hydrogen evolution.
- Epitaxial films of Au, Pd and Rh were successfully deposited onto a Pt{111} electrode, producing single-crystalline thick films similar to the bulk metal electrodes. It was observed that there was no significant effect relating to lattice strain within these thick films as they behaved in a similar manner to the bulk metal, none of the surfaces producing higher hydrogen evolution rates than the Pt substrate.
- Further surface investigations showed that rough deposits of Ir and Pt on a Pt{111} electrode enhanced the hydrogen evolution activity. The deposits are thought to be highly dispersed islands, with diffusion domains greater than those of the planar substrate, leading to the increased hydrogen evolution rate observed.
- Pd was deposited onto a Pt{111} electrode in small increments, showing that Pt dominated the hydrogen evolution mechanism on the surface at Pd coverages up to one monolayer and was still highly influential on the kinetics at two monolayers of Pd.
- Pd-Pt surface alloys showed that Pd had little or no influence on the HER activity even when the alloy composition was 75 % Pd. This led to the suggestion that hydrogen evolution is occurring on subsurface sites which is highly influential on the overall HER rate, providing an explanation as to why Tafel kinetics are still influential when thin Pd films are deposited onto Pt and why the surface arrangement for Pt{*hkl*} electrodes has no significant influence on the HER kinetics.

There are still many areas of interest which could be further investigated. The MFACV was not used to the extent it could have been. It is potentially a powerful tool, though the measurements in this project were performed at AC frequencies too low to monitor the frequency dependence of OPD-H.

Also, much further work could be invested into the investigation of alloys. Although no rate-enhancing results were observed in this work, recent work on Pt-Bi alloys[17] and Ni-S-Co alloys[18] have given exchange current densities greater than those observed on Pt.

Another avenue which requires further exploration is the deposition of metals onto Pt to give "rough" surfaces. Firstly, scanning probe techniques could be used to view the structure of the surfaces, followed by investigation into the reproducibility of the surfaces. Refinement of the island size and dispersion may lead to much greater HER enhancement and it may prove possible to produce microelectrodes to mimic this activity and even more "active" supported electrocatalysts.

This study also poses the possibility that the complete elucidation of the kinetics of HER on different metals (particularly Pd on Pt) may lie in a full understanding of the selvedge region. This would explain clearly the lack of structural sensitivity of the HER on Pt{*hkl*} electrodes and thin films deposited onto Pt electrodes in the present study.

However hydrogen evolution advances in the future, it is hoped that this study may, in some small way contribute. It is also hoped that hydrogen fuel cell technology and hydrogen storage advance alongside this, in order to provide a cleaner and more sustainable fuel source for generations to come.

References

[1] J. Maruyama, M. Inaba, K. Katakura, Z. Ogumi, Z.-I. Takehara, *Journal of Electroanalytical Chemistry* **1998**, *447*, 201.

[2] N. M. Markovic, B. N. Grgur, P. N. Ross, *Journal of Physical Chemistry B* **1997**, *101*, 5405.

[3] R. Gomez, A. Fernandez-Vega, J. M. Feliu, A.Aldaz, *Journal of Physical Chemistry* **1993**, *97*, 4769.

[4] K. Seto, A. Ianelli, B. Love, J.Lipkowski, *Journal of Electroanalytical Chemistry* **1987**, *226*, 351.

[5] H. Kita, S. Ye, Y. Gao, *Journal of Electroanalytical Chemistry* **1992**, *334*, 351.

[6] N. M. Markovic, S. T. Sarraf, H. A. Gasteiger, P. N. Ross, *Journal of The Chemical Society Faraday Transactions* **1996**, *92*, 3719.

[7] J. H. Barber, S. Morin, B. E. Conway, *Journal of Electroanalytical Chemistry* **1998**, *446*, 125.

[8] S. E. Huxter, G. A. Attard, *Electrochemistry Communications* **2006**, *8*, 1806.

[9] F. J. Vidal-Iglesias, A. Al-Akl, D. J. Watson, G. A. Attard, *Electrochemistry Communications* **2006**, *8*, 1147.

[10] T. H. M. Housmans, M. T. M. Koper, *Journal of Electroanalytical Chemistry* **2005**, *575*, 39.

[11] D. Bizzotto, J. Lipkowski, *Journal of Electroanalytical Chemistry* **1996**, *409*, 33.

[12] N. M. Markovic, C. A. Lucas, V. Climent, V. Stamenkovic, P. N. Ross, *Surface Science* **2000**, *465*, 103.

[13] B. E. Conway, B. V. Tilak, *Electrochimica Acta* **2002**, *47*, 3571.

[14] R. Gomez, J. M. Feliu, A.Aldaz, *Electrochimica Acta* **1997**, *42*, 1675.

[15] Z.-Q. Tian, B. Ren, D.-Y. Wu, *Journal of Physical Chemistry B* **2002**, *106*, 9463.

[16] R. J. Nichols, A. Bewick, *Journal of Electroanalytical Chemistry* **1988**, *243*, 445.

[17] J. Greeley, T. F. Jaramillo, J. Bonde, I. Chorkendorff, J. K. Norskov, *Nature Materials* **2006**, *5*, 909.

[18] Q. Han, K. Liu, J. Chen, X. Wei, *International Journal of Hydrogen Energy* **2003**, *28*, 1345.

Appendix I

(A) The Matlab fitting routine used to find Volmer, Tafel and Heyrovsky rate constants from Tafel data.

```
function
[fitted_values,err_value,flag,counter]=fit_routine(E,I,initial_values
,params)
 [fitted_values,err_value,flag]=fit_routine(E,I,initial_values,params
)
 Fits Tafel slope for hydrogen evolution based on the
 Volmer (k1f k1b), Tafel (k2f k2b) and Heryovsky (k3f k3b) steps
 E
 I
 initial_values - estimates for the parameters to fit (can be quite
crude)
 initial_values=[k1f,k1b,k2f,k2b,k3f,k3b]
 params - constants for the dataset
 params=[alpha,T,Cs/Cb,cH,A]
 fitted_values - parameter values from routine
 err_value - final least squares error
 flag - 1 converged or 0 failed

 set options for fitting
options=optimset('Display','iter','TolFun',1e-9,'TolX',1e-
12,'maxiter',2000);


 start the solver
[fit,fval,flag]=fminsearch(@(fit)fitfun(fit,params,E,I),initial_value
s,options);
fitted_values=abs(fit);
err_value=fval;


 plot the result

stepup=logspace(0,3,1000);
for l=1:6
    counter(l)=0;
    sens=fval;err=0;
    test(l)=0;
    while (counter(l) < 1000 & test(l) < 0.001)
        counter(l)=counter(l)+1;
        tfit=abs(fit);
        tfit(l)=tfit(l)*stepup(counter(l));
        k1f=tfit(1);
        k1b=tfit(2);
        k2f=tfit(3);
        k2b=tfit(4);
        k3f=tfit(5);
        k3b=tfit(6);

        alpha=params(1);
        T=params(2)+273.15;
        CsCb=params(3);
        cH=params(4);
        A=params(5);
```

```
        F=96485;
        R=8.3145;
        f=F/(R*T);

        a=(k2b*CsCb)-k2f;
        b=-((cH*k1f*exp(-alpha*f*E))+(2*k2b*CsCb)+(k1b*exp((1-
alpha)*f*E)));
        c=(cH*k1f*exp(-alpha*f*E))+(k2b*CsCb);
        theta=-(b+sqrt(b.^2-(4.*a.*c))./(2.*a);
        v1=cH*k1f*(1-theta).*exp(-alpha*f*E)-(k1b.*theta.*exp((1-
alpha)*f*E));
        v2=(k2f.*theta.^2)-(CsCb.*k2b.*(1-theta).^2);
        v3=cH*k3f*theta.*exp(-alpha*f*E)-(k3b*CsCb*(1-theta).*exp((1-
alpha)*f*E));
        J=A*F*(v1+v3);
        err=0;
        for k=1:length(E)
            t(k)=(real(log10(I(k)))^2-
real(log10(J(k)))^2)/real(log10((I(k))));
            err=err+log10(1+(0.5*t(k)^2));
        end
        test(1)=abs(sens-err)/sens;
    end
end

fit=abs(fit);
k1f=fit(1);
k1b=fit(2);
k2f=fit(3);
k2b=fit(4);
k3f=fit(5);
k3b=fit(6);

alpha=params(1);
T=params(2)+273.15;
CsCb=params(3);
cH=params(4);
A=params(5);
F=96485;
R=8.3145;
f=F/(R*T);

a=(k2b*CsCb)-k2f;
b=-((cH*k1f*exp(-alpha*f*E))+(2*k2b*CsCb)+(k1b*exp((1-alpha)*f*E)));
c=(cH*k1f*exp(-alpha*f*E))+(k2b*CsCb);
theta=-(b+sqrt(b.^2-(4.*a.*c))./(2.*a);
v1=cH*k1f*(1-theta).*exp(-alpha*f*E)-(k1b.*theta.*exp((1-
alpha)*f*E));
v2=(k2f.*theta.^2)-(CsCb.*k2b.*(1-theta).^2);
v3=cH*k3f*theta.*exp(-alpha*f*E)-(k3b*CsCb*(1-theta).*exp((1-
alpha)*f*E));
J=A*F*(v1+v3);


figure(1)
hold off
plot(E,real(log10(I)),'r:')
hold on
plot(E,real(log10(J)),'b--')
legend({'Data' 'Fit Result'})
xlabel ('E / V')
```

```
ylabel('I')
figure(2)
plot(E,theta)
xlabel ('E / V')
title('\theta')
figure(3)
plot(E,real(log10([v2 v3])))
legend({'\itv\rm_2' '\itv\rm_3'})
xlabel ('E / V')

 fitting function
function err=fitfun(fit,params,E,I)
 function err=Tafelfit(fparams,params,E)
 Fits Tafel slope for hydrogen evolution based on the
 Tafel, Volmer and Heryovsky steps
 fparams=[k1f,k1b,k2f,k2b,k3f,k3b]
 params=[alpha,T,Cs/Cb,cH,A]

fit=abs(fit);
k1f=fit(1);
k1b=fit(2);
k2f=fit(3);
k2b=fit(4);
k3f=fit(5);
k3b=fit(6);

alpha=params(1);
T=params(2)+273.15;
CsCb=params(3);
cH=params(4);
A=params(5);
F=96485;
R=8.3145;
f=F/(R*T);

err=0;

a=(k2b*CsCb)-k2f;
b=-((cH*k1f*exp(-alpha*f*E))+(2*k2b*CsCb)+(k1b*exp((1-alpha)*f*E)));
c=(cH*k1f*exp(-alpha*f*E))+(k2b*CsCb);
theta=-(b+sqrt(b.^2-(4.*a.*c))./(2.*a);
v1=cH*k1f*(1-theta).*exp(-alpha*f*E)-(k1b.*theta.*exp((1-
alpha)*f*E));
v2=(k2f.*theta.^2)-(CsCb.*k2b.*(1-theta).^2);
v3=cH*k3f*theta.*exp(-alpha*f*E)-(k3b*CsCb*(1-theta).*exp((1-
alpha)*f*E));
J=A*F*(v1+v3);

for k=1:length(E)
    t(k)=(real(log10(I(k)))^2-
real(log10(J(k)))^2)/real(log10((I(k))));
    err=err+log10(1+(0.5*t(k)^2));
end
```

(B) The Matlab fitting routine used to find Volmer and Tafel rate constants from Tafel data.

```
function
[fitted_values,err_value,flag,counter]=voltaf_fit(E,I,initial_values,
params)

 set options for fitting
options=optimset('Display','iter','TolFun',1e-9,'TolX',1e-
12,'maxiter',2000);

 start the solver
[fit,fval,flag]=fminsearch(@(fit)fitfun(fit,params,E,I),initial_value
s,options);
fitted_values=abs(fit);
err_value=fval;

Check the sensitivity of the values

stepup=logspace(0,3,1000);
for l=1:4
    counter(l)=0;
    sens=fval;
    test(l)=0;
    while (counter(l) < 1000 & test(l) < 0.001)
        counter(l)=counter(l)+1;
        tfit=abs(fit);
        tfit(l)=tfit(l)*stepup(counter(l));
        err=0;

        tfit=abs(fit);
        k1f=tfit(1);
        k1b=tfit(2);
        k2f=tfit(3);
        k2b=tfit(4);

        T=params(1)+273.15;
        cH=params(2);
        A=params(3);
        CsCb=params(4);
        alpha=params(5);

        F=96485;
        R=8.3145;
        f=F/(R*T);
        a=(k2b*CsCb)-k2f;
```

```
  b=-((cH*k1f*exp(-alpha*f*E))+(2*k2b*CsCb)+(k1b*exp((1-
alpha)*f*E)));
        c=(cH*k1f*exp(-alpha*f*E))+(k2b*CsCb);
        theta=-(b+sqrt(b.^2-(4.*a.*c))./(2.*a);

  v1=cH*k1f*(1-theta).*exp(-alpha*f*E)-(k1b.*theta.*exp((1-
alpha)*f*E));
        J=F.*v1;
        for k=1:length(E)

  t(k)=(real(log10(I(k)))^2-real(log10(J(k)))^2)/real(log10((I(k))));
            err=err+log10(1+(0.5*t(k)^2));
        end
        test(1)=abs(sens-err)/sens;
    end
end

%% Plot the results

fit=abs(fit);
tfit=abs(fit);
k1f=tfit(1);
k1b=tfit(2);
k2f=tfit(3);
k2b=tfit(4);

T=params(1)+273.15;
cH=params(2);
A=params(3);
CsCb=params(4);
alpha=params(5);

F=96485;
R=8.3145;
f=F/(R*T);
a=(k2b*CsCb)-k2f;
b=-((cH*k1f*exp(-alpha*f*E))+(2*k2b*CsCb)+(k1b*exp((1-alpha)*f*E)));
c=(cH*k1f*exp(-alpha*f*E))+(k2b*CsCb);
theta=-(b+sqrt(b.^2-(4.*a.*c))./(2.*a);
v1=cH*k1f*(1-theta).*exp(-alpha*f*E)-(k1b.*theta.*exp((1-
alpha)*f*E));
J=F.*v1;
figure(1)
hold off
plot(E,real(log10(I)),'r:')
hold on
plot(E,real(log10(J)),'b--')
legend({'Data' 'Fit Result'})
```

```
xlabel ('E / V')
ylabel('I')
figure(2)
plot(E,theta)
xlabel ('E / V')
title('\theta')

%%
%fitting function
function err=fitfun(fit,params,E,I)
%function err=Tafelfit(fparams,params,E)
%Fits Tafel slope for hydrogen evolution based on the
%Tafel, Volmer and Heryovsky steps
%fparams=[k1f,k1b,k2f,k2b,k3f,k3b]
%params=[alpha,T,Cs/Cb,cH,A]

fit=abs(fit);
tfit=abs(fit);
k1f=tfit(1);
k1b=tfit(2);
k2f=tfit(3);
k2b=tfit(4);


T=params(1)+273.15;
cH=params(2);
A=params(3);
CsCb=params(4);
alpha=params(5);

F=96485;
R=8.3145;
f=F/(R*T);
a=(k2b*CsCb)-k2f;
b=-((cH*k1f*exp(-alpha*f*E))+(2*k2b*CsCb)+(k1b*exp((1-alpha)*f*E)));
c=(cH*k1f*exp(-alpha*f*E))+(k2b*CsCb);
theta=-(b+sqrt(b.^2-(4.*a.*c))./(2.*a);
v1=cH*k1f*(1-theta).*exp(-alpha*f*E)-(k1b.*theta.*exp((1-
alpha)*f*E));
J=F.*v1;
err=0;
if alpha > 1
    err=alpha*1e6;
end
for k=1:length(E)
    t(k)=(real(log10(I(k)))^2-real(log10(J(k)))^2);
    err=err+log10(1+(0.5*t(k)^2));
end
```